Application of Pressure Sensitive Paints to Hammerhead Launcher Aerodynamics

Master of Science Thesis

Vinicius Merlin Santos Costa

Delft University of Technology

Application of Pressure Sensitive Paints to Hammerhead Launcher Aerodynamics

Master of Science Thesis

For obtaining the degree of Master of Science in Aerospace Engineering at Delft University of Technology

Vinicius Merlin Santos Costa
4473779

September 10, 2024

Faculty of Aerospace Engineering · Delft University of Technology

DELFT UNIVERSITY OF TECHNOLOGY
DEPARTMENT OF AERODYNAMICS

The undersigned hereby certify that they have read and recommend to the Faculty of Aerospace Engineering for acceptance the thesis entitled **“Application of Pressure Sensitive Paints to Hammerhead Launcher Aerodynamics”** by **Vinicius Merlin Santos Costa** in fulfillment of the requirements for the degree of **Master of Science**.

Dated: September 10, 2024

Supervisors:

Dr. ir. A. D’Aguanno
Reader 1

Dr. ir. B.W. van Oudheusden
Reader 2

Dr. ir. F.F.J. Schrijer
Reader 3

Preface

Herein lies my MSc thesis report on titled "Application of Pressure Sensitive Paints to Hammerhead Launcher Aerodynamics". This study was performed as part of my graduation project for the MSc. Aerospace Engineering at the Delft University of Technology, with a track focusing on aerodynamics.

My personal goals for this study were twofold. The first goal is for this thesis report, to form a basis for future PSP research at the TU Delft. I wish to create a document that extensively goes over the relevant aspects of PSP, such that future researchers may delve into PSP literature well informed after having read this report. The second goal is to help contribute to ongoing hammerhead fairing research. This is a very difficult topic that has been studied for more than half a century, but our understanding is currently still lacking due to the complex aerodynamic and structural interactions involved. With the results obtained in this thesis, I hope to contribute to the development of the Vega-E launcher, one of the two models studied in this thesis.

I would like to thank my supervisors Alessandro, Bas and Ferry for guiding me through this journey. Their input throughout the process really helped me focus and narrow down what I want to research and how to approach this. I would furthermore like to thank them for all the guidance they provided in performing experiments inside the TST-27 and everything that goes into that.

Furthermore, I would like to thank all the technicians of the HSL and LSL for all the help they provided throughout the experimental phase of my study. Especially in regard to finding equipment, as this proved to be one of the most time-consuming aspects of experimenting. Special thanks to: Frits Donker Duyvis for answering all questions I had regarding optics and operating the tunnel; Gert-Jan Berends, for all the help in setting up computer equipment and getting that pesky PTU and thermocouples working after countless hours; Henk-Jan simmers, for the patience to paint all the models and to listen to my feedback regarding the painting; Peter Duyndam for operating the tunnel and any help I needed with installing things in the tunnel; Dennis Bruikman for setting up the peltier element and any other small help that I needed during the experiments.

In addition, I would also like to thank Alberto Felipe Rius Vidales, for helping me set up the DLR lamp and discussing PSP with Alessandro and I at the start of my thesis. And not to forget, I would like to thank Hirotaka Sakaue and Nicholas Slusher from the University of Notre Dame, for taking time from their busy schedules to answer PSP questions that I had during the start of my experimental campaign.

Of course, last but not least I would like to thank all my friends and family for keeping me sane during the busiest times of my thesis. Without their continued company, my thesis would have felt a lot more arduous and slower.

Abstract

As humanity becomes more attentive to the necessity of sustainable design, so too is spaceflight placed under scrutiny. As a result, sustainability is now of key importance in modern space design. An approach to make spaceflight more sustainable is by making use of the 'hammerhead fairing' (HHF) configuration. In this configuration, the payload fairing (PLF) has a larger diameter than the launch vehicle (LV). This allows for larger payloads to be carried using the same LV components, thereby reducing manufacturing and design costs. The HHF configuration is used for many modern launchers, such as the Falcon 9 and Vega-C.

The difference in diameter between PLF and LV exposes the LV to strong aerodynamic forcing in the transonic regime called buffeting. Buffeting occurs due to unsteady flow separation caused by the area decrease along with shock wave-boundary layer interactions (SWBLI). When unaccounted for, buffeting can lead to LV failure. Historically, buffeting has been studied using pressure taps and CFD. However, pressure taps offer limited spatial resolution and CFD fails to predict the extent of the flow separation.

To remedy the limitations of historical methods, in this study Pressure Sensitive Paint (PSP) was applied to investigate the flow phenomena of HHF launchers. PSPs are a relatively new flow measurement technique that allows for quantitative measurements of surface pressure levels in a non-intrusive manner with high spatial resolution. This is done by using luminescent dyes that react to surface pressure levels. Prior to this study, PSP had not been successfully applied before in Delft. Therefore, along with investigating the aerodynamics of HHF launchers, the second main goal of this study was to successfully implement PSP.

PSP was implemented using the "standard intensity based method" and a commercial PSP formulation (UniFIB PSP). This method uses the ratio of the luminescent intensity at a reference condition divided by the intensity at the measurement condition to calculate the time averaged pressure by means of a calibration. Data processing was implemented by virtue of an in-house PSP code created from scratch in python. The implementation was found to have an uncertainty of up to $1.5-2.5kPa$, with repeated measurements of the same configuration showing a precision of around $1kPa$. The biggest error sources were found to be related to erroneous painting, calibration curve uncertainties and temperature gradients along the model.

Measurements were taken on two HHF LV models in the TST-27. The goal was to study the impact of Mach number and angle of attack variations on the aerodynamics. The first model used was the (Coe and Nute) Model 11, which is a commonly used buffeting test case in literature. The second model was the Vega-E launcher, that is currently being developed by the European Space Agency. Both models have two shocks over the PLF in the transonic regime and flow separation at the edge of the PLF. On the Model 11, the flow separation is caused by the change in geometry, whereas for the Vega-E a separation shock can be found.

Pressures obtained with PSP on the Model 11 were found to have a good match with historical data when accounting for blockage. The Mach number effect was studied at $M = [0.7, 0.75, 0.8]$, $\alpha = 0°$. With increasing Mach number, the shocks were found to shift downstream and the separation length slightly increased. Outside the separation and the shocks, C_P levels were independent of M. Changing α to 4° caused a downstream shift of the shocks and an upstream shift of the reattachment on the leeward side, with the opposite effect on the windward side. This was coupled to an increase in pressure jump past the shocks on the leeward side and the opposite on the windward side. These findings are consistent with literature.

On the Vega-E, a similar Mach number effect was found for $\alpha = 0°$. While the separation length was found to be much smaller, a similar increase in length with M was found. The lower separation length can likely be attributed to the smooth geometry transition on the Vega-E. The impact of $\alpha = 4°$ was found to be slightly different from the Model 11. The same pattern was seen for the reattachment point and the first shock, but a smaller shift in shock position was see. Instead, the second shock was found to have the opposite pattern. On the leeward side, the shock moved slightly upstream and decreased in pressure jump, with the opposite pattern on the windward side. Lastly, protuberances were installed that mimic the geometry of the real launcher. These were found to cause a downstream shift in flow reattachment, and lower the pressure jump on the second shock wave. Downstream of the protuberances, the impact of the protuberances on the pressure was found to be limited to their direct proximity.

Results obtained in this study will aid in the design of the Vega-E launcher, paving the way for more sustainable spaceflight. The surface pressure data obtained here can serve to validate and verify CFD simulations that are planned in the future. In addition, they can help inform structural and aerodynamic design decisions. Furthermore, the PSP implementation work carried out in this thesis enables future PSP research to be performed in Delft, which can deliver a wealth of data that was previously unavailable.

Keywords: Hammerhead Fairing, Transonic Flow, Model 11, Vega-E, Flow Separation, Shock Waves, PSP, Standard PSP, Intensity Based PSP, PSP Temperature Corrections

Contents

List of Figures

List of Tables

Nomenclature

List of abbreviations

AC	Alternating Current
AEB	Agência Espacial Brasileira
AL	Ambient Light
b.l.	Boundary Layer
BFF	Buffet Forcing Function
BFS	Backwards Facing Step
CCD	Charge Couple Device
CFD	Computational Fluid Dynamics
CMOS	Complimentary Metal Oxide Semiconductor
DC	Dark Current Noise
DC	Direct Current
DIC	Digital Image Correlation
DLR	German Aerospace Center
DLT	Direct Linear Transformation
DMD	Dynamic Mode Decomposition
DNS	Direct Numerical Simulations
ESA	European Space Agency
FOV	Field Of View
HHF	Hammerhead Fairing
HSL	High Speed Laboratory
IR	Infrared
ISSI	Innovative Scientific Solutions Incorporated
JAXA	Japanese Aerospace Exploration Agency
LES	Large Eddy Simulation
LV	Launch Vehicle
LWIR	Long Wavelength Infrared
MWIR	Mid Wavelength Infrared
NETD	Noise Equivalent Temperature Difference
NI	National Instruments
NIR	Near Infrared
OML	Outer Mold Line
PIV	Particle Image Velocimetry
PLF	Payload Fairing
POD	Proper Orthogonal Decomposition
PSP	Pressure Sensitive Paint
PTU	Precision Timing Unit
R&D	Research and Development
RANS	Reynolds Averaged Navier-Stokes
RGB	Red Green Blue
SLS	Space Launch System
SNR	Signal to Noise Ratio
SWBLI	Shock Wave Boundary Layer Interaction
SWIR	Short Wavelength Infrared
TSP	Temperature sensitive paint
TST-27	Transonic/Supersonic Wind Tunnel
TUPLE	Transonic PIV based unsteady pressure measurements for launcher environment
Vis	Visible light
VLT	Vision Light Tech

List of symbols

$[O_2]$	Oxygen concentration	$\frac{mol}{m^3}$
$\bar{p}_{tot}$	Mean total pressure	Pa
$\delta(t)$	Dirac delta	–
δ	Boundary layer thickness	m
ϵ	Emissivity	–
γ	Heat capacity ratio of air	–
ι	Light incidence angle	°
λ	Wavelength	m
λ_ι	Central filter wavelength at incidence ι	m
μ_∞	Freestream dynamic viscosity of air	$\frac{kg}{m \cdot s}$
μ_{ref}	Reference dynamic viscosity of air	$\frac{kg}{m \cdot s}$
ω, ϕ, κ	Euler angles	°
ϕ	Azimuthal angle	°
ϕ_n	Orthogonal basis functions	–
ρ	Density	$\frac{kg}{m^3}$
ρ_∞	Freestream density	$\frac{kg}{m^3}$
σ_I	Standard deviation of pixel intensity	–
σ_p	Standard deviation of pressure	Pa
τ	Luminescent lifetime	s
τ	Transmissivity	–
τ_0	Luminescent lifetime in vacuum	s
τ_{dif}	Diffusion timescale	s
ζ	Test section coordinates	m
A	Pulse amplitude	$\frac{W}{m^2 \cdot sr}$
a	Reduced height of light beam (Schlieren)	m
A, B	T-dependent Stern-Volmer coefficients	–
a_P, b_P, c_P	Empirical p-dependence coefficients	–
a_T, b_T, c_T	Empirical T-dependence coefficients	–
A_{TI}	Temperature and intensity ratio constant	–
B_r	Blockage ratio	–
c	Concentration	$\frac{kg}{m^3}$
C_P	Pressure coefficient	–
C_i	In-situ PSP coefficients	–
$C_{P_{PSP}}$	C_P from PSP data	–
$C_{P_{rms}}$	RMS pressure fluctuation coefficient	–
C_{P_X}	C_P gradient along model L/D	–
D	PLF diameter	m
D_{CA}	Dark current and ambient correction	–
D_{O_2}	Oxygen diffusivity	$\frac{m^2}{s}$
E	Excitation light intensity	$\frac{W}{m^2 \cdot sr}$
f_c	Principal distance	m
f_l	focal length	m
f_l2	focal length schlieren head	m
H	Biconvex rod height	m

h	Hour	$3600s$
h	Paint layer thickness	m
H_0	Field of view	m
H_b	Boat-tail height step	m
H_s	Small BFS height step	m
H_T	Test section height	–
I	Luminescent intensity	$\frac{W}{m^2 \cdot sr}$
I_0	Luminescent intensity at vacuum	$\frac{W}{m^2 \cdot sr}$
I_{amb}	Ambient light intensity	$\frac{W}{m^2 \cdot sr}$
I_{body}	True emitted intensity	$\frac{W}{m^2 \cdot sr}$
I_{corr}	Corrected intensity / image	–
I_{FFa}	Flat field averaged imaged	–
I_{filt}	Filtered flat field image	–
I_{meas}	Measured light intensity	$\frac{W}{m^2 \cdot sr}$
I_{med}	Air/window light emission	$\frac{W}{m^2 \cdot sr}$
$I_{rat,ref}$	I_{rat} between measurement reference and calibration reference	–
I_{rat}	Intensity Ratio	–
I_{raw}	Raw image / intensity	–
I_{ref}	Reference intensity or image	$\frac{W}{m^2 \cdot sr}$
K	Gladstone-Dale constant	$\frac{m^3}{kg}$
k_q	Oxygen quenching rate constant	$s^{-}1$
Kn	Knudsen number	–
L/D	Non-dimensionalized model length	–
L_s	Separation length	m
L_i	DLT coefficients	m
L_p	Plate length	m
M	Mach number	–
M	Magnification factor	–
m_{ij}	Distortion parameters	–
min	Minute	$60s$
n	Refractive index	–
n_F	Filter refractive index	–
n_{air}	Refractive index of air	–
p	Pressure	Pa
p_∞	Freestream pressure	Pa
p_{O_2}	Oxygen partial pressure	Pa
p_{PSP}	Pressure computed with PSP	Pa
p_{ref}	Reference pressure	Pa
p_{rms}	Root Mean Square Pressure fluctuations	Pa
p_{tap}	Pressure measured with a transducer	Pa
p_{tot}	Total flow pressure	Pa
pr	Prandtl number	–
q	Dynamic pressure	Pa
R	Specific gas constant	J/kgK
r	Recovery factor	–
Re	Reynolds number	–
Re_D	Reynolds number using model radius	–
S	Solubility	$\frac{mol}{m^3 \cdot Pa}$
S_0	Electron ground state	eV
S_μ	Sutherland's constant	K

S_n	Singlet excited state n	eV
T	Temperature	K
t	Time	s
T_0	Sutherland's law reference T	K
T_n	Triplet excited state n	eV
T_∞	Freestream temperature	K
T_{air}	Air temperature	K
T_{aw}	Adiabatic wall temperature	K
T_{ref}	Reference temperature	K
T_{room}	Room temperature	K
T_{tot}	Total flow temperature	K
TB	Terabyte	$Byte$
U_∞	Freestream velocity	$\frac{m}{s}$
W_T	Test section width	–
x, y	Image plane coordinates	–
X, Y, Z	Object space coordinates	m
X_c, Y_c, Z_c	Camera Aperture coordinates	m
X_{O_2}	Oxygen molar fraction	%

1 Introduction

In the past 20 years the number of orbital launches sees an increasing trend[1,2]. As humanity becomes more attentive to the necessity of sustainable design in other industries, so too is spaceflight placed under scrutiny. As a result, sustainability is now of key importance in modern space design. An approach to make spaceflight more sustainable is by making use of the 'hammerhead fairing' (HHF) configuration.

In the HHF configuration, the nose cone and payload fairing (PLF) have a bigger diameter than the launch vehicle (LV). The PLF is connected to the LV by a frustum, called the boat-tail, which decreases the area in the intersection (see Figure 1.1). By making use of the HHF, the same LV that is used for straight configurations can be reused for bigger satellites, reducing the design and manufacturing costs of LV components. This works especially well with reusable stages, allowing one stage to be used for a wide variety of launches. Various modern and past LVs make use of the HHF configuration, including the Falcon launchers [3], Vega family launchers[4] and Atlas V[5] among others.

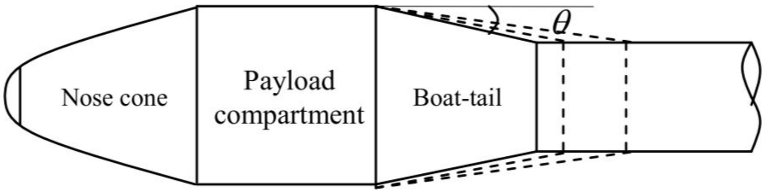

Figure 1.1: Schematic overview of the HHF configuration. Source: The work of Avelar et al. [1].

While the HHF is a promising way to make spaceflight more sustainable, it exposes the LV to strong, unsteady aerodynamic forcing in the transonic flow regime called 'buffeting' [2]. Buffeting occurs due to unsteady flow separation caused by the area decrease along with shock wave-boundary layer interactions (SWBLI). The fluctuations can cause vibrations that damage measurement hardware [3–5] and can lead to structural failure. In addition, the transonic flight regime is near the max dynamic pressure that occurs during LV ascent [6, 7], which makes it of key importance in the structural design of LVs.

Buffeting loads caused by the HHF have been studied since the 1960s using pressure transducers [3]. However, they offer insufficient spatial coverage to accurately reconstruct the buffet forcing and flow phenomena, even when using hundreds of pressure transducers [3, 8–10]. Additionally, pressure transducers are expensive to install and limited on where they can be installed depending on the geometry of the model.

Alongside pressure transducers, computational fluid dynamic (CFD) solvers are often used to predict LV loads and buffeting behaviour. Reynolds averaged Navier-Stokes (RANS) solvers are capable of predicting the steady loading environment with decent accuracy compared to wind tunnel data [11]. However, RANS is bad at predicting unsteady forces and requires wind tunnel validation. State of the art large eddy simulations (LES) and direct numerical simulations (DNS) are currently too costly or too inaccurate to be used for LV design [7]. The inaccuracies of CFD often stem from the fact that they use empirical models, which themselves are lacking due to limitations of the available measurement data [4, 12].

To overcome the aforementioned limitations, 'Pressure Sensitive Paints' (PSP) can be used [8, 10, 13]. PSP is a relatively new flow visualisation method that has recently been gaining traction [14]. It works by

---

[1] `https://www.statista.com/statistics/1343344/orbital-space-launches-global/`,retrieved August 2023
[2] `https://www.nature.com/articles/d41586-023-00048-7`, retrieved August 2023
[3] `https://www.spacex.com`, retrieved September 2023
[4] `https://www.avio.com/vega-e`, retrieved September 2023
[5] `https://ula.bsshost.me/rockets/atlas-v`, retrieved September 2023

using luminescent paints that act as optical sensors for pressure. This allows for quantitative measurements of surface pressure levels in a non-intrusive manner with high spatial resolution (see Figure 1.2). In addition, PSP is best applicable in the transonic flow range, thereby matching with the requirement for HHF research.

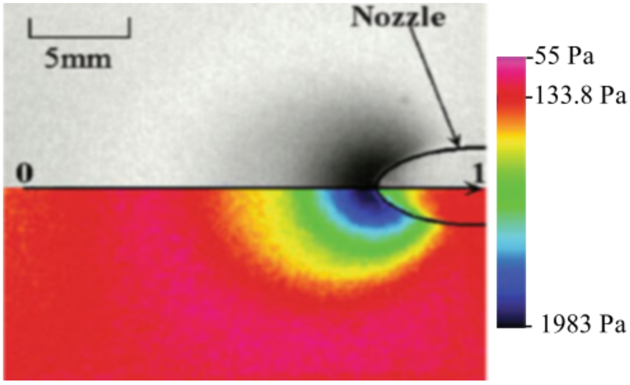

Figure 1.2: PSP results of a supersonic jet impinging on a plate at low static pressure. The top half shows the luminescent intensity, whereas the bottom half shows the obtained pressure after processing. Source: Image adapated from the work of Niimi et al. [15]

Over the past 10 years, HHF buffet research has been conducted by NASA and the Brazilian space agency (AEB) using PSP [1, 8]. Others, such as the Japanese aerospace exploration agency (JAXA) and NASA, have additionally performed PSP research for a straight PLF configuration [14, 16]. In these, PSP has been proven to be promising and powerful tool for LV research.

Recently, the TU Delft has been carrying out research on HHF geometries as part of the "TUPLE" project (Transonic PIV based unsteady pressure measurements for launcher environment) [17, 18]. This project focuses on comparing CFD and particle image velocimetry (PIV) data to better understand the buffeting flow phenomena. A key focus of this project is to characterize the aerodynamic forces on the new VEGA-E launcher currently being developed by the European Space Agency (ESA). To this end, in the current thesis project PSP measurements were performed on the same launcher model. The data obtained from PSP will help understand the flow phenomenon and can directly be compared with the PIV and CFD results. From this follows the first research objective:

The first research objective is to investigate the flow phenomena surrounding hammerhead payload fairings by analysing experimental pressure sensitive paint data.

To achieve this goal, measurements were taken on two HHF geometries, namely the Vega-E with a boat tail angle of 30° and the Coe and Nute Model 11 geometry, a commonly used test case in hammerhead literature. In addition, on the Vega-E model protuberances could be installed to mimic the geometry of the real launcher. Tests were performed under different Mach numbers and two angles of attack, 0° and 4°. The results obtained in this research will contribute to the verification of CFD simulations and better understanding of the transonic buffet, allowing for more efficient and sustainable design options. However, PSP as a method had never previously been successfully applied in Delft. Therefore this study should also serve as a pilot study for future PSP uses. From this follows the second objective of this thesis:

The second research objective is to apply and calibrate pressure sensitive paints for trans- and supersonic wind tunnel experiments at the TU Delft.

In order to achieve the first research objective, this second objective had to first be achieved. This was done by first performing an extensive literature study on PSP measurements. Following this, a commercial PSP formulation was selected (UniFIB PSP[6]), which was calibrated using square coupons in a pressurized box. After the calibration, measurements were taken on models with pressure taps and known pressures

---

[6] `https://innssi.com/single-component-pressure-sensitive-paints/`, retrieved June 2024,

to verify that the method was working. The data was processed using a inhouse PSP code that was created from scratch during the thesis. The original calibration and verification measurements yielded good results, thereby achieving the second research objective.

Research Questions

Similarly to the research objectives, it was chosen to split the main research questions into two, one regarding the implementation of PSP and another regarding HHF aerodynamics. Both questions were devised based on the literature study that follows in the first part of the report. Each question is complemented with sub-questions that help answer the main question.

Question [1], Implementation of PSP Measurements

The first research question was formulated as:

[1] ***What is the most optimal way to implement standard PSP for use with rigid models at the trans- and supersonic wind tunnel facilities of the TU Delft?***

This question is partially answered in the literature study presented in the report. In literature, there are no strict guidelines on how exactly PSP should be implemented for different applications. There are many potential ways to implement and analyse PSP data, leaving a lot of leeway on the experimental design. For this thesis, it was chosen to use the so called standard intensity based PSP. This is a relatively simple method to implement and is capable of providing time averaged pressure fields. The downsides of this method are not relevant for the rigid models used in this study and the implementation can be further used as a building block for more advanced methods. Note that the chosen implementation is not the most optimal for non-rigid or moving models. Further explanation for this choice can be found in Chapter 3.

To further help answer the first research question, the following sub-questions have been devised:

[1.1] **How should PSP calibration be performed with the resources of the TU Delft?**
[1.2] **What temperature corrections can be used?**
    [1.2.1] **How can temperature corrections best be applied at the TU Delft tunnels?**
    [1.2.2] **Can infrared measurements be used to corrected for temperature related errors?**
    [1.2.3] **Can thermocouples be used to correct for temperature related errors?**
[1.3] **What non-temperature related corrections are needed for experiments with rigid models, at the facilities of the TU Delft?**

These sub-questions all target specific aspects of PSP implementation, with a focus on the resources available in Delft. The combined answers to these will "paint a picture" of how to best implement PSPs.

Question [2], Hammerhead Fairing Investigation

It was chosen to research the buffeting phenomenon by looking at the impact of Mach number and angle of attack on the pressure distribution and flow features. The main research question is therefore:

[2] ***What is the impact of Mach number and angle of attack variations on the pressure field of hammerhead payload fairings at transonic Mach numbers?***

As previously mentioned, the investigation pertained to the Coe and Nute Model 11 and the Vega-E model. Data on the Model 11 is readily available in literature, so it can be used for direct comparisons of PSP results with other methods. For the Vega-E, a boat-tail angle of 30° was used as this is the one the ESA is most interested in. As the Vega-E is is currently being developed, research on this model contributes to future HHF design. To help answer the main research question, the following sub-questions were devised:

[2.1] **How does Mach number and / or angle of attack impact the pressure field?**
    [2.1.1] **Near the shocks?**

  - [2.1.2] **In the separated flow and reattachment point?**
  - [2.1.3] **Downstream of the reattachment?**
- [2.2] **How does the addition of protuberances impact the pressure field?**
  - [2.2.1] **Upstream of the protuberances?**
  - [2.2.2] **Downstream of the protuberances?**
- [2.3] **What is the pressure uncertainty of the PSP measurement?**
- [2.4] **How do the PSP results compare to the results from other measurement techniques?**
  - [2.4.1] **Is the paint intrusive?**
  - [2.4.2] **What similarities can be observed with PIV measurements?**

The second sub-question will only be answered for the Vega-E model, as scaled down protuberances were created that can be installed on this model. The last two sub-questions are again on the implementation of PSP, however, specific to the HHF models. These focus on verification and validation of PSP results.

Report outline

Besides the introduction, the report is divided into three parts and 8 chapters. Part I, titled "Theoretical Background", spans three chapters which cover the literature research that was necessary to carry out the experiments. Chapter 2 gives an overview of the aerodynamic phenomenon of the HHF PLF configuration. This is followed by an overview of PSP theory in Chapter 3. Lastly, at the end of the first part, PSP error sources and corrections are discussed in Chapter 4.

Part II is titled "Methods and PSP development". As suggested by the name, it contains two chapters which portray the experimental setup and the PSP implementation for the experiments that were performed in the TST-27. First, a description of the TST-27, test models, experimental setups and other experimental methods is given in Chapter 5. Then Chapter 6 gives a detailed description of the data analysis and PSP implementation that was used during this thesis.

Lastly, Part III is titled "Results and Discussions". Here, the results of the two HHF models that were investigated, namely the Coe and Nute Model 11 and the Vega-E, are presented and discussed. Chapter 7 presents the Model 11 results, whereas Chapter 8 the Vega results. These chapters focuses mostly on the aerodynamic results, as PSP related topics are discussed in the previous part. At the end of the third part, the report is rounded off with the study's conclusions and future recommendations given in Chapter 9.

PART I

Theoretical Background

2 Hammerhead Payload Fairing Aerodynamics

The present thesis focuses on the analysis of the Coe and Nute Model 11 and Vega-E HHF models using PSP. To this end, a literature study was performed to better understand the underlying aerodynamic principles and phenomena of the HHF LV configuration. This study is summarized in the current chapter. First, Section 2.1 starts with a description of the HHF geometry and commonly seen flow features. Section 2.2 then follows with an overview of how HHF research is generally performed. After, Section 2.3 describes past studies on the Model 11 and Vega launchers and gives a summary of the TUPLE research project. At the end of the section conclusions are drawn regarding the topics that were discussed.

2.1. Hammerhead Payload Fairing Description

As mentioned in the introduction, the HHF configuration is commonly used to adapt larger payloads while reusing existing LV components. Examples of past, present and planned HHF LV's are given in Appendix E. The HHF is desirable due to the increased sustainability and cost reduction associated with the re-usability of existing LV components, despite the increased aerodynamic challenges in the form of buffeting.

The HHF configuration is characterised by a payload fairing that has a bigger diameter than the LV. A generic HHF geometry is shown in Figure 1.1. The main components of the HHF are described below:

- **Nose cone:** The nose cone is designed to reduce drag, protect the payload from the strong aerodynamic forces during launch and withstand high thermal loads during ascent [19]. Typically, the nose cone has a conical, elliptic, parabolic or ogive shape followed by one or more frustums. In terms of drag reduction and overall aerodynamic performance, the Sears-Haack shapes (ogives) are the most optimal, with the von Karman shape providing the theoretical minimum drag[7].
- **Payload compartment:** The payload section is a cylindrical section that shrouds the payload and protects it from the outside environment. Most launchers have varying diameter options for this compartment, allowing for different payload types to be carried.
- **Boat-tail:** The boat-tail is used to decrease the PLF diameter to the diameter of the LV. This reduces the drag of the rocket [6] and can alleviate buffeting [13]. The boat-tail is commonly a straight frustrum and can be defined using the boat-tail angle θ, which is often between 15° and 35°. Boat-tail shape optimization studies have been performed in the past to improve aerodynamic performance (e.g. Sunil et al. [20]). However, the straight configuration is commonly used due to manufacturing and structural requirements. Furthermore, vital electronics are often stored on or in the boat-tail [21].
- **Boat-tail step and diameter ratio:** The diameter ratio between the LV and the payload compartment is an important factor for the aerodynamic behaviour [20, 21]. Most LV have a ratio between 0.6 - 0.95. This ratio is primarily dependent on payload requirements and available LV engine diameter [6]. Generally, higher ratios tend to lead to lower unsteady buffeting [21].

2.1.1. Hammerhead Payload Fairing Flow Phenomena

While the HHF configurations offer various cost, manufacturing and sustainability benefits, it exposes the PLF and LV to strong aerodynamic forcing called "buffeting"[2, 6]. Buffeting is characterised by high pressure fluctuations on the outer mold line (OML) at a broad range of frequencies. Buffeting can lead to resonant coupling between structural bending / torsional modes of plates on the LV and the unsteady flow, which when unaccounted for can lead to catastrophic failure [5, 22]. Additionally, the frequencies caused by buffeting can damage and impede the function of vital electronics installed near the boat-tail [4, 21, 23].

The importance of buffeting is further amplified by the fact that it occurs near the maximum dynamic pressure (q) of the flight [6, 22]. This takes place during the transonic flight regime, roughly between M = 0.7 and M= 1.2. From a structural and control point of view, the max q flight stage is the most critical of the

---

[7] `https://en.wikipedia.org/wiki/Nose_cone_design`, retrieved August 2023

flight. The intensity of pressure fluctuation is directly related to q, therefore buffeting takes place at almost the worst time. Characterising and accounting for these loads is therefore of utmost importance.

In the transonic flow regime most HHF configurations experience three key phenomena that lead to unsteady loading and buffeting. First is the formation of supersonic pockets over the payload compartment that lead to shock formation and unsteady SWBLI. Secondly, flow separation on the payload compartment & boat-tail junction leading to a separation bubble with reverse flow. Lastly, the separated shear layer reattaches further down stream, causing high forcing. A schematic drawing of these is shown in Figure 2.1.

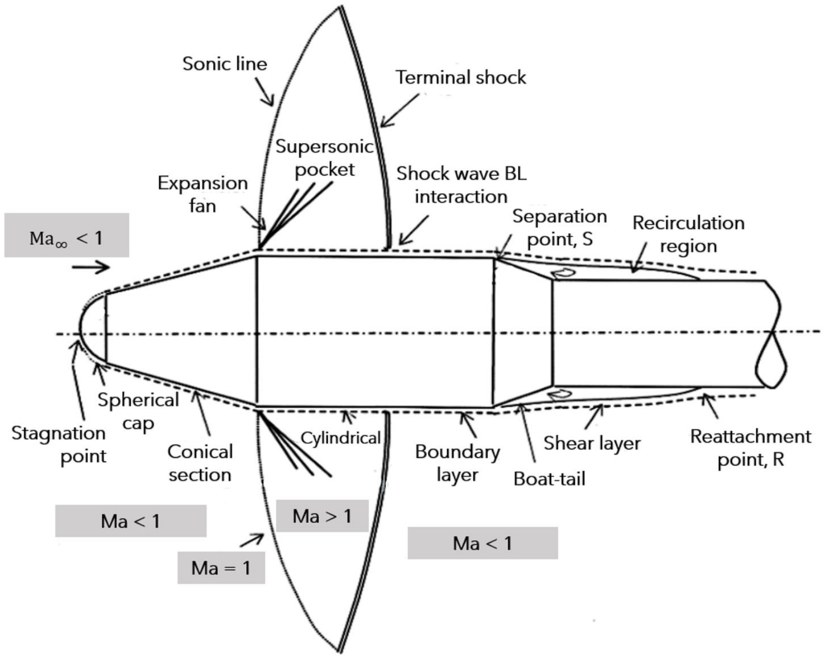

Figure 2.1: Overview of flow features commonly seen on a generic HHF geometry. Source: the work of Mehta [24].

2.1.2. Shock Waves over the HHF Transonic Speeds

The shock waves over the payload compartment form due to two reasons. The first is flow acceleration past the nose cone & payload compartment junction. This leads to supersonic pockets that are compressed as they travel over the payload compartment, eventually ending in a shock. The second reason, not portrayed in Figure 2.1, is a separation shock upstream of the payload compartment & boat-tail junction. An example of this can be seen in Figure 2.2 for the Vega-E model [17].

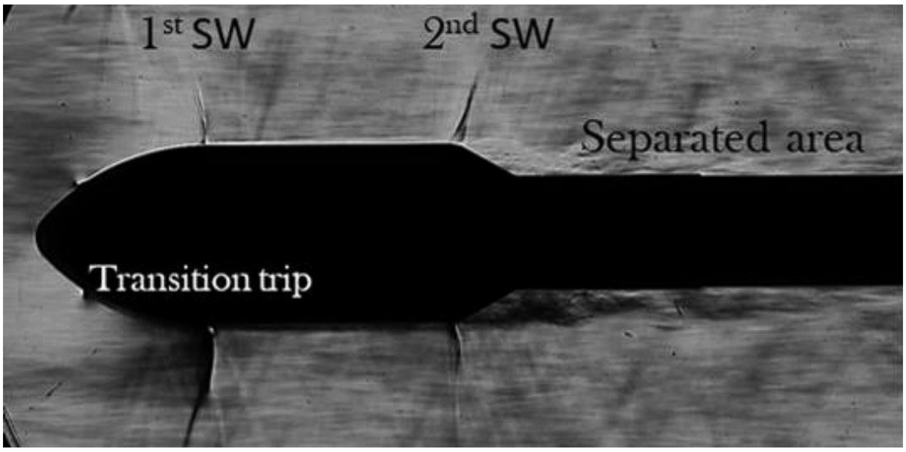

Figure 2.2: Schlieren visualisation of the two shock waves that form over the Vega-E HHF at $M = 0.8$. Notable is also a flow pertubation due to the transition trip. Source: the TUPLE investigation by D'Aguano et al. [17].

In addition, two more shocks can form over the LV at transonic conditions. The first is a shock over the boat-tail, that is formed for shallow boat-tail angles [25]. An example can be seen in Figure 2.3 for a generic HHF model with a 5° boat-tail. It does not always form, as was the case in the studies of Avelar et al. [1, 13], whereas it was seen in Romero's study [26]. This can likely be attributed to a difference in payload to LV ratio between studies, where Romero's study used a bigger ratio. The second is a reattachment shock where the separated shear layer reattaches on the LV [8, 27]. This often takes place at higher M numbers.

Figure 2.3: Schlieren visualisation of a secondary shock forming over a boat-tail with a 5° angle. Image taken at M=0.8 for a generic HHF configuration with a von Karman nose cone. Source: The MSc thesis of Romero [26].

The Mach number at which shocks first start occurring, their strength and how many shocks are present significantly depends on HHF geometry. In general shocks first start appearing between M=0.7 and M=0.8 [2, 13, 23], where nose geometries with an abrupt transition at the nose cone & payload compartment junction lead to stronger and more unsteady shocks over the entire Mach number range [26, 28]. In addition, nose geometries that are split into multiple frusta can cause multiple supersonic pockets ending in multiple shocks. Each pocket occurs due to expansion at geometry jumps. An example of this is the Coe and Nute Model 11. Lastly, the separation shock near the boat-tail junction is not always present. An example of a LV family where it does occur is the Vega family of launchers [23, 29], whereas for the Brazilian VLS-1 only a single shock is seen throughout the entire M number range [1, 13].

Due to the oscillatory behaviour of SWBLI interactions, shocks often merge. In Romero's MSc thesis [25], the shock on a shallow boat-tail and the main shock had overlapping intermittent regions, leading to periodic merging events. Shock merging also takes place for shocks that originally have separated intermittent zones. With increasing Mach number shocks become stronger and show a downstream shift over the geometry [2, 13]. This is caused by growth of the supersonic pocket over the payload compartment. The associated Mach number effect is also seen for straight PLF configurations [9]. In geometries with multiple shocks, such as the Model 11, the shocks eventually merge once the M number approaches unity.

Eventually with Mach numbers very near unity, the shock shifts from the payload compartment to the boat-tail region. At even higher M number above 1, the presence of a reattachment shock can be found downstream of the boat-tail in the reattachment zone. Beyond a certain Mach number, the shocks disappear entirely as a bow shock starts forming over the nose cone. This can be seen in Figure 2.4 for the Model 11, over a range between M=0.6 and M=1.2. Note however that the exact effect of Mach number on the flow field is highly sensitive to M and the geometry [2, 5, 23]. While the above descriptions are general patterns seen over different HHF geometries, they do not always hold true.

Whereas the shock strength increases with increasing M, p_{rms} tends to decrease beyond M = 0.8 [29, 30]. According to Panda et al. [4], the decrease in p_{rms} is likely associated with compressibility effects suppressing the turbulence in the flow. Alongside this, Camussi et al. [29] postulated that the reduction p_{rms} fluctuations also occurred due to the shocks becoming more oblique with increasing M number. This was based on their schlieren visualisations of shocks on the Vega-C model. They also saw max p_{rms} around

M=0.8 leading to this M number being most critical in the design for buffeting.

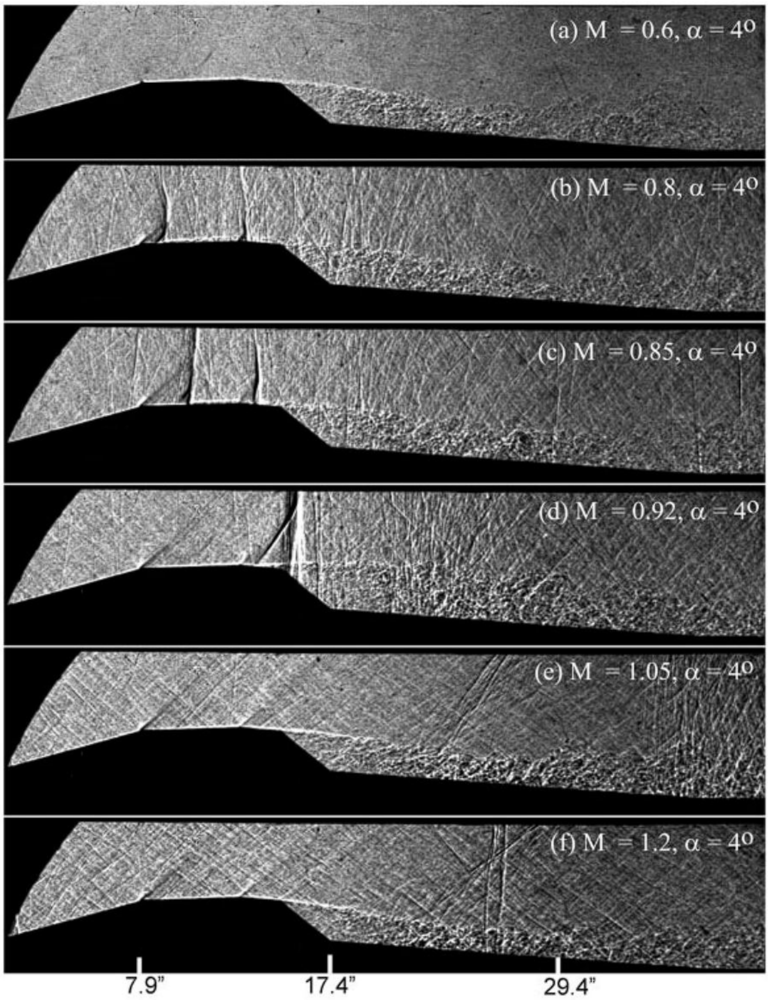

Figure 2.4: Shadowgraphy images taken on recent Coe and Nute Model 11 tests performed by NASA. Images were taken for different Mach numbers and $\alpha = 4°$, as shown in the image. Source: The work of Panda et al. [4].

Besides M number, p_{rms} is also highly dependent on geometry. Nose geometry, boat-tail geometry and diameter ratios all significantly impact it. The nose geometry mostly affects shock strength and position(s), as previously discussed. Bigger diameter ratios between LV and payload compartment tend to have lower fluctuations and mean pressures, as the geometry approaches a straight PLF. The boat-tail, much like the nose cone, mostly impacts shock position(s) and strength. According to the study of Kumar et al. [21] a θ beyond 30° only weakly impacts the p_{rms} distribution.

The SWBLI is characterised by large scale & low frequency unsteadiness [6, 21, 29, 30]. This phenomenon is reminiscent to SWBLI that can be found in canonical flow configurations [31, 32]. The driving mechanisms are also similar, with correlation studies having found that the interaction is driven by both upstream and downstream effects. The unsteadiness of the shock is highly correlated to frequencies found in the separated region downstream of the boat-tail. The shock waves cause a local lifting of streamlines due to the adverse pressure [4], which with sufficient strength can lead to early separation. This form of separation was observed for a conical nose during Romero's tests [25].

2.1.3. Boat-tail Flow Separation and Reattachment.

Separation on the payload compartment & boat-tail junction starts occurring due to the geometry change at subsonic conditions. The flow here resembles a backward facing step [26, 33], which corresponds to the case where $\theta = 90°$. The separation point most commonly takes place right at the junction between payload compartment & boat-tail. A schematic of the streamlines for subsonic separation is shown in Figure 2.5. For low values of θ however, separation may not take place [25].

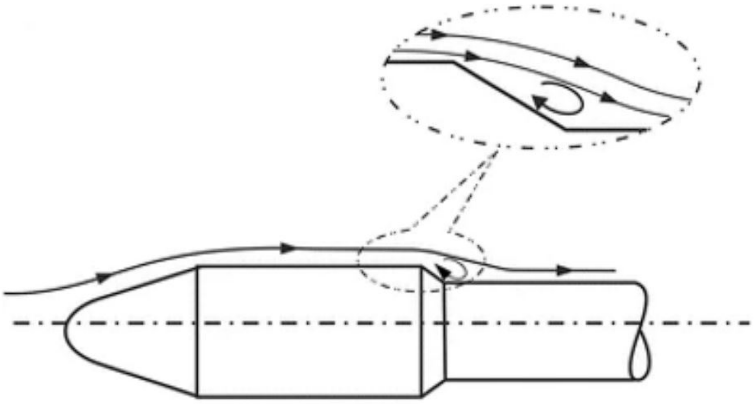

Figure 2.5: Streamlines for subsonic separated flow due to the boat-tail geometry step. Source: the book of Suresh and Sivan [6].

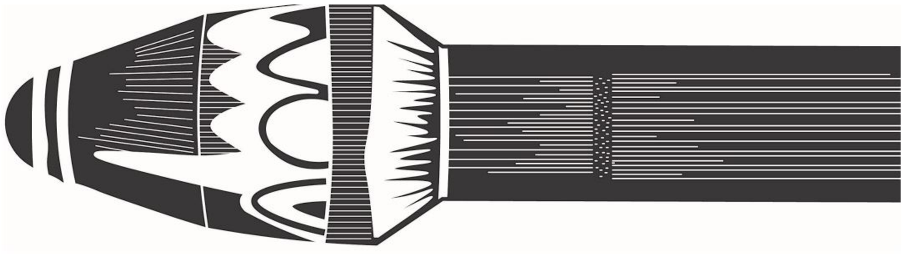

(a) Bi-conic nose (BC34)

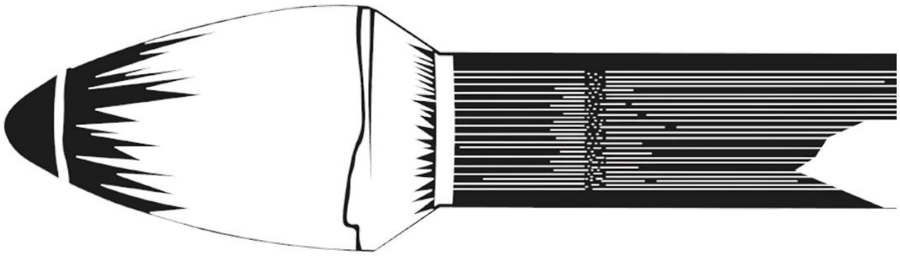

(b) Ogive nose (SH34)

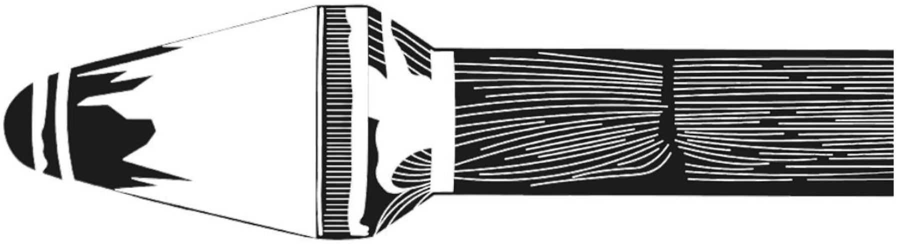

(c) Conic nose (C34)

Figure 2.6: Schematic representation of the results of oil flow visualisation taken on three different generic HHF models with different cones. Oil flow visualisation was performed at M =0.8 and $\alpha = 0^\circ$. The first two cases show a similar reattachment position, whereas the third case with a conical nose shows a downstream shift of the reattachment zone. This is associated with a stronger shock for the conic case. Source: The MSc thesis of Romero [26]

As previously mentioned, in addition to the separation found at the geometry change, shocks can induce separation. Shock induced separation can start at the payload fairing for sufficiently strong shocks [25] or can occur due to shocks over the boat-tail for shallow boat-tail angles. According to the work of Kumar et al. [21] the latter predominantly occurs at higher M number, above unity.

Although the SWBLI are always not strictly responsible for the separation, both still highly impact each other. In the previous subsection it was already mentioned that separated flow oscillations are highly correlated to shock oscillations, with upstream pressure convection. Furthermore, the reattachment position depends on the shock position and strength. Increasing shock strength, and therefore M number, leads to a backwards movement of the separation zone [3, 30]. An example of this is seen in Figure 2.6, where three nose cones were tested with the same geometry at the same M number. The case with a conical cone showed a stronger shock, which lead to reattachment further downstream than the other cases.

This backwards reattachment zone movement occurs until the shocks over the PLF disappear at low supersonic conditions, where after the reattachment point shows an upstream shift in location [3, 30]. Similarly to the shocks, the exact extent of the separation bubble is highly dependent and sensitive to the M number and flow geometry, among other parameters.

Similarly to canonical SWBLI [32], the reattachment zone and separation bubble oscillate. This leads to elevated levels of p_{rms}, with peak p around the mean reattachment point [27, 30]. The oscillatory behaviour can be seen in Figure 2.7, where the percentage of reverse flow is shown for the Model 11. As the reverse flow occurs in the separation bubble, zones with a sub 100% reverse flow move in and out of the bubble.

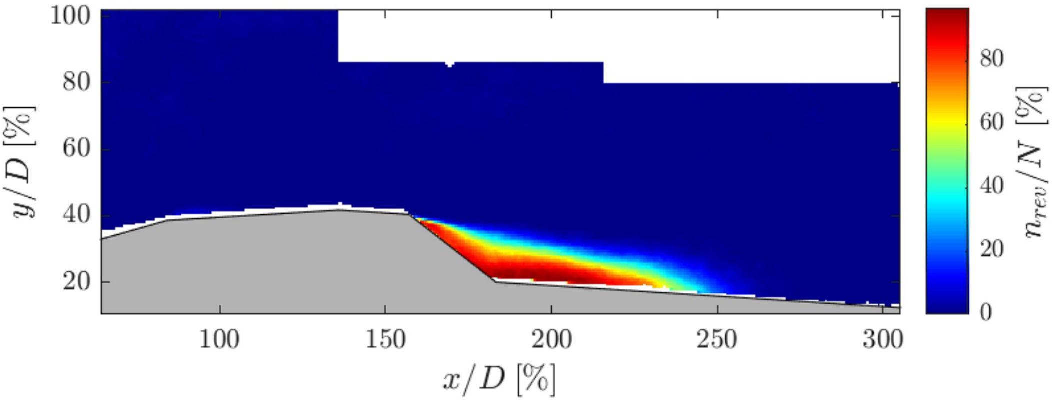

Figure 2.7: Percentage of reverse flow vectors from PIV for the Model 11 at M=0.8 and $\alpha = 4°$. Source: The MSc thesis of Romero [26]

The reattachment zone shows broadband frequency behaviour over a large range that is typical of separated-reattaching flows and shear layer flapping [4, 8, 25, 27]. This flapping behaviour is also found for the buffeting of base flow on the thrusters and backwards facing steps [33–35]. From DDES simulations, Liu et al. [27] found that the driving mechanism behind the shear layer flapping was Kelvin-Helmholtz instabilities in the shear layer creating vortical structures that impinged on the LV at the reattachment zone. The frequency content from these structures was found to be highly correlated with the SWBLI.

2.1.4. Angle of Attack Effects and Flow Asymmetry

During (nominal) ascent conditions, the angle of attack of LV oscillates between roughly ±6° [6]. Due to this it is important to quantify the impact of small α variations on the flow phenomena surrounding HHF. As with all other phenomena, the exact extent and impact of α variations highly depends on geometry, M number among other parameters. Due to this it is difficult to define exact relations between α and other aspects. However, some similarities between geometries can be defined and are discussed here.

With an $\alpha \neq 0°$, the flow changes from an axisymmetric flow to one where there is some degree of asymmetry. The biggest impact is a change in reattachment location on the leeward and windward sides, which move upstream and downstream respectively. This asymmetry can be seen in Figure 2.8, where oil flow visualisation images taken on the Model 11 for $\alpha = 0$ and $\alpha = 4°$ at M = 0.8 are shown. Furthermore, Sellers et al. [8] saw a significant increase in p_{rms} near the reattachment zone of the shear layer on the side walls caused by shock oscillations due to this asymmetry.

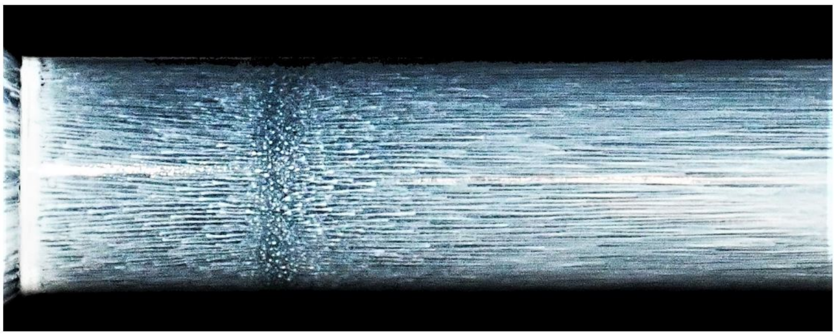

(a) AoA = 0 degrees (run 30 at Table B.1)

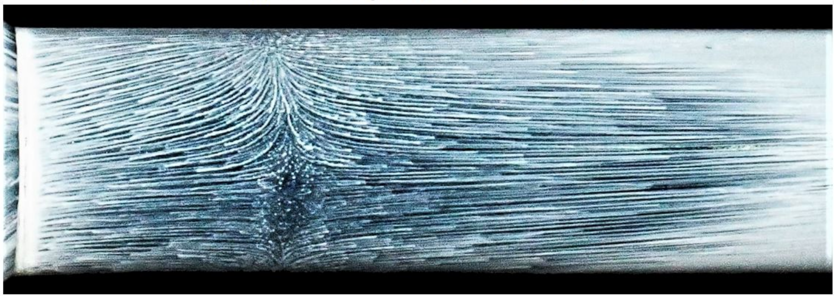

(b) AoA = 4 degrees (run 28 at Table B.1)

Figure 2.8: Change in reattachment zone flow patterns with α for the Model 11 at M=0.8. Source: The MSc thesis of Romero [26]

The shock locations barely change with increasing α for numerous geometries, including the Model 11 [26] and the Vega family of launchers. For these a small downstream shift in the leeward side and upstream shift in windward can be seen. For the Vega launchers, Camussi et al. [23] saw minor changes in the shape of $C_{P_{rms}}$ and spectral content (PSD) with α. Changes to shock strength also seem to be small. An increase in p_{rms} was seen in the PSP research of the Model 11 by NASA [4, 8]. Increased shock strength was also seen by Romero [25] using PIV. Instead, in the study of Heany et al. [9] on the SLS, a straight PLF, α variations were seen to move shock a lot more. The lower shock movement is therefore likely inherent to HHF.

Along with flow asymmetry caused by α, there is some degree of asymmetry at $\alpha = 0°$ that is caused by shock and shear layer oscillations not being in phase over the circumference [21, 25]. Overall, the flow field shows high degrees of correlation and relatively large coherence lengths over the circumference. This was observed by both Panda et al. [30] on the Model 11 and Sorana et al. [36] for the SLS.

2.2. Hammerhead Research and Development

In this section, research and development strategies (R&D) for LVs that use the HHF configuration are briefly discussed. Both wind tunnel experiments and CFD simulations are used to obtain a flight envelop for LV. Of interest are time averaged quantities, such as drag, lift, forces and moments along with time resolved pressure fluctuations quantities for structural and stability analysis purposes.

2.2.1. Wind Tunnel Experimentation

Wind tunnel experiments mostly focus on obtaining loading and moment coefficients for a select number of LV configurations [9, 37]. This is most often done by using pressure taps, accelerometers and six axes balances [38]. More recently PSP has gained traction for LV R&D, as seen by the recent NASA and AEB research. Due to the high cost associated with performing wind tunnel measurements, they are often used to validate CFD and analytical calculations.

In regards to buffeting, so called "buffet forcing functions" (BFF) are used to estimate the degree of buffeting [9]. These are often very limited in their prediction as they were originally developed using empirical wind tunnel data, yielding conservative forcing predictions. The empirical data was obtained using pressure taps, which offer insufficient spatial resolution to properly predict buffeting. Coherence analysis using the full pressure field data from fast PSP will likely improve upon these in the future [36].

Wind tunnel models are often rigid, made from thick metals. While buffeting is mostly important due to the forcing it imposes on the OML, due to the use of rigid models, wind tunnel research into buffeting phenomenon only analyses it from an aerodynamic perspective. By doing so the complex fluid-structure interactions are decoupled, and the measured fluctuations originate solely from aerodynamic effects [5, 7, 9, 22]. The measured aerodynamic fluctuations are instead used as inputs for structural analysis techniques.

An approach that was used in the Vega-C development by Camussi et al. [29] is to scale the measured fluctuations inside wind tunnels to those that would occur on real sized rockets. The comparison can then be made between the resonant structural frequencies and the aerodynamic phenomenon. In the case of the Vega-C, buffeting frequencies were found not to resonate with the structural modes.

2.2.2. Computational Fluid Dynamics

Alongside wind tunnel testing, CFD is of key importance in the design of LV and prediction of HHF loads. However, simulations are limited to "simpler" RANS, URANS and (D)DES simulations due to the high computational cost associated with LES and DNS simulations [7, 27, 39, 40]. These are capable of predicting the time averaged loading with reasonable accuracy, depending on the chosen turbulence model. However, these simulations completely fail at predicting fluctuating loads.

On the HHF configuration specifically, shock positions are predicted with high accuracy. Issues start arising with the prediction of the reattachment point of the shear layer [20, 27, 35, 40]. Time averaged predictions overshoot the reattachment point, often predicting a more downstream position than experimental data suggests. An example is shown in Figure 2.9 for the study of Liu et al on the Coe and Nute Model 11. In terms of time resolved predictions, general trends are seen where SWBLI loads and fluctuations are under-predicted whereas reattachment loads are over-predicted. Due to the aforementioned inaccuracies, verification of CFD predictions by means measurements are required. In these, PSP provides a valuable tool to validate and improve future CFD models due to its high spatial and temporal resolution data [9, 39].

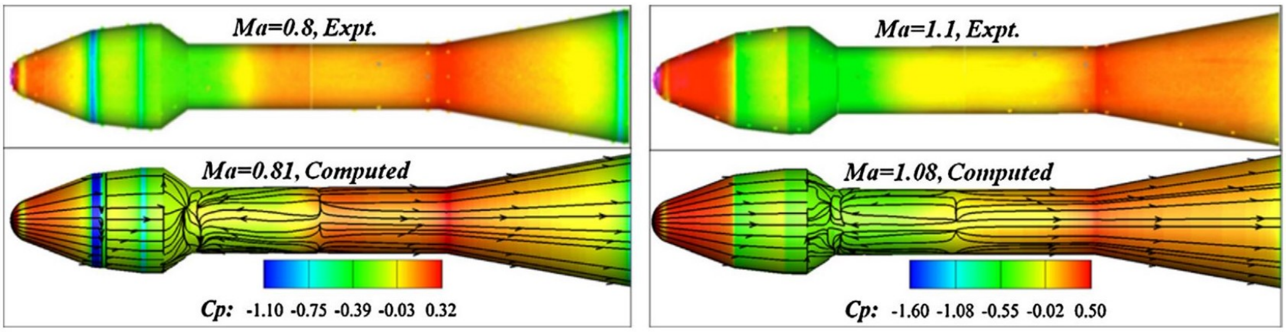

a). Ma=0.81, AOA=0.0° **b). Ma=1.08, AOA=0.0°**

Figure 2.9: Comparison between the mean C_P distribution of a DDES simulation and PSP results on the Model 11 for two Mach numbers. Notable is a similar pressure level with a mismatch of the reattachment zone. Source: The work of Liu et al. [27].

2.2.3. Buffet Free Guidelines

Based on various wind tunnel measurement campaigns into the buffeting phenomenon in the 1960's, NASA developed design criterion guidelines to avoid the buffeting on HHF configurations [41]. To this day, these guidelines are often adhered to during LV design. An example where these were used was during the design of the Vega-C launcher. According to Camussi et al. [29] it is customary to use them during the pre-design of launchers, where after more sophisticated CFD and wind tunnel experiments are used for validation.

Following the NASA guidelines however does not guarantee a complete absence of buffeting. Despite the Model 11 adhering to these guidelines, significant forcing is still present due to coupling between SWBLI and the separation bubble [30]. In addition, Ericsson [5] found that the guidelines often only looked at the buffeting on the PLF, ignoring potentially strong fluctuations downstream of this region. Both findings again highlight the importance of both CFD analysis, and in turn wind tunnel testing, for the R&D of HHF LVs.

2.3. Past Launcher Studies

In this section, an overview is given of past Model 11 and Vega launcher research. First, the Model 11 discussed followed by research on previous Vega launchers. Then, the TUPLE research is summarized, which includes both the Model 11 and Vega-E. At the end, a brief overview is given of other LV research using PSP. This includes both HHF and straight PLFs in order to highlight the effectiveness of PSP at LV research.

2.3.1. Coe and Nute Model 11 Overview

In this section, a brief overview of the Coe and Nute Model 11 is given. The original study, performed by Coe and Nute in 1962 [2], was a follow-up study from an earlier study [3] on the aerodynamic performance of HHF launchers. In this study, three HHF models were investigated, where the "Model 11" showed the most important flow features present on HHF geometries. To this day, it is considered an important test case when investigating HHF PLFs. The geometry of the original Model 11 can be seen in Figure 2.10.

The model used in the original study employed over 40 mean pressure orifices and 30 high speed pressure transducers. To not lose information on the shocks, mach numbers were set such that the highest pressure fluctuations were situated on the pressure transducers. In addition to pressure taps, shadowgraphy was employed to quantify the flow features. The data obtained during these original runs can be used to validate PSP results on a similar model that was previously tested by Romero [26].

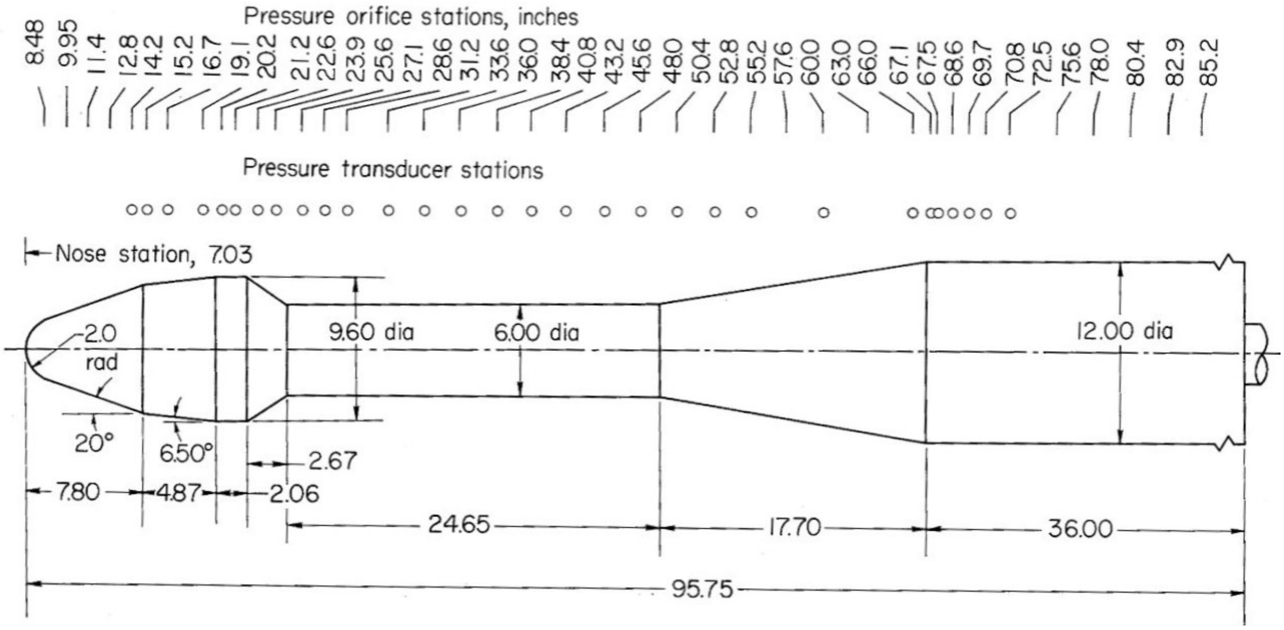

Figure 2.10: Dimensions in inches of the original Model 11 used by Coe and Nute. Source: The work of Coe and Nute [2].

In Figure 2.11, the mean C_P profiles obtained by Coe and Nute is shown for six different M numbers. Here the downstream shift of the reattachment location is evident. In addition, the strengthening of the shock wave with increasing M can be seen until M=1, after which it disappears. Finally, a change in the shape of pressure distribution of the attached flow zone beyond M =0.88 can be seen.

A comparison between the $C_{P_{rms}}$ results obtained by Coe and Nute to a more recent investigation by Panda et al. [4] is shown in Figure 2.12 for five mach numbers. From these, the decreasing trend in $C_{P_{rms}}$

with M number is evident. Again, the downstream shift of the reattachment point can also be seen for subsonic mach numbers, whereas for M = 1.08 the reattachment point shifts forward. Lastly, for this model it can be seen that the geometry increase associated with the booster stage around 60 inches is the point with the most fluctuations. The geometry increase is not included for the model used in this project.

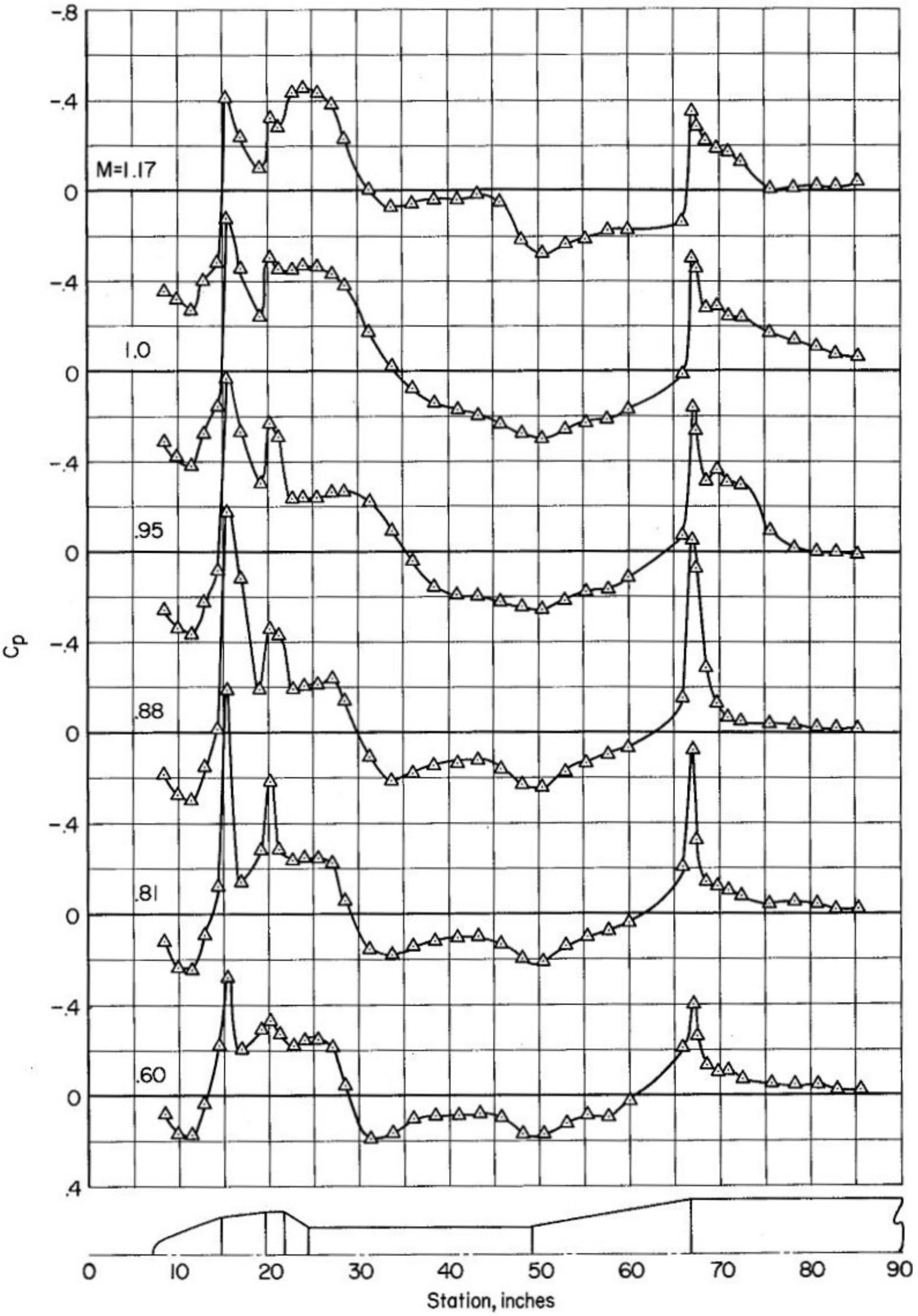

Figure 2.11: Mean C_P profiles on the Coe and Nute Model 11 for six M numbers. Source: The work of Coe and Nute [2].

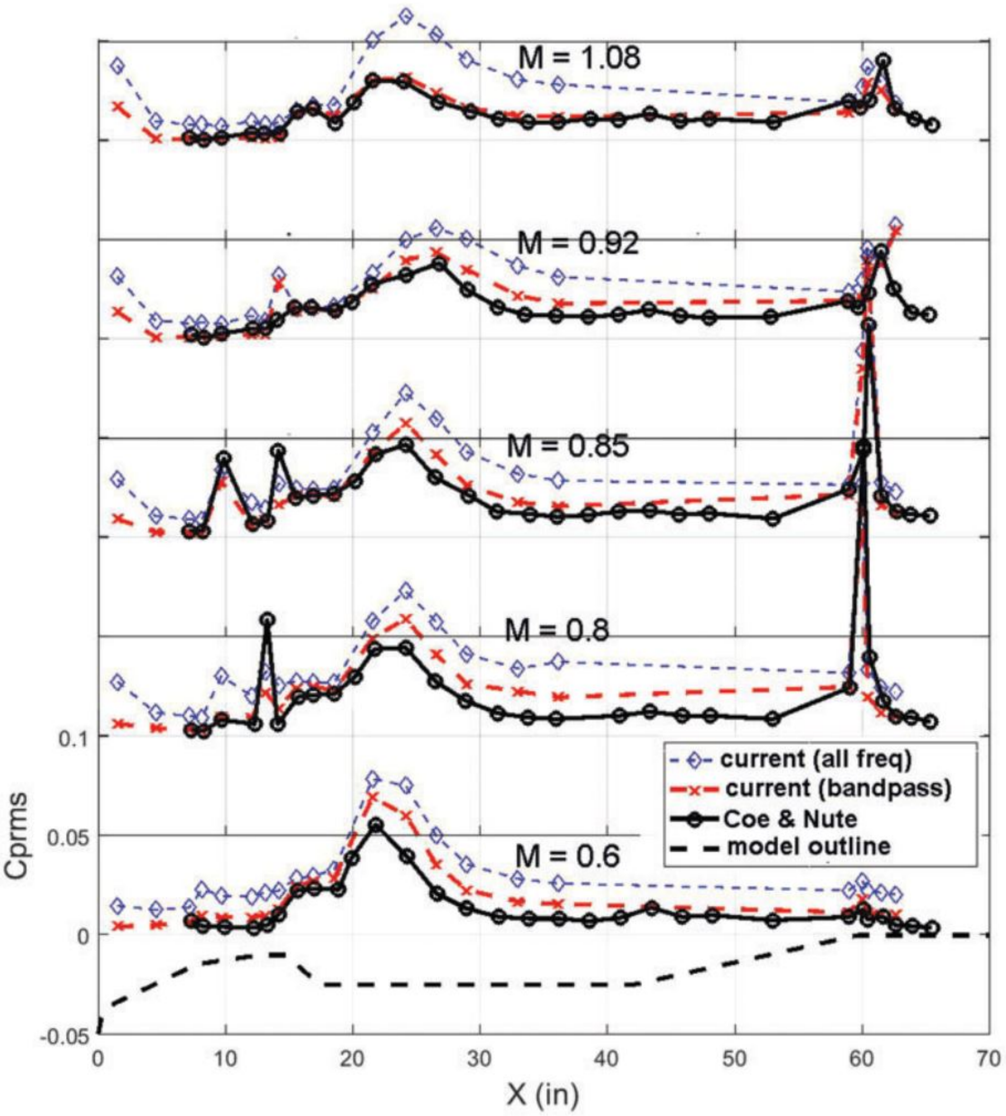

Figure 2.12: Comparison between $C_{P_{rms}}$ computed using kulite pressure tap data and the original Coe and Nute tests on the Model 11 for different M numbers at $0^{\circ}\alpha$. The blue dashed lines indicate the recent test results obtained with kulites. Red lines are recent results band-pass filtered to match the original Coe and Nute pressure tap range. Solid black lines represent the original Coe and Nute data. Finally, at the bottom of the chart the outline of the Model 11 can be seen. Source: The work of Panda et al. [30].

2.3.2. Articles on the Vega Launchers

The Vega family of launchers are small payload LVs developed by the ESA that make use of HHF. Two rockets have been developed, namely the Vega and Vega-C. A comparison between both can be found in Figure 2.13. The Vega-C recently finished development, during which a mix of CFD and wind tunnel testing was performed to finalize the design [29, 37, 42]. Currently, the Vega-E is in development with an expected maiden voyage in 2027 [8]. The research performed in this thesis contributes to the development of the Vega-E by providing PSP data. In this section, a brief summary of notable flow features is given from past articles.

During an aerodynamic investigation into the original Vega launcher by Camussi et al. in 2007 [23], two mechanisms were once again found to lead to turbulent propagation, one upstream and one downstream mechanism. The first was attributed to "pseudo sound effects" (downstream propagation, $U_c = 0.7$) and the latter related to purely acoustic effects (upstream propagation, $U_c = U_{\infty} - U_{sonic}$). Here, the pseudo sound was found to be the advection of vortical structures with the flow. In addition, as with previous HHF studies, the flow was found to be highly dependent on M number. Furthermore, similarly to the Coe and

---

[8] `https://en.wikipedia.org/wiki/List_of_Vega_launches`,retrieved April 2024

Nute model, α very weakly impacts $C_{P_{rms}}$ and PSD[23]. However, due to the discrete nature of pressure taps the author believes that a lot of important flow features may have been missed in that study.

The aerodynamic performance of the Vega-C launcher was again investigated by Camussi et al. in 2020 [29]. Here two shocks are present, one after the cone and one at the boat tail, similarly to the Vega-E. The most important frequencies for buffeting are around a few hundred hertz in the wind tunnel environment, consistent with other HHF models. The obtained spectra were then scaled to the full size model to investigate fluid structure coupling. To do so, a method for eliminating the tonal noise from the wind tunnel was applied. It was found that no coupling is expected from comparing the buffeting spectra and the bending / torsion modes from the structural analysis. In addition, the shocks become more oblique with increasing M number which additionally leads to a decrease in $C_{P_{rms}}$ as aforementioned.

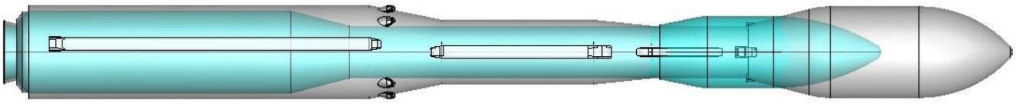

Figure 2.13: Vega launcher geometry comparison. In blue the original Vega launcher is shown, whereas white shows the newer Vega-C launcher. Source: Vitagliano et al. [37]

2.3.3. TUPLE Research Summary

Prior to the PSP measurements performed in this thesis, the Vega-E and Coe and Nute Model 11 were used to characterise the flow features using PIV, oilflow, High speed Schlieren and high speed pressure taps as part of the TUPLE project [17, 18, 25]. Here a brief summary of the findings of these investigations is given. Only findings relevant for the current thesis are presented. These findings can be compared to those obtained with PSP and help better understand the flow features.

First, an experimental investigation into the impact of different nose cone and boat-tail geometries was performed by MSc student Romero and later published by D'Aguanno et al. [25]. Three different nose cone geometries and three different boat tail angles were investigated. The models used here were designed to have similar proportions to the Vega model, with the Model 11 being used as a baseline configuration.

Here the location of flow features for the Model 11 are presented which were observed using oilflow, Schlieren and PIV. Schlieren was used for shock locations, whereas PIV and oilflow were used for reattachment locations. Shock locations were extracted by plotting the time evolution of a line of pixels 0.5cm above the surface. The resulting plot can be seen in Figure 2.14. PIV locations were instead extracted 1cm above the surface due to FOV limitations from laser reflections.

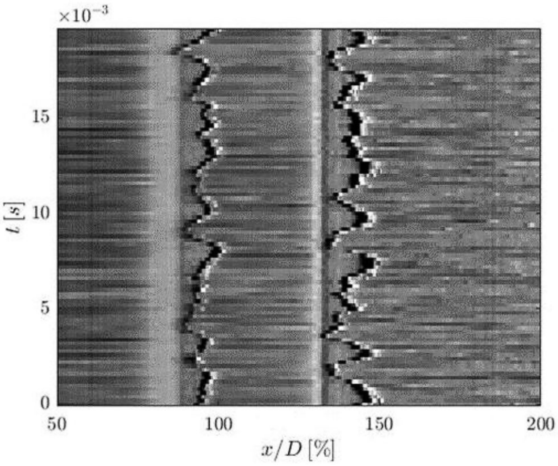

Figure 2.14: Time evolution of a Schlieren pixel line intensity above the surface of the Model 11 at $M = 0.8$ and $\alpha = 0°$. Source: The work of D'Aguanno et al. [18].

A discrepancy can be found in the flow reattachment location between PIV and oilflow. The likely cause for this was the impact of oilflow on the flow and the fact that PIV can not measure the flow directly near the surface. Discrepancies are also found in the intermittent region of the shock between PIV and Schlieren. This was attributed to 3D integration effects from Schlieren.

Blockage effects of the model inside the TST-27 were found to cause an increase in effective test section Mach number around 0.05. As the test setup that is used in the PSP experiments is similar, the same blockage effect can be expected. In the $\alpha = 4°$ cases, blockage was found to cause lower near surface subsonic velocities on the leeward side due to the divergent region between model and wind tunnel wall. Similarly, the same effect would lead to higher supersonic speeds.

On the Model 11, only the more upstream shock was seen for M = 0.7. A second shock could be seen in some schlieren images, therefore displaying an intermittent behaviour. Lastly, angle of attack effects induced a more upstream shock location on the leeward side, and a more downstream reattachment point compared to the $\alpha = 0°$ case. No comparison was made between leeward and windward sides.

In the second paper by D'Aguanno et al. [17], the Vega-E model was analysed with different boat tail angles using PIV and Schlieren. On the clean model experiments were performed at M = [0.8,0.75,0.7], $\alpha = [0°, 4°]$ and $\theta = [55°, 30°, 15°]$. In addition, some configurations were investigated with and without protuberances. Here, the mean shock and reattachment locations are reported from Schlieren and PIV respectively. These were obtained the same way as the ones on the Model 11. The focus of this summary will be on the results of the $\theta = 30°$ configuration, as this is the one used for PSP measurements.

Unlike the Model 11, at M = 0.7 both shocks are intermittent. For M = 0.75 they become permanent. No shift in location was reported for the second shock between M=0.75 and M =0.8, whereas the first shock showed significant downstream movement and increase in intermittent region. With angle of attack, no difference was seen on the first shock between leeward and windward sides. The second shock was found to move downstream on the windward side and to oscillates more due to the flow staying attached longer, whereas on the leeward side it was found to weaken. This lead to a decrease of the separation bubble.

Two protuberance rings were installed on the model which can be seen in Figure 5.11. The big protuberance on the second ring was found to reduce the separated area. Behind this protuberance, a large wake formed on the LV. Measurements taken at an offset of 90° of this protuberance, showed similar reattachment locations as the clean configurations. Therefore smaller protuberances only weakly impact the flow. However, the shocks were sharper in the clean configuration and lower fluctuations were found on the boat tail. No differences in fluctuations were seen at the pressure taps.

From the PIV data, C_P values were obtained. These revealed flow features that were not detected near the surface. The conclusion was therefore drawn that a combination of surface pressure measurements and flow field measurements is required to fully characterise the flow. Additionally, low fluctuations were seen directly in the vicinity of the boat tail.

M	$\alpha(°)$	Prot	Side	Shock 1 location (L/D)	Shock 2 location (L/D)	Reattachment location (L/D)	Tap 1 (C_P)	Tap 3 (C_P)
0.8	0	no	-	-1.57	-0.30	0.30	-0.11	0.05
0.8	0	0°	-	-1.56	-0.29	0.29	-0.12	0.07
0.8	0	90°	-	-1.56	-0.29	0.31	-0.13	0.03
0.8	4	no	Lee	-1.59	-0.29	0.24	-0.03	0.05
0.8	4	no	Wind	-1.58	-0.28	-	-	-
0.8	4	0°	Lee	-1.58	-0.29	0.23	0.04	0.08
0.8	4	both	Wind	-1.59	-0.28	-	-	-
0.75	0	no	-	-1.67	-0.30	-	-	-
0.75	0	both	-	-1.67	-0.30	-	-	-
0.75	4	no	both	-1.68	-0.3	-	-	-
0.7	0	no	-	-	-	0.27	-0.05	0.07
0.7	0	0°	-	-	-	-	-0.03	0.05

Table 2.1: Location of flow features on the Vega-E from PIV and Schlieren. Source: The TUPLE report of D'Aguanno et al. [17].

2.4. HHF Literature Conclusions

From the HHF literature, it was found that HHF can lead to more sustainable LV design. However, HHFs cause high levels of aerodynamic forcing called buffeting in the transonic flow regime. The buffeting is caused by unsteady SBWLI and flow re-attachment downstream of the boat-tail. These are highly coupled and impact each other. In addition, model geometry, Mach number and angle of attack significantly impact the location and extent of buffeting. To fully characterise buffeting, the pressure levels, location and fluctuation spectra have to be determined.

The transonic flow regime occurs near the maximum dynamic pressure (q) of LV ascent. As buffeting scales in intensity with q, buffeting takes place at a crucial time of the ascent, causing it to be one of the more important design forces. When not accounted for, buffeting can lead to resonance and structural failure. Furthermore, the vibrations caused by buffeting can break vital electronics. CFD simulations of the buffeting are not enough to quantify the effects of buffeting with high degrees of accuracy. Therefore, wind tunnel investigations are required, in which PSPs is a valuable tool.

3 PSP Theory

This chapter describes the applications, working principles and data analysis methods used for PSP. The chapter starts off with a brief introduction of what PSPs are and their working principles. For a more comprehensive description, readers are referred to the book of Liu et al. [10]. This is followed by a summary of the two main analysis methods in Section 3.2, namely the lifetime and intensity based methods. For the experiments in the current thesis, the intensity based method was used. Therefore, this method is more thoroughly described in Section 3.3. This is followed by an overview of past LV studies that used the intensity based approach in Section 3.4. At the end of the chapter, conclusions that were drawn from the PSP literature in regards to the application to HHF research is given.

3.1. Introduction to PSPs

PSPs act as optical sensors that allow for quantitative measurements of surface pressure levels in a non-intrusive manner. The working principle behind PSP is luminescent emissions of the paint. The intensity of the luminescence is directly related to the pressure and temperature of the model [10]. By measuring the amount of emitted light, with for example cameras, a surface mapping of the emission can be made, where the light intensity decreases with increasing pressure; Areas with low pressure appear as bright areas in PSP images, whereas high pressure zones appear as dark patches (see Figure 1.2). From these surface mappings, the pressure levels can be obtained by means of paint calibration.

Traditionally, quantitative pressure measurements are done with pressure transducers. These are expensive to install, offer limited spatial resolution and can miss important flow phenomena if not installed in the correct places [10]. An example of the latter can be found in Figure 3.1. Here a comparison is made between the root mean square (RMS) pressure fluctuations, denoted as σ_p / q_∞, resolved by PSP and kulites for a shock impinging on a flat plate. Due to the discrete placement of kulites, the shock is not captured. Note that the PSP does not match the kulites downstream of the shock due to errors in the PSP data.

In the past, for example in the original hammerhead buffet investigation of Coe and Nute [3], wind tunnel M numbers were set such that the shock wave position coincided with a pressure tap, to ensure that pressure taps captured the effects of shock waves on the pressure. This was done using schlieren. Without this approach, the impact of the shock wave could have been missed from the pressure tap data. However, this approach is very time consuming and expensive as multiple wind tunnel runs are required.

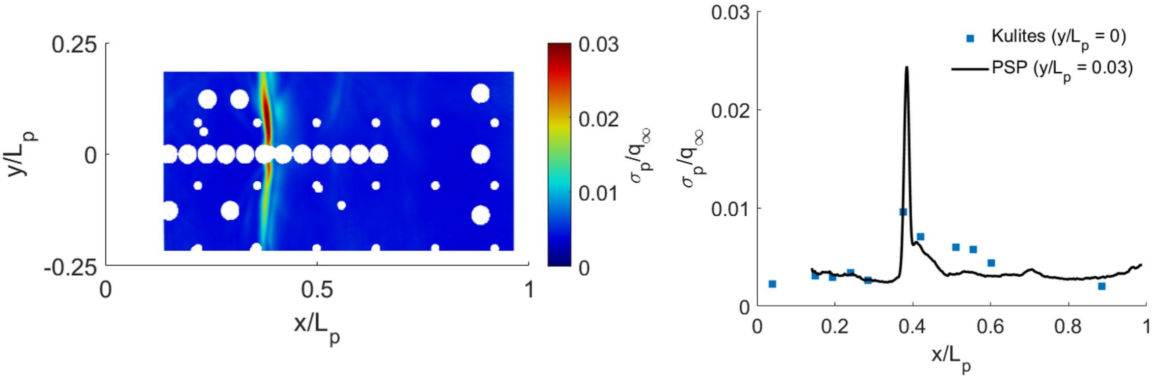

Figure 3.1: Comparison between RMS PSP and kulite data for a shock impinging on a flat plate. Distance is non-dimensionalized with plate length L_p. On the left, the full field PSP results can be seen. White circles are masked out taps. On the right, a comparison is shown between the kulite and PSP data (shifted slightly off-centre). Source: Brouwer et al [43].

More recently, better spatial resolution for p measurements can be achieved by with PIV. This works very well for low speed, incompressible flows, but obtaining accurate p fields in high speed flows with PIV is challenging. An example is the TUPLE project, where PIV was used to reconstruct the p field [44]. Due to laser reflections, p values can not be obtained close to the surface [17]. PSPs offer a comparatively cheap alternative to obtain high spatial resolution p measurements on the surface. Standard PSP measurements are capable of achieving accuracies in the order of 100-1000 Pa [10]. Due to the high spatial resolution, visualisation of flow phenomena and integrated force measurements can also be achieved with PSP [36].

The limited pressure accuracy makes PSP best applicable in compressible subsonic to supersonic flow, ranging from 0.3M to 3M. In this range large pressure gradients are often found. Standard PSP measurements are capable of measuring time averaged pressure fields on surfaces of stationary and moving wind tunnel models at around 1 bar pressure. Additionally, PSPs are also applicable to cryogenic wind tunnels [10], turbomachinery [10], low pressure and rarefied flow regime [15], high frequency measurements [45], subsonic flows [10], wing flutter studies [46] and acoustic measurements [47] (including wind tunnel acoustics [14]). In this project PSP was applied to LV research in the transonic flow regime, which is the most optimal range for standard PSP due to the high pressure gradients and relatively low temperature gradients. Measurements were taken around 2 bar total pressure (p_{tot}), with most points being around 1.3 bar.

3.1.1. Physical Working Principle

PSP works by measuring the luminescent intensity emitted from the paint. Standard PSP paints are composed of luminophore molecules that are held in place by a polymer [10, 48]. Luminophores are molecules or atoms that luminesce under excitation from an external source. An overview of the available luminophore options can be found in Appendix A. For PSPs, luminophores are excited by absorption of light. The emitted photon has a higher wavelength than the excitation photon, a phenomenon described as Stokes shift [10].

Alongside luminescence, luminophores can return to their ground state by other mechanisms. The two most important ones are thermal and oxygen quenching [10]. Thermal quenching is a temperature dependent process wherein luminophores exchange energy with surrounding molecules by atomic vibrations. Higher temperature leads to a higher level of quenching. Instead, oxygen quenching is directly linked to interactions with O_2 molecules. The rate at which oxygen quenching occurs is proportional to the O_2 concentration in the polymer ($[O2]_{polymer}$). The $[O2]_{polymer}$ can be described by Henry's law [10]:

$$[O2]_{polymer} = S \cdot p_{O_2}, \tag{3.1}$$

where S is the polymer's solubility of O_2 and p_{O_2} the partial pressure of O_2. p_{O_2} is then given by:

$$p_{O_2} = X_{O_2} \cdot p, \tag{3.2}$$

where X_{O_2} is the molar fraction of O_2 molecules in air and p is the pressure of the outside air. Therefore, using Henry's law, the amount of oxygen quenching that takes place is proportional to the outside air pressure. By using this principle, pressure measurements can be taken using the change in luminescent intensity of the luminophores. As thermal quenching is an inherent process of any luminophore, temperature gradients are a significant source of measurement error, as will be expanded upon in Chapter 4.

3.1.2. Luminescent Intensity Characteristics

Luminescent light intensity can be assumed to have a linear relation with excitation light intensity for a wide range of temperatures and pressures [10]. Increasing the excitation light intensity beyond a certain threshold leads to the linear relation assumption to no longer be valid. When the excitation intensities exceed the threshold, the ratio between intensities becomes non-linear. Further increasing intensity beyond the non-linear region can lead to luminophores becoming saturated with excitation [10].

The change of luminescent intensity (ΔI) for a given Δp or ΔT is given as a percentage at a reference condition (often p = 100kPa and T = 293K) per 1kPa or 1K. For example, the paint that was used during this thesis, namely Innovative Scientific Solutions Incorporated's (ISSI) UniFIB® PSP[6], has a pressure sensitivity of 0.8%/kPa at 293K and a temperature sensitivity of 0.4%/K at 100kPa.

Parameters such as binder material, binder type, surface finish, manufacturing procedure and solvent can all affect the luminescent intensity of a luminophore [10, 49]. This can lead to the same luminophore having different sensitivities when one of the parameters is changed. An example is another of ISSI's products, UniCoat PSP[6], that is based on the same luminophore as UniFIB® PSP. UniCoat PSP has a pressure sensitivity of $0.5\%/kPa$ and a temperature sensitivity of $1.3\%/K$ at $293K$ and $100kPa$ respectively.

The luminescence from luminophores can be assumed to be isotropic [10], but when looking at the emissions from a point on the surface of a painted model, the Lambertian cosine law can be assumed to hold [50]. This law states that the emission observed from the surface is proportional to the cosine of the observation angle with respect to the surface normal. The Lambertian behaviour can lead to errors in the measured intensity due to light reflections. Reflections can also be used to improve measurements. Due to the isotropic emission of luminophore, using a white reflective basecoat underneath the PSP allows for more light to be reflected away from the surface of the material, increasing outward light emission.

3.1.3. Paint Response Time

Two main characteristics determine the response time of PSPs to temporal p changes, namely [10, 51]:

1. The luminescent lifetime (τ) of the luminophores.
2. The oxygen diffusion rate.

Both characteristics are furthermore dependent on the temperature. For standard PSP, the luminescent lifetime is much smaller than the oxygen diffusion rate. Therefore, the response time is dominated by the diffusion rate. Note that the luminescent lifetime is strongly dependent on the type of PSP binder, much like the oxygen diffusion rate [51]. The diffusion rate of oxygen depends on the polymer layer thickness (h) and the oxygen permeability of the polymer [10]. Thicker polymer layers lead to lower response times as oxygen takes longer to diffuse into the layer. The time response follows a square law with layer thickness given by:

$$\tau_{dif} \propto \frac{h^2}{D_{O_2}} \tag{3.3}$$

Where τ_{dif} is the diffusion timescale and D_{O_2} the oxygen diffusivity. Permeability is a function of solubility multiplied with diffusivity. A higher oxygen permeability leads to a faster response time in PSP [10]. Typical PSP polymer layers with a thickness of $10\mu m$ offer response times of $\mathcal{O}(0.1-1s)$. This response time is too high to apply standard PSPs to solve time resolved flows. The response time of the paint that was used during this project was not measured, but is is expected to be around $\mathcal{O}(0.1)$ based on the properties.

3.1.4. Stern-Volmer Relation

The Stern-Volmer relation is a key equation in PSP, describing the relation between I and O_2 concentration. A linear version can be derived from a simplified kinetic model of excitation, emission and quenching [10]:

$$\frac{I_0}{I} = \frac{\tau_0}{\tau} = 1 + k_q \cdot \tau_0 \cdot [O_2], \tag{3.4}$$

where I_0 is the luminescent intensity without O_2 (e.g. vacuum), I the intensity at a given oxygen concentration ($[O_2]$), k_q the rate constant that can be attributed to the oxygen quenching process and τ the luminescent lifetime at $[O_2]$. Here the 0 subscript signifies τ without O_2. Both τ_0 and k_q are temperature dependent properties. By plugging in Henry's law (Equation 3.1) the oxygen concentration in Equation 3.4 can be converted to pressure. Obtaining the zero oxygen quenching quantities, τ_0 and I_0, is very difficult in normal wind tunnel testing environments. Instead, Equation 3.4 is divided by a reference condition with known pressure (p_{ref}) and temperature giving [10, 52]:

$$\frac{I_{ref}}{I} = \frac{\tau_{ref}}{\tau} = A(T) + B(T) \cdot \frac{p}{p_{ref}}, \tag{3.5}$$

where A and B are temperature dependent Stern-Volmer coefficients. For standard polymer-luminophore PSPs, coefficient A is related to thermal quenching whereas coefficient B has a temperature dependency due to changes in oxygen diffusivity with temperature. This change is related to changing air and polymer properties with T. Equation 3.5 also holds for other types of PSP measurements, but B has a different physical relation. Two Stern-Volmer curves are shown in Figure 3.2 for ISSI's single luminophore paints[6].

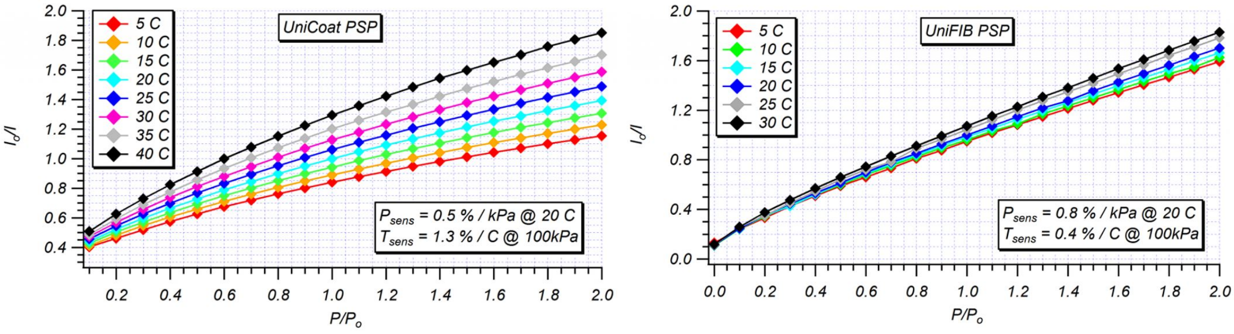

(a) Stern-Volmer Curves for ISSI's UniCoat PSP[6]

(b) Stern-Volmer Curves for ISSI's UniFIB® PSP[6]

Figure 3.2: Examples of Stern-Volmer curves for two standard PSP formulations based on PtTFPP as luminophore. Source: ISSI[6]

The linear Stern-Volmer relation of Equation 3.5 holds relatively well for a limited range of pressures. The range for which Equation 3.5 is valid depends on paint properties, static pressure and temperature. Higher order terms can be included in the Stern-Volmer equation to account for non-linear effects, allowing the equation to be valid for a bigger range [10, 52]. The higher order Stern-Volmer equation is then given by

$$\frac{I_{ref}}{I} = \frac{\tau_{ref}}{\tau} = A(T) + B(T)\cdot\frac{p}{p_{ref}} + C(T)\cdot\left(\frac{p}{p_{ref}}\right)^2 + D(T)\cdot\left(\frac{p}{p_{ref}}\right)^3 + ... \tag{3.6}$$

For standard PSP, Equation 3.5 generally holds for the entire measurement range. Non-linearity is mostly relevant for fast PSP at low pressures and high frequencies [53]. However, it can be seen from Figure 3.2 that the standard PSP curves are also slightly non-linear, especially at lower pressures.

3.1.5. Basic Measurement Setup

A generic measurement setup used for any PSP application can be seen in Figure 3.3. Each component is briefly discussed. A more detailed overview of the available optical equipment can be found in Appendix C.

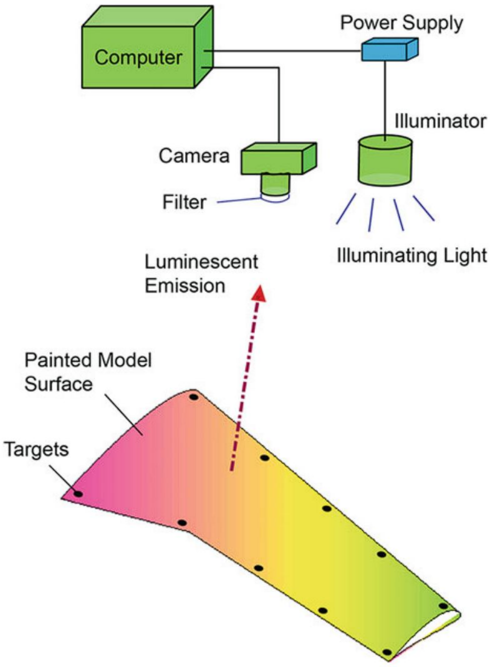

Figure 3.3: Generic PSP measurement setup. Source: Liu et al. [10]

1. **Fiducial marks:** On the model, targets are shown. These are used to align wind-on and wind-off images with (image registration) and remapping the 2D images into a 3D space (image resection) [10]. Wind-on and wind-off images are often misaligned due to model aeroelasticity.
2. **Filter:** A filter is used to remove excitation light from impinging on the light detector.
3. **Illuminator:** Illuminators are chosen such that their emitted light has desirable properties. Properties which must be chosen include emission band, central λ, light source stability and power among others. Lamp arrays are often used to generate an approximately homogenous illumination field.
4. **Camera:** To take images, light detectors are need. For PSP measurements cameras are the most common detector. The correct choice of camera depends on the exact experimental setup.
5. **Computer:** A computer is used to collect and process data. Computer requirements for data processing heavily depend on measurement type and the corrections that are applied. Datasets can range anywhere from a couple gigabytes for standard PSP up to hundreds of terabytes for fast PSP [54]. Recent fast PSP NASA measurements on various scale models of the space launch system (SLS) and on the Coe and Nute model yielded over 50 TB of raw data per test, and additionally required use of supercomputers to process the data [30, 39, 55].
6. **Power Supply:** These are used to power the cameras, illuminators and computers. Illuminators often require a separate power supply due to specific power needs.

3.2. PSP Processing Methods

The conversion from luminescent intensity to pressure can be achieved using two distinct methods [10]. The first method is called the "intensity based" method. Here, the pressure is obtained using the intensity ratio between a reference condition, and the measurement condition. The second method is called the "lifetime based" method, which relies on measuring the luminescent lifetime to obtain the pressure.

Both methods are applicable to a wide range measurements and can often be used interchangeably. Each has their own unique advantages and disadvantages. In the following subsections, both are briefly summarized. For the measurements that were performed in this thesis, the intensity based method was chosen as it was deemed to be more beneficial. In the next section, a more detailed description is given of this method and the data analysis approaches

3.2.1. Intensity Based

The intensity based method makes use of the Stern-Volmer equation (3.5) to obtain pressure ratios. For this, a reference image (I_{ref}) is taken at known (p, T) conditions, often done at wind-off conditions. By dividing I_{ref} with images taken during a measurement, the intensity ratio is obtained. As p_{ref} is known, p can then be computed. Figure 3.4 shows the basic data processing associated with the intensity based method.

The intensity based method provides various advantages over lifetime methods. This is mostly the case in terms of error sources that are negated and fast PSP measurements. According to Liu et al. [10], taking the intensity ratio theoretically eliminates errors caused by uneven paint thickness, nonuniform illumination field and nonhomogeneous luminophore concentration (see Chapter 4 and Section D.1 for a description of these errors). The aforementioned dissimilarities between spatial points can lead to errors in luminescent intensity and luminophore lifetime, which need to be corrected for in lifetime based measurements. However, model deformation due to aeroelasticity is a big error source for intensity measurements.

According to Henne [52], at DLR (in 2023) the intensity based method is most commonly used for fast PSP, rigid models (low aeroelasticity), temperature sensitive paint (TSP) measurements and sometimes low speed testing applications. Intensity based measurements are additionally applicable to special PSP measurements. Various cryogenic experiments have been performed using intensity based analysis [10]. Laser scanning systems can also be used for special intensity based measurements. These provide advantages in measurements where optical access with cameras is difficult to achieve [10].

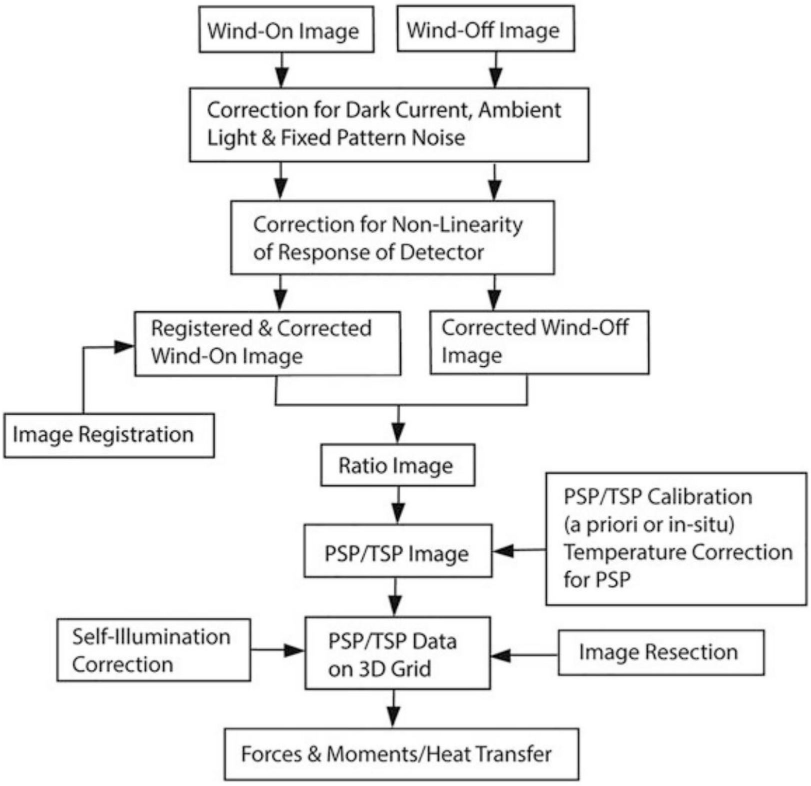

Figure 3.4: Basic data processing flow chart for the intensity based methods. Source: Liu et al. [10]

3.2.2. Lifetime Based

Lifetime based methods make use of τ to measure pressure levels. These methods are well suited for moving models, such as helicopter or propeller blades, and aeroelasticity studies, such as wing flutter. They are furthermore used for any steady PSP application. An example of this are the studies of Avelar et al [1, 13], who used lifetime based PSP to quantify the time averaged pressure on a select few boat-tail configurations. Lastly, as of the timing of writing this report, unsteady PSP measurements using lifetime methods is a hot ongoing research topic [56]. Recently, Imai et al. [46, 57] investigated wing flutter in transonic conditions using a novel PSP method that combines DIC and PSP, allowing for simultaneous time resolved displacement and pressure measurements.

Lifetime based methods offer several benefits over intensity based analysis. According to Yorita [56] measurements are independent of camera pixel sensitivity, model deformation and illumination intensity. Disadvantages include a (relatively) complex measurement system when compared to the intensity method and a lower luminescent signal intensity. Theoretically, another benefit of lifetime based analysis is that no reference image is required to obtain pressure fields. In reality however, due to uneven paint thickness and nonhomogeneous luminophore concentration errors, the luminescent lifetime of the model has a spatial variation that requires additional corrections [10]. To do so, reference images are often taken and used with the ratio-of-ratios method that is described at the end of this section.

There are two approaches to determine τ. The first is direct measurement of luminescent decay by using fast responding sensors (e.g. photomultiplier tubes (PMT)). The second method uses multiple (camera) gated images. Here a very short excitation window, that can be approximated as pulse, is used. During and right after this pulse the sensitivity of PSP to p and T is very small. The first gated image, I_1, is generally taken such that it covers the duration of the pulse. Other images are then taken after. Generally, two or three gated images are taken. A visualisation of the gates is shown in Figure 3.5.

The gated ratios I_1/I_i are a function of p and T which can be determined experimentally, by use of a coupon for example. For two gated images, only the pressure can be obtained from the gated ratio. When using three images, both the p and T field can be obtained. This relies on the gates having sufficiently different p and T dependency. The optimal placement of each gate can also be determined with experimental calibration data. The set up used here is very similar to the set up used in PIV measurements, and can be performed for both high and low frequency measurements.

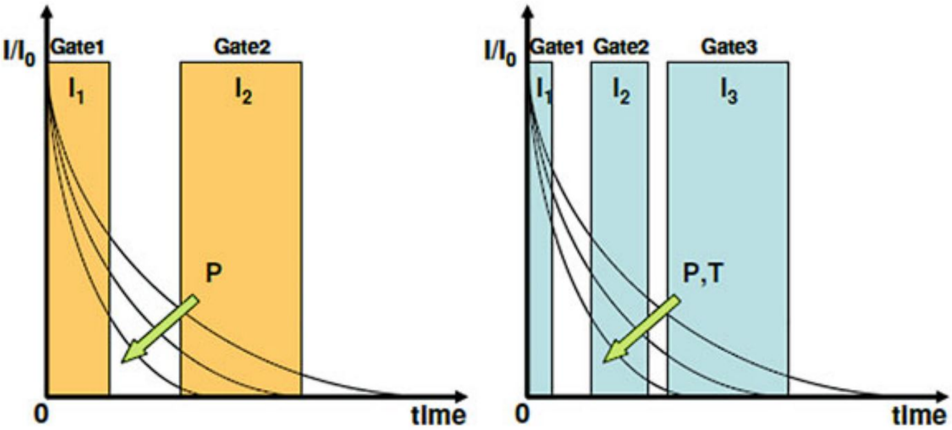

Figure 3.5: Visualisation of the two and three gated image windows. On the left, the exposure time of a two gated method is shown. On the right, exposure times of a three gated method can be seen. Source: Liu et al. [10]

Ratio-of-Ratios Method

As aforementioned, additional corrections are needed to account for uneven paint thickness and nonhomogeneous luminophore concentration. The most common approach is to take reference gated images at wind-off conditions. The gated image ratios taken during the measurement are then divided by the same ratio taken at reference conditions. This gives the following calibration for the pressure

$$p = f\left(\frac{I_1/I_i}{I_{1,ref}/I_{i,ref}}\right). \tag{3.7}$$

Similarly to the intensity based method, Equation 3.7 eliminates the error sources related to uneven thickness and nonhomogeneous luminophores concentrations. This correction approach is called the "ratio-of-ratios" [10] method. Neither the book of Liu et al. [10] or the lifetime PSP lecture series by Yorita [56] mention any other correction method for these error sources.

3.3. Intensity Based Data Processing

Data processing flowcharts used for the intensity method often follow similar steps, with small variations depending on the exact application and corrections. The flowcharts can be seen as variations of Figure 3.4, in which all the basic building blocks are used. In this section each block is described. Afterwards, other steps not stated in the flowchart are mentioned. Some blocks refer to corrections of specific errors, which are described in the next chapter.

3.3.1. Flowchart Building Blocks Description

The flowchart shown in Figure 3.4 can be seen as a "generic" processing flowchart for the intensity based method. It contains all the basic processing steps required to obtain pressure data for a camera imaging system using one luminophore. Other imaging systems (such as PMT) follow similar processing steps, with small differences depending on the system. Below follows a description of the different blocks used in the processing flow chart. The code that was created for data analysis in this thesis follows similar steps.

- **Wind-on and Wind-off Images**

The wind-on and wind-off images are taken at identical camera and illumination conditions. The amount of images, exposure time and acquisition rate depend on testing setup. Standard PSP articles often do not mention most of the aforementioned parameters. In a perfect world without errors, one image of each would suffice. In reality, multiple images are taken and averaged to mitigate the errors. Three examples were found where imaging parameters were mentioned for standard PSP:

1. Nakakita et al. [58] used 20-40 images per test configuration with an exposure time of 1s to 2s. The author presumes that the same was done for wind-off images.
2. C. Huang et al. [59] took 50 images for both wind-on and wind-off per configuration. Exposure times and acquisition frequency are not mentioned.
3. Avelar et al. [60] used a $20Hz$ acquisition frequency. No other parameters are mentioned.

For the wind-off images it is key to ensure the temperature of the model does not change during acquisition. This is mostly relevant when taking images after a run, to reduce thermal quenching errors. Exposure times can be high, as seen from Nakakita's study [58], which allows the temperature on the model to change. When reference images are instead taken at ambient conditions, no gradients are expected.

- **Corrections for Dark Current, Ambient Light & Fixed Pattern Noise.**

After the images are taken, camera system corrections are first applied. Mentioned here are the dark current, ambient light and fixed pattern corrections. To take dark current images, the camera cap is placed on top of the detector and images are taken using the same parameters as used during the tests. A similar amount of images should be taken as was done for the wind-off images. The dark current images are then averaged and subtracted from the wind-on and wind-off images. For the wind-off images this should be done on the averaged wind-off image, to lower computational time.

Ambient light corrections follow a similar approach as the dark current. Here the images are taken without the excitation light but everything else the same as the test setup. Dark current once again has to be subtracted from the ambient light. After this is done, the ambient light images can be subtracted from the wind-on and -off images. The author is unsure as to why these are mentioned as two different corrections in [10], as the dark current is present in the ambient light images. Due to this, the author presumes that just taking ambient light images and averaging them also accounts for the dark current.

Lastly, flat-field corrections are applied to remove the fixed pattern noise. The procedure for obtaining these corrections is described in Subsection 4.4.2. The result is a gain matrix for each pixel, which is multiplied with the ambient light and dark current corrected wind-on and -off images. This must be done before obtaining the intensity ratio, as different pixels are used for division after image registration. Another approach used in the study of Bitter et al.[35] on rocket nozzles, where the flat field correction was not applied, is to take the associated errors as a pressure uncertainty using the expected pixel-to-pixel variation.

Other camera corrections are also applied at this stage or after image registration, such as:

1. Bias corrections due to paint aging, excitation light unsteadiness or dust and oil sedimentation. This can be applied as a simple multiplication factor to the intensity values.
2. Filtering corrections. Various errors can be corrected using filtering. Filtering can be applied to both the wind-on and -off images. It is sometimes instead applied to the calculated pressure image.

- **Correction for Non-Linear Response of the Detector**

This correction is often not mentioned or accounted for. It refers to the non-linear pixel response to light. The flat field corrections account for some of this error, but as the error is dependent on light intensity level, flat field corrections can not fully remove this error source. The book of Liu et al. [10] notes that scientific cameras can be assumed to have a linear output.

- **Image Registration**

Image registration is the process of aligning wind-on and wind-off images with each other. During experiments model aeroelasticity and vibrations cause a change in model position between wind-on and wind-off images. To compute intensity ratios, these two image sets must be realigned. Image registration algorithms are capable of correcting for model translation and deformations (such as rotation, stretching, shearing etc.) [10]. More on the procedure is explained in Subsection 4.2.3.

For rigid models, image registration is sometimes omitted. There it is assumed that models barely move when the wind tunnel is turned on. An example can be found in the PLF study of Nakakita et al. [16]. In general it is better to always apply image registration.

- **Ratio Image**

After images are register with each other, the intensity ratio between images can be computed. This is mostly done on a pixel-by-pixel basis. A common approach prior to calculating the ratios, is masking the images to lower computational costs. Large parts of the image plane are often wind tunnel background or areas with no paint (such as fiducial marks). On a good PSP setup, these areas only show noise and luminescent reflections. Therefore, calculating the image ratio here is a waste of time. As the images are registered onto each other, the same mask can always be used. When images are not masked at all, the displayed data is messy and full of unnecessary noise. An example can be found in the article of Huang et al. [59].

Instead of masking the fiducial marks, some research patches the areas without paint using the intensity of the surrounding area. This approach is used for all NASA SLS PSP research [14, 54]. Patching allows for a "cleaner" reconstruction of the pressure over the model. An example can be seen in Figure 3.6.

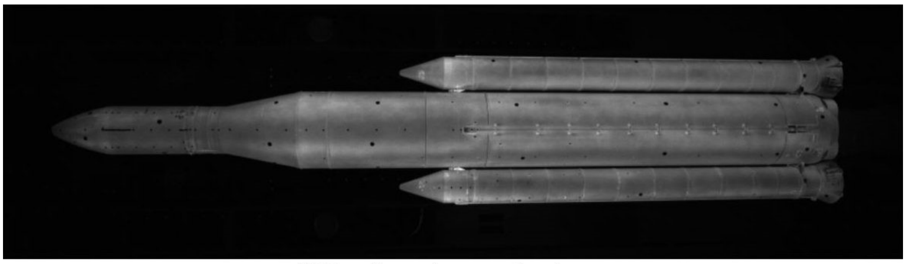

(a) Raw intensity snapshot image

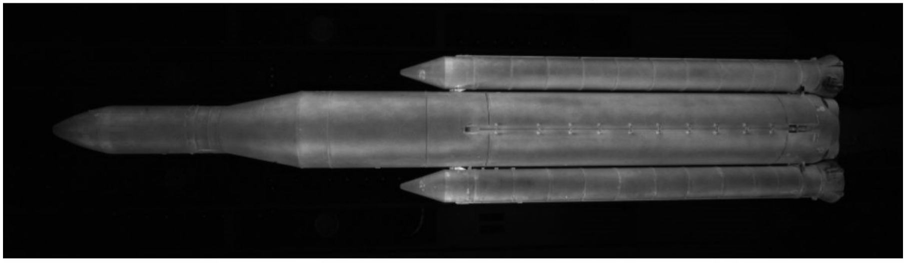

(b) Patched snapshot intensity image

Figure 3.6: Raw intensity image from the 2.5% scale test of the SLS prior and after fiducial mark patching. Source: Powell et al. [54]

- **PSP/TSP Image**

With the intensity ratios computed, the pressure can be calculated using the Stern-Volmer curve. The exact application significantly depends on the type of temperature corrections (if any is used) and the paint calibration itself. More on temperature corrections can be found in Section 4.1.

Most facilities calibrate the Stern-Volmer curve prior to testing using coupons. The coupons can be assumed to show the same behaviour as the painted model. This requires the paint to be applied in the same manner. Other facilities, such as the NASA Ames Unitary Plan Wind Tunnel [54], allow for the wind tunnel (p, T) to be changed independently. Paint calibration is instead performed on the painted model itself, yielding a Stern-Volmer curve for each point on the model. Lastly, some research groups (e.g. Pokela et al. [61]) instead only perform an in-situ calibration using pressure taps and greyscale values.

For standard PSP, individual pressure frames are often first corrected for bias (if not done earlier) and temperature errors. Sometimes it is assumed that the temperature does not change, so no corrections are applied. Afterwards the images are all combined and averaged to obtain a mean pressure field over the experiment. The frames are often highly correlated due to the response time of the paint and therefore can not be used for temporal analysis of the pressure field.

The result of this step is a 2D image with computed pressure values. Often acquiring and correcting the 2D image is the final step in the intensity based method, especially for flat and convex models. Depending on the type of noise, the temporal filtering applied by averaging the images can be enough to reduce overall noise levels. For some noise types and in special PSP applications, additional spatial filtering is required. An example of additional spatial filtering being used can be found in the DLR PSP lecture series by Mébarki [62]. The final image can then be used to extract forces and moments.

- **PSP/TSP Data on a 3D Grid**

Some research follow the 2D image step with a 3D image resection. Here, image resection refers to the process of reconstructing the image on a 3D grid of the model. Generally the 2D images are reconstructed on a CFD model grid. In more complex test setups image resection is required in order to correct for self-reflection errors [50]. In general however, a 3D representation of the data allows for easier comparison with CFD and a better spatial understanding of the flow field physics. The downsides of applying image resection (and self-reflection corrections) are the often high computational costs. Resection was not applied in the processing of PSP data for this project. More on image resection is discussed in Section D.4.

The order of events in the data processing do not necessarily match the flowchart from Liu et al. Figure 3.4. In the SLS research campaigns [14], NASA first registered the intensity images then reconstructed them on a 3D grid. Corrections, averaging and pressure determination were applied after reconstruction. Furthermore, after the 3D images were constructed and corrected, 2D images were generated with "unwrapped" 3D models. Instead, when following the flowchart, spatial filtering and other corrections is often applied during the 2D to 3D conversion.

- **Forces & Moments/Heat Transfer**

After the full pressure field is computed, further analysis can be performed. For standard PSP, the pressure field can be used to extract forces, moments, locations of flow features (shocks, separation, etc.) among other parameters. As only the time averaged data is available, the options are limited. As mentioned before, information can also be extracted from the 2D images, but the 3D view instead gives a more intuitive representation of the forces and moments.

- **Multiple Camera Alignment**

Not shown in the flowchart is the use of multiple cameras, which yields overlap areas. The author found two approaches to deal with this during data assimilation. The first approach, described by Powell et al. [54], was used during the 4% model scale tests of the SLS. Here the raw camera images were directly projected onto a 3D grid of the model. In the regions of camera FOV overlap, Powell et al. [54] used "the data from the camera with the largest angle between the grid normal and the vector from the camera to the node". The data from the other camera was simply neglected. Furthermore, camera data was rejected when the angle between surface normal and vector to the camera was larger than 80°.

Instead, during the 2.5% scale tests of the SLS a second approach was used, as described by Heany et al. [9]. Camera data here was combined, yielding data with reduced noise in the overlap regions. The noise was reduced by approximately a factor $\sqrt{2}$, as for their setup the most prominent noise source was photon shot noise (see Subsection 4.4.1). Other noise sources are also reduced by overlapping camera data.

3.4. Launch Vehicle Studies Using PSP

In this section, past LV studies that used PSP are highlighted. The goal of this section is to demonstrate the capabilities of PSP when applied to LV research. All studies mentioned here made use of the intensity based method with standard or fast PSP.

- **Brazilian Space Agency LV Studies using PSP**

Four PSP articles have been written by Avelar from AEB on different simple LV geometries [1, 13, 60, 63]. Three of these studies pertain to HHFs. The author is sceptical of the quality of their quantitative data. In their time averaged PSP results, significant asymmetry is seen at $\alpha = 0°$, which should not be present. An example can be found in the PSP images that are superimposed over the Schlieren images in Figure 3.7. It is therefore worth questioning whether their reported values are accurate. Additionally, the PSP correction method on their first two articles is sub-optimal. This does however not diminish the qualitative aspects that can be seen in their data, as a lot of different transonic flow features are well represented.

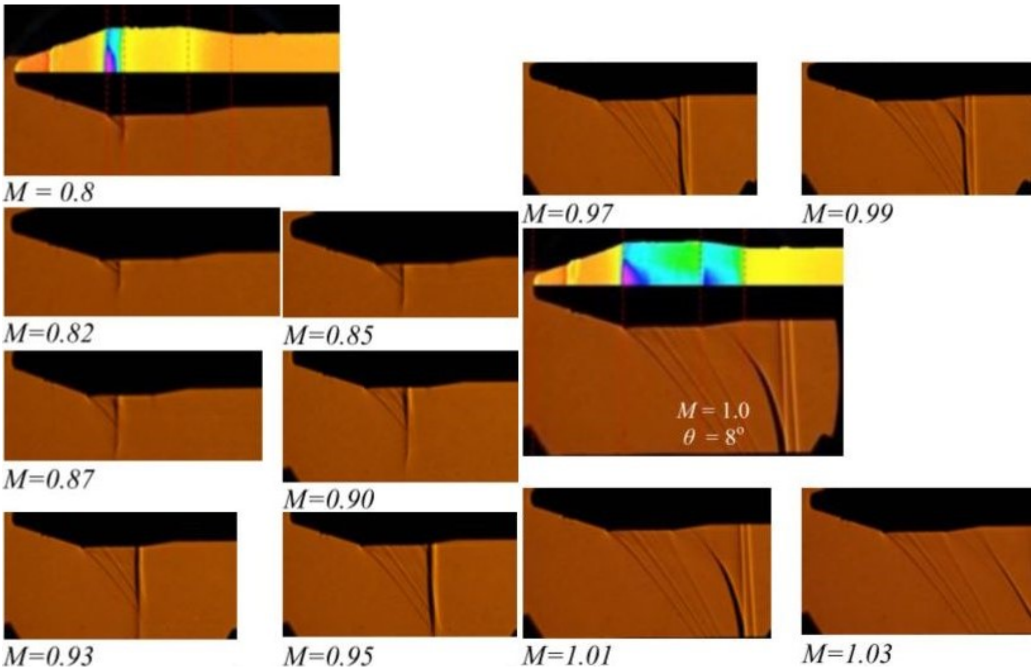

Figure 3.7: Schlieren images of the shock development over a model of the VSL-1 launcher. The downstream shift and strength increase of the shocks with increasing M is evident. Also overlayed are two PSP images taken at the same conditions. These images show significant asymmetry in the pressure field. Source: Image adapted from the work of Avelar et al. [13].

- **NASA SLS 1.3%, 2.5% and 4% Model PSP Studies**

The last couple years, NASA performed at least three PSP campaigns on the space launch system (SLS). The first called the "Ascent Unsteady Aerodynamics Test (AUAT)" used a 4% scale model with fast PSP [36, 54, 55]. The second used standard PSP on a 1.3% scale model [39]. Lastly, a 2.5% scale model campaign labelled "Ascent Transient Aerodynamics Test (ATAT)" was performed with fast PSP [9, 14, 36, 64–67].

Their relevance pertains mostly to the application of PSP on LV research, as the SLS does not have a HHF. Valuable insight can be obtained from the various analysis and noise reduction approaches employed by NASA. A slew of different methods is used to thoroughly analysed the obtained PSP data.

- **JAXA Straight PLF Study**

Nakakita et al. [16] investigated the cone-payload compartment junction of a generic axisymmetric straight PLF at M = 0.8. Time averaged and time resolved PSP data was found to show good match with nearby pressure taps. Shock unsteadiness and strength was found to increase with α, unlike what occurs for HHF.

- **Hypersonic Study on an Axisymmetric Body of Revolution with Fins**

Pokela et al. [61] investigated a generic axisymmetric body with fins. Slender bodies show a linear relation between α and lift up until roughly $\alpha = 6°$, after which separation starts. This separation is characterised by a pair of counter rotating vortices on the leeward side. Fast PSP was used to produce time averaged pressure fields at $\alpha = 6°$ and $\alpha = 12°$, along with oil flow, to characterise flow features over the body and fins.

- **Separating / Reattaching Flows on a Axisymmetric Generic LV model**

Bitter et al. [35] investigated the separating / reattaching baseflow of a generic axisymmetric LV model at M=0.3 and M=0.7 using fast PSP and PIV. The article provides great insight into their error analysis and experimental methods, as a lot of details are given. The fast PSP data was capable of accurately predicting the expected dominant vortex shedding frequencies. Analysis was also performed on the dynamics of the reattachment zone. When compared to CFD, the extent of the separated flow zone was again over-predicted, as is the case in HHF simulations.

3.5. PSP Literature Conclusions Regarding Application to HHF

In this chapter and the next, PSPs as a method is thoroughly scrutinize to determine:

1. How PSPs works.
2. What options there are for PSPs.
3. What equipment is needed.
4. What error sources there are and how to deal with them.
5. What data processing methods are available.
6. The suitability of applying PSPs to hammerhead payload fairing research.

Based on the findings presented in this report, PSP is an excellent way to research LVs. PSP is best applicable at the transonic flow regime, which happens to be the regime of interest. PSPs can be used with different methods, with varying complexities, that yield different types of useful data in HHF research. However, successful implementation of PSPs requires bookkeeping of many error sources that can invalidate results, as will be discussed in the next chapter.

As the most important aspects of HHF buffeting are the location, pressure level and spectral content of flow features, ideally HHF research should be performed using fast, time resolved PSP. Standard PSP are incapable of capturing the dynamics of buffeting due to their high response time. However, fast PSP has a much more complex data analysis and setup than standard PSP. As this is the first time PSP is implemented at the TU Delft, it was chosen early on to first ensure that PSP is implemented successfully by starting with standard PSP. The goal was to move on to fast PSP if standard PSP was done in a timely manner.

To this end, intensity based PSP was chosen over lifetime based for two reasons. First, fast PSP generally uses the intensity method as opposed to the lifetime one. Although fast PSP data processing is more complex, it uses the same building blocks as standard PSP. Creating an intensity based code for standard PSP allows for a more efficient implementation of fast PSP after. Secondly, lifetime based PSP has a more complex data analysis and setup. The main benefits of this method over intensity based are small for the rigid HHF models that were investigated. Thus, intensity based PSP was found to be more appealing.

4 PSP Measurement Error Sources and Corrections

This chapter describes the various error sources that can occur during PSP measurements and when applicable their respective corrections. An overview of all sources mentioned in PSP literature can be seen in Appendix D. The error sources are designated into three groups depending on their origins, namely:

1. Paint related errors
2. Equipment related errors
3. Temporal and spatial errors

The above designation does not strictly originate from PSP literature but was instead adapted as a way to organize all errors. The aim of this is to enable quick identification of errors. Some errors can be designated to multiple groups, giving rise to overlap in the classification. An example are 'paint aging effects', which could be classified as temporal or paint related errors. Errors for which this holds were instead put into one of the groups, with priority to the "paint related errors" group, followed by the "equipment related errors".

The most important errors in Figure D.1 are highlighted yellow. These are errors which are either hard to correct or give rise to extensive uncertainties if unaccounted for. Note that not all of the errors shown in Figure D.1 were relevant for this thesis. In the following section an overview is given of all the error sources that were encountered or mitigated during the measurements. Error sources that are not discussed in this chapter could have caused small errors in the measurement campaigns that went unnoticed or were not recognized. Interested readers are referred to Appendix D for a description of these.

The temperature related errors (thermal quenching) are the most important and most difficult to account for. Due to this, the first section is dedicated to the temperature related errors and corrections. Model aeroelasticity errors and corrections are then discussed in the following section, due to the relative complexity in accounting for these. Other sections follow the designation shown above.

4.1. Temperature Effects and Corrections

Luminophores are impacted by temperature effects that lead to errors in the pressure calculation. The most important temperature effect is the inherent thermal quenching of luminophores. Effectively all compressible PSP applications have temperature gradients, causing spatial differences in thermal quenching. As the luminescent emission of PSPs vary between 0.4% and 4% per K, this can cause large pressure errors, especially in flows with shocks. An example of the potential scale of this error can be seen in Figure 4.1 for a shock impinging on a flat plate. Initially no temperature correction is defined, leading to a large discrepancy with kulite data. A non-linear in-situ calibration is then applied, which mitigates the thermal quenching offset.

Several ways exist to correct for thermal quenching errors, with different degrees of precision. The most commonly used approaches are [10, 68]:

1. Reference image acquisition post wind tunnel run.
2. A-priori corrections using calculated temperature fields.
3. In-situ corrections using pressure tap data.
4. Multi-luminophore dyes (see Section A.2) with similar temperature sensitivity.
5. Direct temperature measurements (TSP, IR, thermocouples).
6. Heat soaking of wind tunnel models [11, 55] (see Section D.1).

The approaches mentioned above are often combined to increase the efficacy of the correction. Below the first five methods are discussed. The last method is not applicable to the blowdown facilities of the TU Delft and has therefore been omitted.

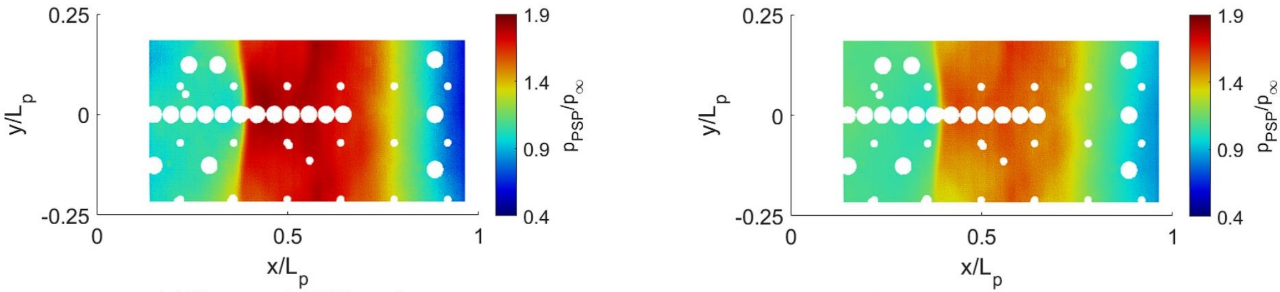

(a) Uncorrected PSP results

(b) Corrected PSP results

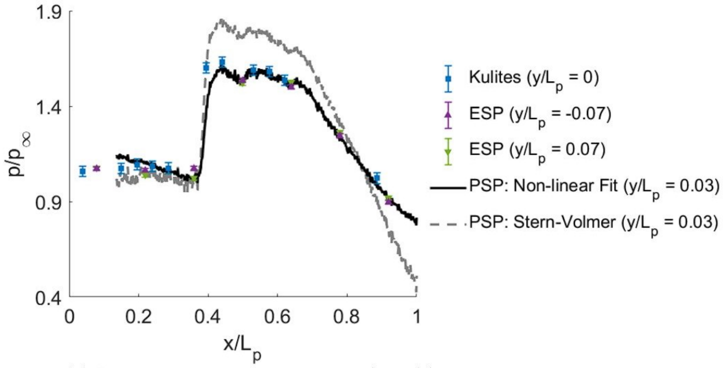

(c) Pressure measurement near the midspan

Figure 4.1: An example of the effect of temperature errors on PSP data of a shock impinging on a flat plate. In (a), the Stern-Volmer equation was applied to the intensity ratio assuming a constant temperature. In (b), a non-linear regression model is applied to match PSP values with pressure tap data. Figure (c) shows the pressure near the mid-span. Here ESP are the locations of static pressure taps. Large errors are present due to temperature gradients caused by the impinging shock. Source: Brouwer et al. [43]

4.1.1. Reference Image Acquisition Timing

For the intensity and ratio-of-ratios methods, reference images are taken at wind-off conditions with known p (often at atmospheric conditions). Taking wind-off images before the measurement ensures that the model temperature is isothermal at the ambient temperature. This allows for Stern-Volmer curve calibrations with I_{ref} at know (p, T). A secondary approach is to instead take wind-off images directly after the measurement. By doing so, the model's temperature will be closer to what it was during the experiments, which reduces thermal quenching errors.

This reduction can be explained using the following equation. Egami et al. [69] and Sakaue and Hayashi [70] found that the effect of temperature on the intensity can be approximated as a second order polynomial:

$$\frac{I(p_{ref}, T)}{I(p_{ref}, T_{ref})} = a_T + b_T \cdot \frac{T}{T_{ref}} + c_T \cdot \left(\frac{T}{T_{ref}}\right)^2 \tag{4.1}$$

where a_T, b_T and c_T are empirical coefficients. As this equation only depends on temperature, the slope of the Stern-Volmer curve can be assumed to be constant when the temperature of the wind-on and -off images is the same. By taking wind-off images directly after the experiments this condition is nearly achieved, which in theory eliminates the thermal quenching. Due to this, the method is commonly used in practice. Sometimes it is used by itself, but it is most often combined with an in-situ pressure tap calibration.

In reality, while this approach does reduce the pressure uncertainty, additional corrections are needed. Wind tunnels require some time to return to ambient pressure. During this time, gradients are diffused by heat transfer phenomena, causing differences between wind-on and -off temperatures. Secondly, model temperatures often do not reach steady state during measurements [10]. Blowdown facilities never reach a steady-state condition due to the decrease in T with reservoir capacity. Lastly, Equation 4.1 is an approximation, whereas in reality the thermal quenching effect on I is non-linear, also depending on pressure.

4.1.2. A-Priori Temperature Corrections

In a-priori corrections, the model temperature field is predicted before the experiments are performed. The calculated temperature is then used for corrections. Higher fidelity predictions lead to better correction results, as the temperature is more accurately predicted. Often simple iterative adiabatic wall temperature (T_{aw}) estimations are used [68]. This method computes the local M number using isentropic expansion relations based on the calculated P from PSP, to then determine T_{aw} according to Equation 4.2 [71]:

$$\frac{T_{aw}}{T_{tot}} = \frac{1+r\cdot\frac{\gamma-1}{2}\cdot M^2}{1+\cdot\frac{\gamma-1}{2}\cdot M^2} \tag{4.2}$$

where T_{tot} is the (known) total flow temperature γ the heat capacity ratio, M the local Mach number and r is the recovery factor. r depends on the state of the b.l. and is often taken as $\sqrt{Pr}$ (=0.84 for air) for a laminar b.l. or $\sqrt[3]{Pr}$ (=0.89 for air) for turbulent b.l.. With T_{aw}, a new p is calculated which updates the M number prediction using isentropic equations. A new T_{aw} is then computed until p converges.

The main benefits of this correction method is that it can be easy to acquire when using low fidelity estimations, or it can directly be taken from CFD. However, predictions differ significantly from the true temperature [10] as the adiabatic wall assumption simply does not hold in reality, giving erroneous temperature predictions. Conductive and radiative heat transfer from the model alter the surface wall temperature compared to the adiabatic prediction. Due to the low reduction in errors of this method, it is not commonly used in literature or combined with other correction methods.

4.1.3. In-Situ Corrections

In-situ corrections are the most used correction types for thermal quenching errors [10, 68]. In this method, pressure taps are used to "anchor" the computed PSP pressure (p_{PSP}) around the tap to the pressure measured by the tap (p_{tap}). This can be done in numerous ways. Here it is assumed that the p_{tap} is the true pressure. By anchoring the p_{PSP} to the true pressure, the thermal quenching of PSP is in theory corrected. Generally, the closer to the tap, the better the corrections works as the temperature will match better. An example of results corrected in-situ using pressure taps can be seen in Figure 4.1.

The author found two methods that are most commonly used for in-situ corrections. The first multiplies the calculated PSP pressure by a correction factor computed with pressure taps. Here, data from various taps is used to devise a correction for all pixels based on pressure tap proximity. No general approach for determining the proximity equation is given in literature. Note that according to Sellers et al. (2017) [8], flow features can still have large errors, depending on tap placement. The second approach directly relates the measured intensity to the greyscale values (as is done for IR [38]). Here no Stern-Volmer curve is determined a priori. Both approaches work best for models with a lot of pressure taps.

Some studies apply in-situ correction using very few pressure taps, leading to corrections with a high uncertainty. An example of this are the studies of Avelar et al. [1, 13], where a few (not clearly stated in articles, either one or two) pressure taps are used to correct the pressure on the entire model. When few taps are present, they are often only used to qualify PSP data and other correction types, as was done in the first study of Bustard et al. [72] where TSP data was available (see Figure 4.2).

4.1.4. Multi-Luminophore Dyes with Similar Temperature Sensitivity.

When two luminophores have the same sensitivity to temperature, their luminescence at constant concentration (c) and p will shift by the same amount for a ΔT. The ratio of intensity between both luminophores thus stays constant for any T at a given (c, p). By using the ratio-of-ratios method to eliminate c variations (see Subsection 3.2.2), the Stern-Volmer curve of the ratio of two luminophores at T_{ref} holds for any other temperature. This eliminates the need for other thermal quenching corrections [10]. In practice, luminophores never have the exact same T-dependency. Instead, for a similar sensitivity, the dependency on T can be significantly reduced. In the commercially available Binary Unicoat PSP[28] by ISSI, the temperature sensitivity is reduced to 0.03% per K due to the use of a pressure independent reference dye.

4.1.5. Direct Temperature Measurements.

Direct temperature measurements can be used to correct PSP data [10, 68]. Most commonly used are thermocouples, IR thermography or TSP measurements. By measuring the (approximate) temperature field of the model, the Stern-Volmer coefficients are determined at a corrected temperature for each pixel. This requires a 2D determination of the Stern-Volmer curve or use of the temperature dependency assumption in Equation 4.1. Figure 4.2 shows an example of TSP-corrected PSP results.

Similarly to pressure taps, thermocouples offer limited spatial resolution and require proximity based corrections. Their placements is also of key importance, as thermocouples can be intrusive when placed inside the flow. When used inside the model, the measured temperature may furthermore not be exactly the same as the wall temperature. Their benefits are that thermocouples are cheap and easy to apply.

The other methods can all give full coverage of the surface, allowing for more spatially precise corrections. Each method offers various benefits and negatives. First, IR thermography is a method that offers a high temperature prediction precision, with a lower measurement accuracy (see Subsection 5.4.1). This offset can lead to a bias error in PSP data if not accounted for. Additionally, the required optical access for IR thermography is not always available. TSP measurements, in contrast to IR, offer high accuracy with lower measurement precision [68]. This leads a higher uncertainty of the actual temperature. An example where this is used is the DLR study on a delta wing by Konrath et al. [73].

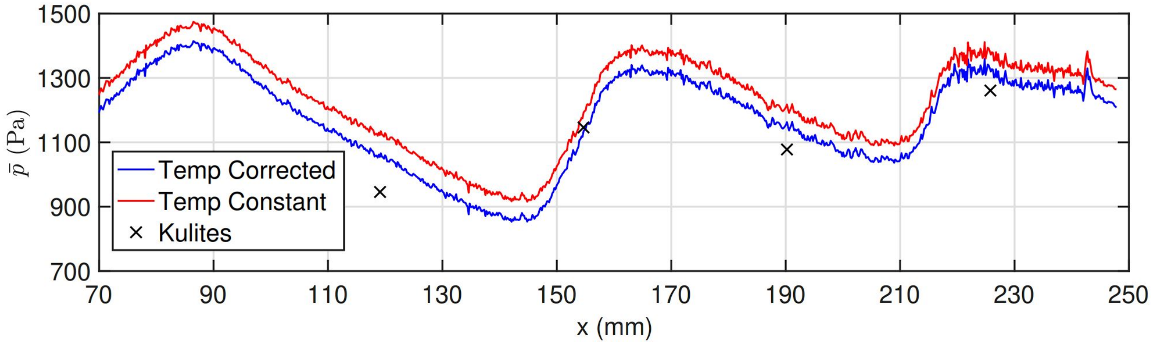

Figure 4.2: Example of the impact of temperature corrections. Here PSP measurements were taken of a scramjet inlet flow using AA-PSP at Mach = 6.3. TSP measurements in identical flow conditions were repeated afterwards to determine the temperature field. Temperatures changed by at most 4K during the run. A 5.7% net change in mean pressure was observed post temperature corrections, with a 37% reduction in errors between PSP and kulites. Source: Bustard et al. [72]

Often temperature measurements are taken separately from PSP measurements at identical flow conditions. The main benefit of doing so is the ability to install a different optical access window for IR or change the paint on the model from PSP to TSP. This requires repeatability of measurement conditions or the measured temperature will be different. An example of a study where this went wrong is the study of Bustard et al. [74]. They ran into an issue wherein the TSP data ended up being taken at a slightly different thermal environment, thereby removing the ability to apply thermal quenching corrections from this data.

For symmetrical test models, such as aircraft models, an approach that can be used is measure the temperature on one half of the model and perform PSP measurements on the other half. It is then assumed that both halves experience the exact same forces and temperatures. The temperatures measured on one half are used to correct the PSP data on the other. Examples of studies that used this approach on aircraft models are a study by Nakakita et al. (2006) [58] and two studies by Huang et al. [59, 75].

4.2. Model Aeroelasticity

During wind tunnel runs models vibrate and deform under the aerodynamic loading. The vibrations and deformations cause the models to displace relative to the camera and light sources. This leads to various errors in PSP measurements. While rigid models experience less deformations than more flexible models (such as aircraft wings or propeller blades [76]), even in the rigid models aeroelasticity can cause significant errors. The three main error types that arise due to model aeroelasticity are [10, 68]:

- Model motion in an inhomogeneous illumination field.
- Pressure mapping errors due to model displacement in images
- Errors caused by model alignment algorithms used to re-align wind on and -off images (fast PSP).

The last type causes frequency domain errors and is not discussed here as it is relevant only to fast PSP.

4.2.1. Model Motion in an Inhomogeneous Illumination Field

Light sources used in PSP measurements often don't produce a fully homogeneous and collimated illumination field. Lenses can be used to ensure the distribution of light is homogenised, but even then some variation exists [35]. Therefore, model movement causes variations in the excitation intensity between wind-on and -off images. Additionally, more flexible models often twist and turn, thereby changing their viewing angle. An example of the impact of this can be found in Figure 4.3 (see Bitter et al. [35]), where the effect of model movement in the illumination field was measured using a white screen. A pressure uncertainty of 350 Pa was found from the model's movement. Note that this data was collected on a rigid axisymmetric LV model, similarly to what was tested in this project.

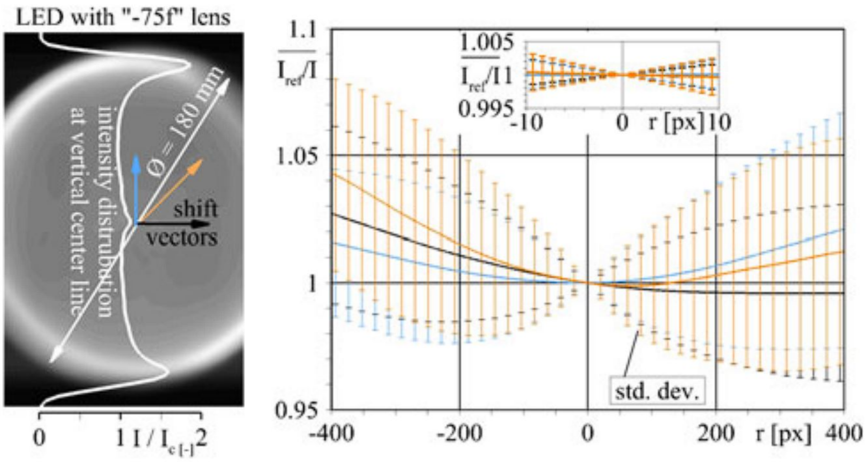

Figure 4.3: Example of the uncertainty in intensity ratio caused by model motion in an inhomogeneous light field. Original study tracked the movement of fiducial marks on the model, then projected the light source onto a white screen to determine the illumination field. By simulating model movement, the illumination error bars and uncertainty values were found. Blue represents vertical motion, black horizontal motion and orange a combined motion. A total pressure uncertainty of 350Pa was found. Note that the study makes no mention of shot noise corrections, therefore this is likely included. Source: Bitter et al. [35]

Correcting for this error type can be difficult when using the intensity based method. Determination of the exact emitted light field is required experimentally (e.g. Bitter et al. [35]), or analytically (e.g. Bell and Mclachlan [77]). Both approaches require additional displacement measurements. Multi-luminophore dyes instead completely eliminate this error source as the ratio of the luminescent emissions is independent of the intensity of the incident light [68, 76]. However, image alignment is still required.

4.2.2. Pressure Mapping Errors due to Model Displacement

When using any method that uses reference images at wind-off conditions, image alignment is required [10, 62]. If alignment is not performed it can cause the following errors:

- Model features are blurred out or repeated [62]. Fiducial marks, paint flaws, unpainted pressure taps and other areas without a paint signal are repeated twice in the image after division. Model edges become blurred, making it hard to distinguish between the edge of the model and the background.
- One of the benefits of the intensity based method, is the elimination of paint inhomogeneity errors (uneven thickness and luminophore distribution). When images are misaligned, the ratio on each pixel is taken for two different points in space, eliminating this correction.

To correct for this error type, image resection and registration algorithms can be used. In image registration fiducial marks are placed on the model. By using a software to identify these marks, they can be aligned between two images. This is a 2D procedure which simply aligns images in the image plane. The image registration procedure is described in Subsection 4.2.3. Image resection in PSP literature refers to the process of reconstructing the image on a 3D grid of the model. According to Liu et al. [10] this requires calibrating the camera by "solving the perspective collinearity equations". This is often done using ray tracing software [52]. A brief summary of image resection can be found in Section D.1 for interested readers.

An example of the impact of model displacement on the image ratio can be found below in Figure 4.4. Here a XB-70A model coated with PSP is shown. This model was tested at M=0.4, causing a displacement of 10 pixels between wind-on and -off conditions. Without image registration, various spurious features can be found in the image, such as repeated fiducial marks. After image registration most of these disappear, giving a more evenly distributed pressure with clear flow features.

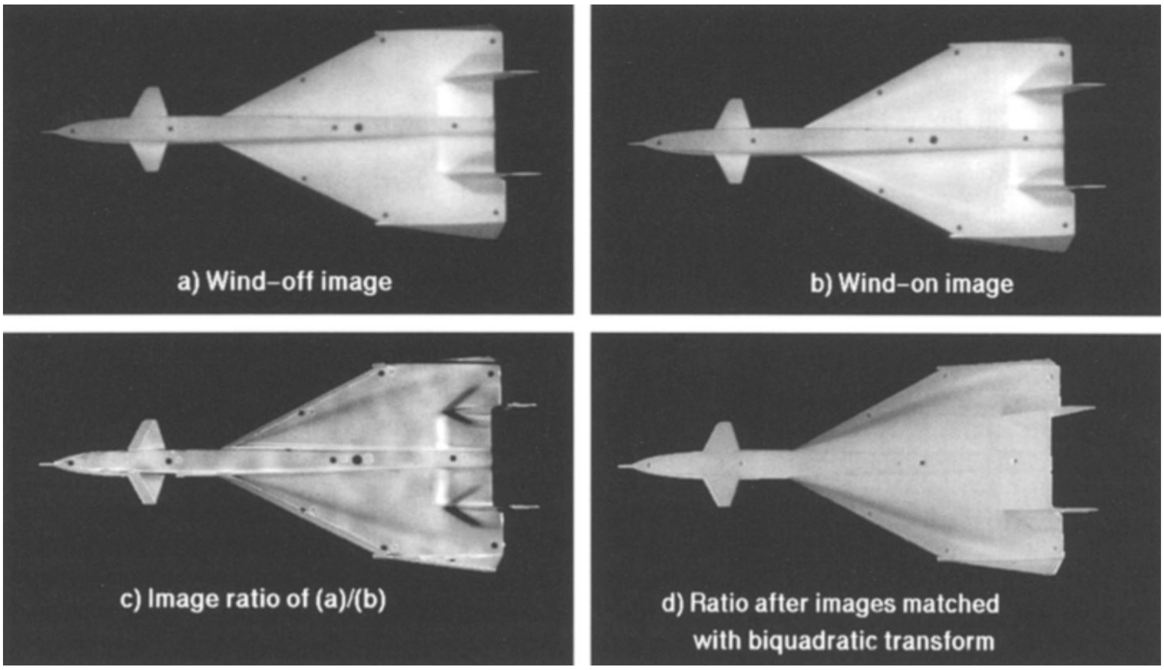

Figure 4.4: Example intensity ratio errors caused by model movement. In figure c) the intensity ratio is shown without image registration and figure d) shows the intensity ratio with image registration. Source: The work of Bell and McLachlan [77].

4.2.3. Image Registration Algorithms

Different mathematical formulations exist to find an image transformation which aligns two images. All approaches are based on finding distinct features on the model, called control points [77], and displacing these on one image to align with the reference. Models often do not have enough "inherent features" that can be used as control points. Therefore fiducial marks are used. Fiducial marks are (black) dots or features that are added to the model whose positions are known. This can be done by masking areas during painting [54], drawing marks on top of the paint [78] or degrading the paint on purpose [46]. Often, pressure taps are masked during painting to avoid damaging them, allowing them to simultaneously act as fiducial marks.

PSP literature most commonly uses the registration algorithms defined in the work of Bell and Mclachlan [77] in 1996. There, the registration problem is defined as follows: For a given wind-off image I_{ref} with image plane coordinates (x, y) and wind-on image I_i with coordinates (x', y'), a transformation from (x', y') to (x, y) needs to be found that aligns the object in I_i with I_{ref}. Three different algorithms are given that are capable of doing this. The first is the projective transform (= perspective transform) given by:

$$
\begin{aligned}
x &= \frac{a_1 \cdot x' + a_2 \cdot y' + a_3}{c_1 \cdot x' + c_2 \cdot y' + 1} \\
y &= \frac{b_1 \cdot x' + b_2 \cdot y' + b_3}{c_1 \cdot x' + c_2 \cdot y' + 1}
\end{aligned}
\tag{4.3}
$$

Where a,b,c are coefficients that need to be found from the displacement. Mathematically this transformation is only valid for rigid body motion of 2D objects, but it gives a good approximation for small displacements of 3D objects, especially when rigid bodies are used. The above system of equations requires 8 coefficients to be found. Each control point gives two equations that need to be solved (one for x and one for y) therefore requiring at least 4 control points in total. More control points can be used to increase accuracy and estimate the errors, as will be expanded upon later.

A secondary approach is using a polynomial series expansion. The equation for this is given by

$$
\begin{aligned}
x &= a_{00} + a_{10} \cdot x' + a_{01} \cdot y' + a_{11} \cdot x' \cdot y' + a_{20} \cdot x'^2 + a_{02} \cdot y'^2 + \mathcal{O}((x', y')^3) \\
y &= b_{00} + b_{10} \cdot x' + b_{01} \cdot y' + b_{11} \cdot x' \cdot y' + b_{20} \cdot x'^2 + b_{02} \cdot y'^2 + \mathcal{O}((x', y')^3)
\end{aligned}
\tag{4.4}
$$

where once again a, b are coefficients that need to be determined. Here $\mathcal{O}((x', y')^3)$ is a collection of third order or higher terms. The polynomial expansion approach can in theory register any type of model motion [10, 77] provided a sufficiently high order is given. According to Liu et al. [10], a second order polynomial is sufficient to register images in most wind tunnel applications. Here a linear polynomial requires finding 6 coefficients, a second order 12, third order 20 and so forth. As with the projective transform method, each control point gives two equations so half the number of coefficients are needed in control points.

Instead of the polynomial expansion, a set of orthogonal base functions can also be used for image resection [10]. Commonly used are Chebychev functions. The general expression for these is given by Equation 4.5, where $\phi_n(x')$ and $\phi_n(y')$ are the nth base function of the orthogonal set.

$$
\begin{aligned}
x &= \sum_i^n \sum_j^n a_{ij} \cdot \phi_i(x') \cdot \phi_j(y') \\
y &= \sum_i^n \sum_j^n b_{ij} \cdot \phi_i(x') \cdot \phi_j(y')
\end{aligned}
\tag{4.5}
$$

Other more sophisticated image registration approaches exist [10]. One such approach is mentioned in the work of Bell and Mclachlan, based on "Delauny triangulation". This approach divides the images into triangles, with control points at the triangle vertices. As both wind-on and -off images have the same pattern of triangles, albeit slightly shifted, their coordinates can be aligned with one another.

4.2.4. Image Registration Accuracy and Error Estimation

The image registration error can be quantified as a pixel misalignment error and a pressure error. The former mainly depends on four parameters, whereas the latter depends both on the pixel misalignment and intensity gradients in both images. The four parameters that determine pixel misalignment are:

- **Number (and location) of control points.** At least as many equations are needed as unknowns, in order to have a solvable system of equations. When more control points are used than required, the system becomes over-determined and can be solved using a least squared approach. The redundancy in the system gives more statistical certainty and can lower the error. Furthermore, control point location can impact the results. Spread out control points are preferred to not introduce bias.
- **Complexity of the transformation method.** More complex transformations do not necessarily yield a better alignment. Higher order methods not only require more control points, but also behave more erratically for simple motions. An example of this can be seen in Figure 4.5, where a third order method gives high errors for mostly rigid body motion.
- **Control point detection accuracy.** To align both images the control point must be accurately de-

tected. Errors in the detection of control point position directly propagate into alignment errors. This depends on detection algorithm, image resolution among other parameters.

- **Type of model displacement.** The type of model displacements significantly impacts how well an alignment algorithm performs. Lower order methods can not accurately align complex body motions (shear, rotation, etc.). Similarly, higher order methods are bad at aligning simple motions.

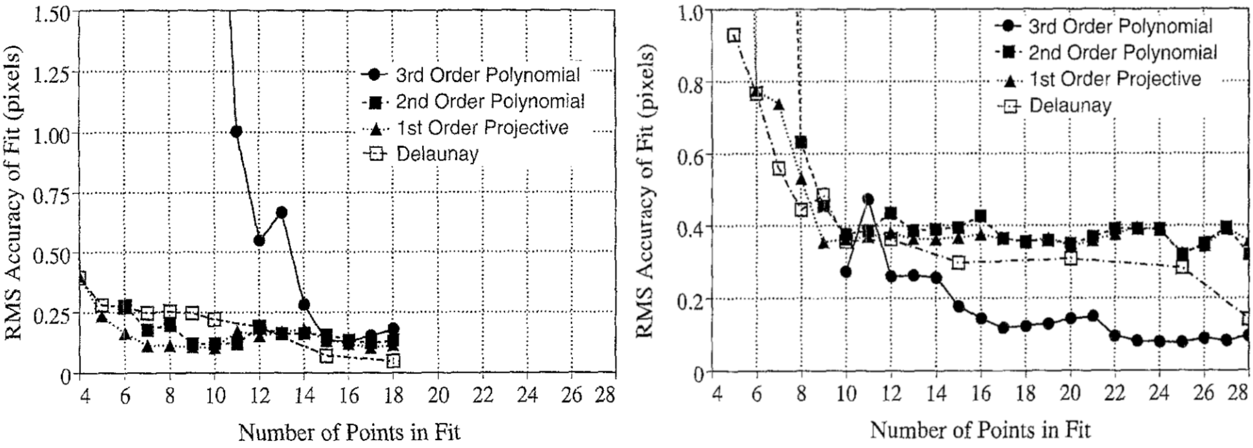

(a) Transformation RMS accuracy of a rigid sting mounted model (b) Transformation RMS accuracy of a flexible half span model

Figure 4.5: Pixel misalignment RMS error for four different image registration methods, applied to two different models. Figure (a) shows the application to a more rigid models, with mostly rigid body motion. Figure (b) shows the application to a more flexible model, where the motion was mostly attributed to wing bending. Source: The work of Bell and Mclachlan [77].

To determine the displacement uncertainty, more control points can be placed on model than needed. A subset of points can then be used to determine the transformation. By calculating the misalignment between points that were not used in the transformation, the alignment uncertainty of the method can be quantified. An example of this can be seen in Figure 4.5 for four methods, using two models. From this analysis, Bell and Mclachlan [77] suggest using around 10 control points with the projective transform or Delauny triangulation for rigid bodies. The models that were used in this thesis fall under this category.

Lastly the pressure error is a function of the image intensity and pixel misalignment. Regions where intensity rapidly change (due to pressure, luminophore inhomogeneity or light inhomogeneity) are more prone to misalignment errors than those with lower gradients. For example, assume an extreme case where the intensity linearly doubles over 4 pixels due to light fields overlapping. Assuming the temperature and pressure of this region in the wind-on image are the same as that of I_{ref}, an image misalignment of 0.4 pixels causes a zone of pixel division with more than 10% difference in intensity over a 4 pixel region. If not accounted for, this will be seen as a pressure difference when converting intensity ratio to pressures.

4.2.5. Detection of Fiducial Marks

The last required step to perform image registration is the detection of the fiducial marks, which can be done manually. However, this is extremely time consuming and inefficient. Therefore algorithms are used to automatically detect the fiducial marks. For this open-source libraries can be used. In python, the libraries "opencv" and "scipy.signal"[9] have functions that can be used [62]. For this thesis, the "opencv" library was used. In "opencv" the functions "simpleblobdetector"[10] and "moments"[11] can be used. "moments" uses both images and the model contours as input to find the control points. "simpleblobdetector" uses the image as input and detects blobs in the image with a given shape.

The latter is used by NASA in their PSP processing software [54]. In their approach, they use the function

---

[9] `https://docs.scipy.org/doc/scipy/reference/generated/scipy.signal.correlate.html`,retrieved October 2023
[10] `https://docs.opencv.org/3.4/javadoc/org/opencv/features2d/SimpleBlobDetector.html`,retrieved October 2023.
[11] `https://docs.opencv.org/3.4/d0/d49/tutorial_moments.html`,retrieved October 2023

to identify all circles with a size similar to the fiducial marks. Function parameters can be tweaked to make the detection more or less strict. When it is set to be more strict, Powell et al. [54] states that some fiducial marks are missed. Instead, a lenient detection can cause spurious marks to be detected. Having more fiducial marks than required allows a more strict approach to avoid no spurious marks.

4.3. Paint Related Errors

In this section paint related errors are discussed, except temperature errors (see Section 4.1). As before, error sources that are not relevant for the experiments in this thesis are included in Appendix D.

4.3.1. Aging Effects

PSPs degrade over time causing them to lose sensitivity and intensity [10]. This can occur due to three reasons, namely photo-degradation, mechanical wear and polymer aging. Photo-degradation is the chemical decomposition of luminophores due to the excitation light. Higher light intensity (and photon energy) leads to a faster degradation. Different PSP formulations have varying rates of photo-degradation. For example, the UniFIB®[6] has a photo-degradation rate of roughly -1% luminescent intensity per hour (h). As degradation is dependent on light intensity, experimental determination of the rate using the same setup as the actual experiments is required. In standard PSP measurements it can often be ignored as decay rates are low.

Mechanical wear occurs due to friction between the air and the paint. It is especially relevant in fast PSP and high speed flows. Over time, the paint slowly gets worn down by the friction. Lastly, polymers slowly degrade over time as molecular bonds are broken due to various reasons. This can lead to the binder polymer losing its oxygen permeability, which reduces the oxygen sensitivity of the paint. Often the luminophores themselves degrade much faster than the polymer, so this error type can mostly be ignored.

4.3.2. Paint Intrusiveness

PSP coating may modify model shape and roughness. When the paint thickness is much smaller than the boundary layer (b.l.) thickness, the inviscid outer flow is not directly affected by the paint. However, according to Liu et al. [10], paint intrusiveness can lead to a local change in flow structures and perturbation propagation. These local changes can cause b.l. thickening, earlier flow separation, b.l. destabilisation, a change in SWBLI among many other effects. The resulting effect of the local changes is a change in integrated aerodynamic forces on the model. A comparison between Schlieren images or pressure taps of the clean and painted models can indicate the extent of the intrusiveness.

4.3.3. Paint Calibration Errors

During the calibration of the Stern-Volmer coefficients errors are made due to measurement uncertainties. Generally, when using a proper calibration setup these errors are very small [10]. In case they are known they can be taken in the uncertainty analysis of the pressure. Otherwise this error type can be neglected.

4.4. Equipment Related Errors

Equipment related error sources and noise originate from the cameras and filters. The impact and importance of errors types from the equipment are dependent on the test setup. In particular, "photon shot noise" and "fixed pattern noise" [10, 68, 79] are almost always an issue in PSP measurements that use cameras.

The noise level caused by these two depend on the amount of absorbed photoelectrons. A generic imaging curve showing the number of noise electrons for a given number of photoelectrons is given in Figure 4.6. At low light levels the noise floor is the dominant noise source, whereas the photon shot noise dominates at intermediate light levels and the fixed pattern noise near full well capacity. Noise floor is only relevant for very low light applications, which is almost never the case in standard intensity based PSP.

4.4.1. Photon Shot Noise

Photon shot noise is a physical phenomenon that occurs due to the discrete nature of the absorbed photons and released photoelectrons [10, 79, 80]. The phenomenon is caused by the fluctuation of photon detection events over different exposures[12]. As photons and the released photoelectrons are not continuous, variance occurs in the number of observations per time period. This variance takes place due to quantum mechanical phenomena which are not described here. The number of detected photons in a pixel follows Poisson statistics, where the variance is the square root of the mean. This results in noise in the measured number of photons. A visualisation of this type of noise can be seen in Figure 4.7.

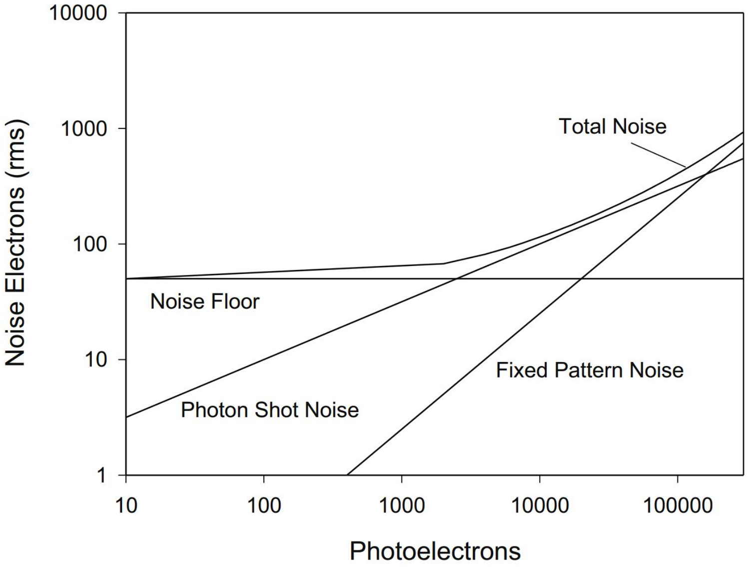

Figure 4.6: Noise electron curve for a generic imaging system with a 50 electron noise floor and a 0.25% pixel non-uniformity. Source: Liu et al. [10]

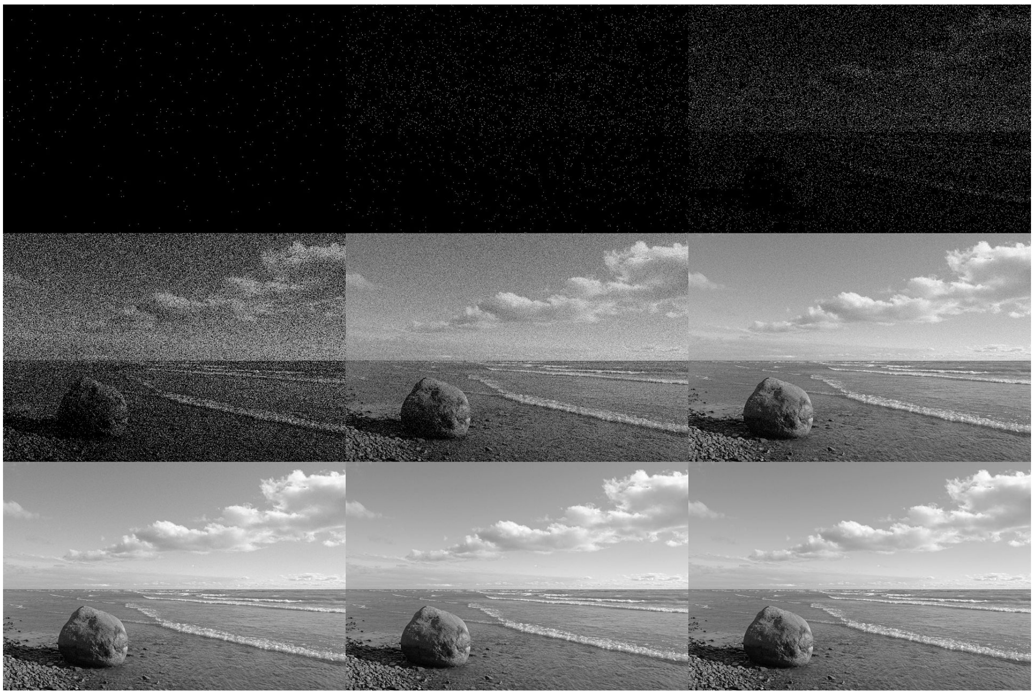

Figure 4.7: Photon shot noise for different photoelectrons levels, increasing left to right and top to bottom. Source: Wikipedia[12]

As it is an inherent physical phenomenon of the measurement, shot noise cannot be avoided. It is the most important camera noise source for fast PSP and when trying to detect small pressure fluctuations [81]. When the photon shot noise is the limiting factor in the SNR, the only ways to reduce the effects is by

---

[12] `https://en.wikipedia.org/wiki/Shot_noise`, retrieved June 2023

increasing the light intensity and image post processing techniques. As the variance is the square root of the mean, the SNR improves. SNR enhancements can be achieved in four ways [67, 80, 81]:

1. Increasing the excitation light intensity.
2. Increasing the camera's light measurement time.
3. Increasing the (effective) measurement area, thereby increasing the photons per measurement point.
4. Denoising by proper orthogonal decomposition (POD) or dynamic mode decomposition (DMD).

First and foremost, experiments should strive to maximize excitation light intensity, while avoiding excitation saturation (see Subsection 3.1.2). If further SNR enhancements are still needed, the other approaches can be used. The fourth approach is mostly used in special PSP applications (fast and low speed) and therefore not further discussed here. The other two approaches can be implemented using post processing techniques (temporal and spatial filtering) or by changing camera settings. For standard PSP the second approach is most commonly used by increasing exposure time or by averaging multiple images in time.

In addition, the third approach can also be used. For this, blur filters are often applied to increase the "effective" amount of light at a measurement point (spatial filtering). The main drawback of using filters is that the increase in measurement area leads to a reduction in spatial resolution, which can lead to the loss of flow features. Due to this, it is not often used in standard PSP (see Section D.1 for the fast PSP application).

An approach that is not used in literature specifically for the sake of noise reduction, but yields less noise nonetheless, is the use of multiple cameras. This effectively increases the number of absorbed photons for the same area and time. In NASA's 2019 2.5% scale model SLS research, four cameras were used to visualise the full rocket. In regions of camera overlap, Heaney et al. [9] found a significant decrease in measured C_{prms} compared to the regions with only one camera. Assuming i.i.d. (Independent and identically distributed) shot noise between pixels, two cameras visualising the same area leads to a noise reduction factor equal to $1/\sqrt{2}$. PSP noise reduction due to multiple cameras is also seen in the other NASA research.

4.4.2. Fixed Pattern Noise

Fixed pattern noise occurs due to variations of pixel responsivity to light and pixel non-uniformity. Pixels are not perfect copies of each other, leading to some degree of variations in their response [10, 79]. This noise type is characterised by a constant recurring pattern of non-uniform response of pixels. It is the dominant camera noise source for high photoelectron intensity (see Figure 4.6) and has an important impact when dividing aligned images. The fixed pattern noise has two components from which it originates

- **Dark Signal Non-Uniformity** is the pixel-to-pixel variation of the dark current (DC). Noise level for this is given as the standard deviation of the DC. It is highly temperature and exposure time dependent.
- **Photon Response Non-Uniformity** is the pixel-to-pixel variation of light sensitivity. Often given as a mean and standard deviation at 50% saturation.

To correct for the fixed pattern noise, flat field corrections can be applied. First, a flat-field image is acquired from a uniformly illuminated field by use of an integrating sphere[13], a tool that returns a uniform light field from an incoming light source. According to Liu et al., when an integrating sphere is not available, flat-field images can be acquired by placing "several diffuse scattering glasses" between camera and light source "to generate an approximately uniform illumination field" [10]. The integration time and light intensity of the flat field images should be identical as during the test. Typically, a set of 15-20 flat field images are taken for low frequency applications[14] and averaged, to account for random photoelectron noise.

The averaged flat-field image is subsequently corrected for the DC noise (see Subsection 4.4.3). Afterwards, a heavily filtered image is created to obtain the mean illumination field. By dividing the flat-field image with the filtered image a pixel gain matrix is obtained, where each cell contains the pixel intensity

---

[13] `https://www.newport.com/t/integrating-sphere-fundamentals-and-applications`, retrieved July 2023

[14] `https://en.wikipedia.org/wiki/Flat-field_correction`, retrieved July 2023

ratio compared to the mean intensity. This gain matrix is used to correct the pixels in the raw PSP images. The aforementioned correction procedure can be described as a set of matrix operations[14]given by [79]:

$$I_{corr} = \frac{(I_{raw} - D_{CA}) \cdot I_{filt}}{I_{FFa} - D_{CA}} \tag{4.6}$$

Where I_{corr} is the final corrected image, I_{raw} the raw measurement image, D_{CA} the DC and ambient light (AL) corrections, I_{filt} the filtered flat field image and I_{FFa} the averaged flat field image. This flat field correction method assumes a linear relationship between pixel sensitivity and incident light intensity. In reality the response of pixels is non-linear [10], making the flat field correction dependent on the saturation percentage. By taking flat field images around the same radiance and exposure time conditions as the measurements, this non-linearity is somewhat mitigated. Bigger errors arise for measurements that occupy a large width of the dynamic range of the cameras.

4.4.3. Dark Current Noise

Dark current noise (DC) is caused by thermal electrons within the camera sensors [10]. In the absence of any incident photons on the camera, electrons are still released in the photosensors due to temperature effects. The amount of noise increases with increasing detector temperature. Scientific cameras often have cooling to reduce thermal electrons. To correct for the DC, an image is taken with no light incident to the detectors. This image is then subtracted from the measurements. A similar correction is also used to account for the AL. Both can also be taken simultaneously.

4.4.4. Image Saturation

Image saturation occurs when the full well capacity of pixels is exceeded, due to a high level of incident light [82]. This can lead to two types of errors:

- **Information loss:** When the full well capacity is exceeded, the intensity captured by the pixel is capped. Additional photons are not measured, leading to a loss of information on the pixel.
- **Blooming (CCD):** Blooming occurs due to charge spilling out of saturated pixels onto adjacent pixels [82]. This leads to bright spots in images becoming larger with apparent light rays emanating from the source. An example of this can be seen in Figure 4.8. It is a characteristic of CCD cameras[15].

Both effects can be avoided by ensuring that the full well capacity is not exceeded. This can be achieved by lowering exposure time, lowering light source intensity or by pulsing the light source.

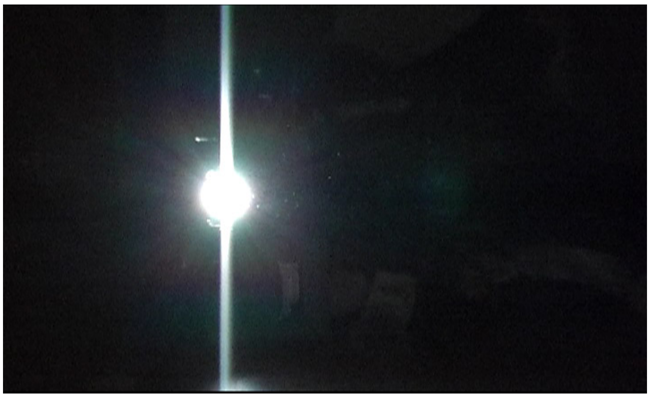

Figure 4.8: Blooming and vertical smear example due to a bright light source. Source: Wikimedia commons[38]

4.4.5. Salt and Pepper (Impulse Noise)

Salt and pepper, also called impulse noise, is a noise source that occurs due to the electronic circuits, memory errors and dead pixels [82]. It causes pixels to have either the maximum or minimum intensity, leading to black and white dots on the image. This is not a big noise source assuming that the equipment is not broken. In case needed, corrections can be applied by removing dead pixels and using image filters.

---

[15] `https://en.wikipedia.org/wiki/Charge-coupled_device#Blooming`, retrieved July 2023

4.4.6. Filter Spectral Leakage

For PSP measurements it is paramount to ensure that filters fully blot out the incoming excitation light. According to Fond [68], leakage of excitation light can lead to a reduction in pressure sensitivity, cause local sensitivity variations and lead to non-linear paint calibration. It should be verified that no excitation light passes through the filter. The net effect of leakage is a flattening of the Stern-Volmer curve, as a constant is added to both the reference and measurement images.

4.4.7. Excitation Light Temporal Unsteadiness and Spectral Variability

The excitation light source can have temporal variations in intensity. This can lead to additional pressure measurement errors over time. Knowing the variance per time unit can be used to measure the uncertainty associated with this. Examples of studies that account for this error are:

- The study of Panda et al. [30] on the wavenumber spectra of the Coe and Nute model. Here the temporal instability of the light source was accounted for using a 6th order polynomial. They additionally measured the light source temporal behaviour beforehand and found that upon turning on the lamp showed high degrees of instability. Measurements were only taken after the lamp stabilized
- NASA's study on the 2.5% scale model of the SLS. In the article of Tang et al. [64] they saw a linear time decrease in LED emission intensity and had to detrend the data to account for this decrease.

Alongside unsteadiness in the luminosity, light sources can have variance in central wavelengths over time. This can increase the uncertainty in pressure measurements of PSP [10]. If known from the product specifications, this property can be used to compute the pressure uncertainty.

4.5. Temporal and Spatial Errors

This section describes the errors that are related to spatial and temporal effects. Of these "change in temperature during wind tunnel activity" and "self-illumination" errors are by far the most important. Each can be very hard to correct for depending on the measurement conditions. Their relevance is also highly dependent on measurement conditions. Model aeroelasticity was previously described in a separate subsection.

4.5.1. Δ T During Wind Tunnel Activity.

Blowdown wind tunnel facilities operate by use of a high pressure reservoir which feeds the air for measurements. Generally, the pressure and temperature of the air decreases as the reservoir is emptied. When not accounted for this can cause a bias in the pressure data. The reservoir at the TU Delft makes use of regulator valves that maintain a constant level for the total pressure. Furthermore, by use of heat exchangers the temperature of the air is regulated, leading to a smaller decrease in total temperature.

4.5.2. Self-Illumination Error

Due to the Lambertian PSP emissions (see Subsection 3.1.2), light from one part of the model can impinge on other parts and reflect to the camera, causing errors in the measured pressure [10, 68]. Self reflection occurs mostly for concave surfaces or multi-component models (such as protuberances). If not corrected for, the pressure can be off by more than 40% near 90° surface junctions [50]. The self-illumination depends on the reflective properties of the paint surface, surface geometry and the luminescent intensity field.

Corrections for self-illumination require a "huge number of computations" [68], rendering them very time consuming. The basic procedure follows below (see Le Sant [50] and Liu et al. [10] for a more comprehensive proceude). First, the image of the model is mapped onto a 3D grid. The surface of 3D grid is discretised into various surfaces. From this, the "view factor"[16] between surfaces is calculated. This depends on surface reflectivity, emission model and reflection model. Surface reflectivity must be determined by measurements or using material data. Reflection model choice can significantly impact correction efficacy [10]. Using the view factor, a corrected intensity field is obtained with a explicit iterative scheme.

When self-illuminating surfaces have the same pressure level, the intensity based method fully mitigates the error. Generally this will not be the case. Nevertheless, for surfaces with varying pressure levels the

---

[16] View factor = Geometric relation for the illumination interaction between surfaces. [10]

intensity based method mitigates some of the error as I_{ref} includes self-illumination.

4.5.3. Viewing Angle

Viewing the model from an angle reduces the spatial resolution of the PSP model, as a bigger model area contributes to the incident light of a single pixel. However, the measured light intensity remains more or less constant up until 70° [50, 68]. The emission intensity over viewing angle can be seen in Figure 4.9. While the area per pixel increases, due to the Lambertian nature of the surface emission, the intensity of emission at an angle is lowered, which cancels out the increase in area. Other than lowering the spatial resolution a change in viewing angle due to aeroelasticity can lead to errors.

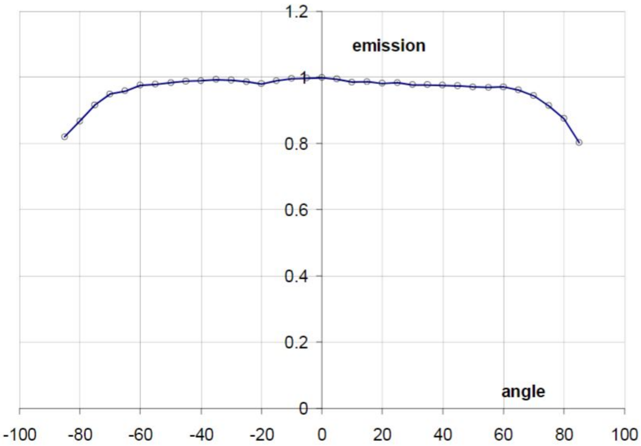

Figure 4.9: Impact of viewing angle on light intensity for B1 PSP. The vertical axis shows the measured intensity relative to the 0 degree intensity. The horizontal axis shows the viewing angle in degree. Source: Le Sant [50]

4.5.4. Relative Humidity

Air humidity can have an impact on the partial pressure of oxygen and the response of PSPs [52]. Kameda et al. [83] investigated the effects of relative humidity on Ru(DPP) based fast PSP. They discovered that relative humidity does not affect the pressure or temperature sensitivity of fast PSP. However, increasing humidity levels lead to an increase in emission intensity. To avoid errors, the relative humidity should be kept constant during experiments.

The air supply to the TST-27 is expected to have a dew point around 230K, according to Dr.ir. F.F.J. Schrijer and a study by Bannink and Nebbeling performed when the tunnel was first installed [84]. It will therefore not be an issue during the runs. However, issues arise after and at the start of runs. During a run, the model is significantly cooled and can reach negative temperatures[17]. When the model comes in contact with outside air after the run, this can lead to dew and ice forming on the model. In between runs this can significantly impact PSP data.

---

[17] This was measured during some preliminary runs using IR thermography to determine model temperature.

PART II

Methods and PSP Development

5 Experimental Methodology

This chapter provides an overview of the materials and methods used to perform the experiments and analyze the data in this thesis. All experiments were performed inside the Transonic/Supersonic wind tunnel (TST-27) at the High Speed Laboratory (HSL) of the TU Delft[18].

The chapter first starts with a description of the TST-27. Then, the test models are presented along with a portrayal of the test matrix. For the full test matrix, readers are referred to Appendix I. This is followed by an overview of the flow conditions. The next two sections focus on the experimental methods. First, non-PSP methods are described in Section 5.4, followed by a delineation of the chosen PSP method and data processing in Section 5.3. At the end of the chapter, aerodynamic data analysis approaches are stated.

5.1. Test Facility Description

All wind tunnel tests in this thesis were carried out at the TST-27. Schematic overviews of the tunnel can be found in Figure 5.1 and 5.2. As the name implies, it is a transonic and supersonic wind tunnel capable of operating between M=0.5 to 0.85 and between M=1.15 to M=4.2. Supersonic conditions are achieved using the continuously adjustable throat upstream of the test section. Transonic conditions are instead achieved with a choke mechanism inside the transonic variable throat, situated downstream of the test section.

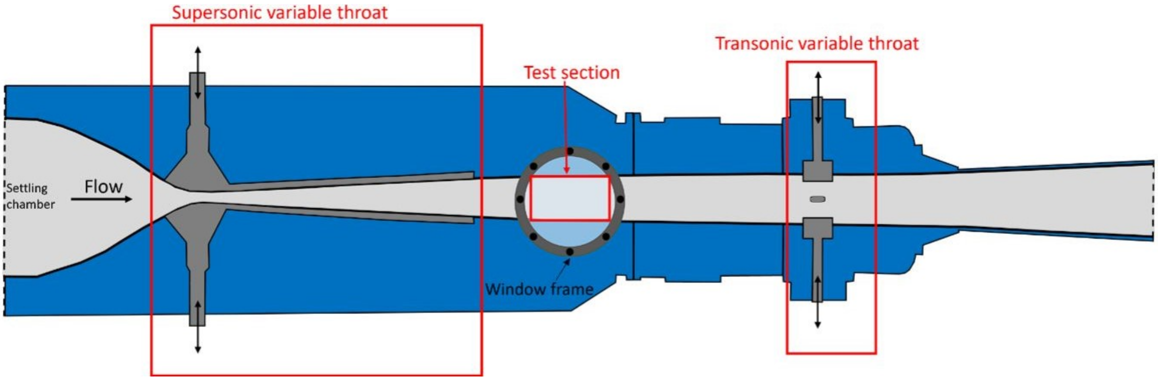

Figure 5.1: Schematic drawing of the TST-27 wind tunnel. Source: The dissertation of Aguanno [85].

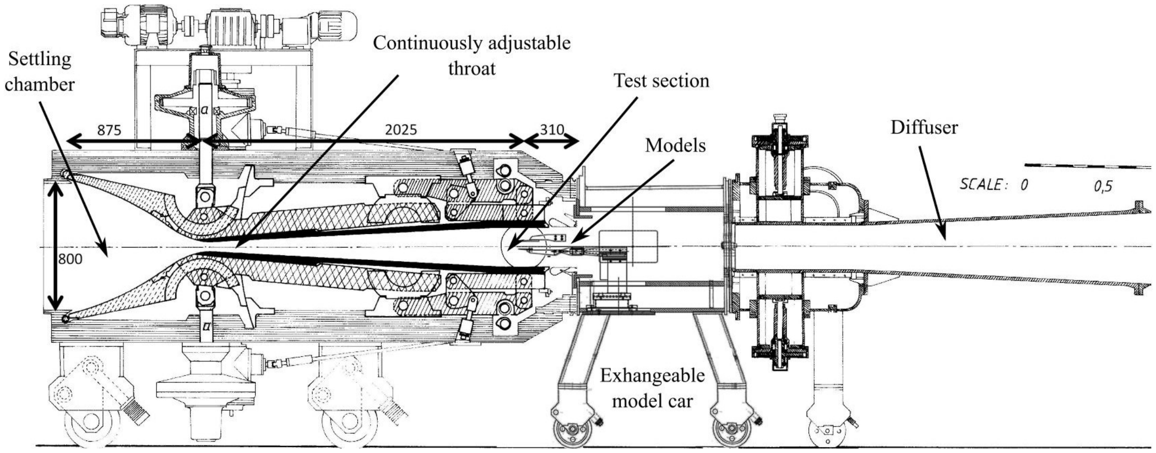

Figure 5.2: Technical drawing of the TST-27 wind tunnel. Models used in this thesis are similarly mounted to a sting on the exchangeable model car. Source: The dissertation of Giepman [86].

---

[18] `https://www.tudelft.nl/lr/organisatie/afdelingen/flow-physics-and-technology/facilities/high-speed-wind-tunnels/tst-27-transonicsupersonic-windtunnel`, retrieved July 2023

The transonic choke consists of eight biconvex rods (four on the top and the bottom walls) and a wing, as depicted in Figure 5.3. This mechanism works by varying the blockage ratio at the transonic throat, thereby setting the Mach number in the test section. The protrusion height (H) of the biconvex rods is used to roughly set the Mach number, where the wing's variable angle of attack (between $\alpha = 0^\circ$ and $\alpha = 60^\circ$) is then used to fine tune it. This choke mechanism is controlled by a labview program, described by van Rijswijk [87]. For transonic conditions are desired, the supersonic variable throat is set to be fully subsonic.

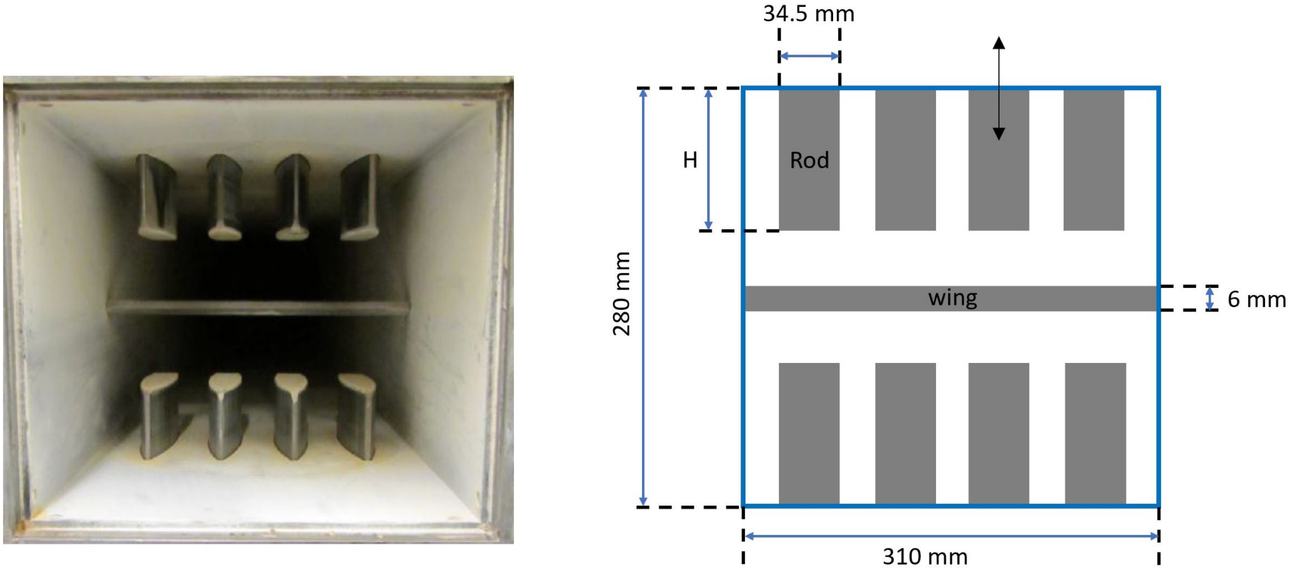

Figure 5.3: Photo (left) and schematic (right) of the transonic choke situated inside the transonic variable throat. H is the protrusion height of the biconvex rods. Source: The dissertation of Aguanno [85].

The tunnel operates as a blow-down facility, with air supplied from a 300 m^3 storage vessel. Air inside the vessel is stored at pressures up to 44 bar [86], allowing for experiments to be performed until the pressure drops to 20 bar. Total pressure (p_{tot}) of the settling chamber can be set between 1.5bar to 4bar, allowing for the Reynolds number in the test section to be varied. This gives up to 5 minutes (min) of total experimental time in a day, depending on flow conditions. When emptied, dry air is refilled by a 230kW compressor. To maintain air temperature, ceramic balls act as heat sinks that heat up the air in the reservoir as it expands.

The test section has a 280mm width and a variable height between 250mm to 270mm depending on M number. For the experiments performed here, the height was 255mm. Three test sections can be installed, with solid, perforated or slotted walls. The slotted walls can be used to reduce the effects of blockage. However, this test section limits the optical access in the tunnel for PIV and Schlieren. Due to this, the TUPLE study on the VEGA-E and Romero's study [17, 25] used solid walls. This setup was kept for the current thesis to better compare results with both studies and to allow for Schlieren measurements to be performed.

The mounting of the models is similar to the one shown in Figure 5.2. A sting is fastened to the bottom of the exchangeable model car, upon which the models are installed horizontally. Different mounting blocks can be installed on the bottom of the sting, which allow for the angle of attack to be set vertically. Stings of different lengths can be used to ensure the model is situated around the center of the window.

5.1.1. Optical Access

The optical access of the wind tunnel is an important parameter for PSP, as it can eliminate luminophore options and measurement approaches. For normal visible light (vis) testing conditions, the TST-27 uses a 300mm diameter Bk7 glass window manufactured by Schott[19] (see Figure 5.15a). Bk7 is a borosilicate glass with high transmissivity (<75%) between 320nm to 2500nm [88], where it is above 90% from 334nm to 1970nm. PSP luminophores are excited by light ranging from 330nm and 520nm, allowing this window

---

[19] `https://www.schott.com/shop/advanced-optics/en/`, retrieved October 2023

to be used for any luminophore. Optical access is available from the left and right sides of the tunnel.

IR measurements can also be performed at the TST-27 using one the TU Delft's multiple LWIR (long wave infrared) cameras. To do so, a germanium window can be installed instead of the Bk7 one. The germanium window is a 15mm thick, anti-reflective coated window with a 160mm diameter manufactured by Najin Creator Optics[20]. A picture of the window can be seen in Figure 5.4. The window installation point can be rotated by 30 degrees, allowing for different viewing configurations. The germanium window has a transmissivity above 75% between 6993nm and 14288, allowing for the full LWIR range of cameras to be measured[21]. The downside of using this window is the fact that it is opaque in the vis range.

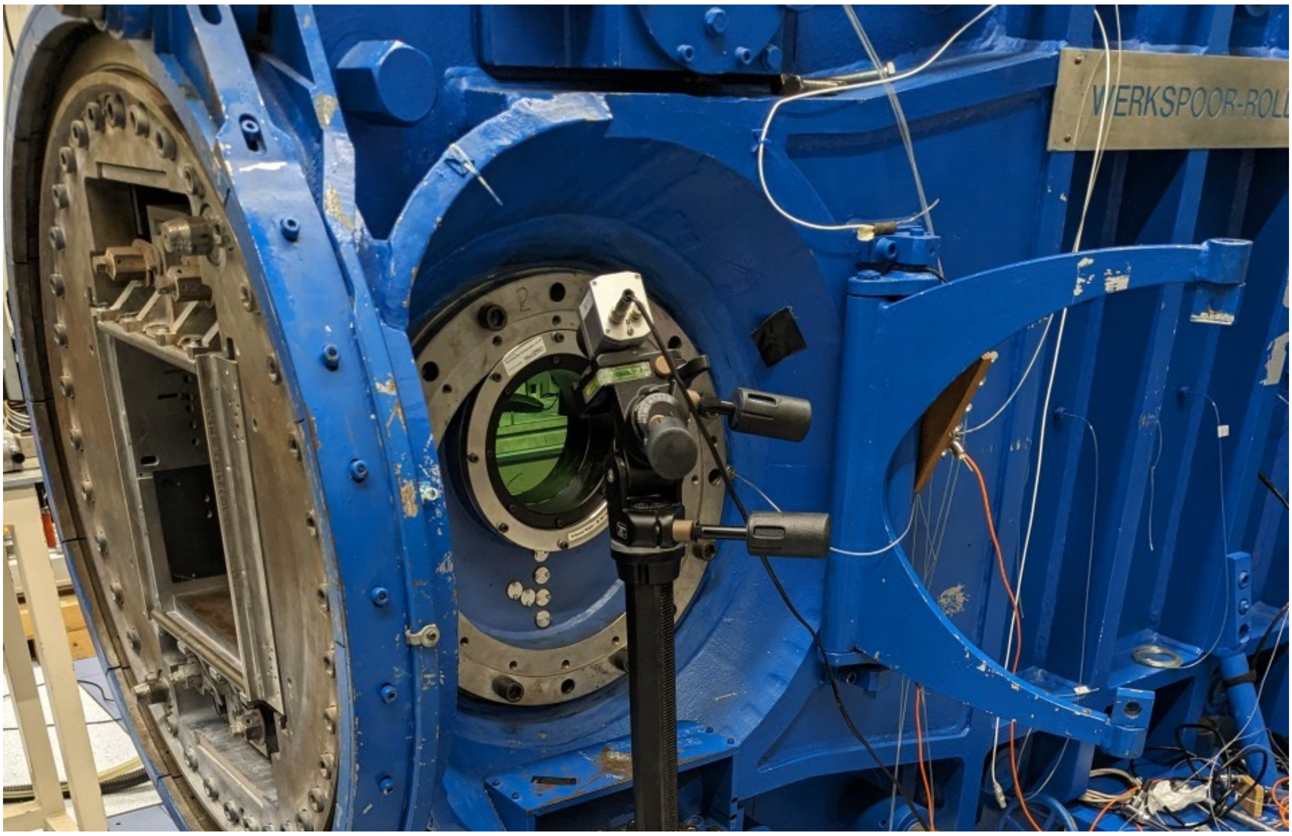

Figure 5.4: Germanium window for IR measurement optical access mounted on the wind tunnel.

5.1.2. Flow conditions

All wind tunnel measurements performed in this thesis were taken at a total pressure of roughly 202.5 kPa, and M = 0.8, 0.75, 0.7 or 0.6. Reference images were taken at atmospheric conditions, which varied between 100-103.3 kPa. Conditions for each measurement can be found in the test matrix in Appendix I. As the tunnel is a blowdown facility, total temperature decreases over time were found based on model cooling. Flow temperature was found to vary depending on a few factors listed below (See Appendix K):

- **Run time.** Longer runs saw a higher decrease in total temperature as the reservoir was emptied more.
- **Outside temperature and weather.** On a hot sunny day, the model temperature reached a minimum of 10.4°, whereas on colder days temperatures below freezing were found.
- **Time between runs.** Runs taken in quick succession saw lower temperature decrease rates.

No direct air T measurements were taken, making it difficult to quantify the exact flow conditions at each M number. It is estimated that the maximum starting T_{tot} for measurements was around 288K, decreasing with number of measurements during the day. At the lowest, total temperatures likely dropped below freezing to around **270K**. Estimates using these values are shown in Table 5.1 for the four M numbers.

---

[20] `https://www.creatoroptics.com/E-ge_p.htm`, retrieved October 2023

[21] `https://www.creatoroptics.com/images/germanium-window-AR-DLC.jpg`, retrieved October 2023

	M = 0.8		**M = 0.75**		**M = 0.7**		**M = 0.6**	
T_{tot}	**286K**	**270K**	**286K**	**270K**	**286K**	**270K**	**286K**	**270K**
p_∞ (kPa)	132.8		139.4		146.0		158.8	
ρ_∞ $(\frac{kg}{m^3})$	1.81	1.93	1.88	2.00	1.94	2.07	2.06	2.20
T_∞ (K)	255	239	259	243	262	246	269	252
U_∞ $(\frac{m}{s^2})$	256	248	242	234	227	220	197	191
μ_∞ $(\frac{kg\cdot 10^{-5}}{m\cdot s})$	1.67	1.58	1.69	1.60	1.71	1.62	1.74	1.65
Re_D (10^6)	1.39	1.51	1.34	1.46	1.29	1.41	1.17	1.27

Table 5.1: Flow conditions based on the expected minimum and maximum total temperature of the flow for the HHF models.

These estimates were derived using the isentropic flow equations, the equation of state and Sutherland's law. For the freestream pressure (p_∞), density (ρ_∞), temperature (T_∞), velocity (U_∞) and viscosity (μ_∞) the following equations were used respectively:

$$p_\infty = p_{tot} \cdot \left(1 + \frac{\gamma - 1}{2} M^2\right)^{\frac{-\gamma}{\gamma - 1}} \tag{5.1}$$

$$\rho_\infty = \left(\frac{p}{p_{tot}}\right)^{\frac{1}{\gamma}} \cdot \frac{p_{tot}}{R \cdot T_{tot}} \tag{5.2}$$

$$T_\infty = T_{tot} \cdot \left(1 + \frac{\gamma - 1}{2} M^2\right)^{-1} \tag{5.3}$$

$$U_\infty = \sqrt{\gamma \cdot R \cdot T_\infty} \cdot M \tag{5.4}$$

$$\mu_\infty = \mu_{ref} \cdot \left(\frac{T_\infty}{T_0}\right)^{\frac{3}{2}} \cdot \frac{T_0 + S_\mu}{T_\infty + S_\mu} \tag{5.5}$$

where γ is the heat capacity ratio of air, R the gas constant of air (=287.05 $\frac{J}{kg\cdot K}$), μ_0 the reference viscosity (= $1.716 \cdot 10^5 \frac{kg}{m\cdot s}$) at the reference temperature T_0 (= $273.15K$) and S_μ is the Sutherland constant (=$111K$ for air). The model diameter based Reynolds number (Re_D) is then found using

$$Re_D = \frac{U_\infty \cdot D \cdot \rho_\infty}{\mu_\infty} \tag{5.6}$$

Note that the values shown in the table are for the HHF models, which have a $D = 50mm$. For the cone model, Re_D is twice as high as the base of the cone is $100mm$. Furthermore, the Re_D values shown assume that the M number at the model is the same as the set point. However, blockage causes the actual M number to be around 0.05 higher, yielding a higher Re_D value. This is discussed in the next subsection. As the exact blockage effect is unknown, it was chosen to calculate the Re_D using the set point.

5.1.3. Pressure and Mach Number Variation

The transonic labview program [87] records the p and M number variations upstream of the test section during runs. Recording starts when the tunnel is turned on, after which values are recorded when the tunnel is stable. This was used to estimate the mean total pressure ($\bar{p}_{tot}$), the uncertainty of $\bar{p}_{tot}$ and the standard deviation of the M number. An example of the variations in p_{tot} during five runs can be seen in Figure 5.5.

The technicians operating the tunnel were instructed to set a total pressure of $2bar$, but $\bar{p}_{tot}$ was found to lie between 202.1 and 203.3 kPa for different runs. The uncertainty in the computed $\bar{p}_{tot}$ values was found to be around $50Pa$, allowing this uncertainty to be considered negligible. The M number was found to have a standard deviation between 0.0005 to 0.0021. Most runs were around 0.0008, without any clear trends between different M numbers and angle of attack settings. A maximum deviation of ±0.006 was found in the M number.

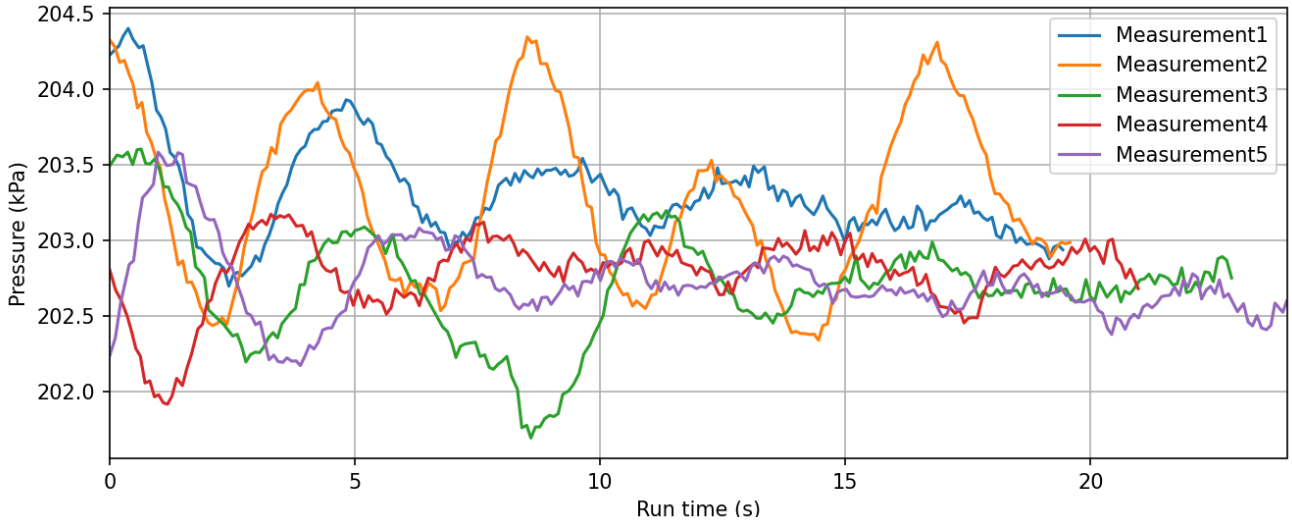

Figure 5.5: Variation in total pressure for five measurements on the Vega-E model (**ESA P13d** to **ESA P17u**).

5.2. PSP Formulation and Models

In this thesis, four models were used. The first are $4cm$ square aluminium coupons, used to construct the Stern-Volmer curve. Secondly, a 40° Cone Model with a $10cm$ diameter was used for verification experiments. Lastly, aluminium models of the Coe and Nute Model 11 and the Vega-E launcher were used for HHF measurements. Models were all painted with UniFIB PSP from ISSI. A description of the paint and the models is found in this section. At the end of the section, model blockage is discussed.

5.2.1. Paint Description

For the experiments performed in this thesis, the UniFib PSP[6] formulation from ISSI was selected. The finished paint was purchased from ISSI instead of locally synthesizing PSP, as the aerospace faculty does not have the required tools. This specific formulation was chosen over other commercially available options as it has a relatively low temperature sensitivity and a simple test setup. Their multi-luminophore paint was also considered due to its negligible thermal quenching. However, it requires a more complex setup and data processing, as multiple cameras and filters are needed to isolate luminophore signals.

UniFib contains PtTFPP as luminophore in combination with the poly(TMSP) polymer. No base-coat was used as aluminium has good paint adhesion. To enhance adhesion, models were lightly sanded with Scotch sand paper. Painted models were handled with latex gloves to avoid damaging the paint. Unless otherwise stated, models were cured for at least two hours at 70° after painting, in accordance to ISSI guidelines[6]. In a prior attempt to use this paint at the TU Delft [89], the paint on the model was not cured, but instead dried using a heat gun. This was found to be detrimental in the current thesis.

5.2.2. Paint Coupons

Six $40mm$ square aluminium coupons were painted in order to be used for calibration experiments (see Subsection 5.3.1). Of these, three coupons were not cured. These delaminated during off-work hours and could not be used for measurements. The remaining ones can be seen in Figure 5.6.

Figure 5.6: Paint coupons used for calibration measurements.

Each Coupon has a different amount of paint layers to test the effect of paint thickness, with Coupon 1 having the least and Coupon 3 the most layers. The coupons were used to measure paint decay rate, luminescence linearity with excitation and the intensity ratio at different p and T with respect to p_{atm}. T was varied between $2-21°C$ and p between $50-205kPa$. A total of 82 calibration points were taken with coupons 1 and 2 for the Stern-Volmer curve. The full calibration matrix can be found in Appendix H.

5.2.3. 40° Cone Model

To validate paint results, it was chosen to take measurements on a simple model with pressure taps. For this, a 40° Cone model with a 10 cm diameter and 5.96 cm length was available from the dissertation of Tambe [90]. The painted model can be seen in Figure 5.7 and 5.19. This cone is made of Polyoxymethylene (a grey polymer) and is equipped with 8 orifices that can be connected to pressure transducers outside the tunnel using tubes. Of these, two were broken at the start and one was clogged when painted with PSP.

The painting procedure was as follows. The model was first lightly sanded to enhance adhesion. After, the pressure orifices were clogged using metal wires to protect the holes from filling up with paint. As the material of the cone is soluble in the solvent of the PSP, a dark brown basecoat was used to protect the model. Then paint was sprayed on the model, while using a heat gun in between layers to help dry the paint. The cone was not cured due to fears of damaging the cone and as the heat gun approach seemingly had worked before. However, this proved to be ineffective as paint on the model showed high degrees of peeling during off-work hours and wind tunnel runs (see Figure 5.7b).

Four measurements were performed with the cone. The first was set to $1.5bar$ and $M = 0.7$, but the tunnel did not stabilize and instead oscillated around M= 0.65. For the other measurements, p_{tot} was increased to $2bar$, which allowed the flow to stabilize. The mach number was set to [0.6,0.6,0.65]. As the model has a high solid blockage, local Mach numbers are expected to be much higher, as seen by Tambe [90].

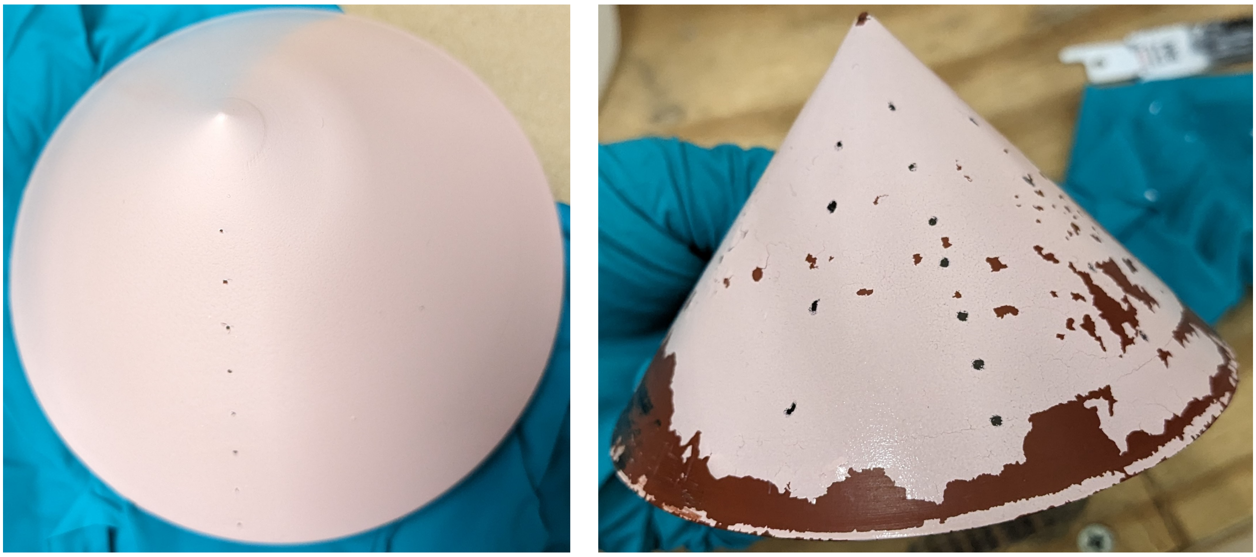

(a) Cone after painting. Black dots are the pressure orifices.

(b) Cone after all measurements were finished.

Figure 5.7: Painted Cone model before and after experiments. Significant peeling is evident after measurements were finished.

5.2.4. Coe and Nute Model 11

The first HHF model tested was based on the Coe and Nute Model 11, excluding the booster stage. This model was previously used in the MSc thesis of Romero [25]. A schematic can be seen in Figure 5.8. The model is made out of anodized aluminium with a steel core. It is constructed in a modular way that allows for the boat tail and the nosecone to be switched, but for this project only the Coe and Nute configuration was used. This configuration has a biconic nose, with a $\theta = 34°$ boat tail. The PLF has a maximum diameter of 5 cm, with a 3.125 cm diameter LV.

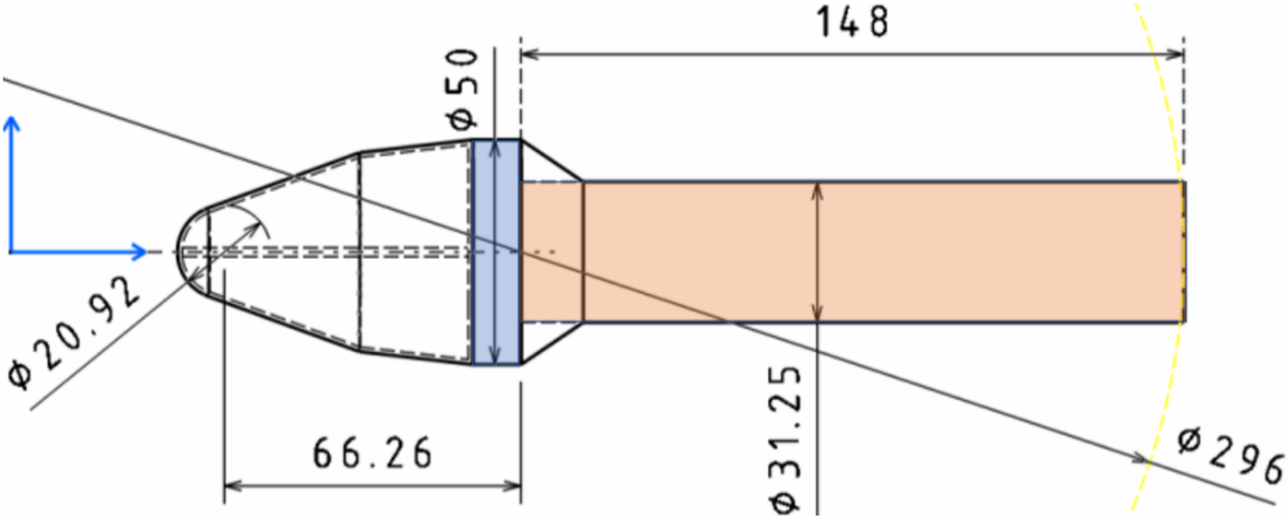

Figure 5.8: Schematic of the Model 11 used in this thesis. Distances presented in this report are normalized using the PLF diameter and taken with respect to the end of the boat-tail, situated 90.59mm from the tip. Source: The MSc thesis of Romero [25]

The b.l. on the model is tripped at the nosecone to mimic the turbulent in-flight conditions. To do this, a $1mm$ transition trip was made with carborundum particles. The transition trip was placed at roughly 20% of the nose, a position that closely resembles the actual transition location [91] and was previously used by Romero and D'Aguanno [17, 18, 26]. The effectiveness of the trip at creating a fully turbulent b.l. was previously shown in the dissertation of D'Aguanno [85].

Eight PSP experiments were performed on this model to compare with historical data and the experiments of Romero [25]. The first six were done at $\alpha = 0°$ and M = [0.7,0.75,0.8]. Each Mach number was repeated twice to ensure repeatability of the tests and reduce thermal errors. The last two were done at $\alpha = 4°$ and M = 0.8 to quantify the angle of attack effects. In addition, four Schlieren measurements were taken at M =0.8 and $\alpha = [0°, 4°]$ to compare with previous Schlieren results without paint. For this, a single coat of paint was used. The painted model can be seen in Figure 5.9. On top of the coat, fiducial marks were placed for image alignment using a black marker. These were placed in a zigzag pattern for data processing reasons, along the top and bottom of the model. Their positions were measured after experiments, as depicted in Figure L.1. More information on the fiducial marks can be found in Appendix L.

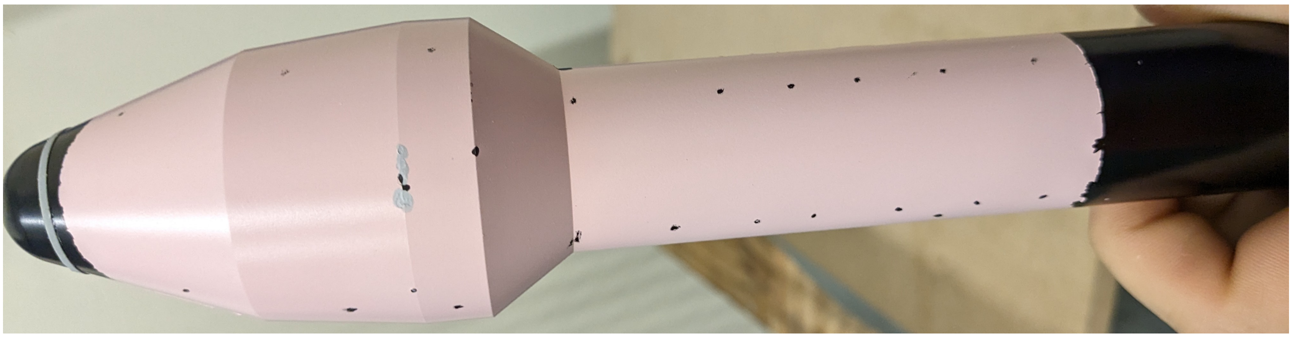

Figure 5.9: PSP painted Model 11 with the fiducial marks and transition trip.

To conserve paint, parts of the model were masked using tape. As only one side of the model was visualized, the painted area was a little over half the model. When the tape was removed, this lead to some roughness at the edges of the model, which can be seen in Figure 5.9. Furthermore, air was trapped between parts of the model. Upon curing, this air expanded causing the paint to bubble. The bubbling locally delaminated the paint and created extra roughness on the model that can be seen in the pressure signal. At the intersection between the second conical area and the straight cylinder, a lot of the paint delaminated. This was replaced with a different, grey paint to remove some roughness. The delamination is further discussed in more detail in Subsection 6.4.4.

5.2.5. Vega-E Model

The second HHF model used in this thesis was a model of the upper stages and PLF of the Vega-E launcher. This model has a 30° boat tail angle with a $50mm$ diameter (D) PLF and $32-31.2mm$ D LV shaft. It is once again made out of anodized aluminium, with a hollow core on the straight cylinder to house three high speed pressure transducers. These were accidently damaged and could not be used with PSP. The model is modular to allow for different boat-tails to be installed. For this thesis, the focus was on the 30° boat-tail configuration, as this is the configuration the ESA is most interested in.

A schematic of the model can be seen in Figure 5.10 and the painted model with protuberances in Figure 5.11. Here, red rings are depicted which can be switched from the clean configuration to one with protuberances. The protuberances mimic those that will be present on the real LV. For both configurations, carborundum transition trips were once again placed near the tip, similarly to the Model 11.

A total of 32 measurements were taken with this model, three IR without-, sixteen PSP without-, one Schlieren without- and twelve PSP with protuberances. Mach numbers were set to [0.6,0.7,0.75,0.8] to study mach number effects and two angles of attack were tested, $\alpha = 0°$ and $\alpha = 4°$. PSP measurements were again repeated twice to ensure repeatability and reduce thermal errors. Not all combinations were tested, readers are advised to see Appendix I for the full test matrix.

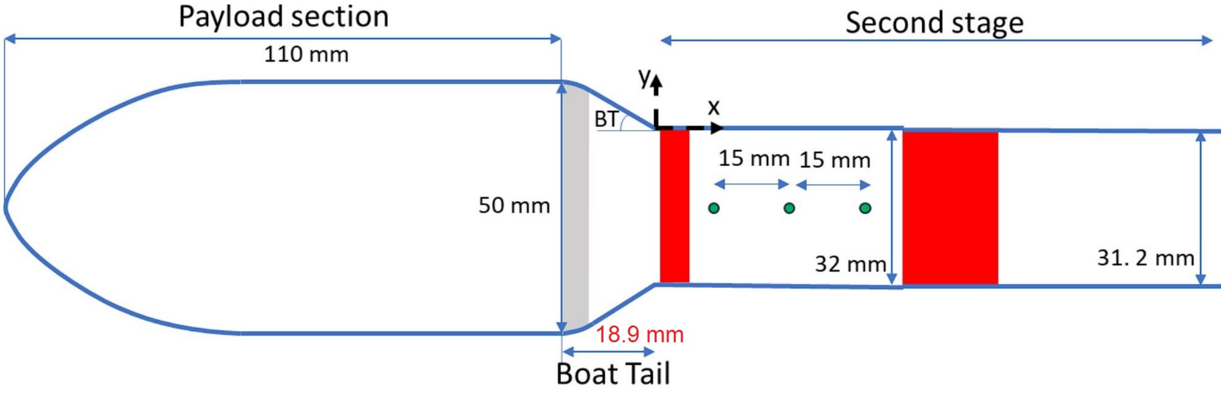

Figure 5.10: Schematic of the Vega-E model used in this thesis. Distances presented in the report are normalized with the PLF diameter ($50mm$) and given with respect to the end of the boat-tail, situated 128.9 mm from the tip. This is positioned in upstream of the first ring. Source: Adapted from the work of D'Aguanno et al. [44].

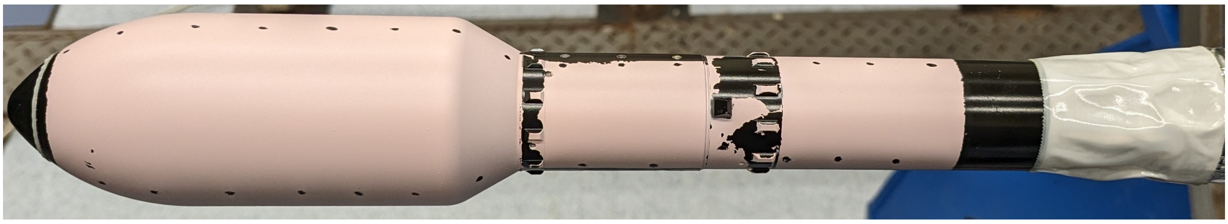

Figure 5.11: Vega-E model with protuberances painted with PSP. Image taken after a couple runs, when the paint on the protuberance rings had significantly peeled.

Two paint coats were used, one for tests with and one without protuberances. Each had a unique set of fiducial marks, placed as done on the Model 11. The goal was to again paint over half the model and mask the other half. However, between both rings the pressure taps had to be masked with tape, as these have a membrane which disallows for the approach used on the cone. On the other side of the model, there is a hatch used to access the pressure transducers (see Figure L.1). This hatch has holes, which were masked away before painting. In between these two, an area slightly smaller than half the model was painted.

On the first coat, paint flakes settled on the model when the tape was removed. After curing, these glued to the surface and stayed during the measurements, leading to localised PSP errors. For the second coat, flakes were removed with pressurized air prior to curing. Similarly to the Model 11, air bubbles were trapped at the edges of the protuberances which expanded during curing, causing delamination at the protuberances. The rings were not sanded prior to painting due to a mistake, likely contributing to the peeling.

5.2.6. Blockage

Previous PIV studies performed on the Model 11 and the Vega-E model made use of solid walls to enhance PIV and Schlieren data [18]. As previously mentioned, the same walls were employed to obtain direct comparisons with these studies. This causes a non-negligible amount of blockage in the tunnel, that increases test section M number. For the Model 11, Romero and D'Aguanno found better comparisons between their M= 0.8 data and the M = 0.85 results from other studies. So the expected net effect of blockage on the Model 11 is a M increase of +0.05. As the Vega-E model has similar dimensions, a similar effect is expected.

Blockage effects are expected to occur predominantly due to solid and wake blockage. At $\alpha = 0°$, the maximum solid blockage ratio (B_r) relative to the tunnel area is given by:

$$B_r = \frac{\pi \cdot D^2}{4 \cdot H_T \cdot W_T} = 0.02750 \tag{5.7}$$

where W_T and H_T are the height and width of the test section respectively. Blockage is further increased for measurements with $\alpha = 4°$. The cross section of cylinder under an angle becomes an ellipse, with a minor axis of length D/2 and a major axis of length $D/2 \cdot sec(\alpha)$. This gives a solid blockage ratio equal to

$$B_r = \frac{\pi \cdot D \cdot sec(4°) \cdot D}{4 \cdot H_T \cdot W_T} = 0.02757 \tag{5.8}$$

which is a relative small net increase in solid blockage. However, the angle of attack leads to additional effects which further increase blockage, namely:

- The model is no longer situated in the center of the test section, giving different levels of blockage on the wind- and leeward sides of the model due to a varying proximity with the wall.
- On the leeward side a diverging section is created, whereas on the windward side a funnel is created, impacting M differently along the length of the model.
- Wake blockage increases.
- The force distribution is asymmetric, leading to other blockage effects, such as buoyancy due to lift.

Note that not only the model induces blockage, but also the attachment sting downstream of the test section. As no exact calculations of the blockage effect were done given the complexity of transonic conditions, it was chosen to analyse and compare data using the set point values. For future studies and comparisons with other methods, blockage corrections may be beneficial. A simple verification of the +0.05 seen by Romero was done using the 1D flow assumption, which showed an expected ΔM of +0.04 to +0.07. The calculations can be found in Appendix F.

5.3. PSP Setup

As aforementioned, the intensity based PSP method was used due to its simplicity and as it can serve as a stepping stone for future fast PSP usage. In this section, the test setup used for the calibration and wind tunnel experiments is given. In the next chapter, the data processing and more detailed PSP implementation results and discussions can be found. Other experimental methods that are mentioned in this section are further elaborated in the next section.

5.3.1. Paint Calibration Setup

The first experiment done with PSP was a calibration experiment to construct the Stern-Volmer curve. ISSI provides a calibration curve (see Figure 3.2b), but for the highest accuracy, each batch should be re-calibrated. Furthermore, the equipment used in this thesis differs from that used by ISSI, so doing the calibration serves as a way to verify its suitability for PSP. Calibration was done inside a metallic vessel that can be pressurized and depressurized to cover the full p range of measurements. To set coupon temperatures, a Peltier element that was extracted from an old fridge was used. Peltier elements and PSP coupons are extensively used for PSP calibration [15, 51]. The setup can be seen in Figure 5.12.

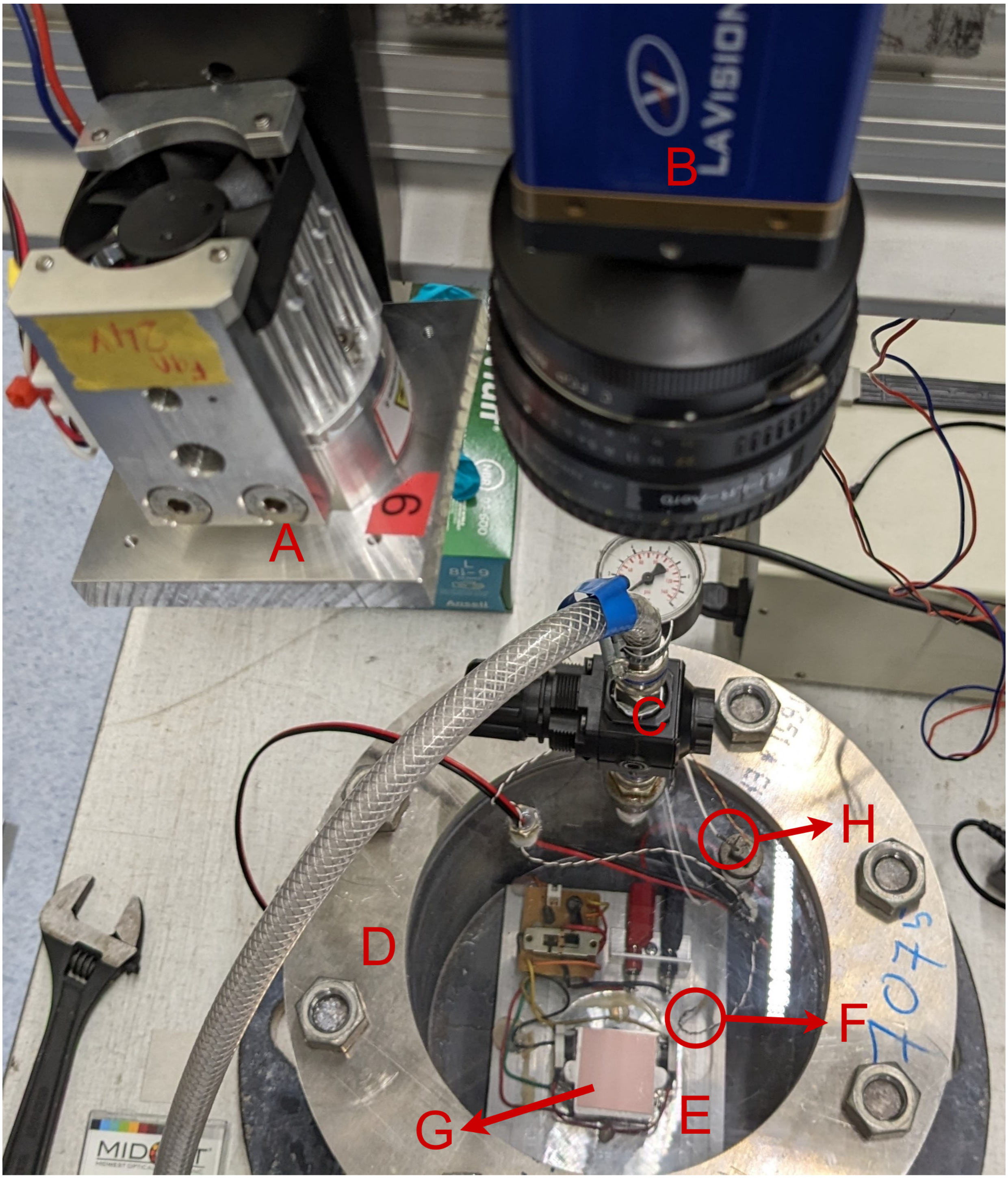

Figure 5.12: Coupon calibration setup. The following components are marked: **A)** is the 400nm DLR LED array. **B)** the Bobcat camera. **C)** The pressure valve used set overpressure. The tube was connected to a 10 bar dry air supply. **D)** the pressure vessel. **E)** is the Peltier element. The metal plate is a heat sink, with the main working element being situated under the coupon. Circuitry of the element can be seen over the heat sink. A switch on the brown element can be used to switch from heating to cooling. **F)** a T-type thermocouple used to measure T of the Peltier element, near the coupon. It is detached in this image. **G)** PSP coupon 3. **H)** Pressure orifice and tube used to measure the pressure inside the box. The tube is connected to the Scannivalve.

The optical access window material is plexiglass, which has a cut-off frequency around $400nm$. According to the ISSI, plexiglass can be luminescent to UV light. The high cut-off frequency and potential luminescence were however not found to cause issues. Instead, scratches along the surface of the window led to some unevenness in the light distribution. Measurements were taken with the same bobcat camera that was used for the wind tunnel experiments. A Vision light tech (VLT) MidOPt LP550-52 orange longpass filter was used to block out the excitation light. A borrowed LED array from DLR built for TSP / PSP applications was used as excitation light. This array has a central wavelength around $400nm$. This filter and lamp combination was found to have a significant amount of light spectral leakage (see Subsection 6.3.2).

The window has a pressure orifice from which p can be measured (see H in Figure 5.12). This was done with the Scannivalve (see Subsection 5.4.2). Vessel pressures varied between p_{atm} $-52kPa$ to $+103kPa$. Overpressure was set by using a valve connected to a $10bar$ dry air supply. The valve was inaccurate, requiring measurements with the Scannivalve to set the p. The pressure inside the box took some time to stabilize, so some variation occurred throughout runs. Underpressure was instead achieved using a vacuum pump. There was no valve to set exact pressures, so the approach used was to let the pump run until a desired pressure was obtained. The box itself was leaky, so p rose again after using the pump.

Coupon temperature was set by using a DC power supply that allowed Peltier element voltage and current to be set. No prior calibration was performed to relate input power to temperature. Instead, T was measured at the edge of the element where the coupon was situated. Power was changed till the desired temperature was achieved. Temperature measurements were taken using a T-type thermocouple (see Subsection 5.4.4) with a TM-947SD thermometer. The thermocouple was placed on the element using duct tape. The placement of the thermocouple was found to impact measured temperature.

5.3.2. PSP Test Setup

All wind tunnel tests were performed with either one or two Bobcat IMPERX IGV-B1610 CCD or the Lavision sCMOS CamLink cameras. The bobcat is an older 1628 x 1236 pixel camera, whereas the sCMOS is a higher end 2240 x 2146 pixel camera with a better light sensitivity and intensity range. The cone and Model 11 experiments were performed with both to determine whether the low spec bobcat camera suffices. For standard PSP, both were found to yield the same results, therefore for the Vega-E only the bobcat was used.

AF Nikon $35mm$ camera lenses with a $52mm$ diameter were used, leading to a spatial resolution around $0.087mm/px$. High aperture was set to increase sensor illumination and reduce the amount of excitation light required, giving lower paint decay rates. For the cone and Model 11, VLT MidOPt LP550-52 orange longpass filters were used. Due to their relatively high spectral leakage, new VLT MidOPt LP610-52 red longpass filters were acquired for the Vega-E experiments. Paint emissions start at $620nm$, therefore this filter does not block luminescent light[6]. The spectral leakage of the $550nm$ filters can be seen in Figure 5.13 and Figure 5.15 in the form of yellow background light. This is further discussed in Subsection 6.3.2.

A $400nm$ central wavelength UV LED array was used for luminophore excitation. The lamp is custom built by DLR, with variable output and a $4.8W$ fan for cooling. Voltage and current were set between $12-13V$ and $0.68-2.0A$, resulting in $8.16-26W$ lamp power. Power was varied depending on lamp-model distance, with most experiments being set to $25.3W$ at a distance of $70-80cm$. Lower power was used for smaller distances to avoid image saturation. Lamp output intensity is dependent on lamp temperature, requiring ~ 10 minutes to stabilize at $25.3W$.

Data acquisition was done using the GEV player when using one bobcat, and with Davis 8 otherwise. When using Davis, a Lavision PTU was used to trigger cameras. This PTU simultaneously triggered T data acquisition for Vega-E tests. Exposure times were set to $55000\mu s$ with acquisition at $10hz$ to $16.7hz$. Lower frequencies and exposures were used due to Davis 8 program not properly operating the bobcat. Exposure times were set as high as possible to capture as much light in a frame. Around 200 total images were taken per measurement to ensure converged flow statistics. This gave between $12s$ to $27.4s$ data acquisition time.

- **Cone Setup**

The setup used for the cone experiments can be found in Figure 5.13.

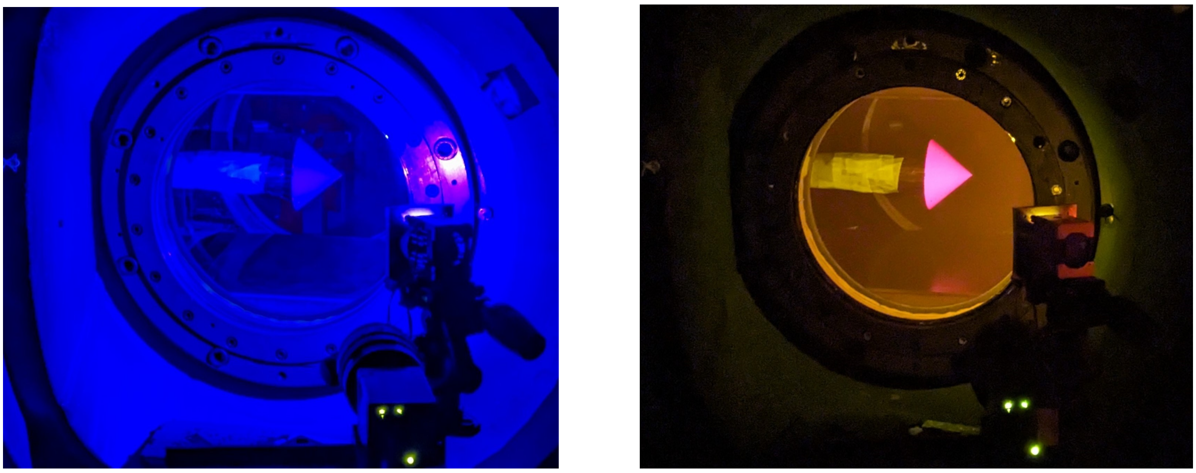

(a) Cone measurement setup unfiltered.

(b) Cone measurement setup filtered.

Figure 5.13: Measurement setup used for the cone measurements. Images taken with a pixel 8a phone. (a) shows the setup with the lamp turned on, whereas (b) shows the same setup filtered with 550nm longpass laser safety goggles.

In reality, the LED light is more purple, but the camera did not register this. To evenly illuminate the cone, the lamp was placed at closed to a 40° angle. The camera was also placed at a slight angle to be closer to the cone angle. Three experiments were done using the bobcat, and two with the sCMOS.

- **Model 11 setup**

Measurements on the Model 11 were taken with the bobcat and sCMOS simultaneously to directly compare results. The sCMOS had a full overlap with the bobcat FOV, with an overall slightly higher FOV. The bobcat was placed under a slight angle to have overlapping FOV. The test setup can be seen in Figure 5.14.

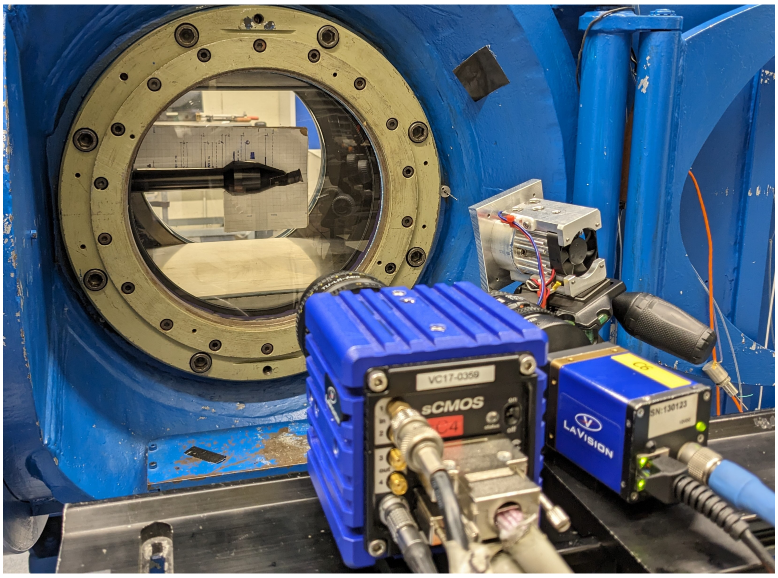

Figure 5.14: Test setup for the Model 11 experiments.

- **Vega-E $\alpha = 0°$ setup**

For the Vega-E model two bobcat cameras were used simultaneously to cover the full model. The lamp was placed underneath the cameras to evenly illuminate the model. The setup can be seen in Figure 5.15.

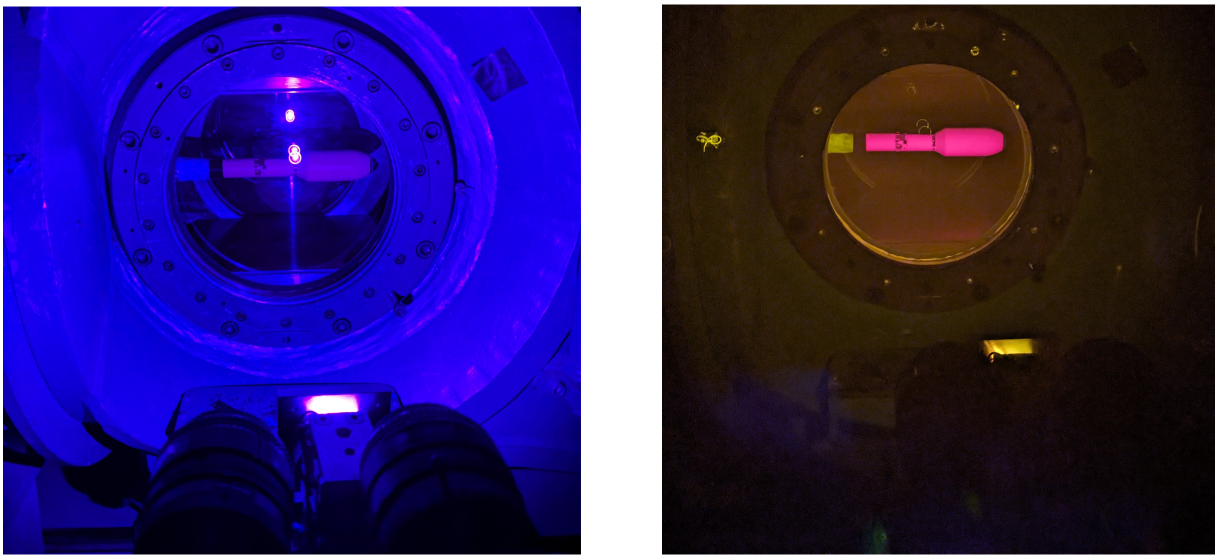

(a) Vega-E measurement setup unfiltered.

(b) Vega-E measurement setup filtered.

Figure 5.15: Measurement setup used for the $\alpha = 0°$ Vega-E experiments. Images taken with a pixel 8a phone . (a) shows the setup with the lamp turned on, whereas (b) shows the same setup filtered with $550nm$ longpass laser safety goggles.

- **Vega-E** $\alpha = 4°$ **setup**

In the TST-27, angle of attack can only be set vertically. To image the leeward and windward sides of the model, cameras had to be placed at an angle relative to the test section, from a high or low perspective. Measurements with a high perspective are denoted with "u" and those with a low perspective with "d" (e.g. **ESA 9u**, **ESA 12d**). The lamp was placed closer to the window at a ±45° angle relative to the window. The setups can be seen in Figure 5.16. A schematic of the perspective that was used can be seen in Figure 5.17.

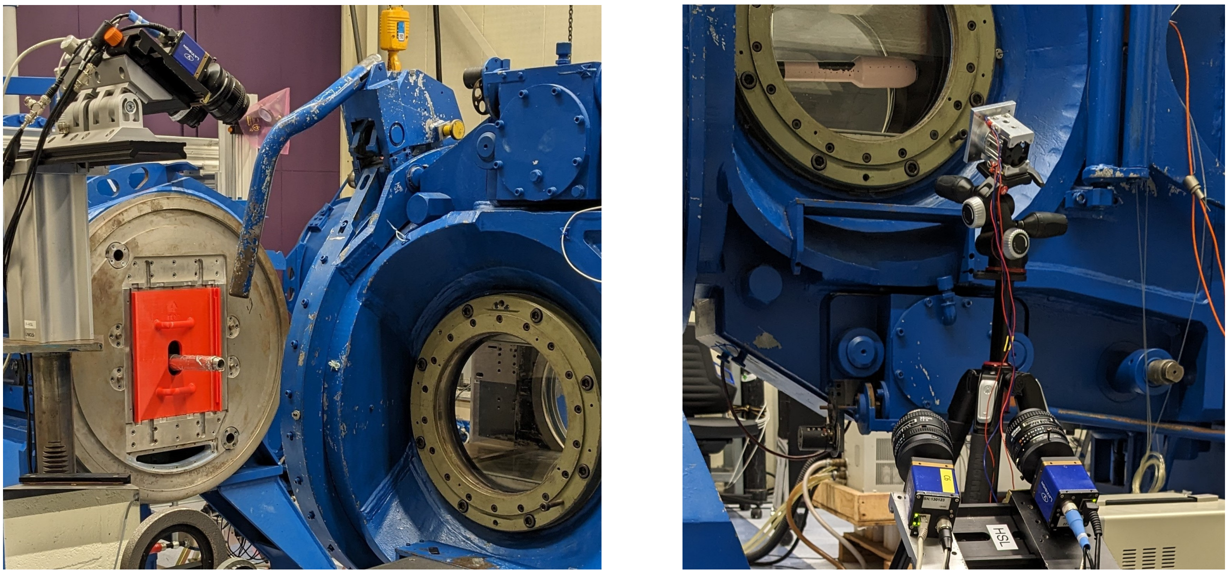

(a) Vega-E leeward side setup.

(b) Vega-E windward side setup.

Figure 5.16: Measurement setup used for the $\alpha = 4°$ Vega-E experiments. (a) shows the up setup and (b) the down setup.

5.4. Other Experimental Methods and Setup

In this section, experimental methods that were used other than PSP are discussed. This includes IR thermography, wall-mounted pressure taps, Schlieren and thermocouples. First, the theory behind different methods is described, followed by their experimental setup.

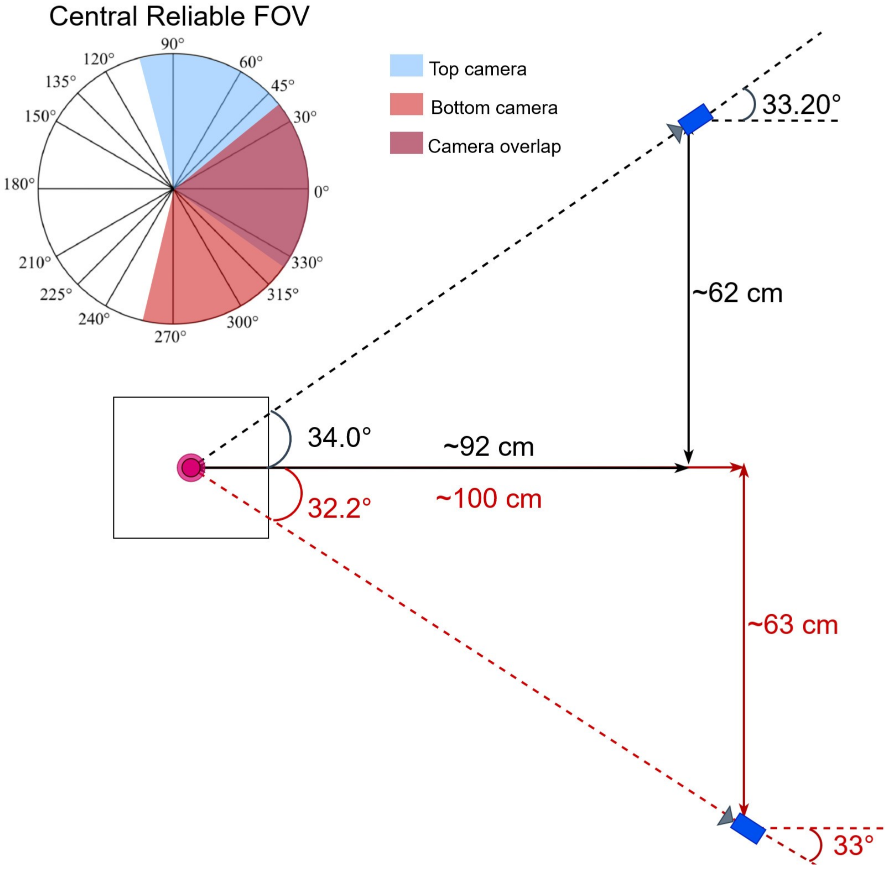

Figure 5.17: Schematic drawing of the camera positioning and FOV for Vega-E measurements at $\alpha = 4°$. The central reliable FOV depicts the FOV for the center of the test section. Due to the angle of attack and window curvature, it differs along the model.

5.4.1. Infrared Thermography

Infrared (IR) thermography is an imaging technique that captures images using the emitted infrared radiation of bodies. This allows for high precision, non-intrusive capture of spatially resolved emissions. In aerodynamic studies, IR is mainly used to measure temperatures, determine transition location, measure heat transfer parameters and determine thermal boundary layers [38, 92]. In this thesis, IR measurements served to quantify the model temperature distribution over time and gauge thermal quenching errors.

- **Working Principle**

All bodies emit radiation according to Planck's law. The intensity and spectral distribution of radiation depend on T, allowing Planck's law to be used to determine a bodies' T by measuring its emissions over a wavelength band. IR thermography measures this radiation in the IR spectrum, which ranges from $0.7\mu m$ to $1\ mm$ [22]. Sensors in IR cameras capture narrow bands of the IR radiation spectrum. Generally, sensors are capable of measuring one of three IR bands shown in Table 5.2.

Planck's law holds for a black body, which by definition is an idealized body that has an emissivity (ϵ) of 1 for all wavelengths. In practice, Most real bodies have an emissivity that is lower than 1 and is dependent on wavelength, as bodies can absorb, reflect and transmit incident light. Additionally, there is often a medium (e.g. air, IR window) between the IR sensor and the body, that absorbs and emits IR light. Due to this, the measured IR radiation (I_{meas}) from a body is given by [93]:

$$I_{meas} = \tau \cdot \epsilon \cdot I_{body} + (1-\epsilon) \cdot I_{amb} + (1-\tau) \cdot I_{med} \tag{5.9}$$

where τ is the transmissivity of the medium between body and sensor, I_{body} is the true radiation emitted

---

[22] https://www.icnirp.org/en/frequencies/infrared/index.html, retrieved October 2023

by the body, I_{amb} the radiation emitted from the ambient and I_{atm} the radiation emitted from the medium. The impact of I_{amb} and I_{atm} on I_{meas} is highly dependent on the surroundings. I_{amb} impact additionally depends on the body's reflective and transmittance properties. Note that this equation is also valid for PSP when $\epsilon \cdot I_{body}$ is swapped for the luminescent intensity.

Wavelength band	**Band range**	**Black body** T	**Camera range**
Near Infrared (NIR) to Short Wavelength Infrared (SWIR)	$0.75\mu m$-$1.4\mu m$ $1.4\mu m$-$3\mu m$	966K-3864K	$0.4\mu m$ to 2-$3\mu m$
Mid Wavelength Infrared (MWIR)	$3\mu m$-$8\mu m$	362-966K	$2\mu m$ to $5\mu m$
Long Wavelength Infrared (LWIR)	$8\mu m$-$15\mu m$	193K-362K	$7.5\mu m$-$14\mu m$

Table 5.2: Operational bands of IR cameras, along with the corresponding black body temperature for which the emission is highest in that band. Data taken from the books of Miller et al. [94] and the book of Tropea et al. [38]

As real bodies are not perfect black bodies, camera calibration is required. This can be done analytically (using Equation 5.9), but obtaining a high accuracy calibration is very complex. Post-processing software in IR cameras generally include a simple analysis based on ϵ of the body, τ of the optical access and T_{air}. A secondary approach exists based on in-situ calibration [38], similar to in-situ in PSP (see Section 4.1). Here, discrete T measurements from a different sensor (e.g. thermocouples) are used to relate between T and I_{meas}. One thermocouple can be used to affix temperature values, more for polynomial regressions.

- **Experimental Setup**

For this thesis the former approach was used. Three measurements were taken on the Vega-E model using the Optris PI 640 camera with a wide angle lens. This is a 640x480 pixels camera that images LWIR from 7.5 to 13 μm at up to $32 Hz$. The camera was operated using the PIX connect program, in which T_{air}, model ϵ and window τ can be set. The program also corrects for image warping due to the lens. This setup yields an expected system accuracy of $\pm 2°C$ and noise equivalent temperature difference (NETD) of 0.075K.

To measure τ, temperature measurements can be made using a surface with known high ϵ. In the dissertation of Giepman [86], a black body simulator was used for this purpose ($\epsilon \approx 1$). Here, a simple calibration was performed using the authors hand. Human skin has an emissivity of roughly 0.98 [95], by simultaneously measuring the T of the authors hand with a thermocouple and the IR camera, the window τ was found to be roughly 0.85. This was verified using the manufacturer data ffor the window[20]. With τ known, the ϵ of the model was similarly measured with a thermocouple and IR, yielding $\epsilon = 0.86$ which was found to closely match values found in engineering tables [23]. Lastly, T_{air} was found to be 19° using a thermocouple.

Two camera orientations were used for the measurements. The first was used for one measurement can be seen in Figure 5.4. Here the imaging plane was oriented perpendicular to the main axis of the model. For the second orientation, the window was rotated 30° clockwise and the camera was placed in a diagonal top right view of the model, in order to increase the FOV. The FOV of both can be seen in Figure 5.18.

5.4.2. Wall-Mounted Pressure Taps

The most common way of measuring wall p in wind tunnel experiments is by use of wall-mounted pressure taps. These are capable of both high accuracy static and fluctuating measurements. The need for PSP arises from the fact that pressure taps are expensive to install, offer limited spatial resolution and are limited in where they can be installed [10]. Despite this, they offer invaluable data and are used to reduce PSP errors.

- **Working Principle**

As the name implies, wall-mounted taps are directly applied to the walls of models. Pressure is measured through an orifice that is connected to a pressure sensor. The presence of the orifice changes the local flow

---

[23] `https://www.design1st.com/Design-Resource-Library/engineering_data/ThermalEmissivityValues.pdf`, retrieved October 2023

slightly, causing a pressure error compared to the true pressure [96]. This error is dependent on various geometry parameters. A summary of the different parameters and their impact can be found in the "Handbook of Experimental Fluid Mechanics" by Tropea et al. [38].

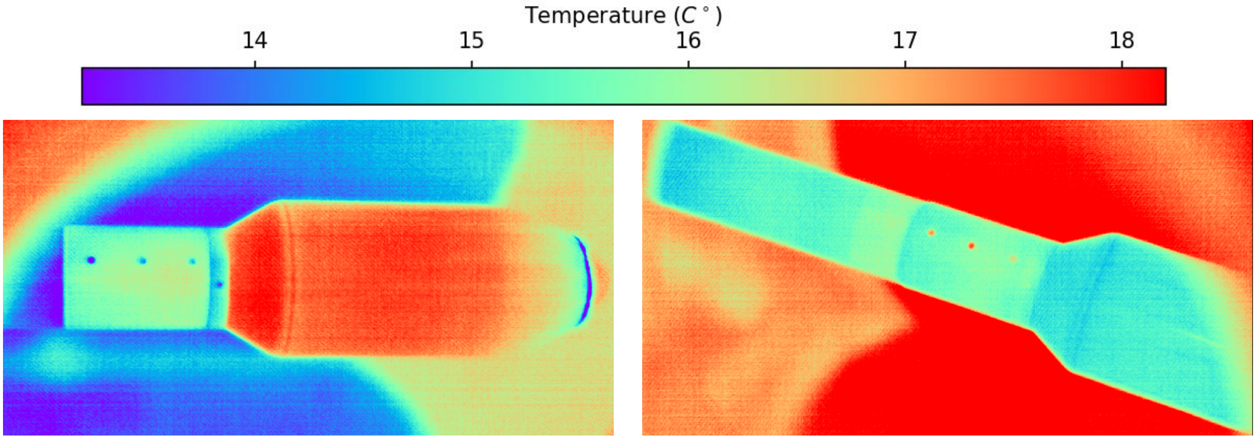

(a) FOV of the first IR measurement on the Vega-E model, snapshot taken at t=10.53s.

(b) FOV of the second and third IR measurement on the Vega-E model, snapshot taken from the second measurement at t=6.89s.

Figure 5.18: False colour IR temperature snapshots showing the two used FOVs on the Vega-E model. The full images have more tunnel background which has been cut off to highlight the FOV on the model. Times listed are after wind tunnel startup.

Three types of pressure transducers exist. Absolute transducers measure the true pressure with respect to vacuum. Gauge transducers measure the difference in pressure between atmospheric conditions and the pressure orifice. This requires additional measurements of the local atmospheric conditions. Lastly, difference transducers measure the pressure at a point with respect to another.

Installation of the transducers can be achieved in two ways [96]. The first is the "flush mounted" approach, where the transducer is mounted directly on the orifice. This allows for high frequency measurements, where Nyquist frequencies of more than $50 kHz$ are achievable. The second approach is to connect the transducer to the orifice through a pipe. The maximum measurable frequency is then limited by resonance in the pipe, decreasing with increasing pipe length. The resonance depends on pipe length, diameter, transducer dimensions and p levels.

- **Experimental Setup**

In this thesis, wall-mounted pressure taps were used on the cone model to validate PSP results. These were connected to the model through $4m$ long pipes, as shown in Figure 5.19. This only allows for time averaged measurements. The pipes were taped to the mounting sting to avoid being blown away. For this, aluminium and double sided tape was used. At the bottom of the exchangeable model car, there is a cavity with a small hole next to where the sting is mounted that allows for the pipes to be taken out of the tunnel.

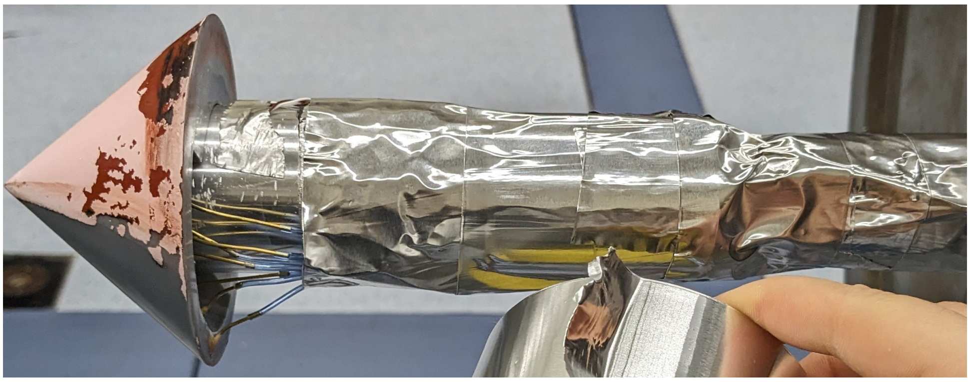

Figure 5.19: Cone setup inside the wind tunnel. Shown is the mounting of the pressure tubes on the sting.

The pipes were connected to a Scanivalve DSA 3217/16 PX digital pressure sensor array. This is a difference transducer capable of measuring a Δp of up to $16psi$ ($110.3kPA$) from p_{ref}. p_{atm} was used as p_{ref}, allowing the full range of expected pressures the models encounter to be measured. Data was collected using the Scantel program and saved as a $.txt$ file. $4m$ long pipes were used as the Scanivalve was expected to be situated far from the tunnel. However, the Scanivalve could be placed right below the tunnel and connected to the PC using USB extension cables. In practice, at most $2m$ of piping was needed.

5.4.3. Schlieren

Schlieren is a qualitative flow measurement technique based on the refraction of light rays through a medium with a varying density field. It gives qualitative information on the structures inside the medium, along with some quantitative data in the form of the location and dynamics of flow structures. In this thesis, it was used to compare the location of flow features with PSP results and to test the intrusiveness of the PSP. The latter was done by comparing Schlieren images on the model with and without paint.

- **Working Principle**

The refractive index of air (n) is given by the Gladstone-Dale equation of refraction [38]:

$$n = K \cdot \rho + 1 \tag{5.10}$$

where K is the Gladstone-Dale constant, assumed to be constant for vis, and ρ is the density. When light passes through a region of varying ρ obliquely, the rays bend towards the higher ρ regions, causing deflections of light. Imaging these deflections allows for flow structures to be visualised. The net deflections are caused by the integrated path of light rays through the test section, leading to blurred structures in 3D fields.

To image the deflections, a collimated light beam is required [38, 97]. After passing through the tunnel, the light beam is converged to a single point by a lens called the "Schlieren head". Here, part of the light beam is cut off by an object called the "knife edge". Rays that are deflected away from the knife edge cause brighter areas in the image, whereas rays deflected towards the knife edge lead to darker patches. This images the deflections in one direction. When the knife edge is positioned horizontally, vertical deflections are detected and vice versa. The change in image intensity (ΔI) for a horizontal knife edge is then given by:

$$\frac{\Delta I}{I} = \frac{K \cdot f_l 2}{a} \cdot \int_{\zeta_1}^{\zeta_2} \frac{\delta \rho}{\delta y} dz \tag{5.11}$$

where f_{l2} is the focal length of the Schlieren head and a is the reduced height of the light beam at the knife edge. (y, z) are the Cartesian coordinates of the setup, where y is along the deflection direction and z along the test section. $\zeta_{1,2}$ are the beginning and end coordinates of the test facility respectively. By decreasing a higher intensity changes (=higher sensitivity) can be achieved at a cost of reduced I in the image [10]. Equation 5.11 shows that Schlieren is sensitive to changes in the first gradient of density. An increase in density along a direction results in a bright area on one half of the image, and a darkened area on the other.

- **Experimental Setup**

The Schlieren setup used in the TST-27 is the "Z-type" configuration [38]. A schematic of this setup can be seen in Figure 5.20. Here, a white LED is used as light source. The light rays emitted from the LED are first focused by a lens. The diameter of the light beam is then set by a pinhole with a certain radius. A mirror after the pinhole reflects the light onto a parabolic mirror, which collimates the beam before passing through the test section. A second parabolic mirror then focuses the light onto a mirror that is lined up with the knife edge and second lens. Here, the knife edge can be changed in orientation and precisely moved into the light beam. The camera is then situated in the path of the incoming beam, downstream of the second lens.

A total of five Schlieren measurements were taken during this thesis, along with three pilot measurements to determine the optimal knife edge setup. From the pilot measurements, a horizontal knife edge with slightly over 50% light blockage was found to be optimal. The goal of these was to visualize the position of the shock waves on the model.

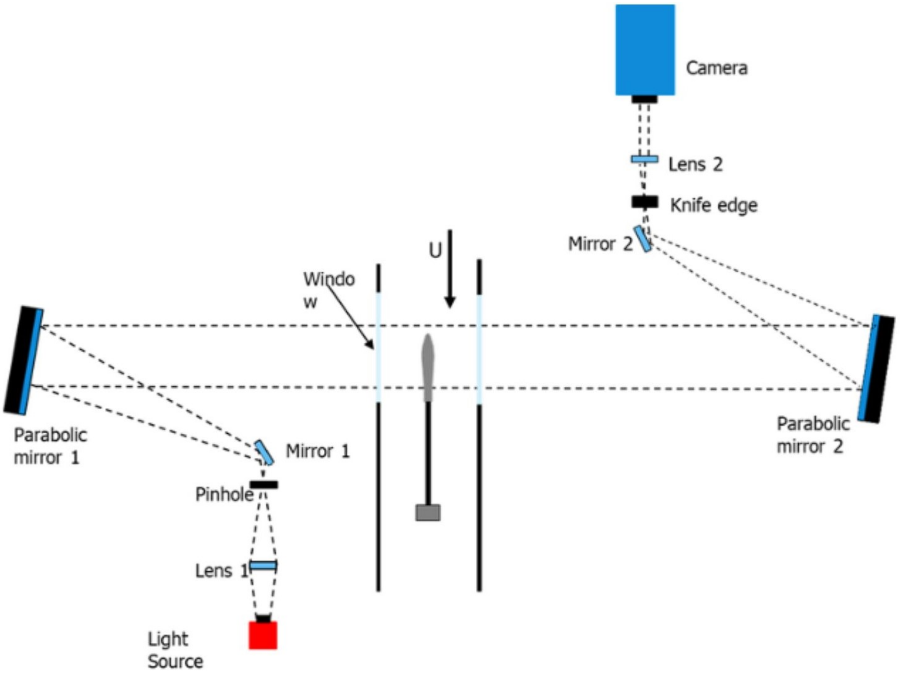

Figure 5.20: Z-Schlieren setup used for the HHF measurements in the TST-27. Source: The work of D'Aguanno et al. [17]

The first four and all the pilot measurements, were done on the Coe and Nute model at $M = 0.8$. Two were taken at $\alpha = 0°$ and two at $\alpha = 4°$. Low frequency measurements were taken using a Bobcat IMPERX IGV-B1610 CCD camera. Ideally, high-speed measurements should have been taken, but no cameras were available. This camera has a $1628x1236px$ resolution, in which around 310 images were recorded at 16.5 fps using the GEV player. The last measurement was taken with a Photron fastcam SA1.1 on the Vega-E model at $\alpha = 4°$ and M =0.8. This is a high-speed camera with a 1024x1024 pixel resolution. Measurements were taken using the fastcam software at 5000 fps for 5375 images.

As the shock waves are oscillatory in their position, a low camera exposure is required. Previously, measurements by Romero and D'Aguanno [18, 26] showed that at most $40\mu s$ exposure time can be used to obtain sharp features. A lower exposure time further enhances detection. For the bobcat tests, an exposure time of $15\mu s$ was used. Similarly, an exposure time equal to $1/70000s$ ($= 14.3\mu s$) was used for the Photron.

- **Data Processing**

Shock locations were determined from the Schlieren data using two approaches. The first one uses the standard deviation of the pixel intensity. Due to the oscillatory nature of the shocks, pixels with a high standard deviation indicate the shock passing through more often. The mean position of the shock is assumed to be at the point with the highest standard deviation. This is approach was used by D'Aguanno et al. [17] in the TUPLE research. It is not entirely accurate, but it gives a good estimate of the mean position. The exact location is found by taking the highest standard deviation pixel on a line $\sim 4mm$ above the surface. An example of a Schlieren snapshot and the standard deviation field for the Model 11 at M=0.8 and $\alpha = 0°$ can be seen in Figure 5.21.

The second approach looks at the most upstream and most downstream location of the shock in the Schlieren data. As with the other approach, locations are found by taking the pixel intesities on a line $\sim 4mm$ above the surface (see Figure 2.14). The mean position is assumed to be at the center between both points. This approach was used in the MSc thesis of Romero [25] and allows for direct comparison with her data. Again, this is not an entirely accurate estimate as the shock position may be biased towards one of the extremes. However, this approach gives accurate information on the oscillation range of the shock.

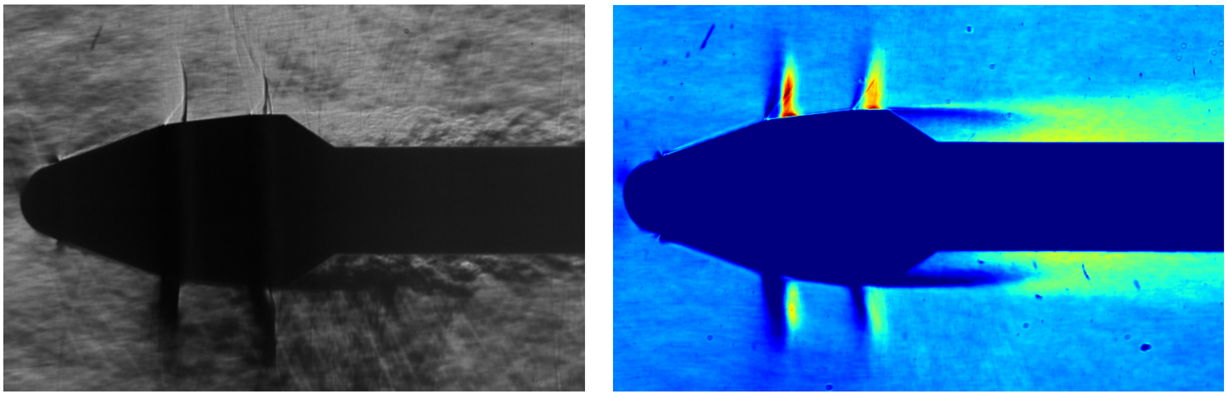

(a) Schlieren snapshot. (b) Standard deviation of pixel intensity.

Figure 5.21: Snapshot and standard deviation field of Schlieren images taken on the Model 11 at $M = 0.8$ and $\alpha = 0°$. Figure (b) uses the "jet" colour map, where blue indicates a low standard deviation and red higher.

5.4.4. Thermocouples

In blowdown facilities, PSP measurements necessitate some manner of temperature correction. In the current thesis, it was chosen to do so with thermocouples. Thermocouples are an industry standard way of measuring point temperatures using the Seebeck effect between two dissimilar metal wires. Due to their limited spatial resolution, data obtained from these was used to capture model wide temperature trends.

- **Working Principle**

Thermocouples consist of two metal wires from different materials that are joined together. One end of the wire is placed on a "heat source", while another is kept at a "cold" reference temperature (see the circuit shown in Figure 5.22). The difference in temperature between both junctions leads to an electromotive force in the wire called the Seeback effect[24] [25]. This induces a voltage in the wires that is proportional to the ΔT between both ends. By measuring this voltage, the temperature on the "heat source" can be obtained.

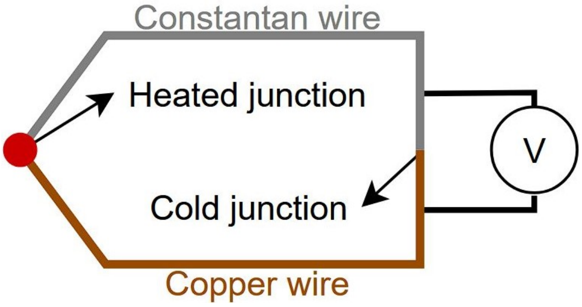

Figure 5.22: Circuit of a T-type thermocouple.

Various types of thermocouples are available that use different metal wires[26]. The different combinations lead to different temperature sensitivities and measurement ranges, along with different areas of application. For wind tunnel testing between $-200°C$ to $350°C$ numerous combinations are available, with expected measurement accuracy around $\pm 1.0°C$ to $\pm 2.2°C$. Alongside the accuracy in measured T, thermocouples have an uncertainty in their ability to accurately measure the T of the intended surface [38]. The measured T is always the temperature of the "heated junction", which may differ from the surface the junction it is situated on. Various factors can impact this, including placement, thermal inertia, other heat transfer sources and thermocouple dimensions among others.

---

[24] `https://en.wikipedia.org/wiki/Thermoelectric_effect`, retrieved July 2024

[25] `https://www.elprocus.com/what-is-a-thermocouple-definition-working-principle-diagram-applications/`, retrieved July 2024

[26] `https://www.omega.com/en-us/resources/thermocouple-types`, retrieved July 2024

- **Experimental Setup**

The HSL has two thermocouple types available for use in experiments, the "K-type" and the "T-type. K-type thermocouples are applicable between $-200°C$ to $\approx 1250°C$ with an accuracy of $\pm 2.2°C$, whereas T-type thermocouples are suited for $-200C°$ to $\approx 350°C$ with an accuracy of $\pm 1.0°C$. Due to the lower uncertainty, it was chosen to use T-type thermocouples. With the unifib PSP, this T uncertainty leads to a p uncertainty of $\pm 400Pa$, not considering any differences between surface T and thermocouple.

Two $4m$ long T-type thermocouples were used for all wind tunnel tests. These were connected to a model 9214 National Instruments (NI) thermocouple module for voltage measurements. An in house labview code was written to operate the module and record data. T and measurement time data was recorded between $10hz$ to $100hz$ depending on test. The $100hz$ data was fairly noisy and was instead downsampled to $10hz$ for data processing. For the cone and Coe and Nute measurements, data was continuously recorded on the same computer as the Bobcat camera acquisition. Images were matched with T data using image times. Latter runs on the Vega-E model were recorded on different computers. A Lavision precision timing unit (PTU) was used to simultaneously trigger both the camera recording and the NI module.

Two thermocouples were used to statistically reduce measurement errors and have a fail-safe in case one fails during a measurement. The latter proved to be crucial. Both were placed in a similar position at the end of the model, near the mounting sting. Their setup on the Vega-E model can be seen in Figure 5.23.

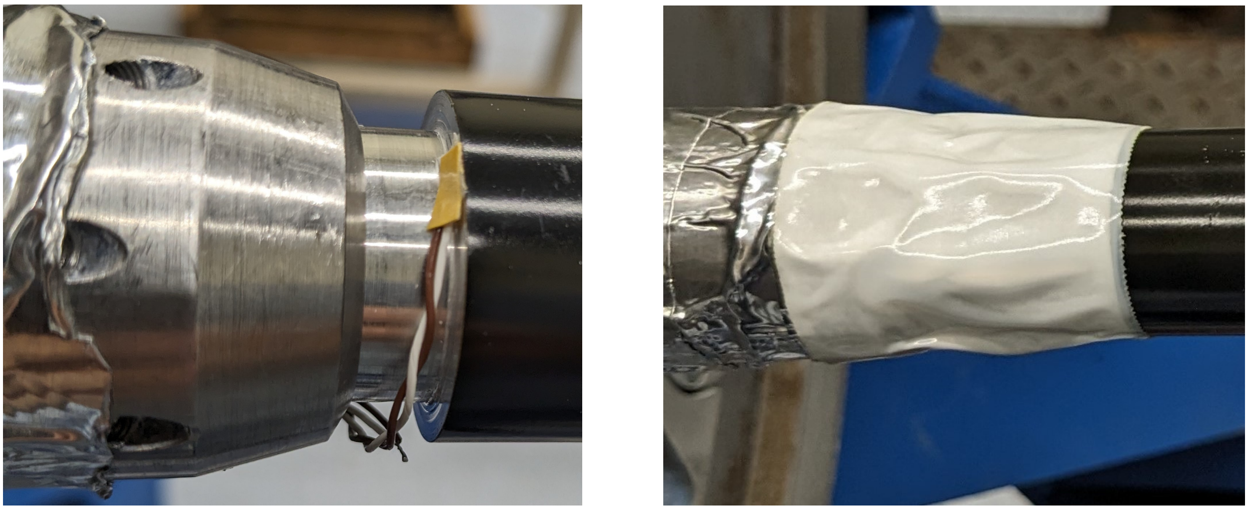
(a) Thermocouple placement.

(b) Thermocouple protected from flow using tape.

Figure 5.23: Thermocouple placements on the Vega-E model. Image (a) shows how the thermocouple is attached to the model. Image (b) shows how the thermocouples are protected from the flow using tape.

The thermocouples that were used had an exposed, ungrounded junction. To avoid interference from the aluminium model, first a piece of double sided tape was placed near the edge of the surface to attach the heated junction. This was done as close as possible to the edge to better capture T_{wall}. A second piece of double sided tape was then placed over the the heated junction to secure the thermocouple in place, as can be seen in Figure 5.23a. This also served to insulate the thermocouple from the outside air. Lastly, a layer of tape was placed over the sting-model junction to shield the thermocouple from the outside flow, as shown in Figure 5.23b. The wires of the thermocouple were taped to the sting and taken out of the tunnel at the bottom, much like was done for the pressure tubes on the cone model.

An identical placement was used on the Model 11 as the one shown above. On the cone model, one thermocouple was instead directly attached to the edge of the cone with a piece of tape, and another to directly to the sting at the base of the cone. The thermocouple on the sting was found to be highly affected by the flow or direct contact with the metal, yielding unrealistic temperatures ($< -20°C$ at times).

6 Implementation and Processing of PSP in the TST-27

In the previous chapter, a description of the PSP test setup is given. This chapter discusses the implementation as a whole, with a focus on the data processing, errors that were encountered, potential improvements and verification and validation of PSP results. The focus of this chapter is purely on the method of PSP; discussion regarding aerodynamic results can be found in the next part of the report.

First, the PSP data processing is described. Next, the Stern-Volmer curve and the calibration experiments are discussed. This is followed by a description of the major error sources that were observed, with a brief mention of lesser errors. Then the first experiments on the cone model are discussed. This is followed by a discussion of the Schlieren results and lastly, image dewarping is discussed.

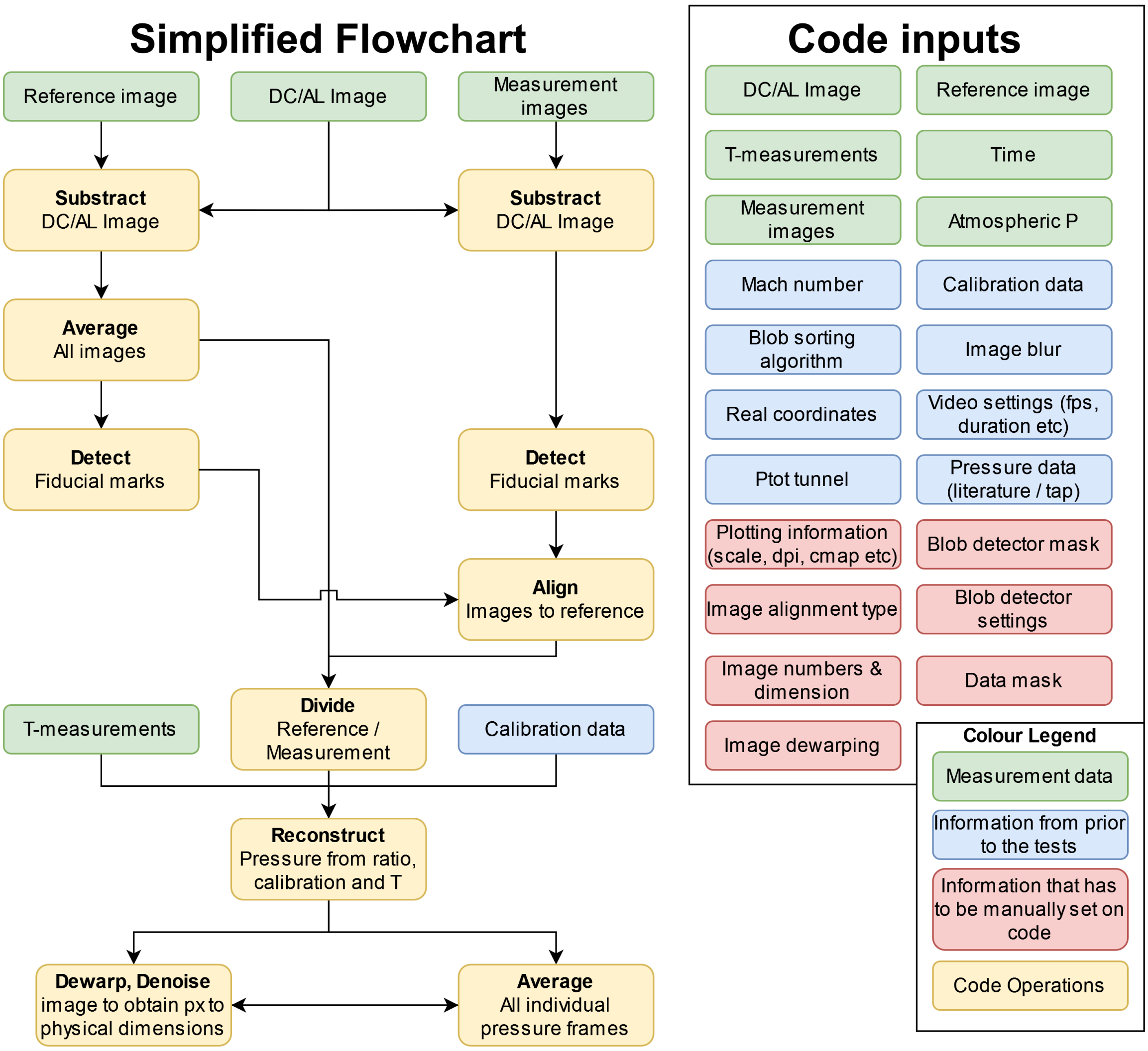

Figure 6.1: Flowchart of created PSP analysis code and required code inputs. Not all inputs are shown in the simplified flowchart. For an overview where each input is used, readers are referred to the full flow chart in Appendix G.

6.1. PSP Data Processing

PSP data processing followed the standard intensity based processing described in Section 3.3, with some adaptations to account for the test setup. The full flow chart of the created inhouse code can be found in Appendix G. A simplified version showing the most important operations and all the code inputs can be found in Figure 6.1. This section describes the data processing by showing the intermediate steps in processing one of the M = 0.8, $\alpha = 0°$ and protuberance experiments (**ESA P10**) for the camera focused on the PLF.

Four image sets were taken for every case, namely a set of DC and ambient light (AL) images, measurement images and two sets of reference images, one before and one after the measurement. Two references were taken for various reasons. From the IR results it was found that taking reference images after the run does not mitigate temperature errors in the TST-27, as described in Subsection 4.1.1. However, two reference sets can statistically mitigate temperature errors caused by either the calibration or thermocouple errors by calculating the pressure using two different T_{refs}. Furthermore, at times something went wrong with one of the reference sets, allowing the other to be used. This is further discussed in Subsection 6.4.7.

Alongside this, two reference sets reduces random noise (such as shot noise), paint decay errors and can be used to verify that the calculated p is correct, as p from both references should be nearly identical. Dark current and ambient light images are taken simultaneously, with PSP lights off. Almost no variations was found in multiple DC + AL images throughout a day, so one set was taken for multiple measurements. The first processing step is then to subtract the AL+DC from all other image sets.

In Figure 6.2, the image sets and the DC+AL subtraction step is shown. The reference after image looks almost identical to the before and was therefore not included. Visually, the DC+AL subtraction does not change images much. However, in the experiment shown, the DC+AL noise accounted for anywhere between 5% to 20% of the total pixel intensity, depending on azimuthal position. This operation is therefore key to obtaining the correct pressure. Other measurements had a similar amount of noise from the DC+AL.

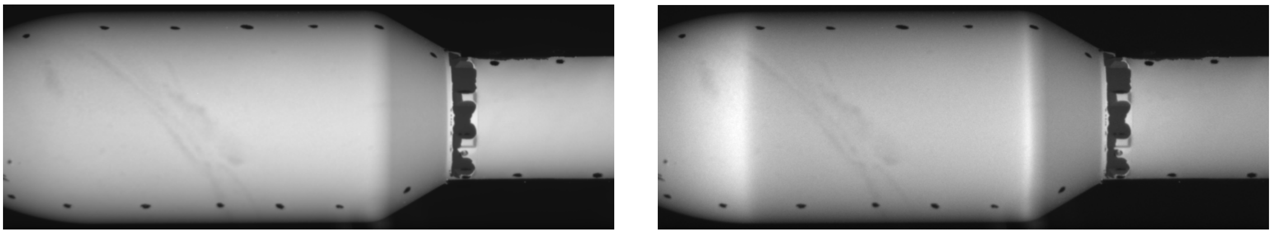

(a) Mean reference before.

(b) Measurement frame 147.

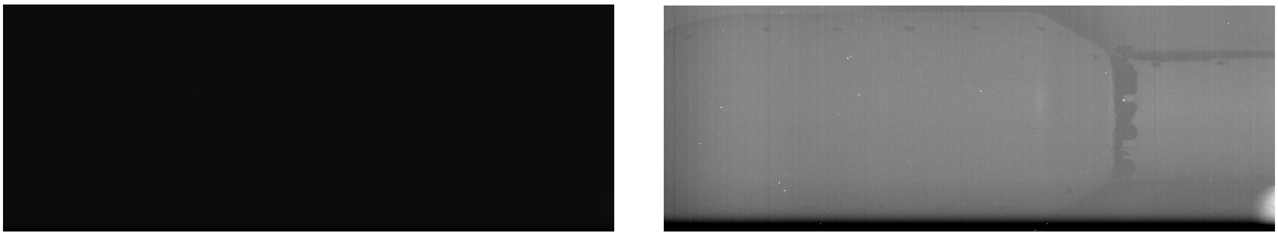

(c) DC + AL image.

(d) DC+ AL with a different color scaling.

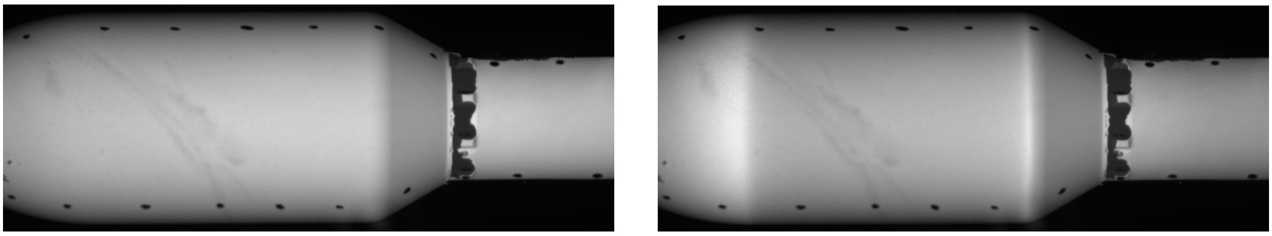

(e) Mean reference before with DC+AL subtracted.

(f) Meaurement frame 147 with DC+AL subtracted.

Figure 6.2: Image sets for a $M = 0.8$, $\alpha = 0°$ and protuberances experiment (**ESA P10**). Images (a),(b),(c) are raw images using the same greyscale intensity scaling between 19 and 2800 counts. Here the mean of all frames is used for the reference. Image (d) uses a scaling between 140 and 160 to highlight the DC + AL noise. Images (e) and (f) have the same scaling as (a) and (b).

After DC+AL subtraction, the loaded reference images are averaged. No additional correction is applied to individual frames, as T was found to vary by at most $0.1K$ during reference image acquisition. The fiducial marks are then detected using Simblobdetector from OpenCv, as described in Subsection 4.2.3. Fiducial mark shape and size differ significantly, requiring a lenient blob detection algorithm. This lead to many spurious blobs being detected. To enhance blob detection, masks were used to filter out areas with spurious blobs and fiducials that could not be detected. The blob detection procedure is shown in Figure 6.3. The same mask is used for both the measurement and the reference images.

The pixel centroids of the detected blobs are then used to align images. All measurement frames are aligned with the mean reference image. To do this, either the projective transform or a second order polynomial transform is used (see Equation 4.3 and Equation 4.4). The most optimal transform is chosen for every measurement. For these images, the projective transform yields the best results. The impact of image alignment can seen in Figure 6.4, where the ratio of an aligned and a misaligned measurement image with the reference image is shown. Here fiducial marks have a net (0.49,0.61) pixel misalignment in (x,y).

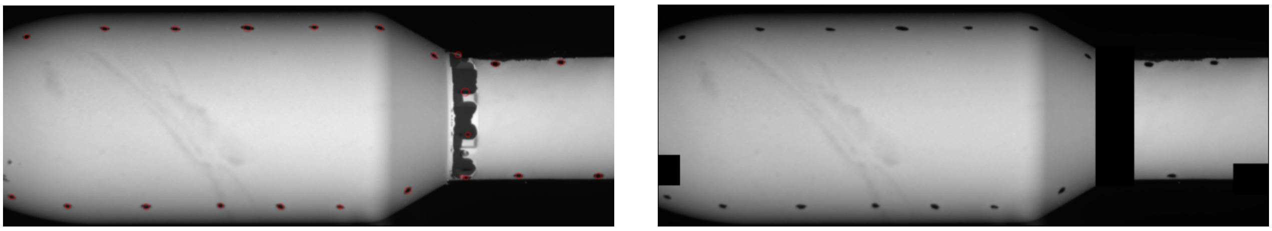
(a) Detected blobs in the full image.

(b) Masked image for enhanced blob detection.

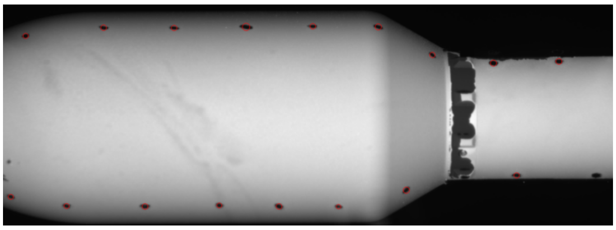
(c) Blobs used for image alignment.

Figure 6.3: Blob detection procedure. Image (a) shows the detected blobs from the full image. A mask is then used, shown in image (b) to enhance blob detection. Image (c) shows the detected blobs when using the mask, which are used for alignment. Note that the mask covers areas that had no blobs in image (a) and a fiducial on the bottom left. In these areas, additional blobs were found in some of the measurement images. The fiducial on the bottom left could not be detected in all images.

The resulting ratio image has a lot of background noise and noise due to fiducial marks. Before calculating the pressure ratio, the background is masked away with a threshold mask and the fiducials with a circular mask. This does not get rid of all the background in the image, as areas with peeled paint have a high intensity. With proper alignment, one mask can be created using the reference image and use for all measurement frames. Individual frames still contain significant amount of shot and flat field noise. No flat field corrections are applied due to the lack of equipment to do so at the HSL. The flat field noise is expected to remains a relatively big error source. To mitigate both noise source slightly, images are blurred with a 3x3 px gaussian blur after division and masking. The resulting image can be seen in Figure 6.4d.

The final two steps are then to calculate the pressure at each frame and to average all images. Pressure calculation is done on a per frame basis in order to apply a temperature correction on each. To do so, a constant temperature is assumed over the model. Each frame is aligned in time with temperature data from the thermocouples. As sampling frequencies are different, thermocouple data is first denoised using averaging, down-sampled to $10hz$ and then interpolated to match with measurement times.

T corrections are applied by approximating the effect of T on the intensity ratio (I_{rat}) as a second order polynomial [69, 70]. Inserting Equation 4.1 into the second order Stern-Volmer equation yields

$$\frac{I_{ref}(p_{ref},T_{ref})}{I(p,T)} = \frac{a_P + b_P \cdot \frac{p}{p_{ref}} + c_P \cdot \left(\frac{p}{p_{ref}}\right)^2}{a_T + b_T \cdot \frac{T}{T_{ref}} + c_T \cdot \left(\frac{T}{T_{ref}}\right)^2} = \frac{f(p)}{f(T)}. \tag{6.1}$$

where $a_P, b_P, c_P, a_T, b_T, c_T$ are coefficients that can be found using a least squares interpolation the calibration data. The coefficients that were used for pressure reconstruction are shown in Table 6.1. Here a second order polynomial in pressure and temperature was found to be most optimal for pressure reconstruction, as opposed to higher or lower order polynomials. The resulting equation approximates the intensity ratio as a function of pressure and a function of temperature.

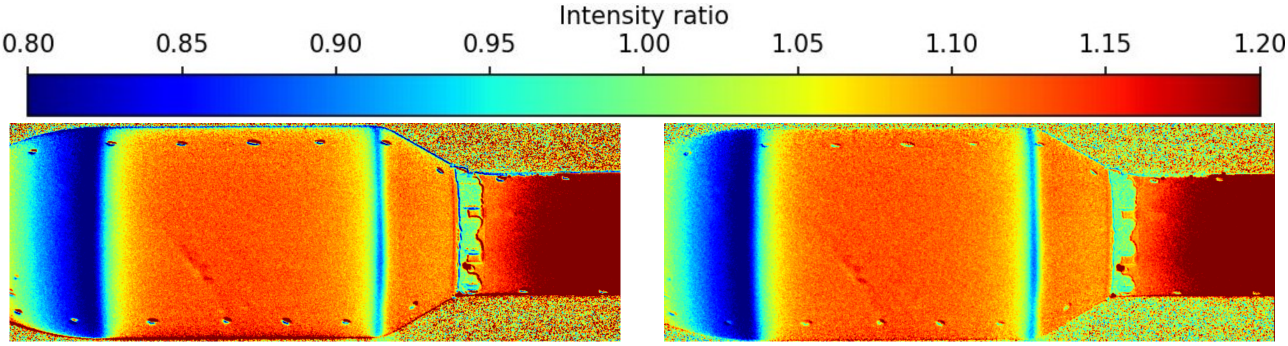

(a) Intensity ratio before alignment for Measurement frame 147.

(b) Intensity ratio after alignment for Measurement frame 147

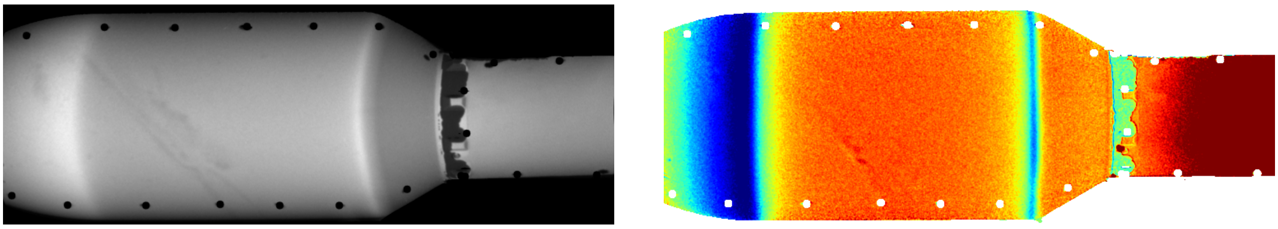

(c) Warped measurement frame 147 due to faulty alignment.

(d) Masked image 147 for pressure calculation.

Figure 6.4: Impact of image alingment on measurement image. Images (a), (b), (d) use the same scale

a_P	b_P	c_P	a_T	b_T	c_T
0.62560088	2.18801363	-0.10830549	7.2550259	-5.80023026	1.24515053

Table 6.1: Coefficients for the Stern-Volmer Equation.

A simpler approach is to create a 3D grid in the (I_{rat}, p, T) space with the calibration data. By placing the measurement points with know I, T on the grid, the pressure can be reconstructed. This only works when the calibration data covers the entire range of the measurements. Equation 6.1 allows extrapolation of the pressure beyond the range of the calibration data, albeit with an unknown uncertainty. From a sensitivity analysis perform on the least squares interpolation, errors are expected to be low (see Section 6.3). Additionally, random errors present on points in the calibration can be mitigated by the polynomial reconstruction of the curve. Measurement points were often found outside of the range of the calibration data, thus requiring the extrapolation approach.

The coefficients in Table 6.1 are for $p_{ref}, (T_{ref}) = (100kPa, 293.15K)$. Prior to calculating p, the I_{rat} must be found with respect to the these conditions. To do so, first the ratio between the calibration and the measurement reference $(I_{rat,ref})$ is computed. As (p, T) of the reference are known, the values can be plugged into Equation 6.1 to obtain the ratio. By multiplying the I_{rat} with the ratio of references, the resulting ratio becomes a ratio between the calibration and the measurement according to the following:

$$I_{rat,ref}(p_{ref,meas}, T_{ref,meas}) \cdot \frac{I_{ref,meas}(p_{ref,meas}, T_{ref,meas})}{I(p_{meas}, T_{meas})} = \frac{I_{ref,cal}(100kPa, 293.15K)}{I(p_{meas}, T_{meas})} \tag{6.2}$$

where the *cal* subscript denotes calibration data and *meas* wind tunnel measurement data. The pressure is then found using the quadratic formula on

$$\left(-a_P + \frac{I_{ref,cal}}{I(p,T)} \cdot \left(\alpha_T + \beta_T \cdot \frac{T}{293.15K} + \gamma_T \cdot \left(\frac{T}{293.15K}\right)^2\right)\right) = b_P \cdot \frac{p}{100kPa} + c_P \cdot \left(\frac{p}{100kPa}\right)^2 \tag{6.3}$$

where the left half is a known constant (A_{IT}). The measurement pressure is then

$$p = 100kPa \cdot \frac{-b_P + \sqrt{b_P^2 - 2 \cdot A_{IT} \cdot c_P}}{2 \cdot c_P} \tag{6.4}$$

The root obtained using plus the determinant was found to be the pressure. The calculated pressure on frame 147 and the mean pressure can be seen in Figure 6.5. Averaging removes a lot of the granular noise, indicating that this is mostly photon shot noise. The resulting 2D plot (= the surface pressure distribution) can then be used for further dewarping and post processing. This is discussed in the next sections.

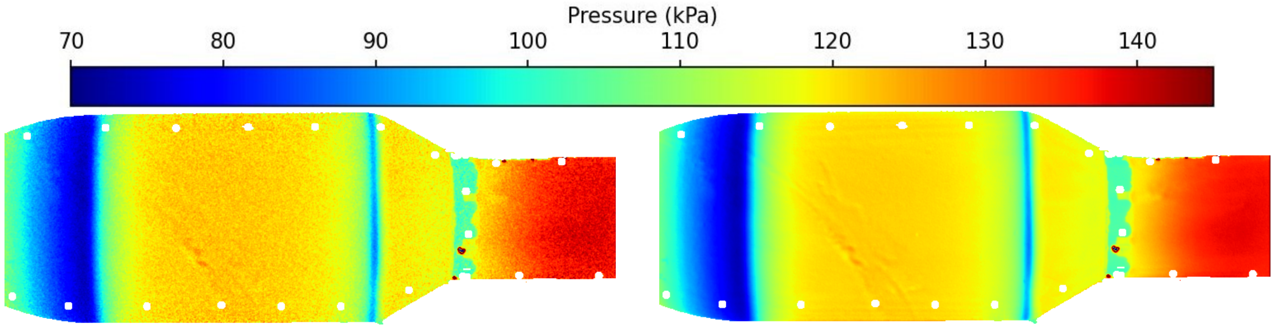

(a) Calculated pressure on measurement frame 147.

(b) Calculated mean pressure of the **ESA P10** run.

Figure 6.5: Computed Pressure at the end of data processing on the **ESA P10** run. (a) shows the pressure for measurement frame 147, whereas (b) shows the mean pressure over all images for .

6.2. PSP Post-Processing

To further process PSP data, the obtained pressure is first converted to C_P to allow for different Mach numbers to be compared. After, images are dewarped to ensure that the image plane is properly scaled to "real" coordinates. The coordinate system of images is changed to $(L/D, \phi)$, where L/D is the length along the model divided by the model diameter and ϕ the azimuthal angle. The origin of this coordinate system is set at the end of the boat tail for both HHF models, with a positive L/D along the downstream direction. Positive azimuthal angles are defined towards the upper side of the model. After dewarping, circumferential mean plots and the position of flow features can be extracted.

6.2.1. Dewarping

The most optimal way to do dewarp images is by use of image resection. However, due to the added complexity of implementing resection, the author chose to forego this approach for the current thesis. Instead, dewarping was done by using the projective transform (see Equation 4.3), a second order polynomial series expansion (see Equation 4.4) or a quadratic transformaton of the image plane x-axis depending on y position, followed by a linear transformation of the x-axis (denoted as "flattening the curve"). The latter is explained later in this subsection.

For this, the axial position (X) of the fiducial marks along the model was measured (see Appendix L). It was expected that the vertical coordinate (Y) could be extracted from the image and be used for dewarping. The dewarping however turned out to be ineffective for five reasons. The first is that the extracting the Y coordinates from the warped image returns inaccurate values due to model's three-dimensionality. As the model is cylindrical, points at the center are bigger in the image plane than those at an azimuthal angle. This error is relatively small, as the model radius is between 1.5 cm and 2.5 cm.

Secondly, the measured X position of the fiducial marks have a relatively large uncertainty in pixels. The axial resolution of most images was around $0.089mm$ per pixel, with an expected measurement error for fiducial mark positions of around $0.5mm$, giving a potential ~ 6 pixel error. This error is expected to be higher for fiducials on the PLF of the Vega-E. This is further enhanced by the fact that the measured center of fiducial marks and the center detect by the blob detection do not necessarily overlap (max expected error of $1mm$ for Vega-E PLF). Some fiducials were found to cause large dewarping errors when included in the image transformation. These had to be removed, which reduced the number of available fiducials. Smaller errors due to this can be seen in the circumferential mean plots of the Vega-E model (e.g. Figure 8.2) upstream of the first shock in the form of kinks in the pressure distribution.

Alongside this, the model geometry proved to be more difficult to dewarp than originally anticipated due to the increase in diameter between LV and PLF. For the Vega-E, all the aforementioned methods failed to dewarp the full image. Instead, dewarping was performed for the LV and PLF separately. As one camera focused downstream of the boat-tail and another upstream, the downstream image was used for the LV and the upstream for the PLF. Afterwards, both were combined to generate the full image. The boat tail in the final plot is then generated from an overlap of both images. This leads to the boat tail always being wrongly dewarped. However, as the pressure is more or less constant along the boat tail, the error caused by this is relatively minor. Note that noise reduction from camera overlap is not expected from this approach.

The fourth issue is that fiducials were only placed on the top and bottom of the model. The author expected that the projective transform would suffice for image dewarping, where fiducials are most optimally placed at the edges of the object. However, due to the aforementioned issues, the polynomial transform was found to perform much better, but only when including marks on the center of the object (see Figure 6.6). For this, the location of geometrical features (model junctions) were used. Having fiducials at the center would have improved the dewarping. Note that the PLF of the Vega model has no geometrical features that can be used. Some curvature can be seen here, especially on the second shock, due to a suboptimal dewarping (e.g. see Figure 8.1). Here, fiducial positions are furthermore more uncertain.

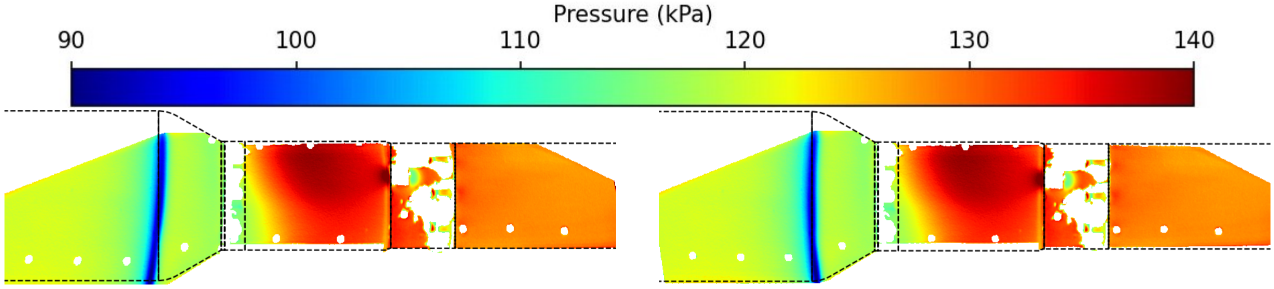

(a) Fiducial mark dewarping.

(b) Dewarping including geometrical features.

Figure 6.6: Comparison between the dewarping using only fiducial marks and dewarping using fiducials and geometrical features. Here, a polynomial image transform is applied to the $M = 0.8$, $\alpha = 4°$ configuration with protuberances. Images were taken with the up perspective. In image (a), curvature can be seen towards the edges near the protuberance rings. By using the known ring locations, this curvature is eliminated in image (b). Note that the nosecone is not correctly dewarped in either case, and had to be dewarped separately.

Lastly, for most measurements the cameras were placed perpendicular to the model axis. For these, dewarping was manageble to an extent. However, for the $\alpha = 4°$ Vega-E measurements one camera was placed at an angle with respect to the axis to better visualize the nosecone. For these images, none of the methods employed were capable of providing a good dewarping due to the added three-dimensionality of the setup. Therefore, no flow positions are extracted from these.

With the aforementioned problems, the final PSP images have dewarping artifacts. These include:

- Some small curvature of geometrical and flow features that should be straight, especially near top and bottom the edges of the fov.

- Slight misalignment of geometrical featured with the model outline presented along the plots.
- The surface C_P plots being larger than the outline in some images (especially near the boat tail).
- Kinks in the circumferential mean plots.
- Curvature of the second shock in the $\alpha = 0°$ surface C_P plots for the Vega-E.

To obtain the best results, different plots were created using different dewarping approaches. For all the Model 11 plots and the $\alpha = 0°$, no protuberances circumferential mean plots of the Vega-E model, the "flattening the curve" approach was used. Here, the curvature on the model due to camera warping was approximated by a second order polynomial. The polynomial was found by placing five or more points along a curved surface. An image plane transformation was then performed to flatten this curve. This process is described in Figure 6.7. After the curvature is flattened, the x-axis was re-scaled using the position of the fiducial marks.

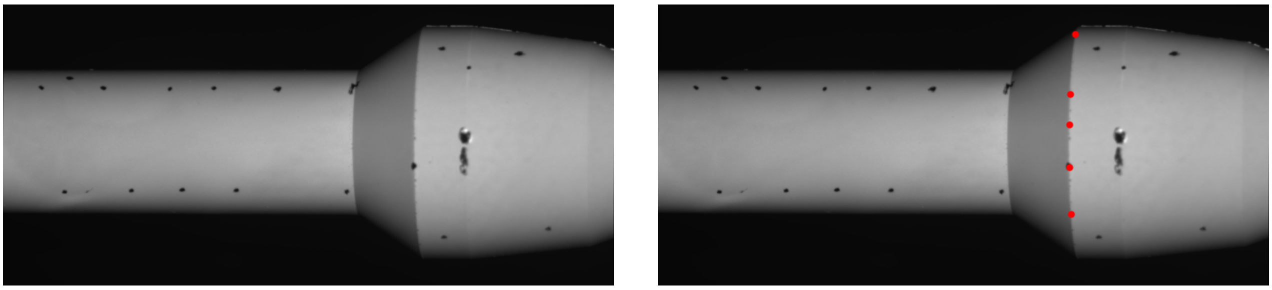

(a) Raw reference image.

(b) Points along image curvature.

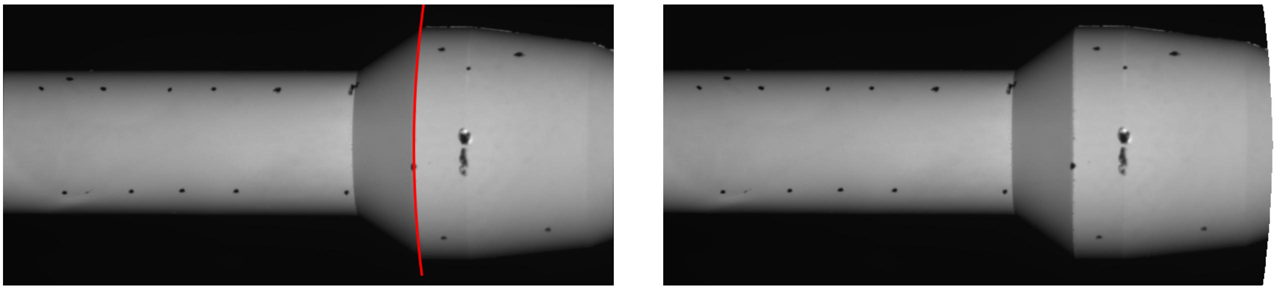

(c) Line to flatten along model.

(d) Flattened curvature.

Figure 6.7: Example of the "flattening the curve" approach used on a reference image of the Model 11.

The "flattening the curve" approach provides a decent dewarping of the x-axis, but it is not perfect as the curvature depends on x-position along the model. Furthermore, the y-axis is not dewarped. Dewarping errors for this approach are mostly dependent on the fiducial mark X uncertainty and the mismatch between blob centroid and measured centroid. An expected error of at most $0.5-1mm$ would be present for the approach (=$0.01-0.02L/D$, highest on the Vega-E PLF). To obtain a better dewarping for the y-axis, other plots of the Vega-E model use the polynomial series expansion for the LV and a projective transform for the PLF. Dewarping errors downstream of the boat tail are expected to be small in this approach.

The dewarping process is applied to both the surface pressure plots and a reference image. From the dewarped reference image, the pixel edges and center-line of the model are extracted. This is needed as the edges of the pressure plots are slightly smaller due to the masking used to remove the background. The location of the edges and the center-line is the used to calculate the azimuthal position of each pixel. The center-line is set to $\phi = 0°$, the upper edge $\phi = 90°$ and the lower edge $\phi = -90°$. For measurements where the camera was at an angle, this angle is added to the above values. Assuming that the y coordinate is correctly dewarped, each pixel's azimuthal position is given by:

$$\phi = arcsin\left(\frac{y_{center} - y_{pix}}{r_{pix}}\right) \tag{6.5}$$

where y_{center} is the position of the center-line, y_{pix} the position of each pixel and r_{pix} the local radius of the model in pixels. Note that as the y-coordinate is not perfectly dewarped, some error is expected in ϕ.

6.2.2. Circumferential Mean Plots

Circumferential mean plots are made by taking the mean value of the dewarped surface pressure images along a given x pixel location. As can be seen in Figure 6.5, despite masking and averaging, images have PSP related noise due to paint damage. To remove this, first large PSP errors are manually masked away. Then, the mean and standard deviation at every x location is computed. Any points more than 2 standard deviations away from the mean are masked away. A new mean is calculated and used as the circumferential mean. This process is visualized in Figure 6.8 for the Model 11 runs at M = 0.8 and $\alpha = 0°$.

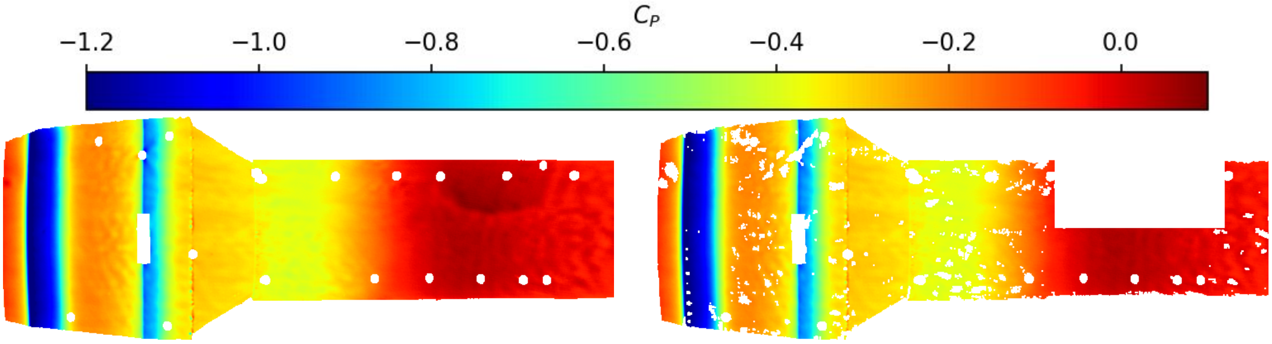

(a) $M = 0.8, \alpha = 0°$ C_P plot.

(b) Outlier removed $M = 0.8, \alpha = 0°$ C_P plot.

Figure 6.8: Outlier removal proces visualized on the Model 11 experiments at $M = 0.8$ and $\alpha = 0°$. Here, a chunk of the original image associated with paint damage due to the paint being touched is masked away before outlier removal using standard deviation. Due to the noisy rash pattern on the Model 11, a lot of points are masked away.

At edges of model parts, small misalignment's tend to create nonphysical spikes in the pressure signal. This is due to sharp changes in intensity from model parts having different viewing angles or gaps between parts that have no paint. For the final mean plots, these are removed. A comparison between the raw and the noise removed C_P plots can be seen in Figure 6.9. In PSP data with less noise, line plots can be extracted from a line of pixels at any position on the model. Due to the relatively high noise present here, other line plots are created using at least an average of 20° azimuthal angle. The approach taken is the same as for the circumferential mean, but only a strip of data is used. This can be seen in Section 7.4.

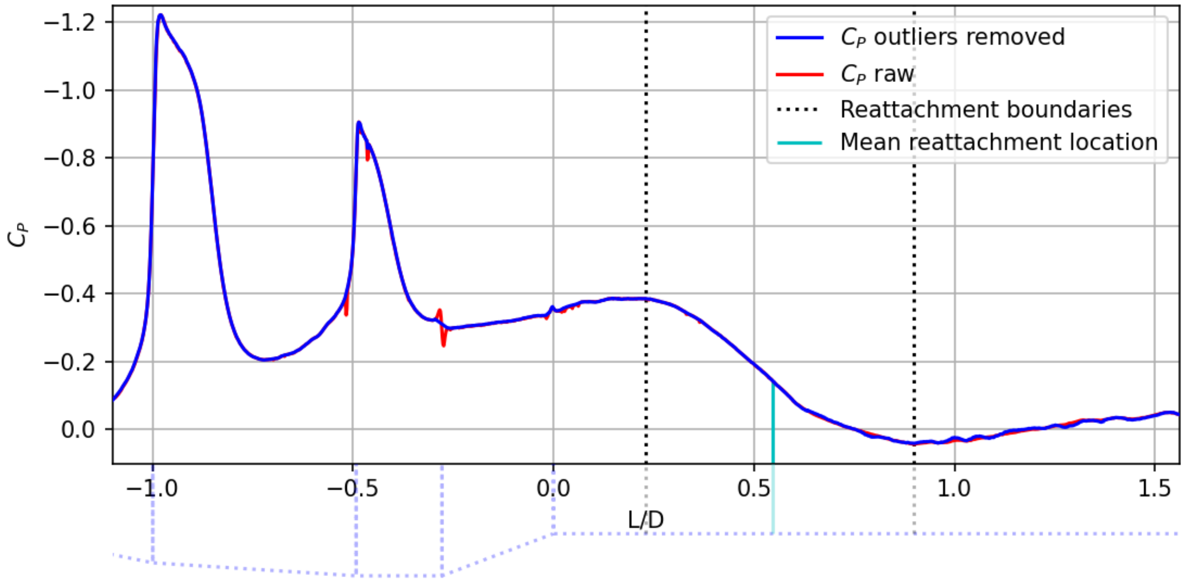

Figure 6.9: Comparison between outlier removed mean C_P and that without outliers removed for the Model 11 at $M = 0.8$ and $\alpha = 4°$. Also shown is the detection of the reattachment location.

6.2.3. Position of Flow Features

Standard PSP data can be used to extract the mean location of the two most important flow features, namely the shocks and the flow reattachment. To do this for the shocks, pressure gradient plots are used. These are created by taking the gradient of the circumferential mean C_P along the length of the model with respect to the L/D. This results in a new variable, denoted as C_{P_X}. This plot is relatively noisy in area of low pressure gradients due to PSP related noise. For a stable standing shock a large, abrupt jump in gradient would be expected. Instead, due to high level of oscillations present in the system and the time averaged nature of the measurement, the shock wave is expected to produce a smeared out zone of positive pressure gradient. The mean shock location is then defined to be near the point with the highest pressure gradient.

Due to PSP noise and the time averaged nature of the measurement, the point of highest C_{P_X} may be situated in a region with a local C_{P_X} plateau. In such a case, the mean shock location is determined to be in the center of the C_{P_X} plateau. Other times there is a clear sharp peak, where the mean shock position is defined. An example of the resulting pressure gradient plot can be seen in Figure 8.3. Here, there is a small C_{P_X} plateau for the first shock and a sharp peak for the second shock.

The reattachment location is more difficult to accurately define using the standard PSP data. The SNR in the C_{P_X} plots is too low to be effectively used for the determination of mean reattachment location. Instead, here a combination of the contour plots and the circumferential mean plots is used. The reattachment location is defined as the center point between the point at which the pressure starts increasing and the point at which the pressure stops increasing. An example of this is shown in Figure 6.9 for the circumferential mean C_P plot of the Coe and Nute Model 11. This approach however is less accurate than the approach used for the shocks, with expected uncertainties in the order of 0.03 L/D.

Another issue is the determination of the separation point. For the Model 11, the separation point can simply be assumed to be situated at the start of the boat-tail ($L/D = -0278$), given the abrupt geometry change. For the Vega-E, the start of the boat tail is smoothed out to weaken separation. Defining the separation point from PSP data is therefore difficult. Instead, it is assumed that the flow separates at the second shock. For the cases without a second shock, the peak C_{P_X} is instead taken.

6.3. Stern-Volmer Curve Calibration

As mentioned in the previous chapter, the main goals of the calibration were to verify the adequateness of the test setup and to obtain a Stern-Volmer curve for the purchased paint batch. The full test matrix of the calibration experiments can be found in Appendix H. It was designed to have most points at room temperature with varying p levels, and some points spread around the temperature range. A scatter plot showing all measured (p, T) points can be seen in Figure 6.10. Due to the box being leaky for vacuum measurements and the pressure valve not accurately setting pressures, the chosen points were more or less random.

Most points were taken around $290 \pm 2.5K$, as experiments were expected to be in this range. The randomness in the point distribution mitigates temporal bias. If points were systematically taken, e.g. from low to high p, a temporal bias would carry over as bias in p. By randomly distributing the points, any bias is spread over the distribution. Sources of bias that could play a role are changes T_{room}, p_{atm} and photodegradation. Changes in p_{atm} were not tracked, but were likely small (up to $\pm 200 Pa/h$). Room T changes instead affect the thermocouple uncertainty.

For the 83 measured points, over 2 h and 40 min was needed. This makes photodegradation a significant noise source. Two experiments were performed on different coupons to obtain the photodegradation rate. From these, a change in intensity of $2.8\%/h$ was found from coupon 1 and $5.1\%/h$ from coupon 3. Due to time constraints, more experiments could not be taken as coupons had decayed by the time the data was processed. The manufacturer states a photodegradation of $4\%/h$ which is dependent on lamp power and wavelength. Finding a different value is not unexpected, however, a difference this large between two coupons created simultaneously is unexpected. The likely cause is filter spectral leakage and lamp instability. Both are discussed later in this chapter.

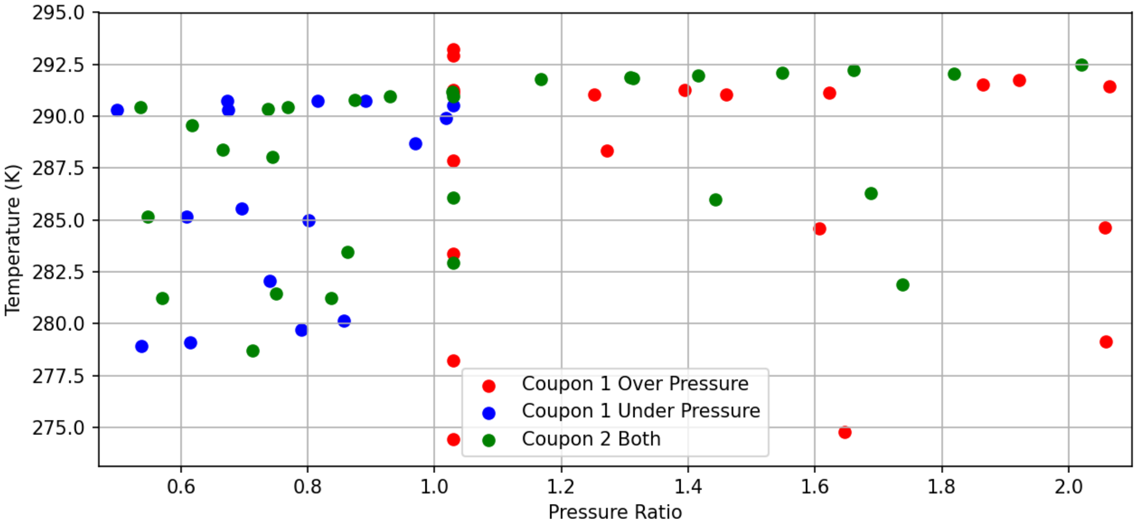

Figure 6.10: Distribution of calibration measurements on coupons 1 and 2.

6.3.1. Comparison with ISSI data

While different batches of Unifib PSP have slightly different calibrations, the overall Stern-Volmer curve should be similar. To validate the calibration measurements, the measured I_{rat} was compared to the ISSI data. This data can be seen in Table B.1. Ratios for the measured points were found by using the mean coupon intensity with respect to the first measurement of each set, at (p_{atm}, T_{atm}). Corrections were then applied using both decay rates. The 5.1%/h rate was found to yield lower discrepancies for coupon 2, and the 2.8%/h for coupon 1. The percentage difference between $I_{rat,meas}$ and the I_{rat} interpolated from the ISSI data can be found in Figure 6.11.

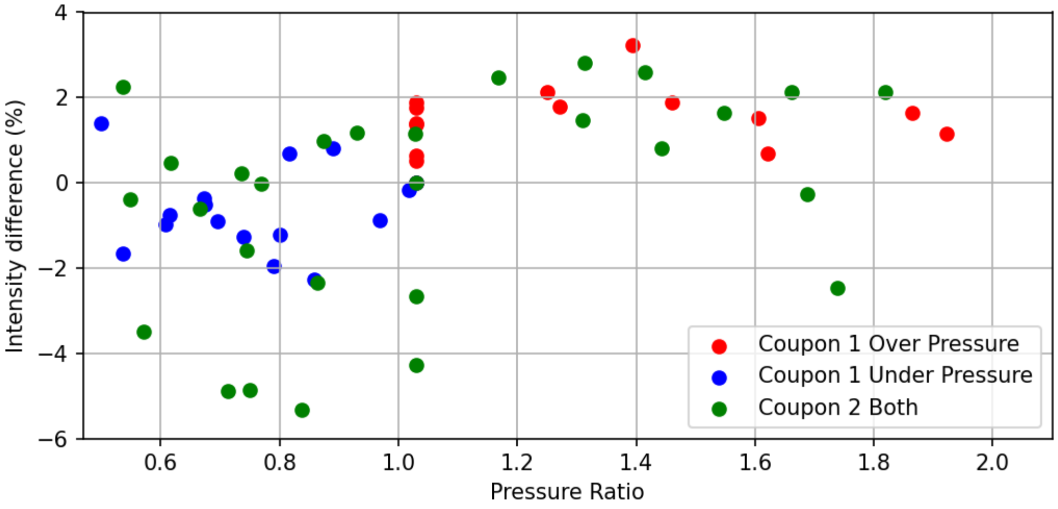

Figure 6.11: Percentage difference in measured intensity compared to the calibration data from ISSI.

Most points are within 2% of the ISSI data, with up to 5.5% difference. Attempts were made to find trends in the percentage differences, to explain potential errors. Plots were made with respect to:

- Temperature
- Time
- Δp between points
- ΔT between points
- Atmospheric conditions
- Coupon numbers
- $\Delta(p, T)$ during data acquisition

Two trends were found, namely that for $p_{rat} > 1$ points tend to have a positive difference percentage, whereas the opposite is true for $p_{rat} < 1$. Secondly, the percentage tends to be more positive at higher temperatures and negative at lower temperatures. Both give the impression that these differences are mainly caused by thermocouple data uncertainty and differences between paint batches. Later on, it was discovered that the $550nm$ filters have significant spectral leakage, which required further investigation.

6.3.2. Spectral leakage

To study the spectral leakage, one experiment at $M = 0.7$, $\alpha = 4°$ and protuberances was performed using both filters with a high camera overlap of 2.7 L/D (**ESA P17**). The resulting circumferential mean plots can be seen in Figure 6.12. Notable is that the raw $550nm$ data has a lower p than the $610nm$ due to spectral leakage. As the cameras took simultaneous measurements, only small differences should be present. Spectral leakage causes a constant intensity value to be added to both the reference and the measurement image. To correct for this, 1.75% of the intensity of the reference image was subtracted from both.

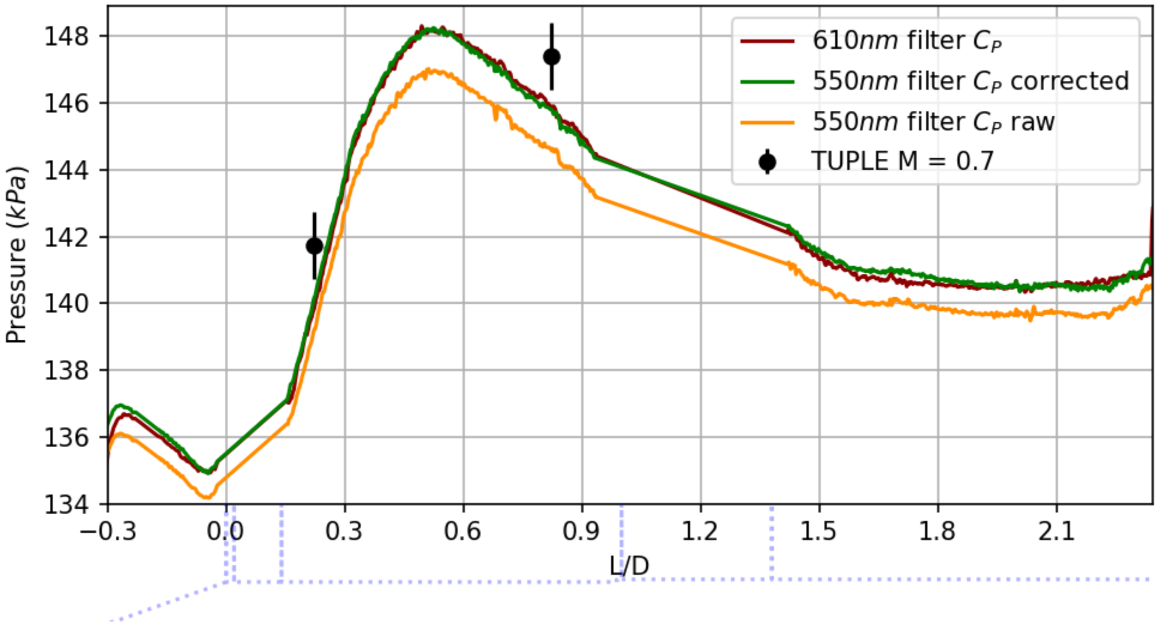

Figure 6.12: Circumferential mean pressure plot of the $M = 0.7$, $\alpha = 4°$ run (**ESA P17**). Data from the $550nm$ filter camera was corrected by subtracting 1.75% of the reference image intensity from the measurement and reference images.

Before correction, a net difference of $0.7kPa$ to $2kPa$ is present between cameras. This difference is dependent on the local p (higher p = higher Δp). The correction almost perfectly aligns both curves, but the 1.75% result is only valid for this test. It is highly dependent on model surface properties (absorbance), paint decay and paint thickness. These properties were not tracked or measured. Spectral leakage is a likely cause of the discrepancy seen in the photodegradation rate of the coupons, as coupon 1 had been illuminated for over $2h$ by the time it was tested for photodegradation. It also had a much thinner paint layer than coupon 3. Therefore, leakage contributed to a larger amount of the total intensity in coupon 1.

6.3.3. Least Squares Approximation of the Stern-Volmer Curve

The spectral leakage adds an extra unknown uncertainty to the calibration data. Interestingly, spectral leakage causes high pressures to have a lower I_{rat}, and low pressures to have a higher one. This is the opposite of the trend seen in Figure 6.10. Due to all these uncertainties, it was chosen to reject the calibration measurements for pressure conversion. Improvements are needed to the calibration setup before this can effectively be used. Instead, potential batch difference errors were accepted and reconstruction was done using the ISSI data. This was found to have good overlap with pressure tap and historical data.

The biggest downside of this dataset is that it does not cover the full temperature range of measurements, therefore extrapolation is needed. The ISSI data ranges from $p_{rat} = 0$ to $p_{rat} = 2$ with a $p_{ref} = 100kPa$ and $T = 278 \pm 1K$ to $T = 303 \pm 1K$. Extrapolation is done using Equation 6.1, where Table 6.1 shows the coefficients that were obtained with a least squares optimization. To get the best optimization, the range of p_{rat} and T used in the optimization was chosen to be close to the measurement range. Data below $p_{rat} = 0.5$ is highly nonlinear which introduces large errors in the optimization, and the minimum p measured on a HHF model was $65 kPa$. Alongside this, wind tunnel T did not go above $293K$. A sensitivity analysis was performed to determine which points provided the lowest error compared to the original data. It was found that using $p_{rat} = 0.5$ to $p_{rat} = 2$ and $T = 278 \pm 1K$ to $T = 293 \pm 1K$ is most optimal.

The optimization was used to reconstruct the original curve, and compared to the ISSI data. The resulting % difference in I_{rat} between the reconstruction and original data can be seen in Figure 6.13. Above $p_{rat} = 0.6$, all but one points have a less than 1% difference in I_{rat}. Most points are around ±0.5%, which is within the expected T uncertainty of the original data. The author furthermore believes that the $T = 288K$, $p_{rat} = 0.7$ point is an outlier in the original dataset, explaining the relatively high difference.

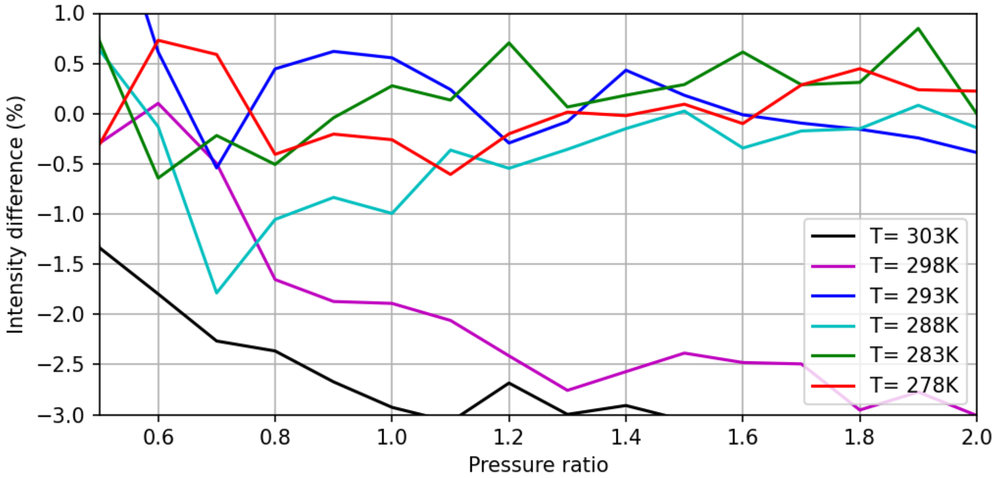

Figure 6.13: Percentage difference in measured intensity compared to the calibration data from ISSI.

The ±1% difference leads to at most a $\pm 1 kPa$ uncertainty in the original calibration range. However, the effectiveness of the optimization at extrapolating has to be tested. As can be seen in the figure, extrapolating to higher T under-predicts the intensity ratio, but only extrapolation to lower T is needed (see Appendix K). Another sensitivity analysis was performed by removing some T curves from the optimization, and reconstructing them using the remaining. Results were found to vary. Most of the time, the reconstruction of the curve was within 1% of the original data, even when two curves were excluded. The exception was when only the $T = 278 \pm 1K$ curve was excluded. Here, the reconstruction errors went up to 2%.

To further investigate this, measurements outside the calibration range were compared to ones within for the same test configurations. The results can be found in Table 6.2. Here, the mean absolute difference in p is shown. All but one configuration are within $1 kPa$ of each other, indicating that the extrapolation is adequate. Note that this mean includes random noise, and would never be zero. For the exact configuration of each measurement, readers are referred to Appendix I. The large difference between **CN 1** and **CN 4** is likely explained by **CN 1** being a first run, which is discussed in more detail in the following section.

Case 1	Case 2	T_1 (K)	T_2 (K)	Δp (kPa)	Case 1	Case 2	T_1 (K)	T_2 (K)	Δp (kPa)
ESA 6	**ESA 3**	281.0	276.2	0.27	**CN 1**	**CN 4**	281.5	275.2	2.30
ESA 13	**ESA 15**	286.7	275.8	0.95	**CN 5**	**CN 6**	279.7	276.4	0.01
ESA 14	**ESA 16**	279.5	273.9	0.38	**CN 7**	**CN 8**	282.7	276.8	0.68
ESA P8	**ESA P10**	284.7	276.5	0.78					

Table 6.2: Absolute mean Δp between tests inside the T range of the calibration data and tests of the same configuration outside this range. Also shown is the mean T of each measurement, where T_1 and T_2 are for the first and second listed cases respectively.

6.4. Observed Error Sources and Corrections

This section discusses different error sources that are known to be present in the processed PSP data. The author expects that the following discussion covers most of the errors, especially major ones. In addition to these, calibration and spectral leakage errors were discussed in the previous section. Furthermore, no further mention is made of DC / AL errors as this is expected to be fully mitigated by subtraction.

6.4.1. Impact of Temperature Corrections

By using the thermocouples to correct for temperature, measurements were found to have almost the same pressure under different temperatures. Duplicates of measurement configurations are within $1kPa$ of each other, with most tests being within $400Pa$. Similarly, pressure distributions using reference before and after are within $400Pa$, unless something went wrong during data acquisition. The impact of not applying temperature corrections can be seen in Figure 6.14 for a $M = 0.8$, $\alpha = 0°$ no protuberances experiment (**ESA 6**).

Here it can be seen that the reference before under-predicts p and that the reference after is close to the corrected value. The former is due to the fact that the model temperature is lower than the reference temperature, whereas for the latter model and reference temperatures are closer. Using only the uncorrected reference after can yield decent results, especially for runs with lower temperature decreases. However, thermocouple corrections allow for both the reference before and the reference after to be used, which can statistically lower Stern-Volmer calibration uncertainty, negate photodegradation and give insight into whether something went wrong during data acquisition, as both references should provide the same results. As acquiring thermocouple data is relatively simple, the benefits outweigh the amount of effort required.

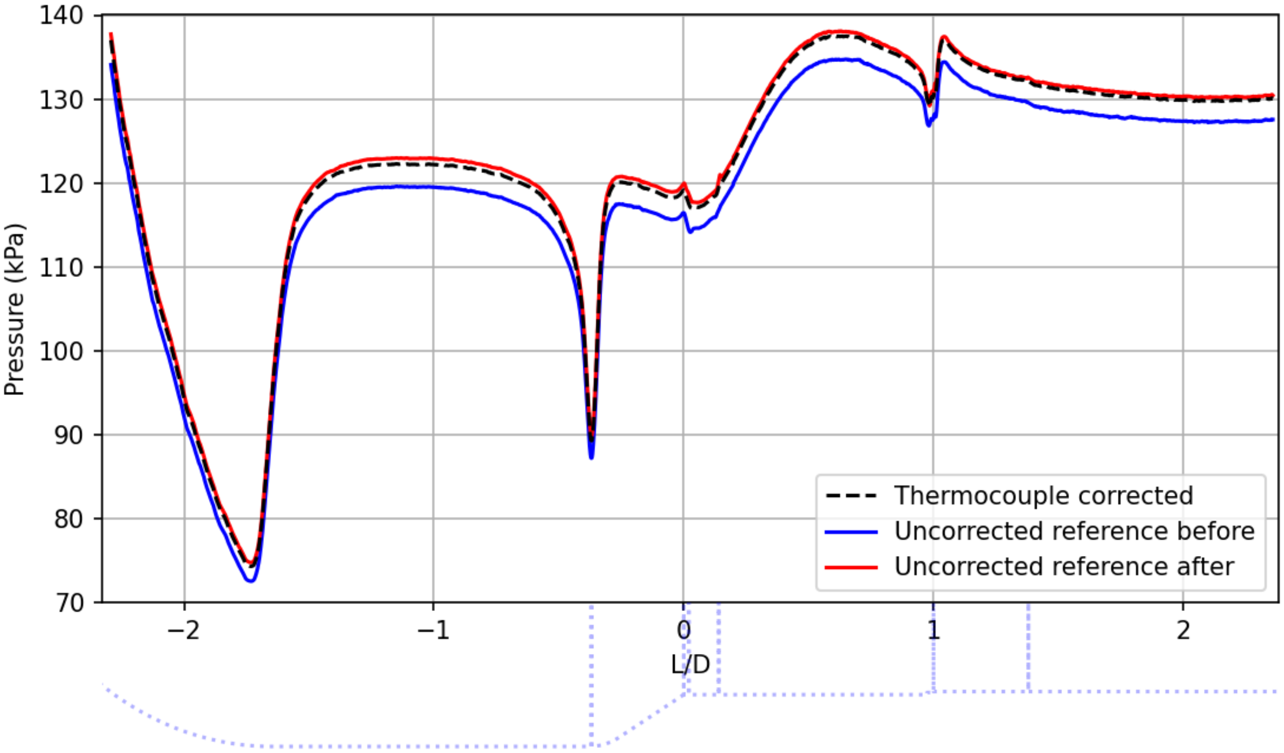

Figure 6.14: Effect of using thermocouples to correct the PSP data, instead of assuming a constant temperature (=293K).

6.4.2. Model Temperature Gradients

While thermocouple is correcting for the net T decrease over time, temperature gradients are still present over the model. These mostly arise due to differences in thermal inertia between parts and aerodynamic cooling. To quantify this, three IR measurements were taken on the Vega-E model. Several snapshots of the circumferential mean T can be found in Appendix M. The distribution was found to depend on the following:

- **Run time.** At the start of the measurement, temperature gradients are small. At first, they increase with time whereafter they decrease as wind tunnel temperature cools down.
- **Starting wind tunnel temperature.** Higher starting temperatures lead to larger gradients.
- **Aerodynamic distribution.** As expected, higher local pressure areas had slightly higher temperatures.
- **Model geometry.** T on the PLF and boat-tail was consistently higher than downstream of it, despite having a lower p, with the boat-tail having the highest T. The protuberance rings were much colder than anywhere else on the model. This is likely caused by the thin walls of the rings.

Due to all these factors, the temperature distribution over the model is complex. A snapshot of T during a measurement can be seen in Figure 6.15. Here, data from two measurements with different FOVs (**ESA IR1** and **ESA IR2**, see Figure 5.18) is combined to obtain the distribution over the entire model. Both data sets overlap for around 5 seconds, after which one measurement ends. The overlap started 12s after the wind tunnel was turned on for the downstream FOV, and after 28s for the upstream FOV. Note that the upstream test starts at a higher T, but after 16s the mean T is the same as the start of the downstream FOV. This indicates that the T distribution is similar for different runs at the same T after the tunnel is on for at least 12s.

Using the aforementioned observation, an attempt was made to find a relation between the thermocouple and the temperature distribution. This proved to be very difficult due to the dependence on both wind tunnel run time and starting temperature. As this result would furthermore only be valid for $M = 0.8$ and $\alpha = 0°$, no further analysis was performed with this. Further investigation with more overlapping measurements is required. Instead, a simple uncertainty analysis is performed using the results shown Figure 6.15.

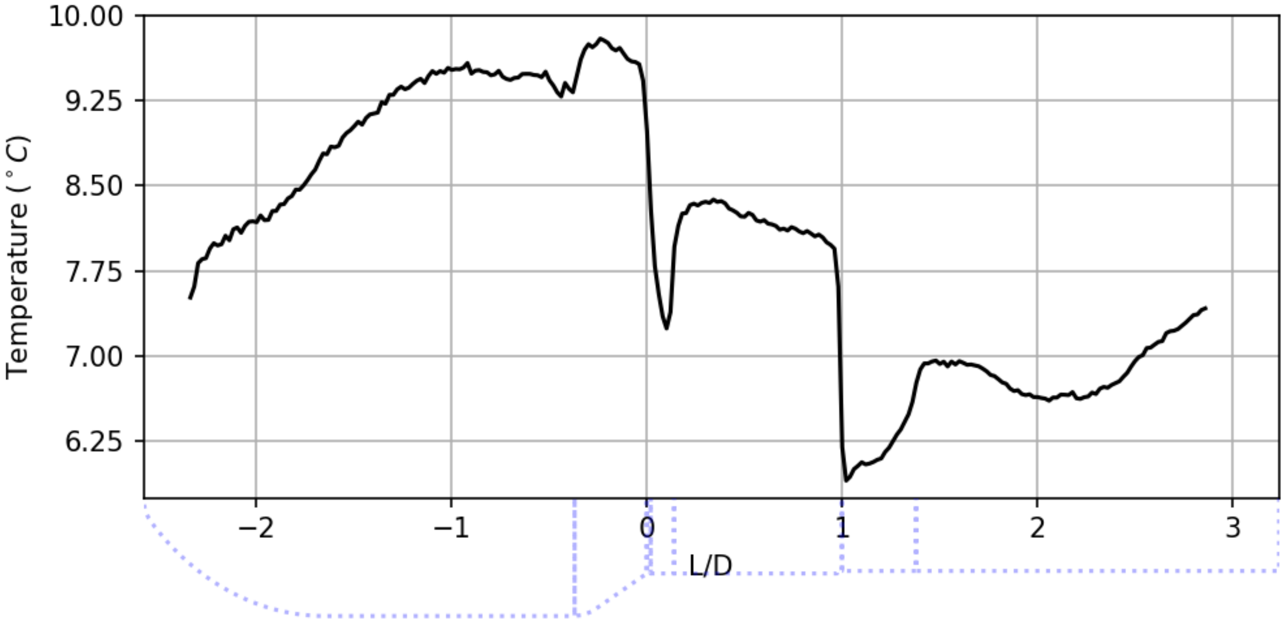

Figure 6.15: Snapshot of the temperature distribution over the entire model. Created from two combined measurements with different FOVs.

The thermocouples were placed at the end of the model, which was not visualized. Towards the end, the temperature is linearly increasing. Assuming this continues, a temperature around 7.9°C is expected at the edge. By further assuming no differences between thermocouple and IR, the pressure error can be computed using the mean p distribution, Stern-Volmer curve and T distribution. This was done for the a test case (**ESA 6**) that had a mean thermocouple temperature of 7.9°C. Results can be seen in Figure 6.16.

In actuality, as the temperature changes during the run, so does the correction. This correction is therefore not entirely accurate given that the data was acquired over 17.35s. However, it does give insight into areas where errors may take place. The maximum expected uncertainty from temperature gradients for M =0.8 and $\alpha = 0°$ is around $+1.3kPa$ to $-1.5kPa$ for measurements at $T = 281K$. This uncertainty is expected to increases with increasing measurement temperature and vice versa. It is unknown how this uncertainty changes with Mach number and α. Furthermore, the uncertainty of the Model 11 is entirely unknown. More IR measurements would be needed to determine this.

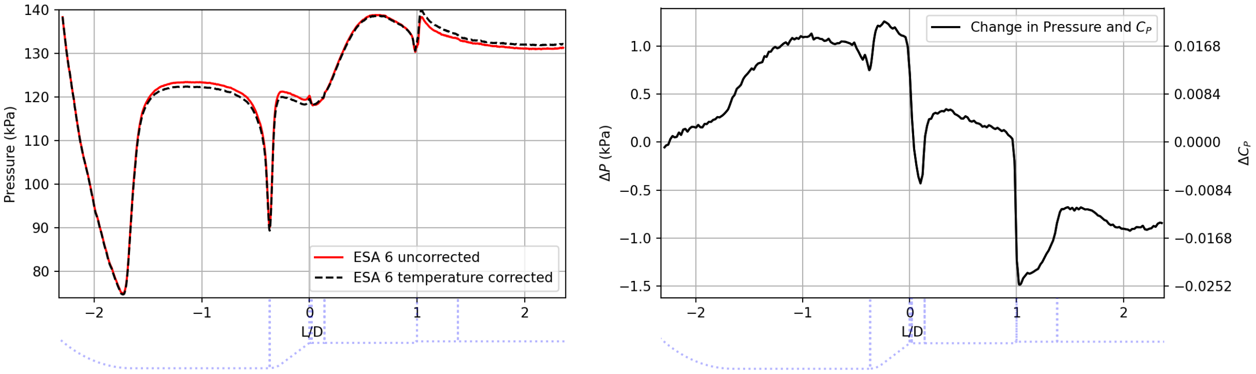

(a) Comparison between uncorrected and IR corrected data.

(b) Difference between uncorrected and IR corrected data.

Figure 6.16: Example of a temperature gradient correction applied the Vega-E model at M=0.8 and $\alpha = 0°$.

Note that the above procedure assumes that the temperature of the model under the reference images is constant. This was found to not be the case, even before any measurements are done (see Appendix M). This is further complicated by the fact that the reference temperature distribution is dissimilar to the one during the run, and therefore adds another small uncertainty (expected to be around $\pm 0.4 kPa$). Proper corrections would require both the measurement and the reference images to be spatially corrected using IR.

6.4.3. Error in the First Run After Opening the Tunnel

All the runs that were performed right after the tunnel was opened had a recurring pattern where the pressure calculated with the reference before had a $7kPa$ higher value on average than the reference after. Furthermore, for the first runs with a paint coat (**CN 1, ESA 1** and presumably **ESA P1**), the pressure predicted with reference after under-predicted the pressure distribution compared to other runs of the same configuration. The under-prediction was about 1-2 kPa depending on the test.

The first observation is likely caused by humidity. Water condensation gives a higher luminosity to PSP as explained in Subsection 4.5.4. This causes the reference image before the first run to have a higher intensity. As tunnel air is dry, the humidity is stripped away during the run leading to a lower intensity. This is seen in the pressure signal as a higher pressure. Future PSP measurements should take this into account by doing a "warm-up" run where no data is acquired. It is unknown how long this run needs to be to remove both effects. The second observation is likely due to friction stripping luminophores from the surface of the paint during the first run. This causes the intensity during the run to be higher than the reference after, which is seen as a lower pressure. Friction is less of an issue after, given that the second observation was only seen for first runs.

6.4.4. Paint Peeling

The predominant source of paint decay was mechanical wear of the paint. As more runs are performed, the paint is slowly stripped away from the surface of the model. This delamination can lead to surface roughness that affects pressure distribution, high levels of noise at delaminated areas and a time limit on how often models can be used. Delamination was worst for the cone model and the protuberance rings of the Vega-E model. An example of roughness due to delamination impacting the pressure distribution can be seen in Figure 7.7a at L/D = -0.5 and $\phi = 45°$. Here a paint bubble led to delamination and some roughness that causes a "<" shaped trail, similar to a turbulent wedge, in the pressure. The delamination can be seen in Figure 5.9, above "PSP" in the caption of the figure.

Delamination was found to start near edges where the model was masked away with tape before painting and at locations where air bubbles were trapped during painting. For the protuberance runs, must of the paint on the protuberance rings peeled away due to bubbles, as the abrupt geometry change caused air to be trapped. In the image, delaminated areas have higher intensities than unpainted paint areas. Futhermore, areas where delamination is starting were found to have higher intensities than the surrounding paint. It is unclear what caused this. An example is shown in Figure 6.17.

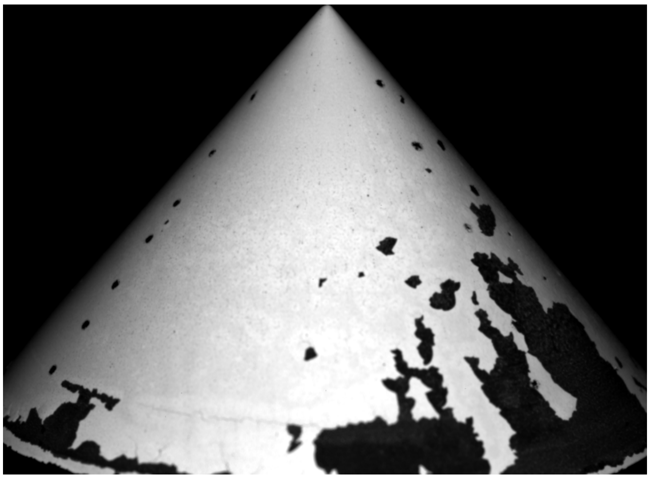

Figure 6.17: Greyscale image of the Cone model in the tunnel. Paint is highly delaminated. Areas where the paint brightness is higher than the surrounding area indicate local paint damage, which ultimately delaminated.

To mitigate this issue, future runs should avoid paint bubbles by approaching painting differently near abrupt geometry changes. Furthermore, a different approach to masking or tape removal can reduce peeling and roughness at the edges. Lastly, ISSI sells a basecoat to use with PSP. This basecoat improves adhesive properties and is therefore expected to lower delamination. In addition, the basecoat increases luminosity by adding a white underground, which reflecting emissions of the paint away from the surface.

6.4.5. Rash Pattern

Due to faulty painting all images show a rash-like pattern in the pressure. This pattern introduces significant noise (up to ±7% of the local pressure) in the surface pressure plots, making it difficult to extract pressure levels from a line of pixels. However, when calculating the circumferential mean the amount of noise introduced by the pattern is reduced (up to ±0.7% of the pressure trend). The main characteristic of this pattern is that it changes over time. When taking ratios of reference images, the pattern is always different between two experiments. An example is shown in Figure 6.18 for the intensity ratio between the reference after and the reference before of a $M = 0.7$, $\alpha = 0°$ and a $M = 0.75$, $\alpha = 0°$ test case on the model 11.

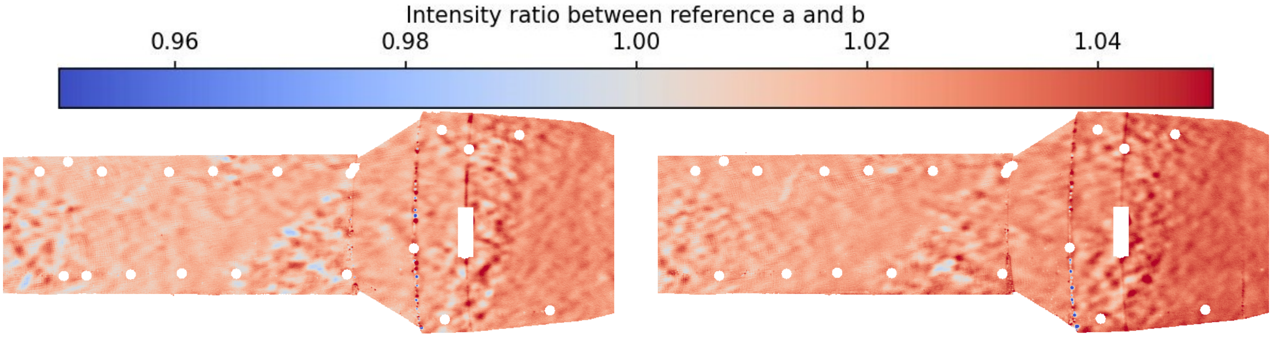

(a) $M = 0.7$, $\alpha = 0°$.

(b) $M = 0.75$, $\alpha = 0°$.

Figure 6.18: Ratio between reference images for two Model 11 experiments to highlight the changing rash pattern. It can be seen that while the distribution is similar, the position of a lot of the blobs has changed.

The pattern was found to be caused by improper model painting. A change of painting strategies for the Vega-E model resulted in a reduced rash pattern over the model. In the new strategy, more paint layers were sprayed on the model than instructed by ISSI[6]. Each layer used less paint resulting in an equal thickness coat. However, some patterns can still be found in the Vega-E model, mostly downstream of the second protuberance ring (see Figure 8.6). Further improvement of the painting is required to avoid this.

6.4.6. Image Alignment

To quantify the alignment uncertainty, two different approaches were used. The first approach, denoted as "rms measurement misalignment", was to compute the rms misalignment of fiducial marks after the image is transformed. This was calculated between the reference to which the measurement images are aligned and all the measurement frames. The second approach, denoted as "rms exlcusion misalignment" is described in Subsection 4.2.3. For this, the reference before and reference after images were aligned with each other multiple times. Each time, one of the fiducial marks in the image was excluded from the alignment. The rms mismatch of the excluded fiducial mark for each alignment was then computed. The results, along with the rms model displacement during measurements are shown in Table 6.3.

Experiment	**Configuration**	**Rms model movement**	**Rms measurement misalignment**	**Rms exclusion misalignment**
CN 6	$M = 0.75, \alpha = 0$	(0.43,1.20)	(0.12,0.18)	(0.26,0.30)
CN 7	$M = 0.8, \alpha = 4$	(0.57,1.41)	(0.17,0.08)	(0.17,0.52)
ESA 8-1	$M = 0.75, \alpha = 0$, clean.	(0.61,0.93)	(0.18,0.13)	(0.10,0.04)
ESA 8-2		(0.61,0.63)	(0.09,0.06)	(0.02,0.01)
ESA P11-1	$M = 0.75, \alpha = 0$, prot.	(0.62,0.93)	(0.11,0.06)	(0.04,0.03)
ESA P11-2		(0.70,0.70)	(0.16,0.08)	(0.06,0.08)
ESA P7-1	$M = 0.8, \alpha = 4$, prot.	(0.60,1.50)	(0.18,0.10)	(0.15,1.01)
ESA P7-2		(0.65,2.5)	(0.19,0.09)	(0.20,1.78)

Table 6.3: Rms model movement and misalignment of fiducial marks. The values shown are the rms (x,y) distances in pixels. Here, the "Rms model movement" is calculated using the distance between reference image and measurement image fiducial mark locations. Runs are denoted with -1 and -2. -1 indicates the first camera that focused on the PLF and -2 the second camera.

The rms misalignment for five different runs are shown, three at $\alpha = 0°$ for each of the fiducial mark sets used for the HHF measurements (see Appendix L) and two at $\alpha = 4°$. It can be seen that for both approaches, the misalignment of images is extremely low for $\alpha = 0°$, below 0.3 pixels in all cases. As expected, model movement is also relatively low, with the model moving at most 1.2 pixels in either direction. In contrast, the $\alpha = 4°$ measurements have a higher model movement in the y-axis, and also higher exclusion misalignment. Values for the protuberance test are even higher due to model rotation (see Appendix J). Note these rms values also include the uncertainty in detecting the centroids of blobs.

From these it can be concluded that the alignment has a high accuracy for the rigid model movement of the HHF models. Similar levels of accuracy could have been achieved using less fiducial marks. However, Large alignment errors are still found in places where the model geometry abruptly changes, such as at the junctions between parts. At these, the intensity changes significantly between two pixels, therefore small misalignments are seen as sharp peaks in the pressure signal. Furthermore, due to image blurring, these peaks are spread out. An example can be seen in Figure 6.19 for the pressure of a $M = 0.75$, $\alpha = 0°$ and no protuberances experiment on the Vega-E. Peaks due to misalignment can be seen at the end of the first protuberance ring, and the start and end of the second ring.

Note that in Figure 6.19 a thicker "pressure bump" can be seen at $L/D = 0$. This is present in all Vega-E measurements, with a similar magnitude, unlike the alignment errors which constantly change magnitude. Furthermore, in some runs additional peaks can be seen within this "pressure bump" that is reminiscent of alignment errors. Therefore, it is expected that this, unlike the other peaks, is a flow feature of the model.

It is important to highlight that while the alignment worked well for the rigid body movement, both alignment algorithms performed poorly for out-of-plane model rotation. This took place for almost all measurements with protuberances on the Vega-E model. Due to poor model fitting, the part at and upstream of the second protuberance ring rotated during measurements. A summary of the amount of rotation for each can be found in Appendix J. Not only are the alignment algorithms not made to deal with these types of movements, but the amount of illumination of a given part changes due to the rotation. Even when aligned perfectly, this would still lead to errors.

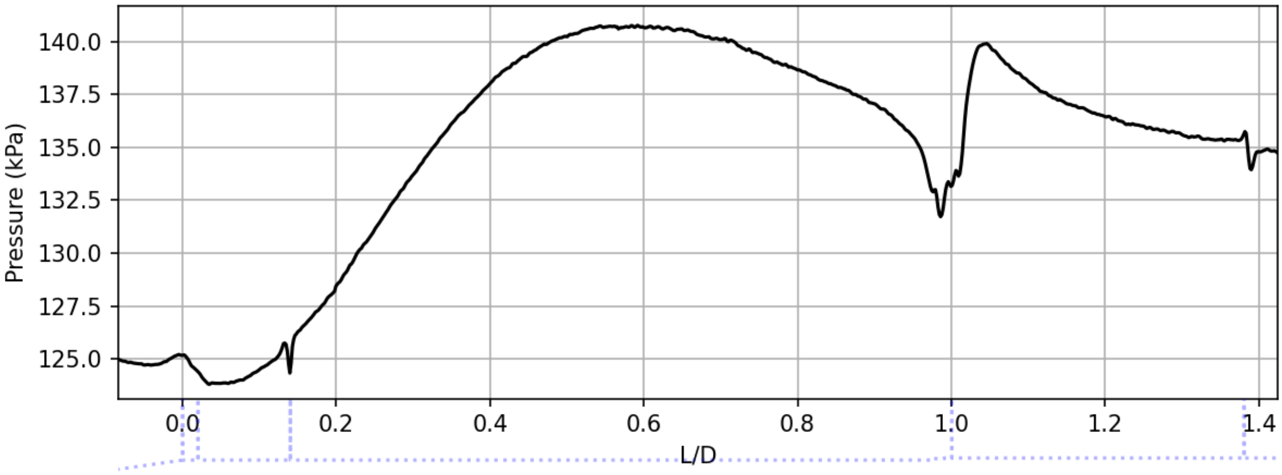

Figure 6.19: Pressure distribution of a $M = 0.75$, $\alpha = 0°$ and no protuberances experiment highlighting peaks due to small misalignments at geometry changes. Misalignments can be seen at L/D = 0.14, 0.98 to 1.01 and 1.38.

The resulting error for the worst case scenario, a measurement at M=0.8, $\alpha = 0°$ and protuberances (**ESA P8**), that had a model rotation of 4.6° during the experiment can be seen Figure 6.20. Shown here is the pressure calculated with the reference before. The reference after had slightly lower errors.

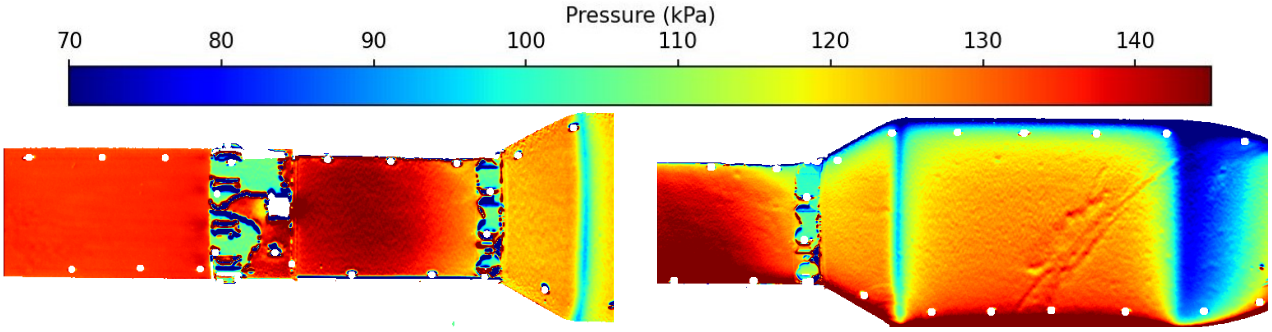

(a) Pressure of the downstream camera.

(b) Pressure of the upstream camera.

Figure 6.20: Computed Pressure for both cameras a measurement at M=0.8, $\alpha = 0°$ and protuberances. Notable is a difference in the impact of misalignment. This is due to the fact that for the downstream camera, alignment could be done using 6 fiducial marks downstream of the second protuberance ring which did not rotate. For the second camera the entire model rotated.

6.4.7. Other Error Sources

Along the aforementioned major error sources, other errors were encountered. These errors are either mitigated by the data processing, small or easy to account for. The exception is fixed pattern noise. Fixed pattern noise was found to cause a granular texture over intensity ratios. An example can be seen in Figure 6.18. By applying a blur, this was somewhat mitigated. However, the fixed pattern noise is evident in gradient plots and when extracting the mean for a given azimuthal position. To account for this noise source, a method of generating flat field corrections is required.

Other encountered error sources are listed below, along with their correction steps when applicable:

- **Self illumination:** This error source does take place, especially near the protuberance rings and the boat tail. However, at the boat tail, angles between surfaces are relatively shallow and the pressures are comparable, therefore it likely does not impact measurements much. For the protuberances a higher impact is expected, but most of the paint near the protuberances peeled away so this is not seen, as the data there can not be analysed.
- **Photodegradation:** As the model is curved, photodegradation differs significantly between points on the model. This occurs due to the fact that the amount of received luminosity per area is highly dependent on the viewing angle with the lamp. However, photodegradation rates are small, and image sets are taken in quick succession. By further combining pressure calculation using the reference before and after the measurement, photodegradation is mostly mitigated.
- **Photon Shot Noise:** As can be seen in Figure 6.5a, photon shot noise is large for individual frames of measurements. As the data is averaged over 200 images and blurred, most of the noise is cancelled. If time resolved data was of interest, this would have been a big error source.
- **Viewing angle:** Related to photon shot noise is the viewing angle. Due to the high curvature of the model, edges receive a lot less light. This causes data to become noisier closer to the edges. Data can therefore only be extracted to an azimuthal angle of about ±80° from the center of the model.
- **Lamp temporal instability:** The DLR LED array was found to require some time before the light signal is stable, roughly 10 minutes. This is likely caused by the lamp heating up. Before runs, the lamp was turned on for 10 or more minutes to let the light stabilize.
- **Salt and Pepper noise:** Dead pixels were found throughout the images. Those with a high intensity were easily removed and replaced by the intensity of the surrounding pixels during data processing. Dead pixels with low intensity were not corrected for, due to the difficulty in detecting them.
- **Errors in some reference image sets:** Unrelated to the tunnel opening error, for some measurements (**ESA 7**,**ESA P12** and **ESA P14d**), the pressure calculated with one or both of the reference image sets was different than the other or than other runs at the same configuration. The cause was not found but is likely due to the lamp instabilities when the lamp is first turned on.

6.5. PSP Implementation on the Cone Model

The Cone experiments served as a guideline on what to do and not do when measuring with PSP, due to the myriad of errors that were encountered. As aforementioned, pressure taps were used to validate the measurement approach. The main issue with the Cone was paint delamination, as shown in Figure 6.17. The delamination was caused by a lack of curing and the basecoat. A basecoat was necessary to protect the plastic model from the solvent of the paint. However, the one used was found to similarly cause delamination on a cured aluminium coupon, indicating that it is inadequate for PSP. For the future, the ISSI basecoat is recommended. In addition, model movement was relatively high, as the model could not properly be fastened without damaging the PSP. This yielded additional errors due to the uneven illumination field.

The errors resulted in extremely noisy PSP data (up to $\pm 100 kPa$). To process it in a manner that allows for comparisons with the pressure taps, the model was first dewarped using the "flattening the curve" approach (see Subsection 6.2.1) such that each line of pixels corresponds to a given L/D position along the surface. The data outliers on each line of pixels were removed using the mean and standard deviations. The process is shown in Figure 6.21 for one of the measurements.

The resulting mean pressure plots can be seen in Figure 6.22. Despite all the errors, overall good agreement is seen between PSP and pressure tap. Trends in the pressure are matched in all cases except for the run with the unstable Mach number. Results from using reference after in Figure 6.22b and Figure 6.22d originally gave the impression that everything was working, and instead something went wrong with the other two, which happened to be the first runs after closing the tunnel. Instead, errors here are cancelling out, causing the pressure to be nearly perfect. If everything was working as intended, the reference before would also have matched. Furthermore, due to the spectral leakage pressures were always going to be under-predicted. A potential cause for this accidental matching is that the thermocouple data is inaccurate.

The thermocouple was attached to the back of the model and exposed to the air. The error in the T data could have cancelled out other errors.

Measurements were taken with two different cameras to verify the adequateness of the cameras in performing PSP measurements. However, due to the high degrees of noise it was chosen to repeat this for the Model 11 experiments. There, both cameras were found to give the same results.

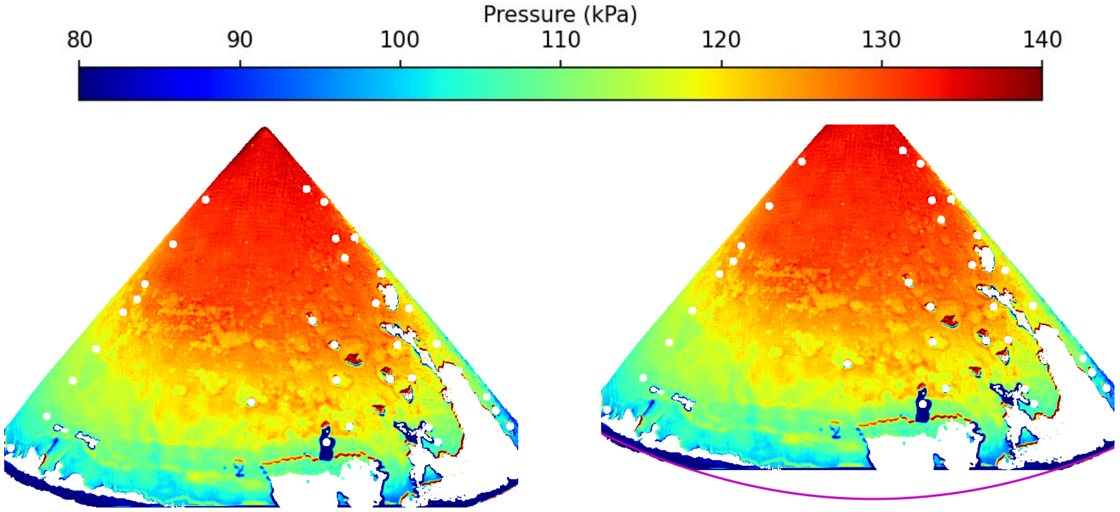

(a) Raw surface pressure plot.

(b) Curve used to flatten the surface plot, shown in purple.

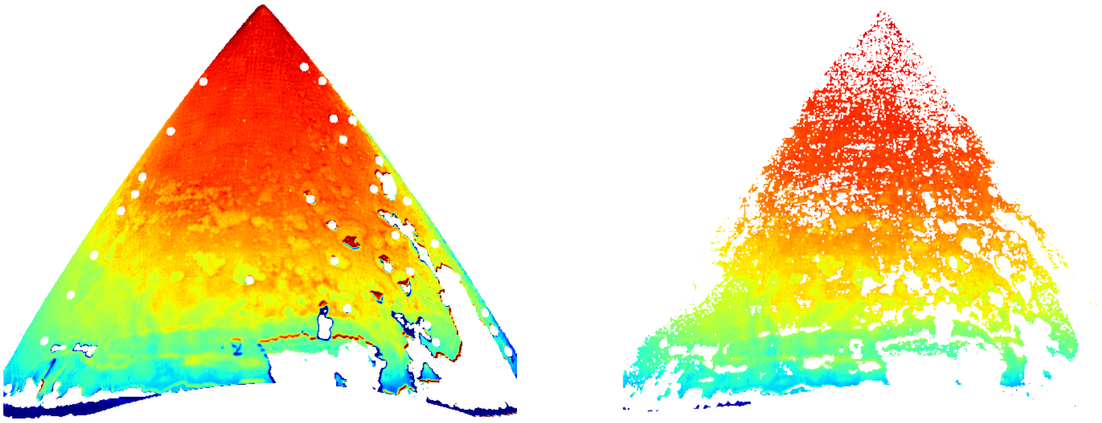

(c) Flattened surface pressure plot.

(d) Outlier Removed surface pressure plot.

Figure 6.21: Post processing of cone data. Shown here are the steps for the first cone run with an unstable Mach number (**Cone 2**, around M = 0.65). Note that due to limitations in displaying the data, the figure (d) looks a lot emptier than it is, especially near the tip. Less points are removed than suggested.

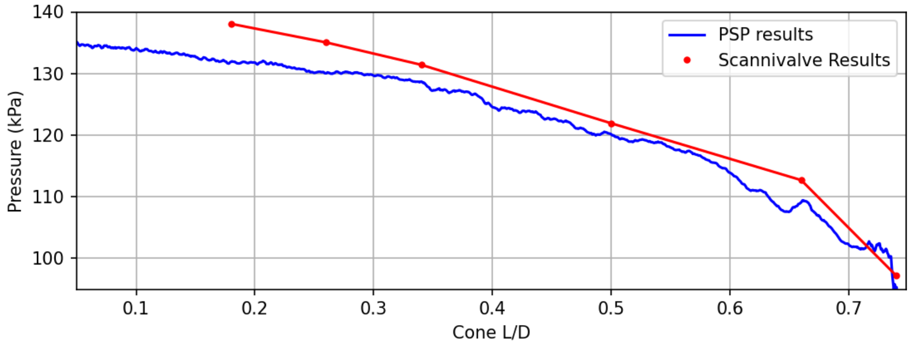

(a) Unstable Mach number (around M=0.658 and p_{tot}=1.5 bar) using the bobcat camera.

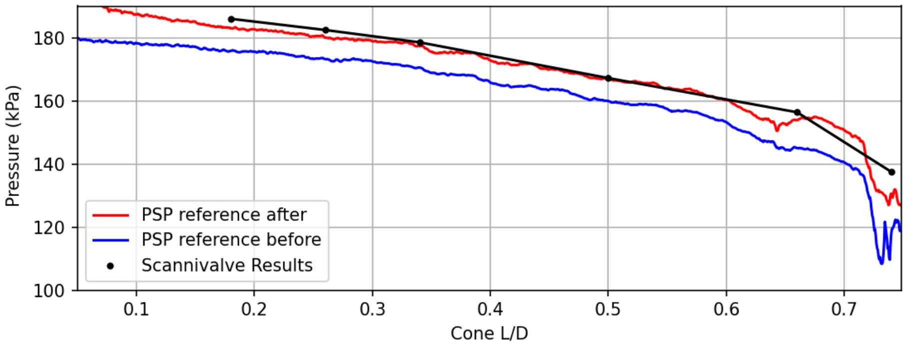

(b) M=0.6 using the bobcat camera.

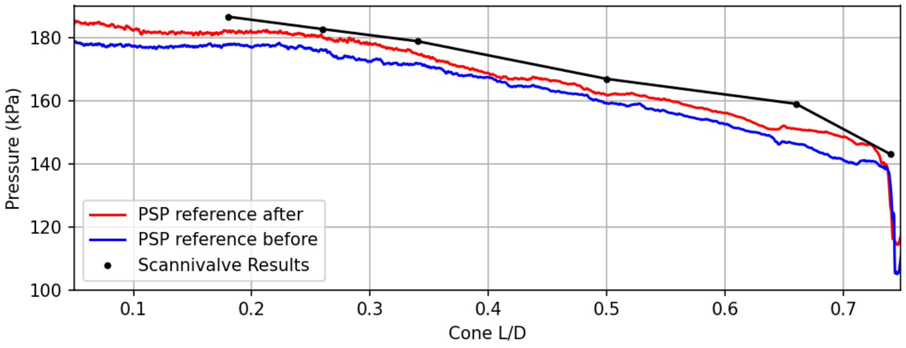

(c) M =0.6 using the sCMOS camera.

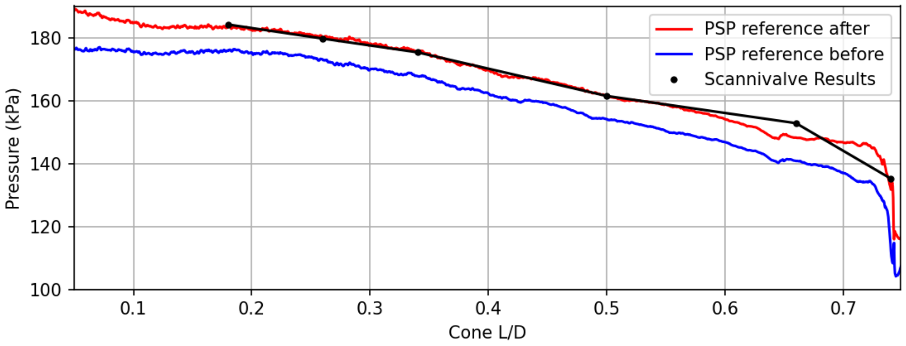

(d) M =0.65 using the sCMOS camera.

Figure 6.22: Circumferential mean pressure plots for the four cone experiments. Shown is the PSP data obtained using the reference after and the reference before. Also shown is the pressure tap data obtained with the Scannivalve.

PART III

Results and Discussion

7 Coe and Nute Model 11

In this chapter, the results and discussion on the Model 11 can be found. A detailed description of the flow phenomena on this model was previously given in Subsection 2.3.1. The focus here is on the location of flow features and the pressure distribution at the OML of the model. The first section starts off discussing the verification and validation of the PSP results. Next, an overview of the surface pressure distribution in relation to the flow features is given for M = 0.8 and $\alpha = 0°$. This is followed by a discussion on the Mach number effect for $\alpha = 0°$. The last section then discusses the effect of introducing an angle of attack.

7.1. Results Verification and Validation

Verification and validation of the obtained PSP results is done in two different ways. First, a comparison is made of the obtained PSP data with the original data from Coe and Nute [3]. This comparison allows the obtained pressure levels to be validated. Secondly, shock locations extracted from Schlieren images of the painted model were compared to images taken with an unpainted model in the TST-27. The unpainted images were taken during the MSc thesis of Romero [26] under the same freestream conditions. This comparison verifies that the paint is not significantly affecting the flow. In addition, the shock locations can be compared to those obtained with PSP.

7.1.1. Comparison with Original Data

In the original Coe and Nute study [3], measurements were taken at $M = [0.6, 0.81, 0.88, 0.95, 1.0, 1.7]$ as can be seen in Figure 2.11. Instead, the current study used $M = [0.7, 0.75, 0.8]$ so Mach numbers do not match exactly. However, Romero and D'Aguanno [18, 26] observed that for the Model 11, the freestream Mach number in the TST-27 test section is roughly 0.05 higher than the set point due to blockage effects. This observation was made by qualitatively comparing the Schlieren results obtained in the TST-27 with shadowgraphy images from Panda et al. [30]. To verify the validity of this observation, a simple solid blockage calculation was made using the 1D flow assumption. An expected blockage between 0.04 to 0.07 M was found depending on M (see Appendix F). Therefore, comparisons are made with higher Mach numbers for the Coe and Nute data. The best matches between data sets are the M = 0.75 and 0.8 cases for the PSP tests and the M = 0.81 and M = 0.88 runs by Coe and Nute. The C_P plots for these is shown in Figure 7.1a.

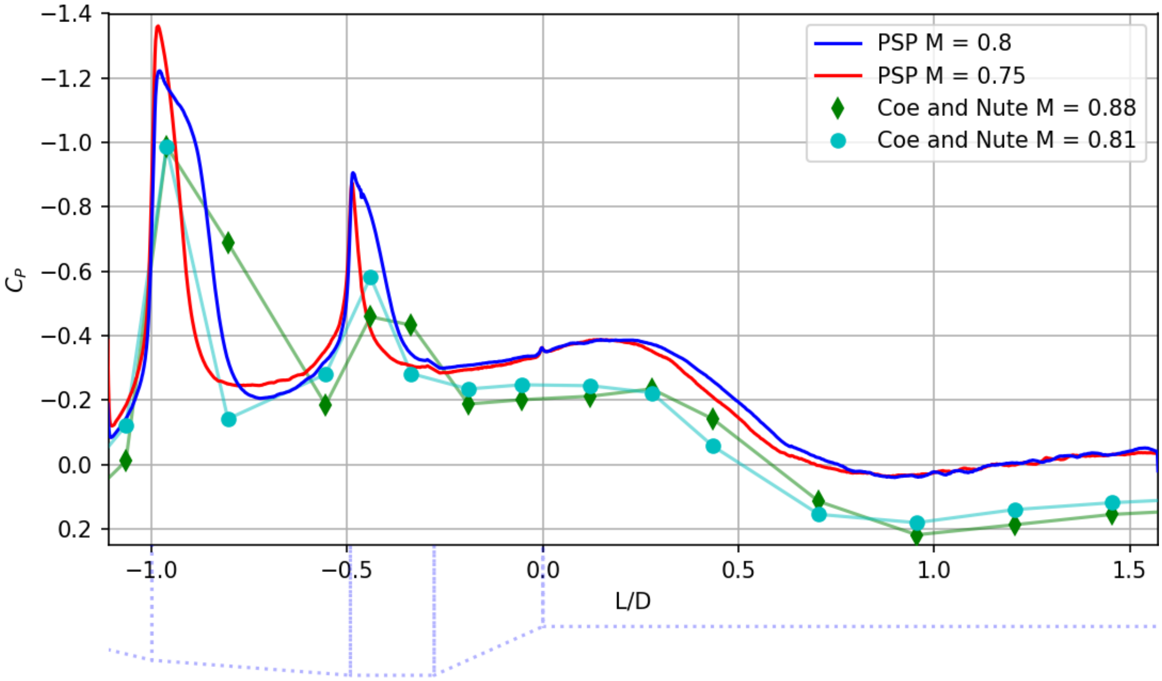

(a) C_P comparison without blockage correction.

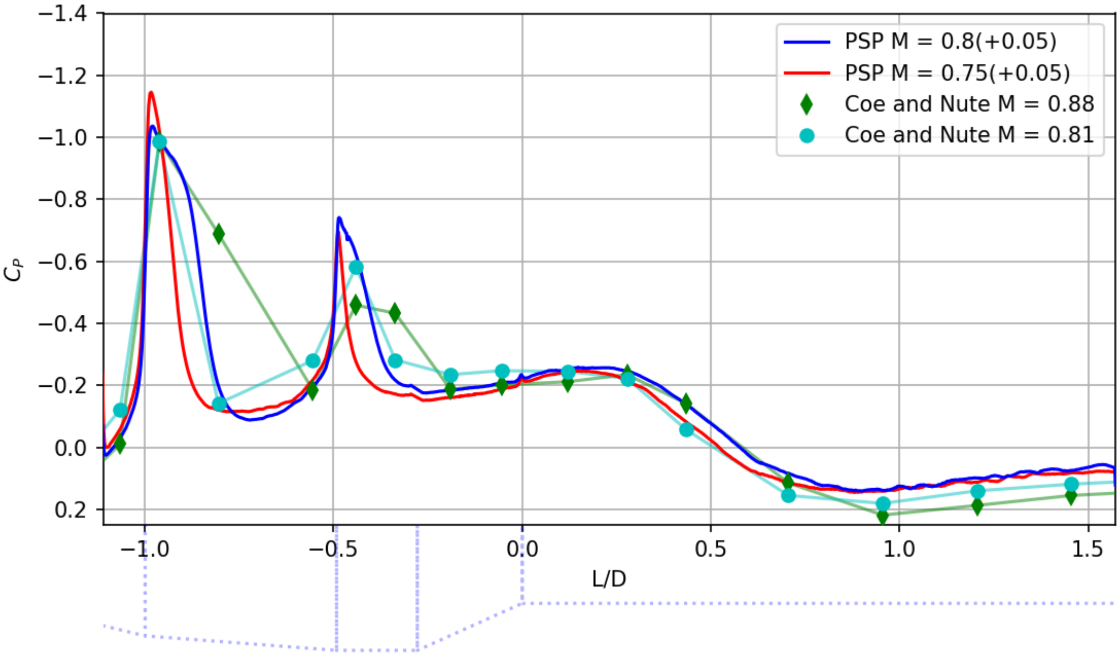

(b) C_P comparison with blockage correction.

Figure 7.1: C_P distribution for the Model 11 at different Mach numbers. In blue and red, PSP results obtained in this thesis are shown. Green and cyan show the original Coe and Nute results [2]. Plot (a) shows the uncorrected comparison, where $C_{P_{PSP}}$ was calculated with the set point Mach number. In (b), $C_{P_{PSP}}$ is calculated using the set point + 0.05 M, to account for blockage.

Here, a difference can be seen in both the magnitude and the shape of the C_P distribution. The difference in C_P magnitudes exhibits as a decrease in $C_{P_{PSP}}$ compared to the Coe and Nute results. As the C_P is calculated using the set point Mach number, a higher Mach number in the test section results in lower C_P values. Computing the C_P using the expected freestream Mach number (set point +0.05 M) results in Figure 7.1b. Here a much better match can be seen in pressure levels, with small differences in places where the shape of the distribution is the same. These differences can be attributed to measurement errors, most likely temperature and spectral leakage (see Section 6.3).

While adding +0.05M when calculating the C_P brings the PSP data closer to the original, it can be seen that the PSP and the original C_P distribution do not match perfectly. Due to the discrete nature of the original data, the extent of the mismatch is hard to quantify. Here, the first shock and the area after reattachment have an almost identical shape for both M numbers compared to the Coe and Nute data at M = 0.81. At the second shock, there is a significant mismatch between PSP and Coe and Nute data. Assuming the +0.05 M due to blockage is true, the M = 0.75 results should have matched the Coe and Nute M = 0.81 data. Furthermore, the M = 0.88 data shows a completely different distribution than the PSP results at M = 0.8.

Alongside this, there is a mismatch in the shape of the separated flow area up until $L/D \approx 0.2$. For the Coe and Nute results at both M numbers, the C_P here is more or less constant. In the PSP cases, a clear decreasing trend can be seen in C_P. The cause of both mismatches can likely be attributed to three different aspects, namely a mismatch in flow conditions (M and Re_D), temperature errors and boat-tail dewarping errors. The latter is discussed in more detail in Subsection 6.2.1. Discussion on the other two follows below.

First, there is a mismatch in M and Re_D between both datasets. As can be seen by the PSP data, small differences in Mach number significantly alter the distribution at the HHF. Even when including the expected blockage effect, none of the measurements are taken at the same Mach number. Furthermore, the blockage effect is expected to be around 0.05 based on Schlieren visualization [25], but has not been precisely computed. The assumption here is also used that the blockage is constant throughout the length of the model, when in reality it changes due to various effects. These include wake blockage and the fact that the model distance to the wall depends on L/D position and azimuthal angle, ranging anywhere from $270mm$ to $230mm$. In terms of the Reynolds number, the PSP tests were taken at a $Re_D \approx 1.5 \cdot 10^6$, whereas the original tests were taken at $Re_D \approx 3.2 \cdot 10^6$. This could account for small changes in the shape of the distribution.

Secondly, the model is expected to have an uneven temperature distribution (see Subsection 6.4.2) that changes the measured pressure distribution. As no IR measurements were taken, the exact impact of temperature on the C_P distribution is hard to gauge. However, it can partially explain the decreasing pressure at the separated flow region. Assuming a constant cooling rate at the OML would result in the PLF having a higher temperature than the LV due to thermal inertial from the larger diameter. Here, the temperature decreases when moving downstream from the boat-tail start. This would be seen as a decrease in pressure in the uncorrected PSP data. The convective transfer rate inside the separated flow region is not expected to significantly vary, thus the increase in C_P seen in this region matches the constant cooling rate assumption.

However, a net temperature difference of $10K$ would be needed during the run to cause the decrease in C_P. On the similarly shaped Vega model, differences of at most $5K$ were seen (see Appendix M). Therefore, it is unlikely that temperature errors are the sole cause for this decrease in C_P. Another contributing factor is that the discrete pressure taps may be misleading about the shape of the distribution. In the CFD study of Liu et al. [27], a small decrease in C_P can be seen in the same region of the boat tail. Furthermore, the pressure after the step decreases when moving away from the step in traditional BFS literature [33]. Therefore, in reality it is likely that there is some decrease in pressure, which may be further enhanced by PSP errors.

Given the differences in test environment, conditions, measurement methods and errors, the PSP data match the historical Coe and Nute results well. The rest of the data can thus be assumed to correctly reflect the flow distribution. A proper validation would require measurements on an instrumented model (with pressure taps and thermocouples and / or IR data). Small improvements can however be made to the test set up and PSP method to obtain even better results. As the exact level of blockage is unknown, all sections used the C_P values calculated with the set point Mach number.

7.1.2. Model 11 Schlieren

Schlieren measurements of the painted model were taken at $M = 0.8$ with $\alpha = 0°$ and $\alpha = 4°$. These were used to compare the location of both shocks on the model with measurements taken on an unpainted model. Snapshots of both measurements can be seen in Figure 7.2.

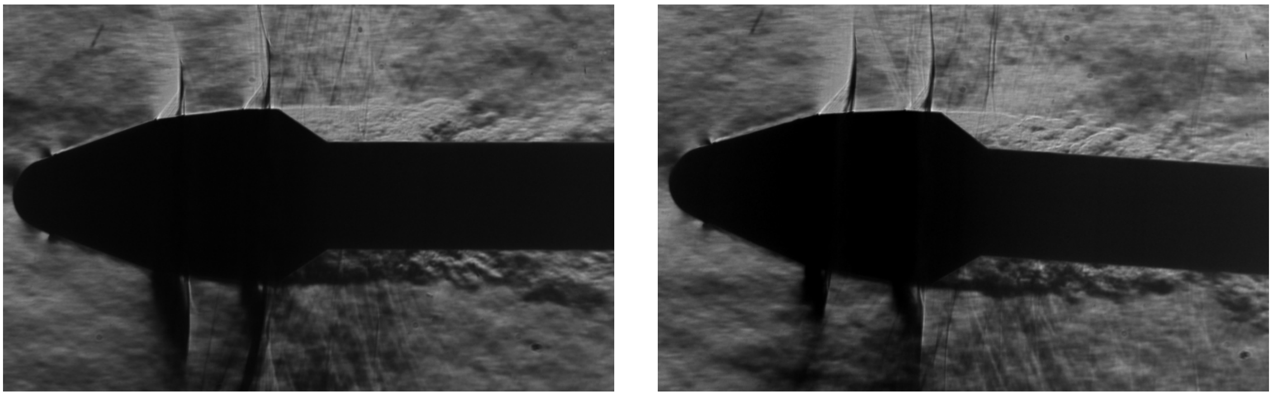

(a) $\alpha = 0°$.

(b) $\alpha = 4°$.

Figure 7.2: Schlieren snapshots of the Model 11 at $M = 0.8$ and $\alpha = [0°, 4°]$, showing more downstream shock positions.

As discussed in Chapter 2, both shocks are highly oscillatory, therefore Figure 7.2 is not representative of the mean flow. This can be seen in Figure 7.3, where other snapshots of the same $\alpha = 0°$ and $\alpha = 4°$ measurements are shown. These have a more upstream shock position.

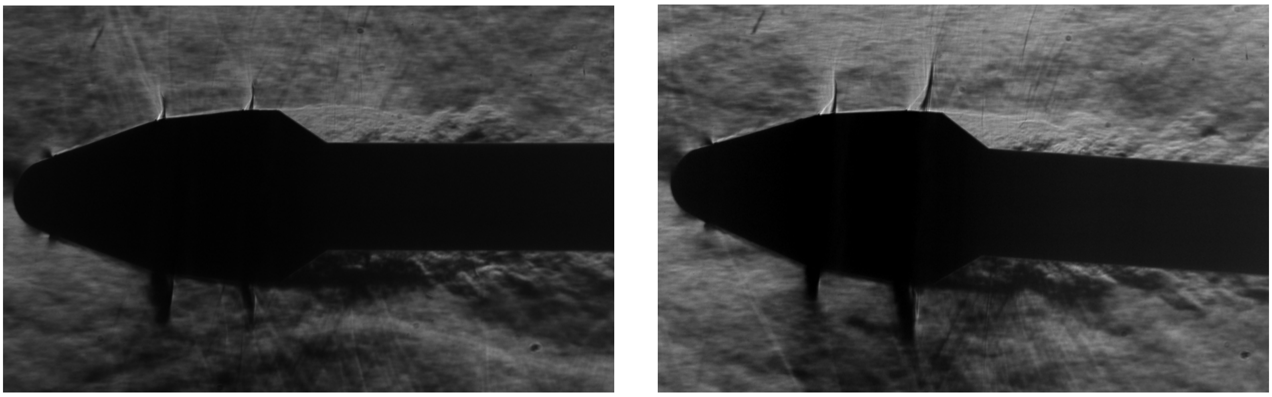
(a) $\alpha = 0°$.

(b) $\alpha = 4°$.

Figure 7.3: Schlieren snapshots of the Model 11 at $M = 0.8$ and $\alpha = [0°, 4°]$. Here more upstream shock positions can be seen.

Due to these oscillations, two approaches were used to determine the shock locations (see Subsection 5.4.3). The first approach used the standard deviation of pixel intensity (σ_I). Here, the shock is estimated to be at the point of highest standard deviation $4mm$ above the surface. Figure 7.4 shows the calculated standard deviation field for both configurations.

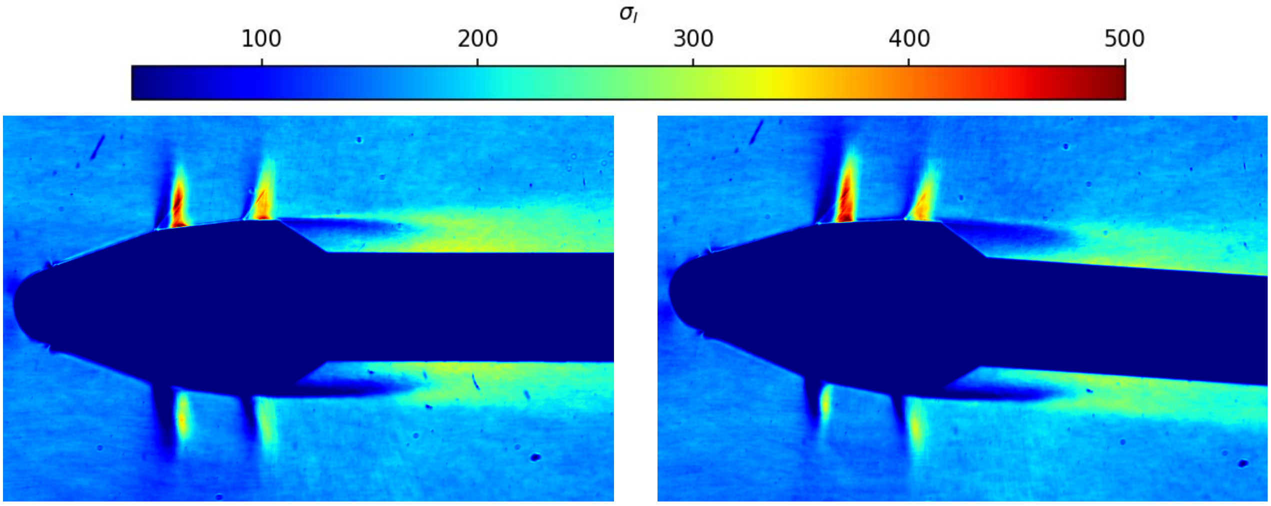

(a) $\alpha = 0°$.

(b) $\alpha = 4°$.

Figure 7.4: Standard deviation of the pixel intensity (σ_I) for Schlieren measurements of the Model 11 at $M = 0.8$ and $\alpha = [0°, 4°]$.

Alongside shock location, other information can be extracted from these. It can be seen that first shock (= the more upstream one) on top appears to oscillate more for $\alpha = 4°$ compared to $\alpha = 0°$ due to an increase in width and σ_I, but this can also be due to the integrated three-dimensional density field. The second shock does not differ much. A clear asymmetry can be seen in the location of the first shock for $\alpha = 4°$. On the windward side this is found more upstream than the leeward side, as expected from literature.

The second approach instead takes the most upstream and most downstream shock position. The mean location is then assumed to be the center between the extremes. Again, the position is estimated using a line of pixels $4mm$ above the surface. Obtained shock locations using both approaches are shown in Table 7.1. Included are also the locations obtained by Romero [25], who used the second approach. Note that no locations were detected for the 4° windward shocks using this approach, due to difficulties in detecting exact shock location at the bottom of Schlieren images.

α	Shock 1 location (L/D)			Shock 2 location (L/D)		
	PSP-1	**PSP-2**	**Romero**	**PSP-1**	**PSP-2**	**Romero**
0°	-0.88	-0.87 ± 0.06	-0.89 ± 0.10	-0.37	-0.38 ± 0.07	-0.42 ± 0.11
4° leeward	-0.83	-0.84 ± 0.07	-0.83 ± 0.11	-0.39	-0.39 ± 0.06	-0.37 ± 0.10
4° windward	-0.86	-	-	-0.35	-	-

Table 7.1: Location of flow features detected with Schlieren for M = 0.8 and $\alpha = 0°, 4°$ on the Model 11. Here PSP-1 denotes the locations obtained using the σ_I field and PSP-2 the locations using the most downstream and upstream shock locations. Schlieren data taken from the MSc thesis of Romero is also shown [25].

Notable is that the detected oscillation range in the Schlieren with PSP is smaller than the one observed by Romero. The most probable cause is the fact that measurements taken in this thesis used $16fps$, with a total of 600 images taken. Shock locations were mostly found to be within a small range ($\pm0.04L/D$) with some outliers being more up- or downstream. Instead, Romero took 5457 images at $5000fps$. It is therefore likely that the full range of oscillation was not captured in the PSP measurements, whereas Romero captured the less likely to occur outliers. However, for all measurements, the range of oscillations detected in this thesis falls within the range of Romero. This indicates that the shocks are unaffected by the paint.

The first shock was found to have a similar mean location in both methods and between investigations, around a L/D = -0.88 for $\alpha = 0°$ and L/D = -0.83 for the leeward side of $\alpha = 0.4°$. The same holds for the 4° leeward shock, which was detected at L/D = -0.39 with both PSP approaches and at L/D = -0.37 by Romero. However, the location of the second shock differed significantly for $\alpha = 0°$. Given that other locations match closely, the author suspects that this difference can likely be attributed to the detection of "outlier" shock positions. Overall, the differences are small enough to conclude that the shocks remain unaffected.

When comparing the σ_I fields between both studies, the locations appear to be nearly identical (see Figure 7.5). This further indicates that the paint roughness does not affect the location of flow features.

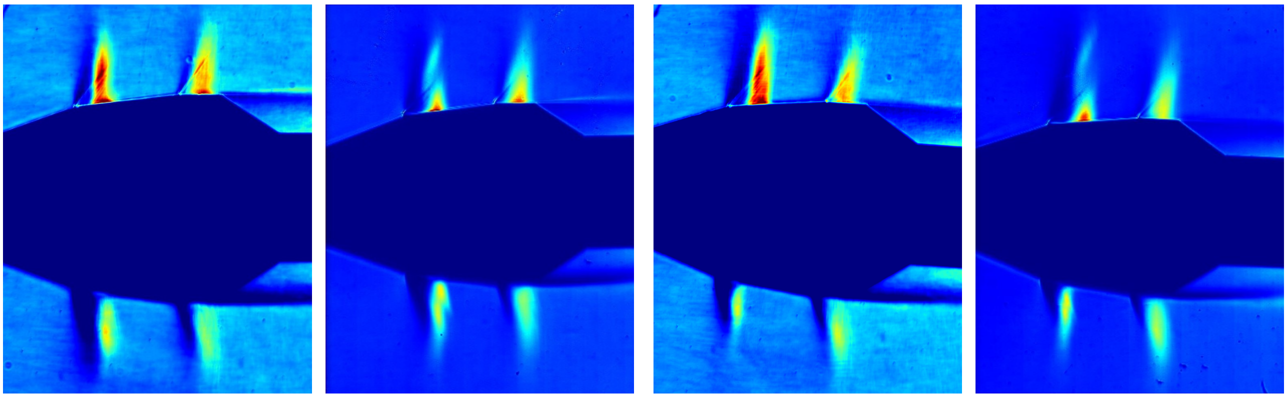
(a) PSP $\alpha = 0°$. (b) Romero $\alpha = 0°$. (c) PSP $\alpha = 4°$. (d) Romero $\alpha = 4°$.

Figure 7.5: Comparison of σ_I fields obtained in this thesis and in Romero's study [25]. In subfigures (a) and (c), the σ_I from this study can be seen, whereas (b) and (d) show the σ_I field obtained by Romero. Differences in standard deviation level occur due to the differences in exposure time and number of images used.

7.2. Surface Pressure Distribution Description

Before discussing the impact of the Mach number and angle of attack on the flow, a brief recap of the flow features discussed in Chapter 2 is given here. This is done for M =0.8, $\alpha = 0°$ to highlight how the flow features appear in the pressure distribution. The surface pressure results for this Mach number can be seen in Figure 7.6. The model was visualized between L/D = -1.11 to L/D = 1.57. As the booster stage was not present in the current model (see Subsection 5.2.4 and Figure 2.10), this FOV captures the main flow features, namely the shocks, flow separation and reattachment.

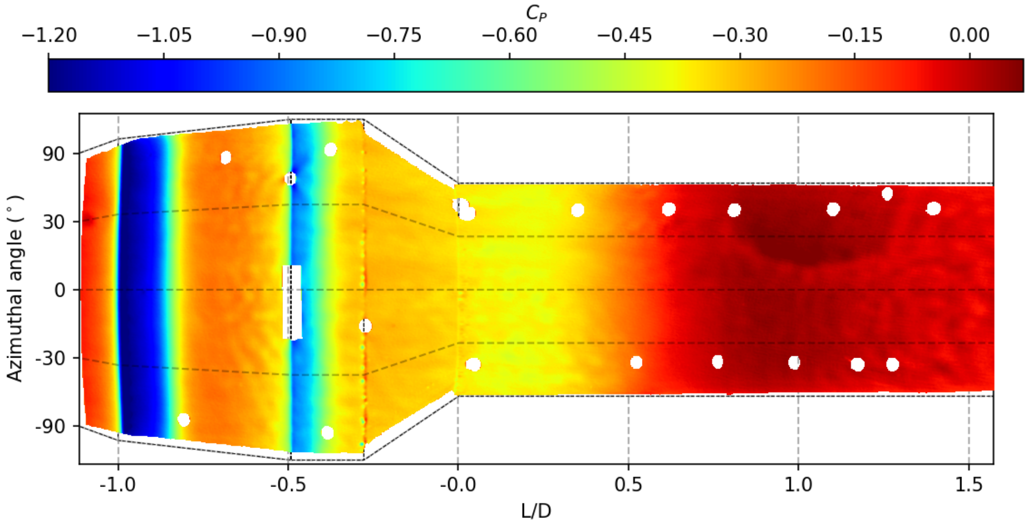

Figure 7.6: Surface C_P distribution for the Model 11 at M =0.8, $\alpha = 0°$.

Starting from the left, the measurement begins towards the end of the first cone in the biconic nosecone of the Model 11. At L/D = −1 the intersection between the first and the second cone is found. Here, a sharp geometry change leads to flow acceleration as it expands over the corner, causing a low pressure zone. This is seen in the PSP image as a sharp change from the red hue before L/D = −1 to the low pressure blue colour. In the Schlieren images (see Figure 7.3a and Figure 7.2a) expansion fans can be seen here. This expansion causes the flow to become supersonic.

The first shock wave forms downstream of the expansion, which compresses the flow to higher pressures. As the shock oscillate over an area, the shock appears as a blurred out increase in pressure over the oscillation range in the PSP images. This can be seen as the transition between blue to orange around L/D = −0.9 to −0.8. After the first shock, the pressure slowly decreases until L/D = −0.49. Here, the intersection between the second cone and the PLF can be found. Similarly to the L/D = −1, the geometry change leads to flow acceleration over the corner, causing the flow to become supersonic and ending in a shock wave further downstream. This second shock again oscillates over an area, causing a similar blurred increase in pressure. Here, smaller pressure jumps are observed due to the smaller angle in the geometry transition.

After the second shock, the pressure slowly decreases between L/D = −0.34 to = 0.26. From other measurement techniques, it is known that the flow separates at the intersection of the PLF and the boat tail, located at L/D = −0.278. This separation can not clearly be seen from the surface pressure distribution. Note that a line of high pressure can be seen in Figure 7.6, which is caused by PSP noise, and unrelated to separation. The mean reattachment location is not clearly defined due to the bubble growth and depletion events leading to a more gradual pressure increase. The increase associated with the reattachment is found between L/D = 0.26 and 0.8, after which the pressure slowly decreases until the end of the model. The mean reattachment point can then be found as discussed in Subsection 6.2.3.

7.3. Mach Number Effect

To quantify the Mach number effect on the Coe and Nute model, tests were performed at M = 0.7, 0.75 and 0.8. The surface pressure results for each Mach number can be seen in Figure 7.7, whereas Figure 7.8 shows the circumferential mean pressure. From these, the downstream shift in shock position and reattachment location with Mach number that is reported in literature is evident (see Table 7.2) [2, 8, 27].

First starting with the shocks, it can be seen that the supersonic pocket before the shocks increase in length with Mach number, related to the downstream shift of the shock position. Interestingly, before the shocks, the magnitude of the peak C_P decreases with increasing M for the first expansion at $L/D = -1$, whereas an increase in magnitude can be seen for the second expansion at $L/D = -0.49$. This indicates that the Mach number after the expansion increases more for the second expansion than for the first.

In addition, the pressure increase caused by the shocks decreases in sharpness with increasing M, signifying a bigger oscillation region for the shock. At M =0.8, both shocks show a slow increase in pressure past the peak C_P followed by a more steep increase. This can also be seen for the first shock at M = 0.75, albeit to a lower degree. This is again likely indicative of the larger oscillation range at higher Mach numbers.

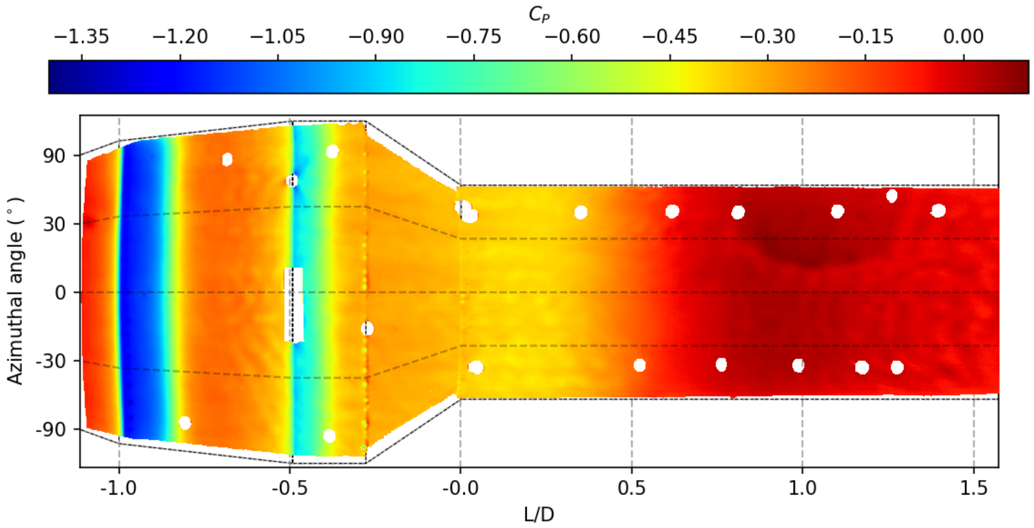

(a) $M = 0.8$ C_P plot.

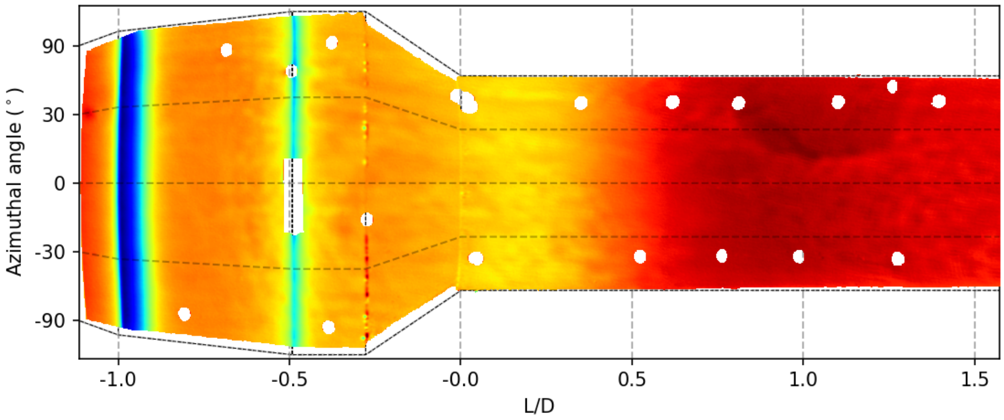

(b) $M = 0.75$ C_P plot..

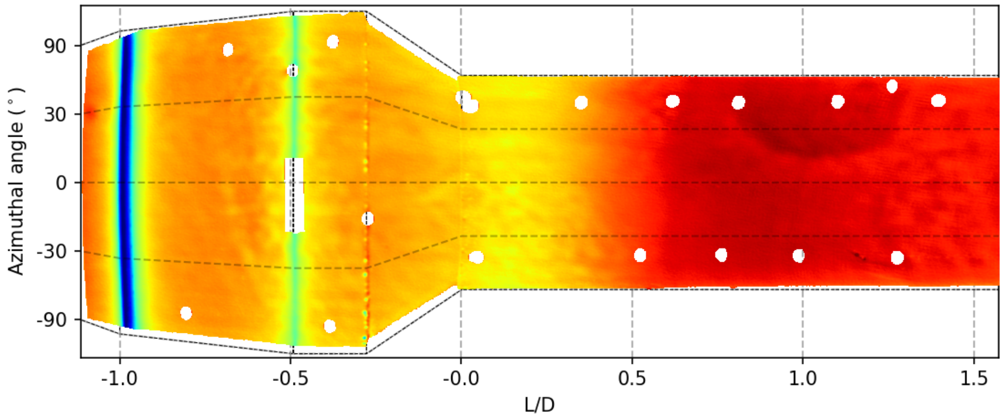

(c) $M = 0.7$ C_P plot.

Figure 7.7: Surface pressure plots of all different Mach number runs with $\alpha = 0°$. Pressure coefficient scaled between highest and lowest non-noise pressures found in all the runs.

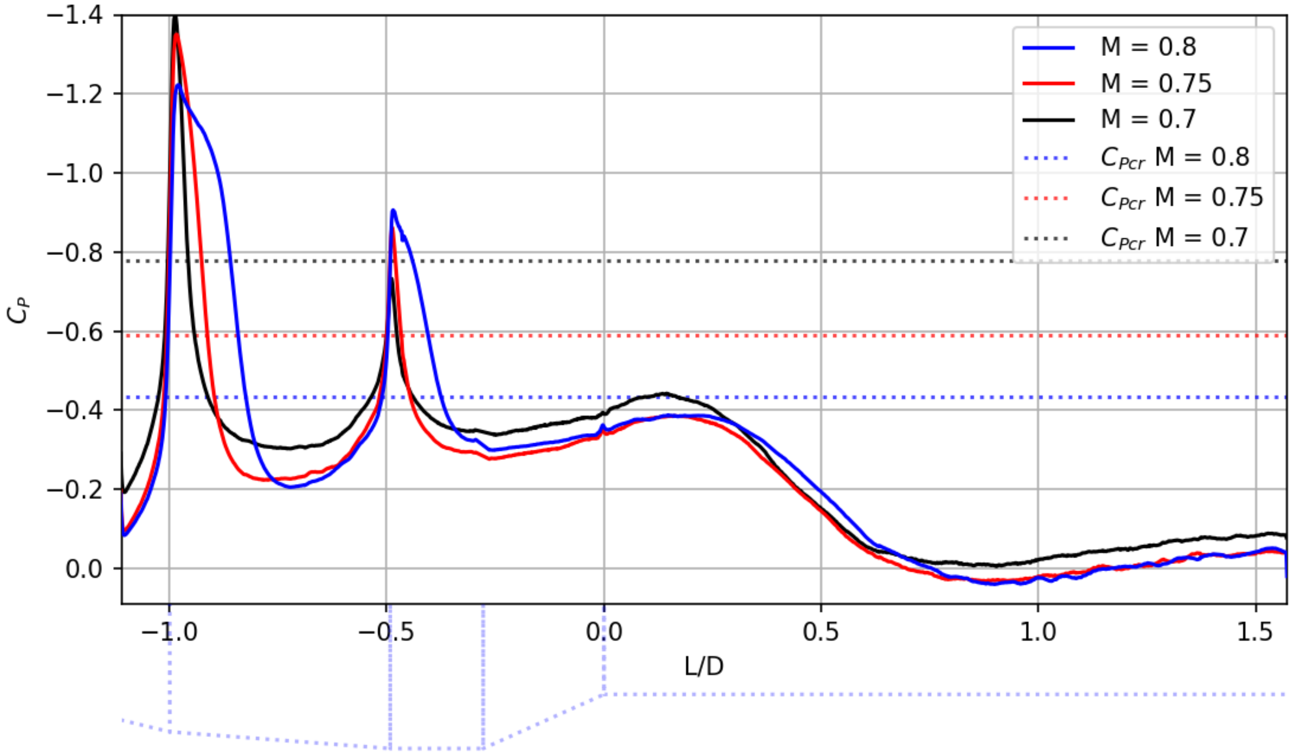

Figure 7.8: Circumferential mean C_P distribution for the Model 11 at three different mach numbers (M = [0.8,0.75,0.7]) at $\alpha = 0°$. Also shown is the critical C_P at which the flow becomes supersonic (denoted with $C_{P_{cr}}$).

For M = 0.7, the second shock was reported to be intermittent in the TST-27 by D'Aguanno et al. [18]. This is reflected in the peak C_P, as the magnitude of $C_{P_{cr}}$ for $M = 0.7$ is larger than the peak around L/D = -0.5. The Mach number at the second shock location calculated with C_P is 0.98 ± 0.1, further indicating that the shock is absent in the mean flow. Outside the main flow features, C_P levels match quite closely for the three tested configurations. This is expected from the original Coe and Nute data. Some differences are seen which are likely caused by measurement uncertainty.

From Figure 7.7 and Figure 7.8 it can be seen that the separated flow area and reattachment point is similar between Mach numbers, as the pressure distribution is almost identical. However, the M = 0.8 case can be seen to have a more downstream reattachment point, given that the pressure starts increasing more downstream. From literature, the reattachment point is expected to shift downstream with increasing M. This was indeed found, as is discussed next.

The location of the main flow features were found as described in Subsection 6.2.3 and are shown in Table 7.2. Here, a comparison is also given with Romero's values [25]. Discrepancies can be seen in the values reported with PSP compared to those obtained by PIV and Schlieren. These discrepancies are primarily caused by differences in image dewarping and feature detection point. For Schlieren and PIV the locations are detected around 0.5 cm away from the surface (= 0.1 L/D), whereas PSP sees it directly at the surface.

Mach	**Shock 1 location (L/D)**		**Shock 2 location (L/D)**		**Reattachment length (L_s/D)**	
	PSP	**Schlieren**	**PSP**	**Schlieren**	**PSP**	**PIV**
0.8	−0.848	-0.89 ± 0.10	−0.404	-0.42 ± 0.11	0.84	0.79
0.75	−0.925	-	−0.474	-	0.79	-
0.7	−0.967	-0.98 ± 0.04	−0.480	-0.49 ± 0.03	0.78	0.79

Table 7.2: Location of flow features detected with PSP for M = 0.8, 0.75 and 0.7 with $\alpha = 0°$ on the Coe and Nute Model 11. Schlieren and PIV data taken from the MSc thesis of Andrea [25]. Note that the flow separation starts at the boat tail, positioned at L/D = -0.278. Adding this value to the reattachment length yields the reattachment point.

For the shock waves, the locations detected by Romero with Schlieren were found to be more upstream than the PSP results. The biggest discrepancy can be found for $M = 0.8$. Here, the first shock was detected to be around $0.04L/D$ more downstream with PSP and the second around $0.02L/D$. At $M = 0.7$ shock locations are more upstream, but the difference between PSP and Schlieren is only around $0.01L/D$. In all cases, the detected shock location with PSP are within the oscillation range found from Schlieren.

Another potential explanation for the differences could be the difference in detection method. Romero's approach used the most upstream and most downstream shock location, and defined the mean to be in the center. This approach is more sensitive to outliers that are further away from the true mean. As the $M = 0.8$ data oscillates over a wider area, this could explain why a bigger discrepancy is found compared to $M = 0.7$. Notable, is that from the Schlieren measurements performed for the current thesis, the second shock at $M = 0.8$ is instead more upstream than what was detected with PSP. Using the σ_I approach this was found at L/D = -0.37 whereas PSP places this shock at L/D = -0.404.

Lastly, the PSP data shows a slight increase in reattachment length with Mach number, whereas the PIV data showed a constant reattachment location between M = 0.8 and 0.7. The increase in reattachment length is expected from literature and potentially highlights the effectiveness of PSP at detecting flow features. In the end, considering the error sources of all methods, the obtained values can be considered to match quite closely to the ones obtained with PIV and Schlieren.

7.4. Angle of Attack Effect

To explore the impact of α on the pressure distribution, the Model 11 was tested at M = 0.8 and $\alpha = 4°$. $\alpha = 4°$ was chosen to match Romero's [25] and past Model 11 studies [3, 4, 30]. The calculated surface C_P is shown in Figure 7.9a. Here an azimuthal angle (= ϕ) of 90° corresponds to the leeward side of the model and $\phi = -90°$ to the windward side. A clear downstream shift in the location of the first shock can be seen with increasing ϕ, as expected from literature. The second shock instead shows less three dimensionality. Here, the effect of the angle of attack is the opposite, with a small upstream movement on the leeward side. A similar effect was reported by Panda et al. [30], where upstream movement of the first shock was correlated with downstream movement of the second shock and vice versa.

In literature, the shocks are often reported to not show much variation in position with angle of attack for HHF geometries [23, 26]. While this holds true for the second shock, the first shock shows a relatively big shift. Blockage effects may have contributed to the bigger shift. On the leeward side of the model, the angle of attack effectively creates a diverging duct where the area between wind tunnel wall and model increases along the length of the model. The opposite is seen on the windward side. Locally, the test section freestream Mach number will be different on both sides due to this. At $\alpha = 0°$ the model is 240 to $230mm$ away from the top and bottom walls. The PLF on the leeward side was roughly $\sim 10mm$ closer to the wind tunnel wall during the tests, whereas the windward side $10mm$ farther away, leading to a slightly higher Mach number on the top than on the bottom.

The reattachment position seems to be more upstream on the leeward side and more downstream on the windward side. This can be seen by the fact that the pressure on the top starts increasing earlier than on the bottom. A similar pattern was seen in the CFD studies of Murman and Disoday [7, 40] on the Model 11. This change in reattachment point with azimuthal angle was also observed in the oilflow experiments of Romero, but no conclusions were drawn in her report. To obtain the positions of flow features at different azimuthal positions, C_P over L/D plots were again created. For This, strips of 20° were averaged to create the C_P plots in order to mitigate random PSP noise. These strips were centered around $\phi = [65°, 30°, 0°, -30°, -65°] \pm 10°$. A visualization of each strip is shown in Figure 7.9b and the resulting C_P plot can be found in Figure 7.10.

High levels of noise can still be seen despite the averaging over 20° due to the rash pattern. The noise was kept in the plots to highlight this. Two types of noise can be seen in the plots. The first are sharp peaks that vary in intensity (anywhere from 0.02 C_P to 0.5 C_P). The second is a wavy pattern, most notably seen downstream of L/D= -0.3. This leads to C_P variations of at most $\pm 0.05 C_P$. The latter makes determination of the reattachment position at each azimuthal location inaccurate with the approach described in Subsection 6.2.3. Despite this, higher azimuthal angles seems to have a more upstream reattachment point as seen in the CFD studies of Murman [7, 40].

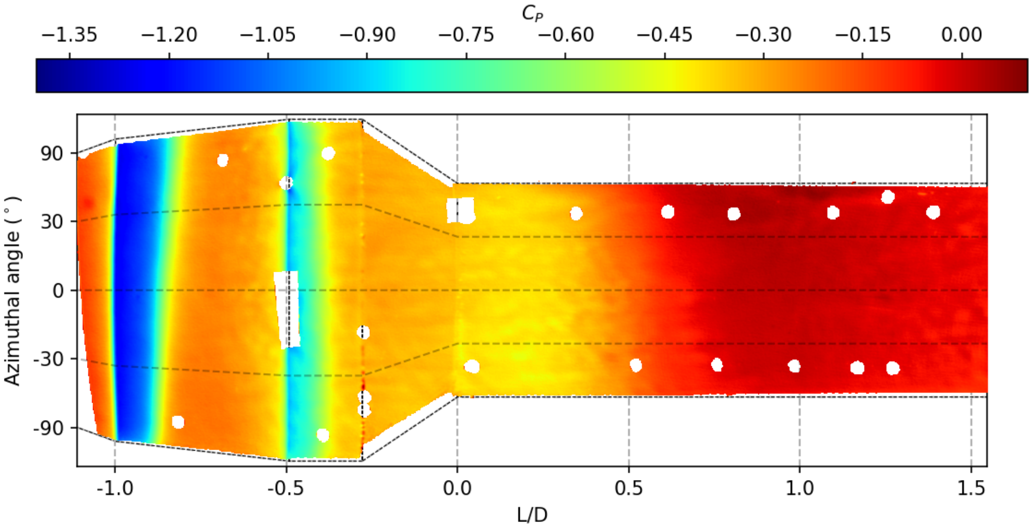

(a) C_P plot.

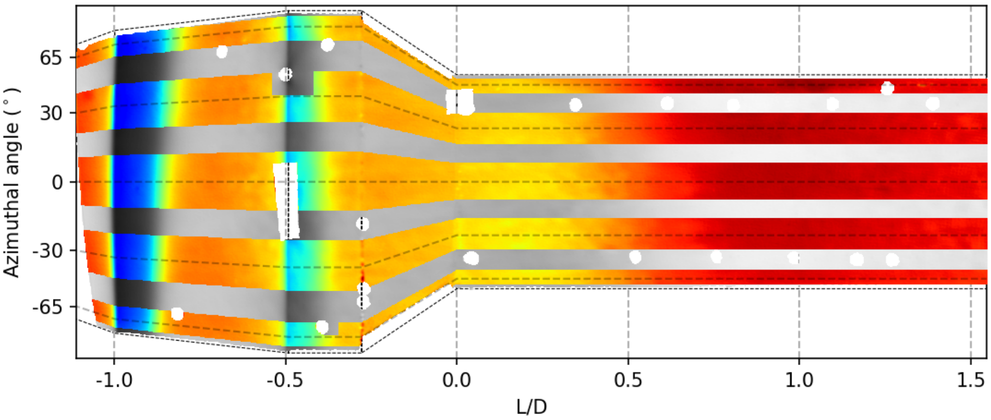

(b) Visualization of the five strips used to obtain the averaged C_P plots around $\phi = \pm 65°, \pm 30°$ and 0°.

Figure 7.9: Model 11 C_P plot for $\alpha = 4°$ at M = 0.8. In the second plot, the strips are shown that were used to create Figure 7.10.

For the separated flow region, a pattern can be seen where higher azimuthal angles have a higher C_P. This occurs mostly after the boat tail, and is likely due to the earlier reattachment. However, while there is likely a ΔC_P in the real distribution, the impact of ΔT and blockage effects are not quantified, therefore from this plot alone no conclusions can be drawn with absolute certainty about the true ΔC_P.

A more zoomed in view of the PLF can be seen in Figure 7.11, including the C_P for $\alpha = 0°$. Notable is that the distribution of the second shock is very similar to that of the $\alpha = 0°$ case for all ϕ, whereas Romero reported a much stronger second shock from PIV on the leeward side [25]. For this shock, a small decrease in C_P and slight downstream shift with increasing azimuthal angle can be seen. The first shock shows significant variations in position and peak C_P. Here, the C_P around $\phi = 0°$ closely matches the distribution for $\alpha = 0°$. Again, the C_P decreases with ϕ, which can be attributed to an increasing supersonic pocket with ϕ.

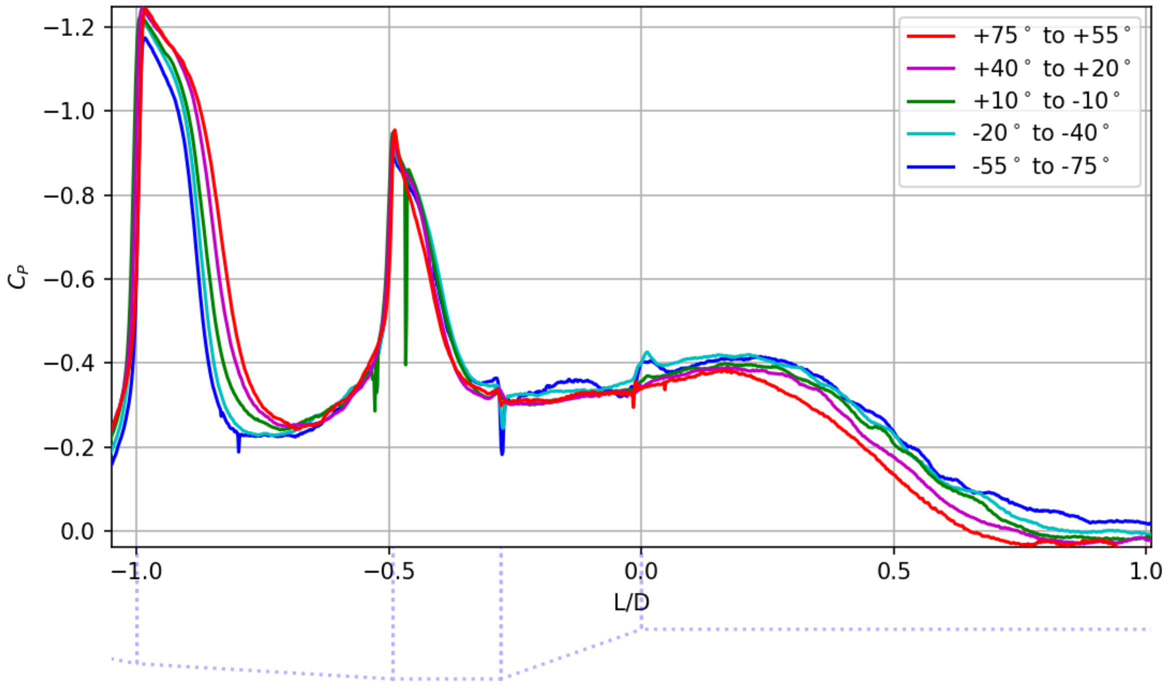

Figure 7.10: C_P distribution for different azimuthal positions on the Model 11 at $\alpha = 4°$. Shown are the C_P distributions centered around $\phi = [65°, 30°, 0°, -30°, -65°] \pm 10°$. The data here has not been corrected for PSP related noise to highlight the errors. Noise levels are higher in the area further downstream of the reattachment point, so it was chosen to exclude this from the graph.

The location of flow features for different azimuthal angles is shown in Table 7.3. Also included are the Schlieren results obtained by Romero and during this thesis [18, 25]. Due to the high noise, the PSP position of the second shock has a higher uncertainty. The first shock can be seen to vary over a range of 0.05 L/D between 65° and $-65°$. Depending on azimuthal angle, it is more up- or downstream than at $\alpha = 0°$.

Compared to the locations detected with Schlieren, the mean at 65° is more downstream, therefore at 90° it is expected to be even more downstream. The opposite pattern is seen for $-65°$, where the position was found to be more upstream than the $-90°$ result (-0.879 compared to -0.858). This pattern is in part caused by how the shock location is measured in both methods. By rotating the model in the image plane, such that the model axis is aligned with the x-axis, shocks on the top of the model appear less oblique and those on the bottom more oblique. As the shock location is determined away from the surface, the location of the top shock is more upstream than on the surface and that of the bottom shock more downstream.

Configuration	ϕ	**Shock 1 location (L/D)**	**Shock 2 location (L/D)**
PSP $\alpha = 4°$	$65 \pm 10°$	-0.826	-0.407
	$30 \pm 10°$	-0.841	-0.414
	$0 \pm 10°$	-0.859	-0.406
	$-30 \pm 10°$	-0.871	-0.396
	$-65 \pm 10°$	-0.879	-0.401
PSP $\alpha = 0°$	all	-0.848	-0.404
Schlieren $\alpha = 4°$	90°	-0.83	-0.39
	$-90°$	-0.86	-0.35
Romero $\alpha = 4°$	90°	-0.83	-0.37

Table 7.3: Mean shock locations at different azimuthal positions on the $M = 0.8, \alpha = 4°$ configuration. Included are also the locations detected with Schlieren using σ_I during this project and by Romero [17]. For comparison, the locations found in the $M = 0.8, \alpha = 0°$ experiment is also shown.

The downstream movement of the second shock with decreasing ϕ that can be seen in the surface pressure plots cannot be seen here. This is due to the highly noisy PSP data and the method used to find the shock locations (see Subsection 6.2.3). As can be seen in Figure 7.9b, at the second shock location the data is perturbed by paint errors or fiducial marks on all strips. Along with the rash pattern, the errors make the detection of the exact locations less accurate, and may therefore not be fully representative. The detected locations are more upstream than the locations found with Schlieren, unlike the $\alpha = 0°$ case. Furthermore, a clear downstream shift with ϕ can be seen from Schlieren that is not visible in the PSP data.

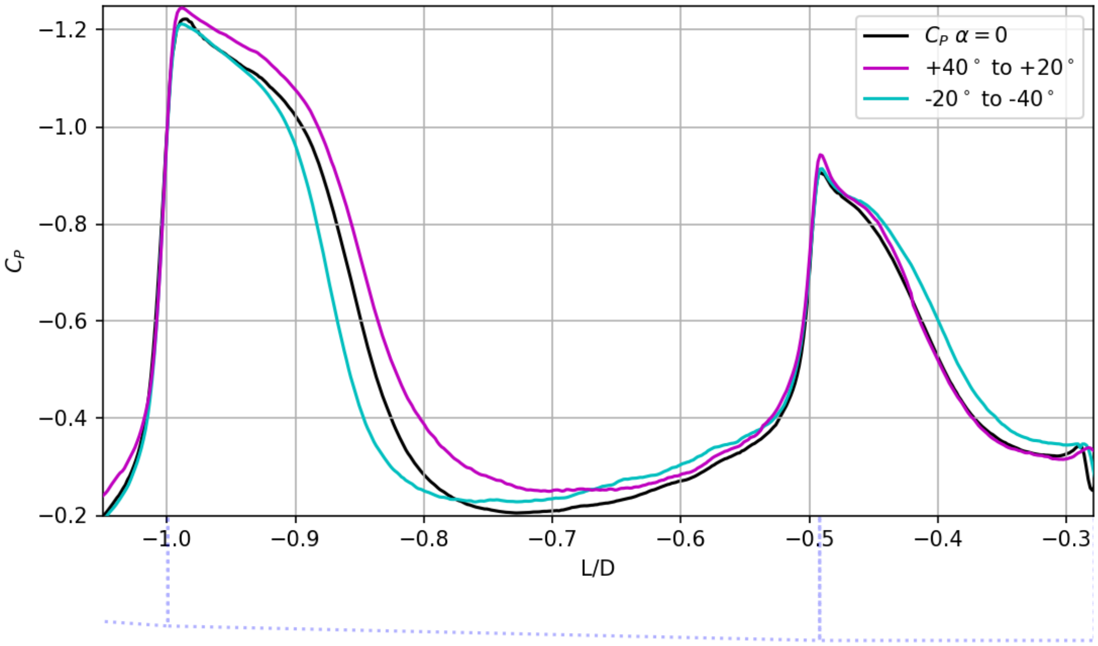

(a) $\phi = [30°, -30°] \pm 10°$.

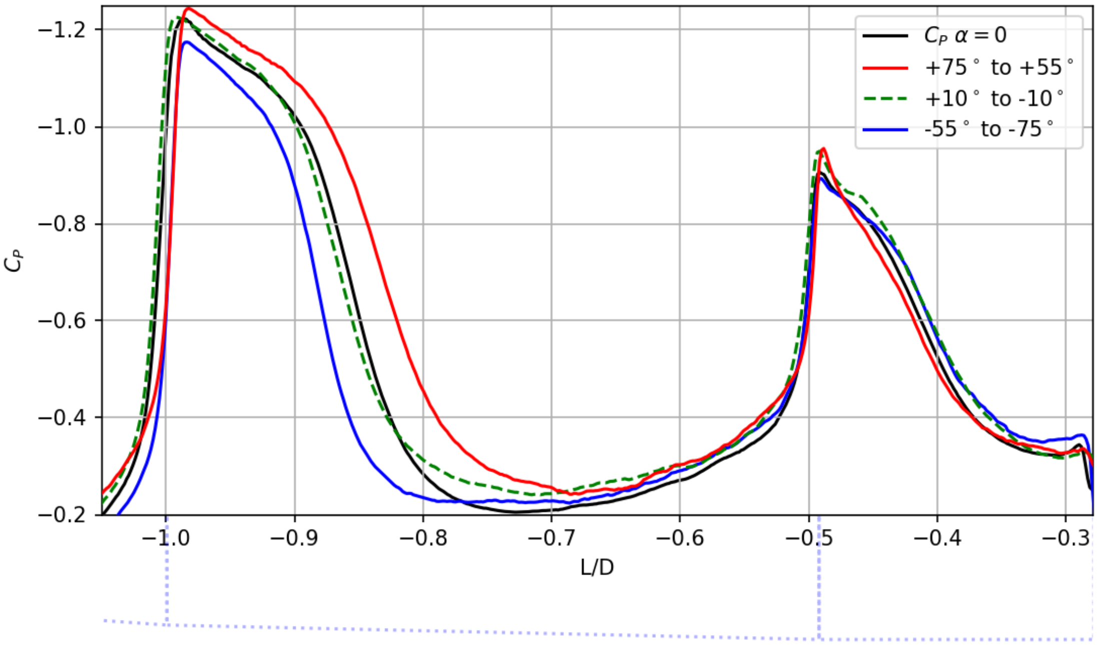

(b) $\phi = [65°, 0°, -65°] \pm 10°$.

Figure 7.11: C_P distribution for different azimuthal positions on the Model 11 at $\alpha = 4°$, highlighting the PLF. Shown are the C_P distributions centered around $\phi = [65°, 30°, 0°, -30°, -65°] \pm 10°$. In addition, the $M = 0.8, \alpha = 0°$ case is included for comparison.

8 Vega-E

In this chapter, the PSP results and discussion on the Vega-E model can be found. The first section presents a "baseline" configuration at $M = 0.8$, $\alpha = 0°$ and no protuberances. Then, the second section highlights the Mach number effect for $\alpha = 0°$ and no protuberances. The third section looks at the effect of $\alpha = 4°$ in the no-protuberance configurations. Finally, Section 8.4 analyses the impact of protuberances.

8.1. Baseline Configuration ($M = 0.8$, $\alpha = 0°$ *and no protuberances*)

The main focus of this research campaign was on the $M = 0.8$ cases. In the past, this Mach number was seen to have the biggest pressure fluctuations in different HHF configurations, as discussed in Chapter 2. Due to this, an abundance of data is available at $M = 0.8$ for similar launcher configurations. Therefore, it was chosen to define one of the $M = 0.8$ cases as a "baseline configuration", in which all flow features are described and compared with other cases. The $\alpha = 0°$ and no protuberances case was chosen as the baseline, due to their relative simplicity and as this was also used as baseline for the TUPLE research [17]. A Schlieren image from TUPLE for this configuration can be seen in Figure 2.2.

Here, data from two measurements is combined (**ESA 3** and **ESA 6**). Figure 8.1 shows the surface C_P distribution after dewarping. Figure 8.2 then shows the circumferential mean C_P, including the C_P from the pressure taps and shock locations found by D'Aguanno et al. [17]. Here, the fiducial mark position uncertainty induces some kinks upstream of the first shock in the pressure distribution. These kinks are persistent for all no protuberance runs. More details on this and the dewarping can be found in Subsection 6.2.1.

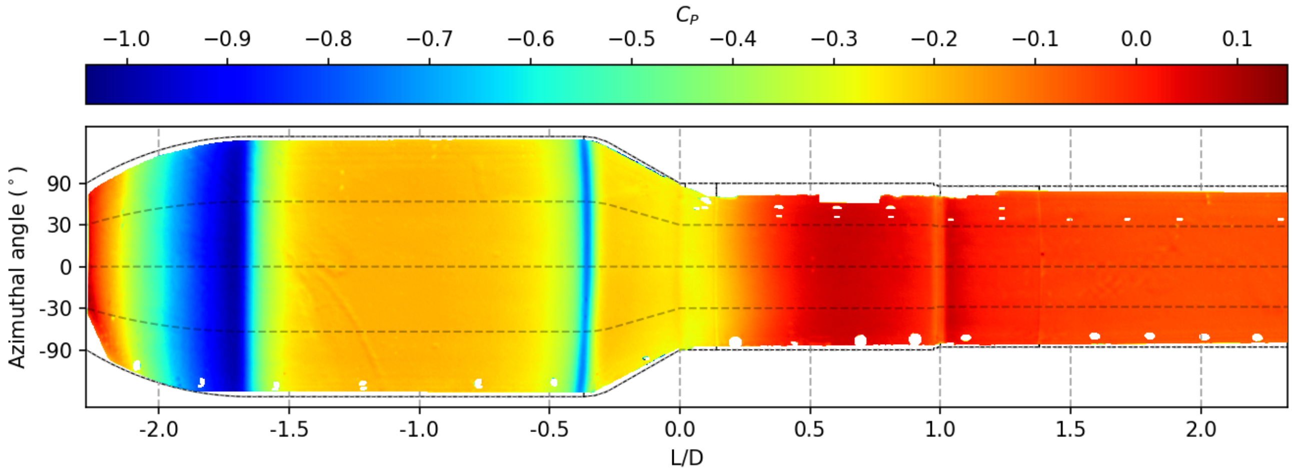

Figure 8.1: Surface C_P distribution for the baseline configuration. M =0.8, $\alpha = 0°$ and no protuberances.

In Figure 8.1 and Figure 8.2 the main flow features previously seen by D'Aguanno et al. [17] can clearly be recognized. Starting at L/D = −2.3 and moving downstream, it can be seen that the flow accelerates over the nose and the pressure decreases until L/D = −1.7. Here, the first shock is present over which the pressure shows a rapid increase. This corresponds to the location where the curvature of the nose decreases and becomes straight. Similarly to the Model 11, the shock position is not stationary but instead oscillates, causing the pressure increase to occur over a small area in the time averaged PSP results.

Beyond the first shock, the pressure is stable over the straight part of the PLF until L/D = −0.7. Here, the flow starts accelerating due to the edge of the boat tail located at L/D = −0.37. The flow expansion around this corner again leads to a supersonic pocked which ends in a second shock wave, located at L/D =−0.35. The shock causes a near instantaneous increase in pressure, indicating a smaller oscillation range than the first shock. Note that there is some apparent curvature in Figure 8.1 for the second shock due to the suboptimal dewarping procedure. In reality, this curvature is not present.

As with the Model 11, the flow separates at the boat-tail. For the Vega-E model, the assumption is made that flow separation occurs at the location of the second shock. In the separated flow, the pressure slowly decreases until about L/D = 0.07. From this point until L/D = 0.55, the pressure increases due to the oscillations of the reattachment point. The mean reattachment position can be found in this region of pressure increase, with an estimated location of L/D = 0.31 based on the method described in Subsection 6.2.3.

To study the reattachment, the Vega-E model was equipped with three high speed pressure taps between L/D = 0.22 and L/D = 0.82. No data was acquired from these in this thesis due to damaged cables, but data from the TUPLE study can be used for comparison. Mean C_P values for two pressure taps are shown in Figure 8.2, as the third one gave wrong values. A good match can be seen between the TUPLE pressure tap values and the C_P from PSP ($C_{P_{PSP}}$). The pressure taps have an uncertainty of roughly $\pm 1 kPa$ for the mean pressure. Here, a difference of $1.3 kPa$ is found with the first pressure tap, while the second one is within the pressure tap uncertainty. Given the uncertainty of the PSP data, this is a near perfect match. For other configurations, the pressure tap values are all within $1.5 kPa$ or less of the PSP values.

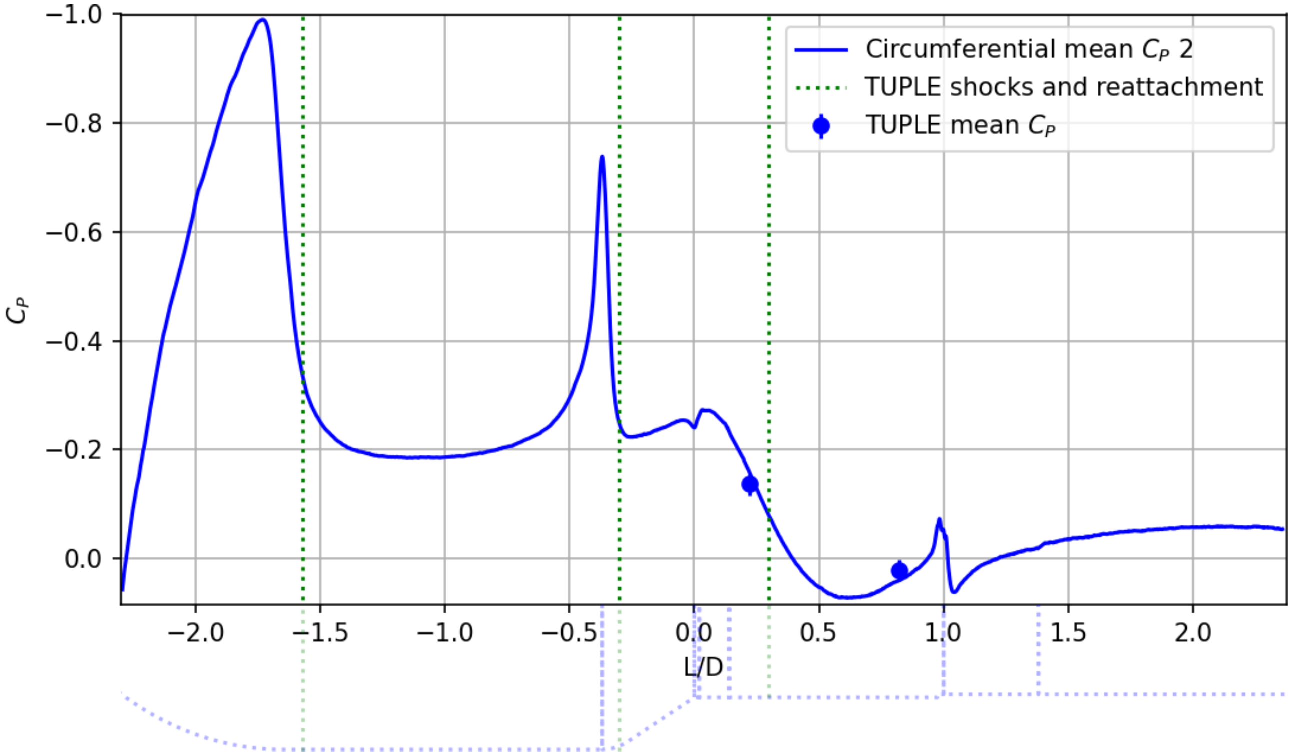

Figure 8.2: Circumferential mean C_P distribution for the baseline Vega configuration (M =0.8, $\alpha = 0°$ and no protuberances). Also shown are the locations of the shocks, the reattachment point and the mean pressure tap C_P values found in the TUPLE study [17].

Two additional features not reported by D'Aguanno et al. [17] can be recognized. First, there is a small area of pressure increase around L/D = 0. This "pressure bump" is more clearly seen in Figure 8.2. The bump was not detected in the PIV data or in previous Model 11 measurements. The exact origin of this pressure bump is unclear. A potential explanation is a re-circulation region or lack thereof. In BFS literature, there is often a primary and a secondary re-circulation region (corner eddy) after the step, as described by Chen et al. [33]. However, in BFS literature no sharp pressure increases associated with the corner eddy are reported. Furthermore, Liu et al. [27] also found this corner eddy in DDES simulations of the Model 11. Assuming the CFD simulations are accurate, the corner eddy should be present on the Model 11.

As no pressure bump was found in PSP data in the Model 11 measurements, a lack of a corner eddy might be leading to the pressure increase. In the TUPLE study [17], a region of relatively low oscillations was found near the end of the boat tail. The higher pressure might then be caused by a stagnation point of the bubble flow in that location. In the end, the geometry found at the edge of the boat tail of the Vega-E is completely different to that of a standard BFS and the Model 11, which could lead to different forces. Further investigation with other methods would be required to determine what is causing the bump. It could also be a PSP related error, but the author does not expect this (see Subsection 6.2.1). As will be shown later, the bump is present in all other configurations.

Secondly, a secondary separation and reattachment region can be seen around L/D =1. This region is caused by a $0.4mm$ step ($=H_s$) located at $L/D = 0.975$ that is similar to a BFS (denoted as "small BFS"). This small step causes a relatively large pressure gradient, with a 0.12 ΔC_P between the separated region and the reattachment. An area of flow acceleration can be seen just before the separation, starting roughly at 0.65 L/D. Downstream of the reattachment point, the pressure gradually decreases similarly to the Model 11. The geometry decrease here happens in two small steps, followed by a small gap between the protuberance ring and the upstream part of the model. In addition, the inflow conditions of this BFS are very complex. It is therefore hard to compare this specific case with general BFS literature. Due to the complexity, obtaining time resolved data in this area is key to quantify the associated forces and vibrations.

Note that some PSP related errors can be seen around this area. The flow is expected to separate at the edge of the small step, however, due to small dewarping misalignment, it seems to separate slightly upstream. Secondly, some sharp peaks can be seen at the minimum C_P due to image misalignment.

These two additional features were found to remain relatively constant for all tested configurations. They are therefore not further discussed in the following sections on the Mach number, angle of attack, and protuberance effects.

8.1.1. Mean Flow Features Investigation

Table 8.1 gives the mean position of flow features that were found with PSP, along with the locations found with PIV and Schlieren in the TUPLE research. The PSP locations were obtained as described in Subsection 6.2.3. Shocks were found to be situated at L/D = -1.67 ± 0.02 and -0.35 ± 0.02, which is more upstream than TUPLE results at L/D = -1.57 and -0.30. The detected reattachment point at L/D = 0.305 is almost identical to the one found with PIV. The offset is lower than the dewarping uncertainty of PSP (expected to be at most $\pm 0.01 L/D$ downstream of the boat tail) and can therefore be ignored.

	Shock 1	**Shock 2**	**Boat-tail**		**Small BFS**	
	(L/D)	**(L/D)**	**Reatt. (L/D)**	**Sep. (L_s/H_b)**	**Reatt. (L/D)**	**Sep. (L_s/H_s)**
PSP	-1.67	-0.35	0.305	3.61	1.022	5.9
TUPLE	-1.57	-0.30	0.30	3.33	-	-

Table 8.1: Location of mean flow features detected for the baseline configuration. Included are also the locations found in the TUPLE research [17]. Reatt. stands for the reattachment point, whereas Sep. the separation length divided by height ratio.

The differences in shock locations are too big to solely be attributed to differences in geometric calibration between Schlieren and PSP. To better understand the shock position, the C_{P_X} ($= \frac{\delta C_P}{\delta L/D}$) plot for the baseline configuration is shown in Figure 8.3. Included are also the positions that were found for the different flow features, along with the locations found in the TUPLE research. The Schlieren results would suggest a mean shock location that is far from the peak C_{P_X} compared to the PSP data.

The likely explanation for the discrepancy is the method that was used to obtain the shock locations. In the Schlieren approach, a horizontal line of pixels $\sim 1cm$ above the surface is used to determine the location of the shocks. The mean location is extracted from the point with the highest standard deviation, while PSP data looks directly at the shock position on the surface. Unlike on the Model 11, the shocks on the Vega-E are more oblique, with a clear lambda shock foot due to the SWBLI (see Figure 2.2). Due to the obliqueness and the lambda shock foot, any point measured above the surface would be more downstream than the pressure impact on the surface itself, explaining the more upstream location on average in the PSP data.

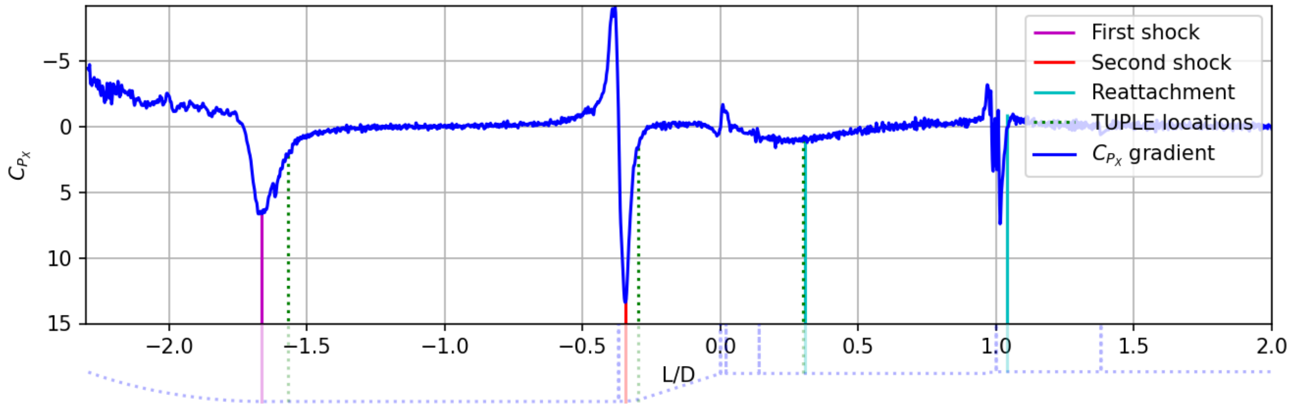

Figure 8.3: Circumferential mean C_{P_X} on the Vega-E at $M = 0.8$, $\alpha = 0°$ and no protuberances. Shown are also the locations of flow features detected with PSP. Similarly, "TUPLE locations" shows the locations of the flow features detected from Schlieren and PIV in the TUPLE study [17]. These include the first and second shocks and the boat tail reattachment.

Figure 8.4a gives a closer look into the reattachment point. Here some curvature is revealed between $\phi = -30°$ and $\phi = -90°$ despite the 0° α. The likely cause is the presence of holes on the model, situated at roughly $\phi = -110°$. The holes can be seen in Figure L.1 and are used to screw a hatch on the model that allows the pressure transducers to be accessed. To account for this, the area below −15° was not included in the determination of the reattachment point. Downstream of the reattachment, the flow does not show significant curvature as can (see Figure 8.4). No impact was seen on the shock location either, in both PSP data and Schlieren [17]. Therefore, the effect of the holes are mostly localized in the separated flow.

Figure 8.4b shows the separation and reattachment associated with the small BFS at L/D = 0.975. To estimate the extent of the separated flow region, pixel distances were measured on the warped PSP image, as the small distances of this flow feature are more prone to dewarping errors. Each pixel is estimated to be $0.088mm$, with a total of 27 ± 2 pixels in the separated flow. This yields a separation length of $2.37 \pm 0.18mm$, with a reattachment point at $1.022 \pm 0.004L/D$. A ratio between step height and reattachment length equal to 5.9 ± 0.5 is found, which is consistent with values reported in BFS literature [98–100]. The ability to detect ΔC_P of this small flow feature highlights the effectiveness of PSP as a virtual pressure sensors.

8.1.2. Comparison with Model 11

Lastly, a comparison between the Model 11 and the Vega-E baseline can be found in Figure 8.5 for M=0.8 and $\alpha = 0°$. It can be seen that both shocks on the Model 11 are stronger given the larger pressure jump. This likely occurs due to the more abrupt geometry changes. Furthermore, the separated zone on the Model 11 is larger, with a net lower pressure and larger range of oscillations of the reattachment point. The latter can be inferred from the larger area of pressure increase for the Model 11 in the separated flow region. Interestingly, past the small BFS, the pressure of the Model 11 and Vega-E overlap. This indicates a reduced impact of the separation bubble on the mean flow.

While θ is slightly different between the Model 11 and Vega-E (34° and 30° respectively), this is not expected to cause the difference in separation, as a θ between 30° and 90° has been reported to show similar separation behaviour [6, 13, 21]. The differences can instead be explained by the separation type. Separation occurs at the start of the boat tail due to the geometry change on the Model 11. For the Vega-E, the geometry decrease is smoothed out, leading to the separation taking place further downstream. The separation there is assumed to be shock induced separation. While the second shock does influence the separated flow [4, 30] on the model 11, the impact is likely different to that of the Vega-E.

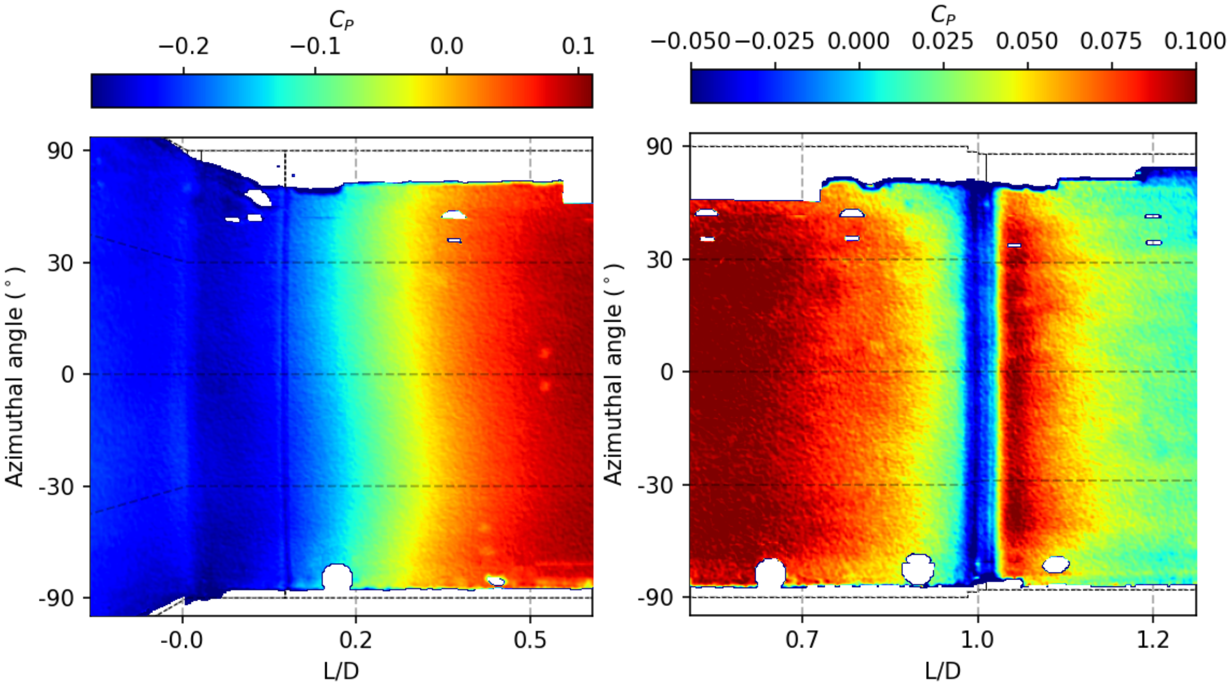

(a) Boat tail reattachment.

(b) Small BFS reattachment.

Figure 8.4: Reattachment locations highlighted using C_P plots. In image (a), the boat tail reattachment is shown, whereas image (b) shows the second reattachment from the small BFS. Here images (a) and (b) directly follow each other in L/D position.

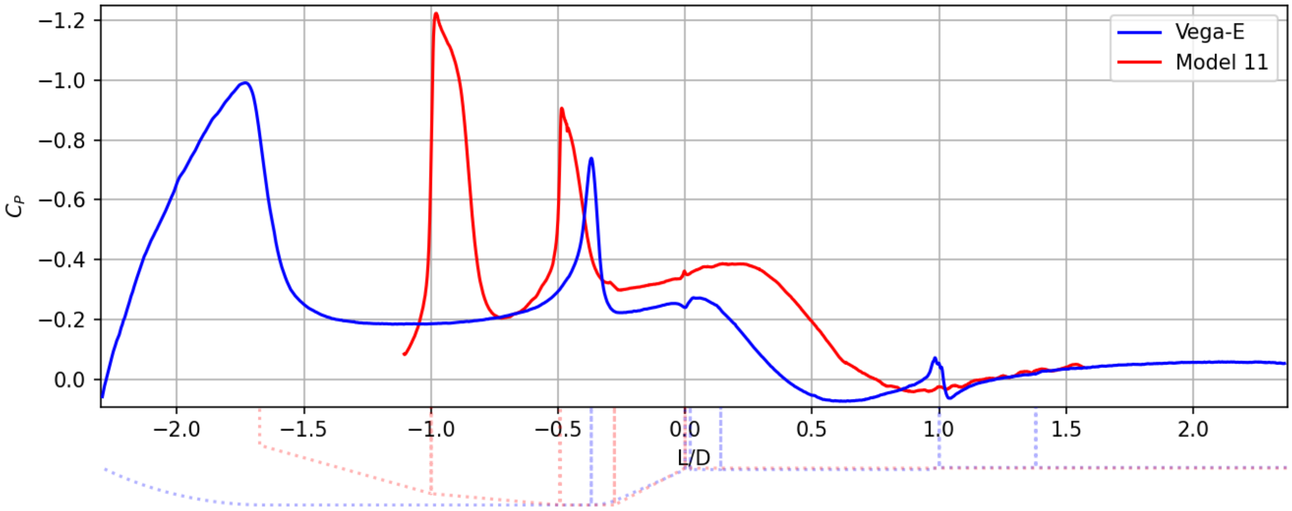

Figure 8.5: Circumferential mean C_P distribution of the Vega-E and the Model 11 $\alpha = 0°$ and no protuberances.

8.2. Mach Number Effect

To quantify the effect of the Mach number on the pressure distribution, four different Mach numbers were tested for the $\alpha = 0°$ and no protuberances configuration. Along with the baseline at M=0.8, tests were performed at M= [0.75,0.7,0.6]. The resulting contour plots for each can be seen in Figure 8.6. The circumferential mean can instead be seen in Figure 8.7. These plots were generated using runs two runs for $M = 0.8$ (**ESA 3** & **ESA 6**) and $M = 0.7$ (**ESA 2** & **ESA 4**) and one run for $M = 0.75$ (**ESA 8**) and $M = 0.6$ (**ESA 5**).

In these plots, common HHF Mach number effects can be seen. With increasing Mach number, the shocks become stronger and shift downstream, whereas the boat tail separation length increases. Outside these flow features, the C_P distribution is more or less identical for all M, as was seen on the Model 11. The changes of each flow feature with Mach number are described in more detail in the next subsections.

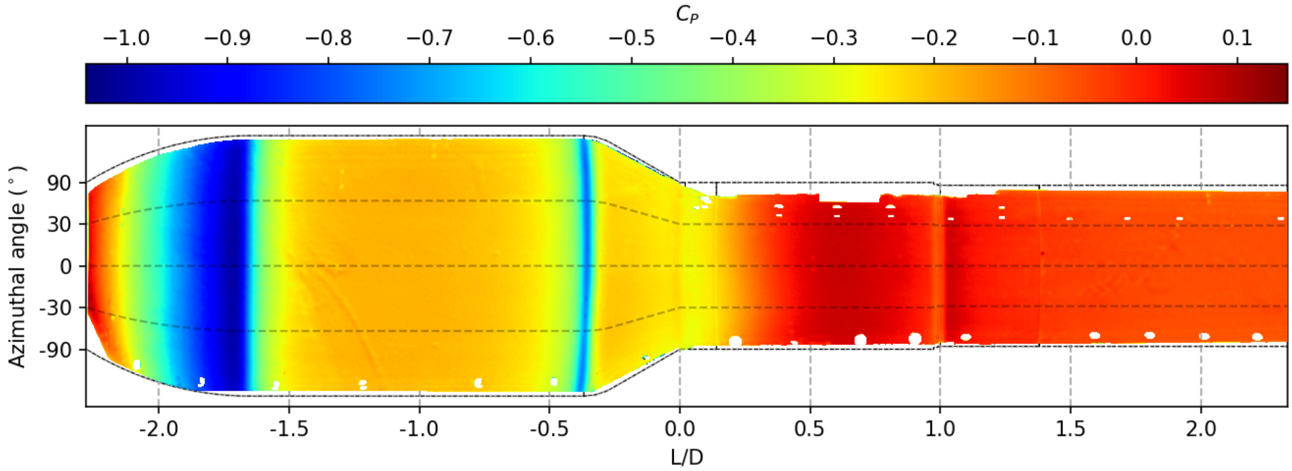

(a) M = 0.8, $\alpha = 0°$ no protuberances.

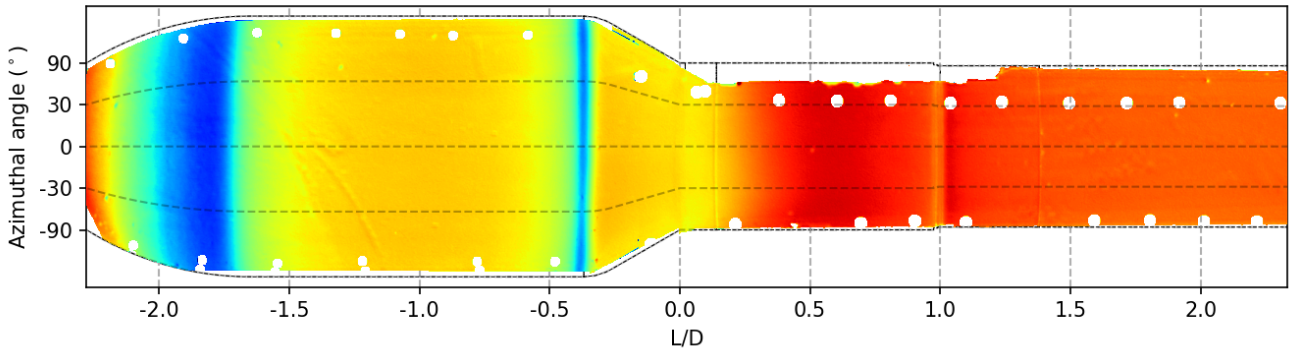

(b) M = 0.75, $\alpha = 0°$ no protuberances.

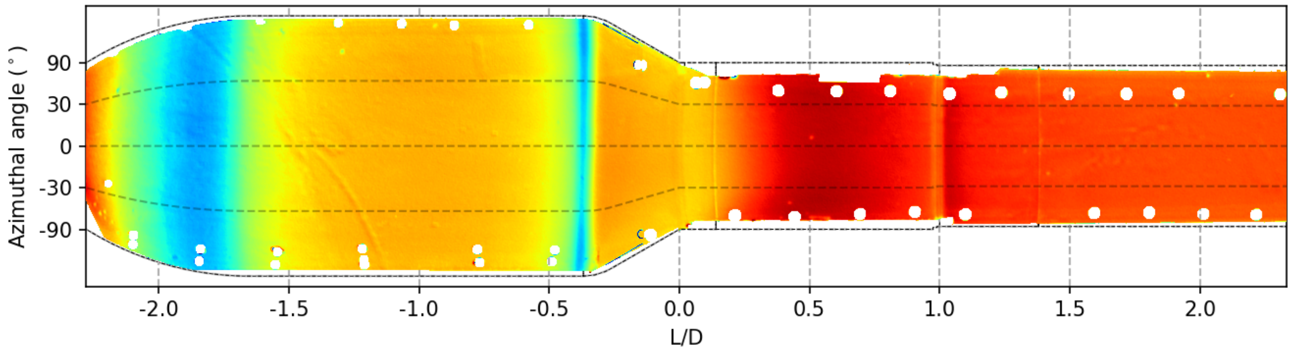

(c) M = 0.7, $\alpha = 0°$ no protuberances.

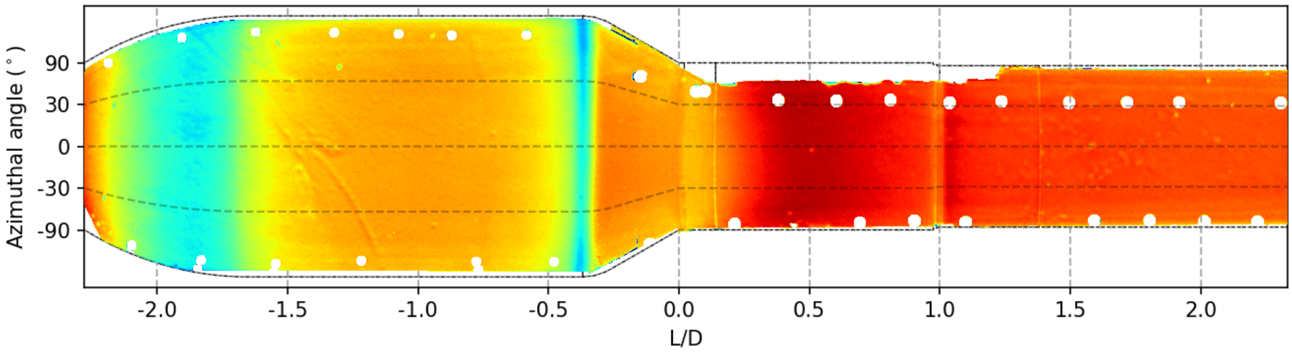

(d) M = 0.6, $\alpha = 0°$ no protuberances.

Figure 8.6: Surface C_P plots of all different Mach numbers tested with $\alpha = 0°$ and no protuberances. Pressure coefficient scaled between highest and lowest pressures found in all the experiments.

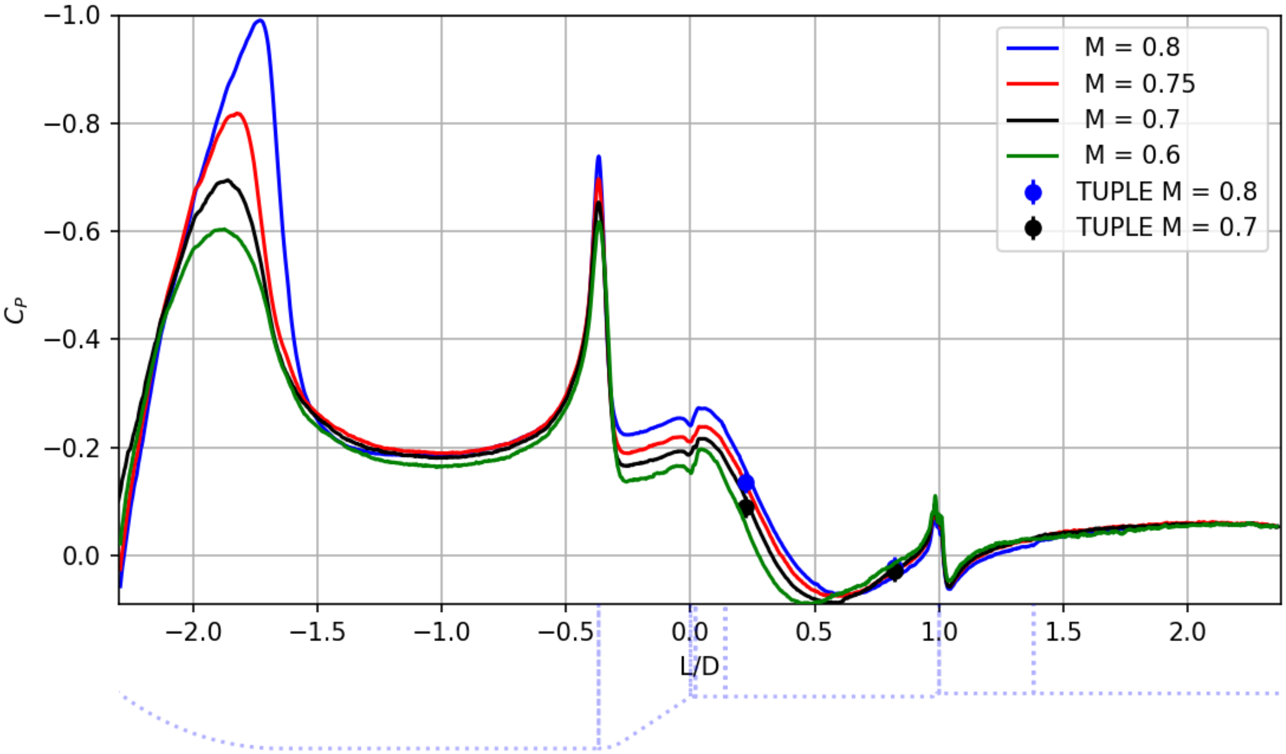

Figure 8.7: Circumferential mean C_P distribution on the Vega-E for different M numbers at $\alpha = 0°$ and no protuberances.

8.2.1. Location of Shock Waves

A zoomed-in plot of the pressure distribution along the first shock can be seen in Figure 8.8. Shown are also the $C_{P_{cr}}$ values for each Mach number, with exception of M=0.6 as this is located at $C_P = -1.3$. Here, the increase in shock strength with increasing M is evident, as sharper gradients are present. Unlike the Model 11, the magnitude of the peak C_P increases with Mach number. This indicates a stronger impact of the Mach number on the first shock, but the peak value is still lower than that of the Model 11 (see Figure 8.5).

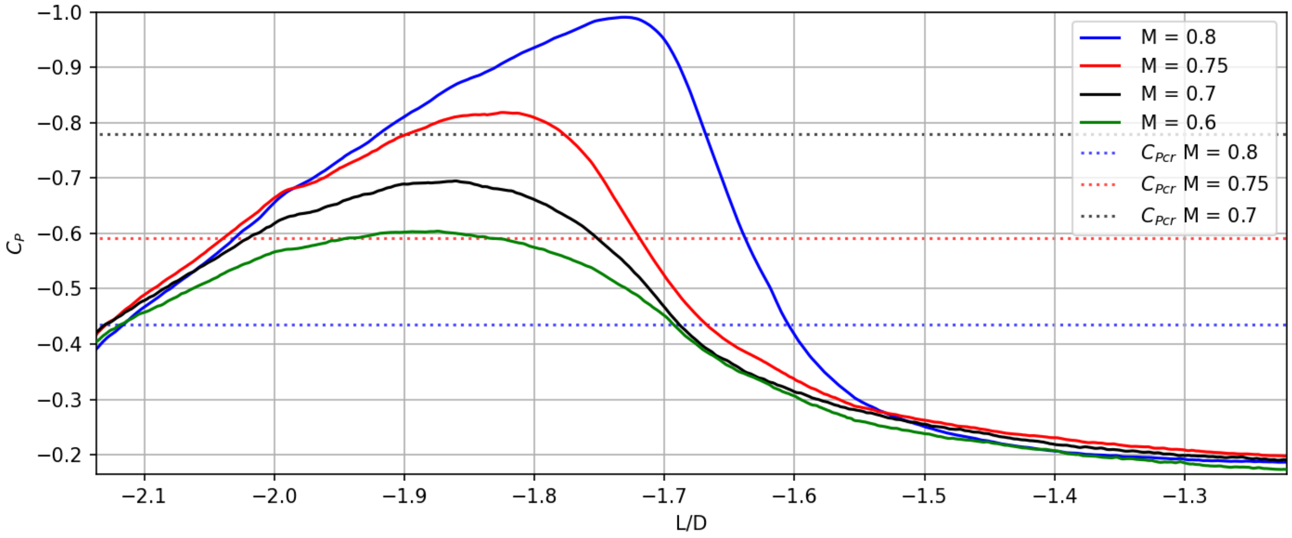

Figure 8.8: Circumferential mean C_P distribution on the Vega-E for different M numbers at $\alpha = 0°$ and no protuberances. Highlighted here is the region surrounding the first shock. Also shown is the $C_{P_{cr}}$ at which the flow becomes supersonic.

No shock is present for M =0.6, which is reflected in the smooth pressure decrease after the low pressure peak. In addition, the minimum C_P is nowhere near $C_{P_{cr}}$. Instead, for M = 0.7 an intermittent shock was observed, where the flow mostly remained subsonic. This is further affirmed by the fact that the average C_P

is lower than $C_{P_{cr}}$. Here, the C_P distribution mostly matches the shape of the distribution at M =0.6. Similarly to the second shock of the Model 11, calculating the Mach number using the C_P yields a maximum of $M = 0.97 \pm 0.01$ around the low pressure peak. Note that a sharper pressure gradient is found around -1.70 L/D that may be related to the intermittent shock.

The C_P distribution around the second shock can be seen in Figure 8.9. Similar to the Model 11, the magnitude of the low pressure peak increases slightly with increasing M, and the position shows a small downstream shift. The subsonic flow case of M =0.6 has the low pressure peak more downstream than M = 0.8, likely due to the absence of shocks. The compression after the peak is furthermore more gradual. This gives a clear distinction between the pressure distribution with and without shocks. Instead, the M=0.7 case is more complex.

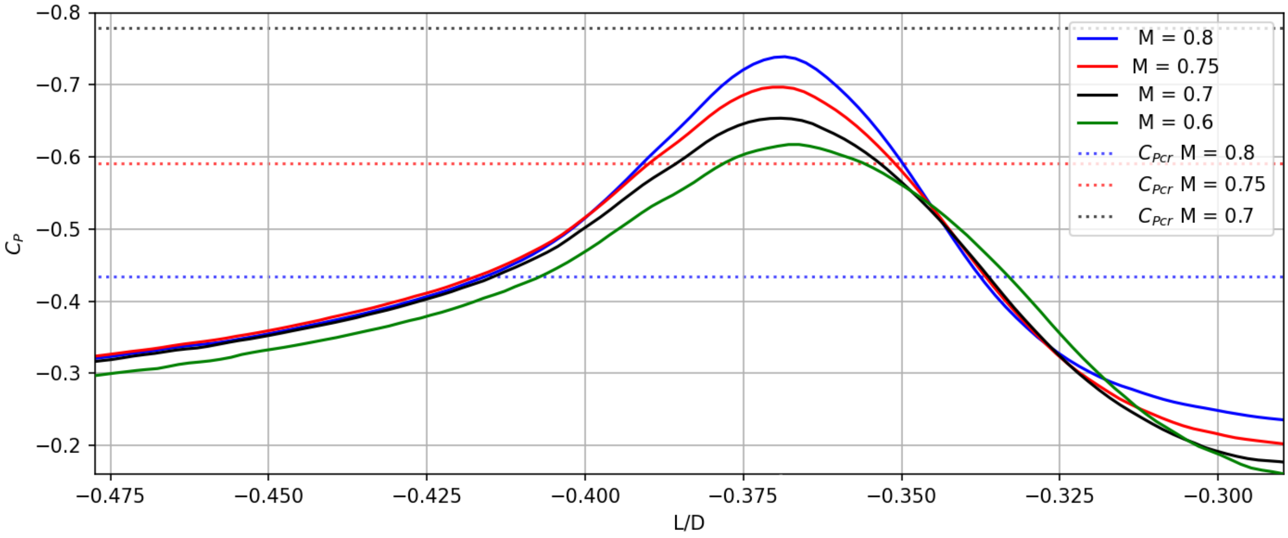

Figure 8.9: Circumferential mean C_P distribution on the Vega-E for different M numbers at $\alpha = 0°$ and no protuberances. Highlighted here is the region surrounding the second shock. Also shown is the $C_{P_{cr}}$ at which the flow becomes supersonic.

Schlieren visualization from D'Aguanno et al. [17] showed that the second shock at M = 0.7 is intermittent, which is also reflected from $C_{P_{cr}}$. Here, the Mach number calculated from C_P is equal to M = 0.95±0.01. However, when comparing the M=0.7 C_P distribution to the other ones, it is more similar to the shock cases. The compression after the peak is more steep than the fully subsonic case, with similar gradients to the shock cases. Lastly, the low pressure peak is behind the higher Mach numbers.

The location of flow features can be seen in Table 8.2. For $M = 0.75$, the first shock is again found more upstream than Schlieren, as was the case for $M = 0.8$. Here PSP found an L/D = -1.73 compared to -1.67 for Schlieren. The downstream shift with increasing M was found to be smaller in the PSP data than Schlieren. This can likely be attributed to shocks becoming more oblique with M number, but more Mach numbers would be needed to affirm this. The second shock was found to be situated at almost the same location for $M = 0.8$ and $M = 0.75$, namely at L/D = -0.345 and -0.342 respectively (rounded in Table 8.2 due to the dewarping uncertainty). This agrees with the results from Schlieren, where no shift in position was found.

Estimated intermittent shock positions are also shown for $M = 0.7$. These do not follow the upstream shift with increasing Mach number. The reason for this is uncertain. A potential explanation could be the limitations of the method, as here an attempt is made to extract mean positions of intermittent flow features from time averaged pressure data. A second potential explanation could be that the shock is only present in a more downstream position. From the Schlieren images on the Model 11 shown in Figure 7.2 and Figure 7.3, it can be seen that the shocks are larger when located more downstream. Similarly, it could be that the shocks can only exist at a more downstream point for M = 0.7.

Mach	**Shock 1 (L/D)**		**Shock 2 (L/D)**		**Boat-tail**	
	PSP	**Schlieren**	**PSP**	**Schlieren**	**Reattachment point (L/D)**	**Separation length (L_s/H_b)**
0.8	-1.67	-1.57	-0.35	-0.30	0.305	3.61
0.75	-1.73	-1.67	-0.34	-0.30	0.286	3.49
0.7	*-1.70*	-	*-0.34*	-	0.265	3.34
0.6	-	-	-	-	0.228	3.05

Table 8.2: Location of flow features from PSP for M = [0.8,0.75,0.7,0.6], $\alpha = 0°$ and no protuberances using the approach described in Subsection 6.2.3. From Schlieren visualization it is known that the M =0.7 case has intermittent shocks on the PLF. The location of these was estimated from PSP, and are shown in italics. Also shown are the shock positions found by D'Aguanno et al. [17].

8.2.2. Flow Separation and Reattachment

A zoomed-in view of the circumferential mean C_P in the separation and reattachment region is shown Figure 8.10. Here it can be seen that with increasing Mach number, the C_P inside the separated flow decreases, which can likely be attributed to the increase in separated flow length. Again, a close match can be seen between pressure tap C_P and $C_{P_{PSP}}$ values for $M = 0.7$. The differences are smaller than the M=0.8 case, likely due to lower temperature gradients, with C_P differences being lower than the pressure tap uncertainty. Further downstream, the C_P for all M numbers recovers to the same level for all configurations.

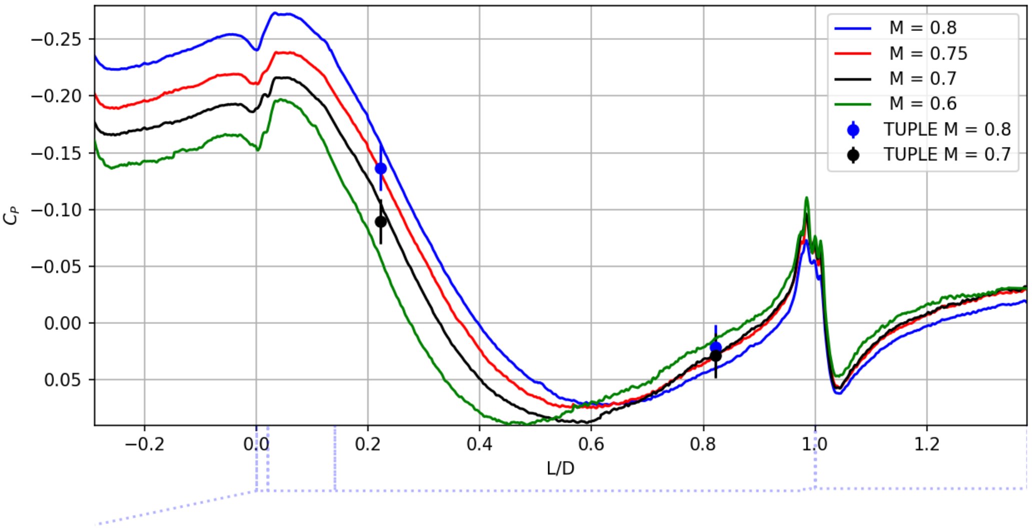

Figure 8.10: Circumferential mean C_P distribution on the Vega-E for different M numbers at $\alpha = 0°$ and no protuberances. Highlighted here is the two flow separation and reattachment regions.

The estimated location of reattachment and separation lengths are shown in Table 8.2. Note that it is difficult to infer the exact separation point from the time resolved PSP data for the cases where there is no shock present. The author furthermore expects that the separation point has an oscillation region, couple to bubble growth and depletion events. It was therefore chosen to similarly estimate the separation point at the point of the highest pressure gradient. This may not be entirely correct.

As expected from literature, a clear downstream shift is found between $M = 0.6$ and $M = 0.8$ for the boat-tail reattachment point, with an increase in separation length. At $M = 0.6$, the reattachment point is located at L/D = 0.228, with a separation length of 3.05 L_S/H_b. The reattachment point shifts to L/D = 0.305 at $M = 0.8$, with separation length increasing to 3.61 L_S/H_b. For $M = 0.7$, D'Aguanno [17] found a reattachment point at L/D = 0.27 with PIV, which again matches almost perfectly to the one from PSP. No PIV data is available for M = 0.75.

Lastly, the three dimensionality in the separated region that was present in the baseline configuration can be seen in Figure 8.6 for all M numbers, and has a similar shape. However, the M = 0.6 case shows a higher curvature towards both edges. The estimated reattachment location for that Mach number is thus more uncertain. Interestingly, the pressure on the BT also shows signs of three dimensionality for M = 0.6, with slightly higher pressures being found at locations where the reattachment is more downstream.

8.3. Angle of Attack Effect

During flight, launchers experience angle of attack variations of up to ±6° in the transonic regime [6]. Here it was chosen to study this by setting α to 4°. This angle was chosen to match with the TUPLE investigation [17] and other previous HHF studies [3, 18, 26]. The impact of the angle of attack was studied for $M = [0.8, 0.7]$ using a high and a low camera perspective (see Section 5.3). Due to difficulties in dewarping, only the boat-tail camera results were successfully dewarped (see Appendix N for the PLF results).

The resulting surface C_P plots are shown in Figure 8.11. Similarly to Section 7.4, the averaged C_P over four 20°ϕ strips was calculated around $\phi = (\pm 90°, \pm 45°)$. The resulting C_P over L/D plots are shown in Figure 8.12 including the $C_{P_{PSP}}$ at $\alpha = 0°$ and pressure tap data for $\alpha = 4°, \phi = 90°$ from the TUPLE study. From these plots, the location of the reattachment point was extracted as tabulated in Table 8.3.

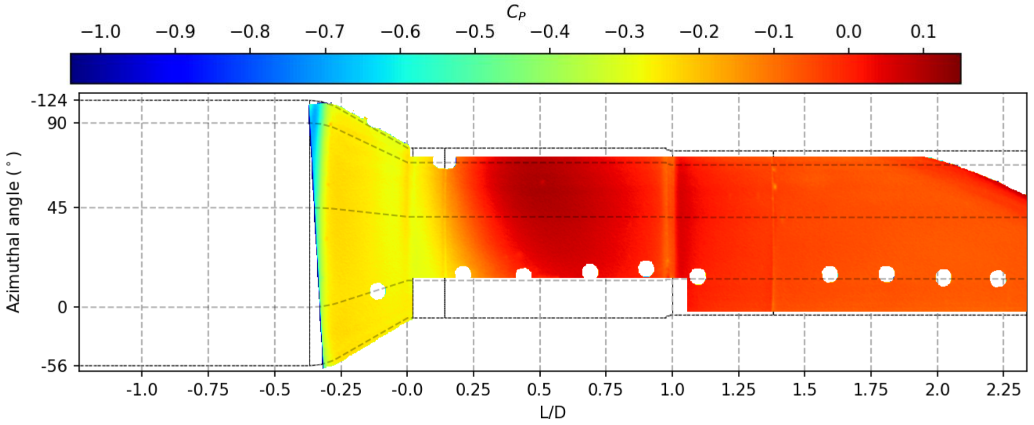

(a) M = 0.8 upper perspective.

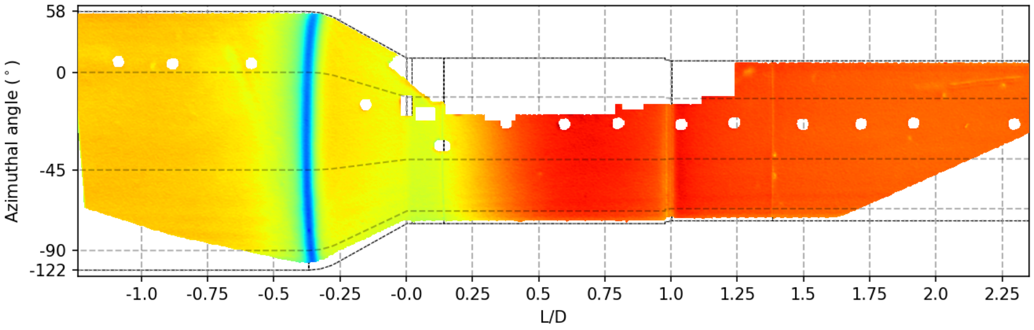

(b) M = 0.8 lower perspective.

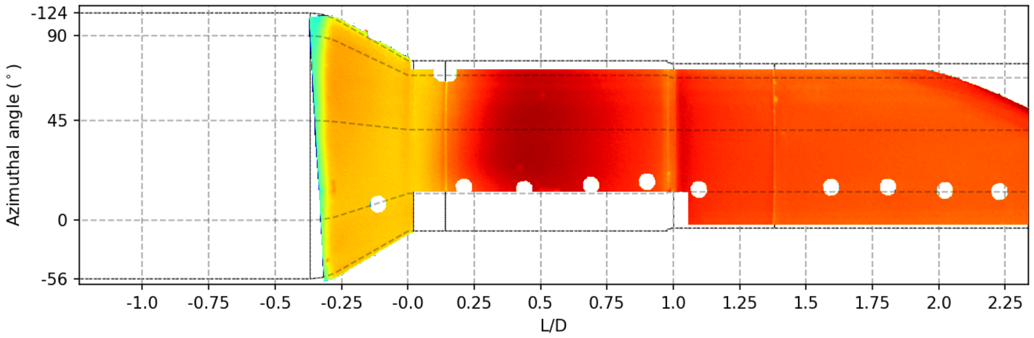

(c) M = 0.7 upper perspective

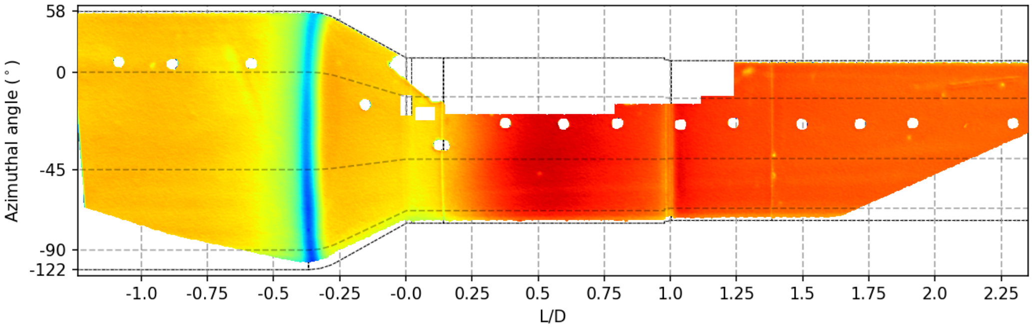

(d) M = 0.7 lower perspective.

Figure 8.11: Surface C_P plots of the $\alpha = 4^\circ$ measurements with no protuberances at different Mach numbers. Measurements were taken with different camera perspectives.

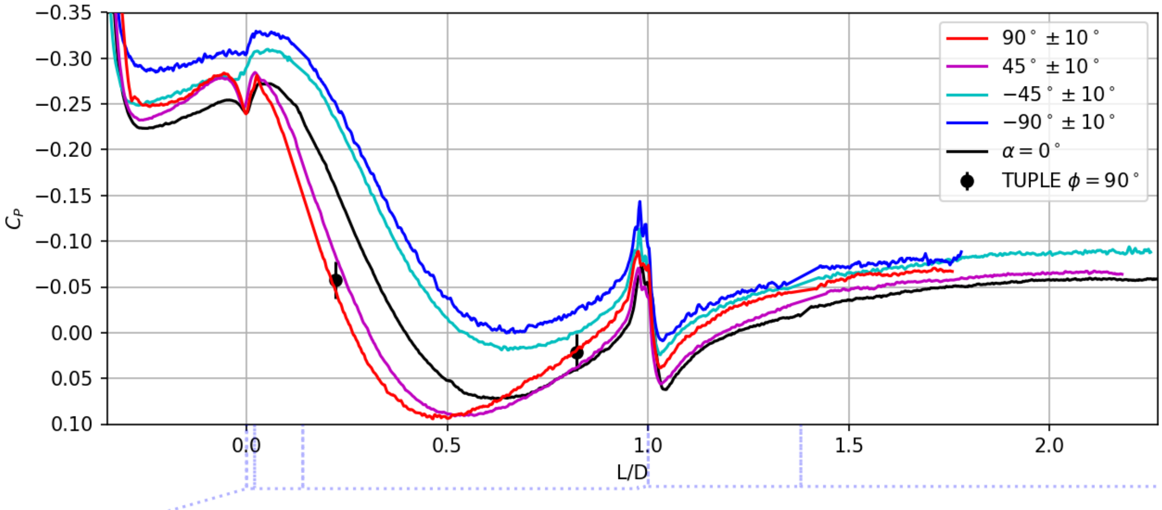

(a) C_P at $M = 0.8$.

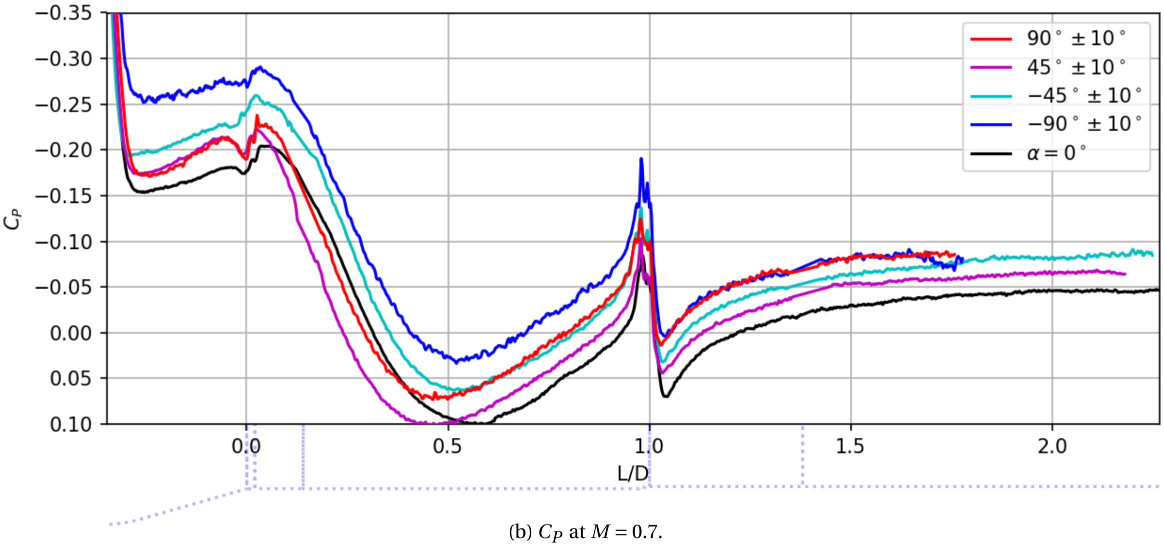

(b) C_P at $M = 0.7$.

Figure 8.12: C_P distribution on the Vega-E without protuberances at $\alpha = 4^\circ$ over 20° strips centered around $\phi = \pm 90, \pm 45$. Figure (a) shows the $M = 0.8$ results, (b) the $M = 0.7$ ones. Included are also the mean C_P at $\alpha = 0^\circ$ and TUPLE pressure tap values [17].

Starting with M = 0.8, it can be seen that the separated flow C_P increases with increasing ϕ. A similar effect can be seen on the Model 11 in Figure 7.9, albeit to a lesser extent. The cause for this is likely related to either the PSP uncertainty, differences in separation mechanism or blockage. First, a large jump in pressure can be seen between $\phi = 45^\circ$ and $\phi = -45^\circ$. The data shown in Figure 8.12a was taken from three different experiments, one using the upper perspective (**ESA 15u**) and two using the lower perspective (**ESA 10d** & **ESA 11d**). Here, temperature uncertainties may have caused opposite biases in both datasets, leading to a larger pressure difference than what is present in reality. Additional measurements or temperature data would be needed to verify this.

Secondly, the separation is heavily influenced by the second shock. As will be discussed later, the second shock was found to be weaker on the leeward side, which is the opposite that was seen on the Model 11. This could be related to the differences. Lastly, due to blockage, the leeward side acts as a diverging nozzle, whereas the windward side acts as a converging nozzle. Slightly lower velocities are therefore expected on the leeward side than the windward side. However, on the Model 11 the blockage effect did not cause large differences in the C_P of the separated flow. While model lengths are different, other dimensions are similar, thus the blockage is not expected to be the sole cause for the difference.

$\phi(\pm 10°)$	**Reattachment L/D at M = 0.8**	**Reattachment L/D at M = 0.7**
90°	0.23	0.25
45°	0.27	0.22
−45°	0.34	0.26
−90°	0.34	0.26

Table 8.3: Reattachment point on the Vega-E for different circumferential positions at $M = 0.8, 0.7$, $\alpha = 4°$ and no protuberances.

Depending on azimuthal position, the reattachment point is more up- or downstream than $\alpha = 0°$, where it was found at $0.305L/D$. It moves upstream with increasing ϕ, as expected from literature (see Subsection 2.3.3). At $\phi = 90° \pm 10°$ the reattachment point was found at $L/D = 0.23$, which again is almost the same as the PIV value of $L/D = 0.24$ report by D'Aguanno [17]. The reattachment point increases to $0.34L/D$ for $\phi = -45° \pm 10°$, after which it stays more or less constant until $\phi = -90° \pm 10°$.

The exact point at which the reattachment point stops moving backwards was not visualized, due to lack of data between $\phi = 0°$ to $\phi = -20°$. At $\phi = 20°$, it is situated around $L/D = 0.30$. From this, the author suspects that instabilities associated with the angle of attack are most critical on the leeward side of the model, due to the increased asymmetry compared to the windward side and the $\alpha = 0°$ case. Indeed, on the sidewalls of the Model 11 an increase in p_{rms} was reported by Sellers et al. [8].

Past the small BFS, the C_P for different ϕ have slightly different values that are all lower than the $\alpha = 0°$ C_P. Here, the author expects that this difference is caused by temperature related errors and increased blockage (see Subsection 5.2.6 and Section 7.1), instead of being an angle of attack effect.

A different pattern is seen for $M = 0.7$. Here, the most upstream reattachment point is found around $\phi = 15°$ in Figure 8.11c. The exact cause for this is unknown. On the $\alpha = 0°$ measurements, it is suspected that holes on the model led to a more forward reattachment point, as can be seen in Figure 8.6c. This could have played a role in the reattachment being most upstream. However, if this was the sole cause, some impact would also have been expected in Figure 8.11a. PSP related errors are unlikely to have caused this, as the $M = 0.7$ experiments were taken in between the $M = 0.8$ ones. Other methods, such as oil flow visualization, would be needed to verify whether this is indeed a flow pattern or a measurement error.

Outside the $\phi = 45°$ curve, the reattachment point shifts downstream between $\phi = 90°$ and $-90°$, but to a lesser extent than for $M = 0.8$. Unlike $M = 0.8$, the most downstream point is almost identical to the $\alpha = 0°$ case at $0.265L/D$. A potential explanation for this are the shocks, which are intermittent for $M = 0.7$. In the absence of shocks, it could be that the mean flow is less affected by the $\Delta\alpha$, much like the small BFS. Lastly, a similar increase in pressure with ϕ is present. However, no conclusions can be drawn without determining whether the upstream reattachment point at $\phi = 15°$ is physical or a measurement error.

8.3.1. Shock Wave Characteristics

Although the exact shock locations can not be extracted due to warping, patterns and pressures can be found in the PSP images. These were consistent for both Mach numbers. In Figure 8.13 the $M = 0.8$ results are shown, highlighting the pressure distribution before the shocks (see Appendix N for other plots). The impact of α is further discussed in Subsection 8.4.1 for the $M = 0.8$, $\alpha = 4°$ and protuberances configuration.

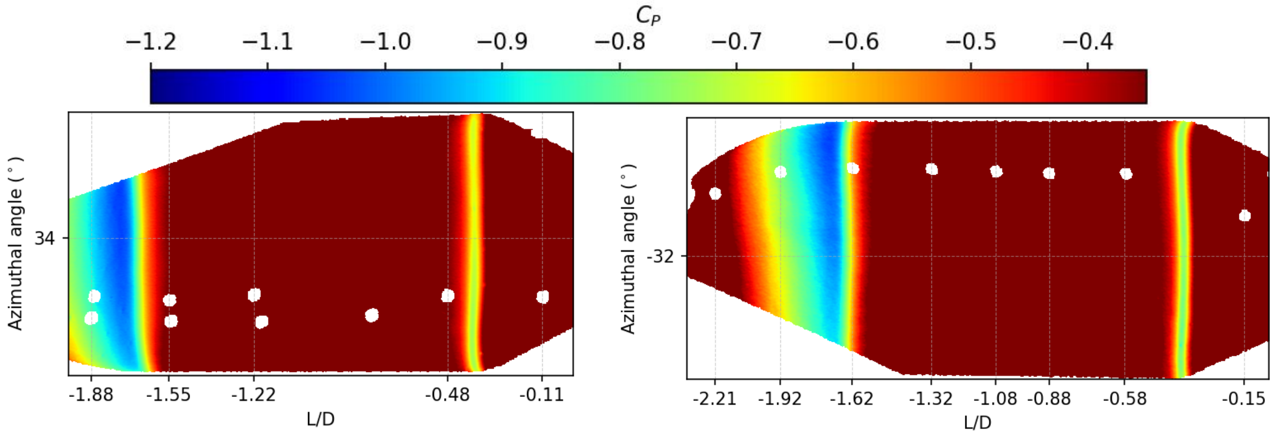

(a) Upper perspective.

(b) Lower perspective.

Figure 8.13: Pressure distribution on the PLF for the $M = 0.8$, $\alpha = 4°$ and no protuberances measurements on the Vega-E model. Highlighted here is the pressure in front and just after the mean shock location. Note that the L/D locations shown are only valid for the center of the masked away fiducial marks. Other positions along the circumferential direction may be misaligned.

Of particular interest is the pressure distribution around the first and second shock. For the first shock, the minimum C_P before the shock decreases with increasing ϕ, going from a -0.89 at the bottom of Figure 8.13b to -1.05 at the top of Figure 8.13a. The C_P in between both shocks sits around 0.2 for all phi ϕ. This indicates that shock strength increases with ϕ, as the pressure jump increases. The opposite pattern is seen for the second shock, albeit to a lesser extent. Here with increasing ϕ the minimum C_P in front of the shock increases from -0.76 to -0.68. This pattern can also be seen in Figure 8.11d for $M = 0.7$.

The decrease in C_P in front of the first shock is expected from the geometry, as the flow has to turn around a steeper corner due to the α. Similarly, this leads to a higher C_P on the windward side. This pattern can also be seen for the Model 11 in Section 7.4. However, on the Model 11 the same holds true for the second shock, again to a lesser extent, whereas here the opposite is seen. This is likely due to the unique geometry transition of the Vega-E. As with Figure 8.12, the question remains to what extent this difference is caused by PSP errors. As the azimuthal temperature distribution is unknown, this is hard to estimate. Expected temperature differences should not exceed $3K$, which would give an error of at most $0.021C_P$. Therefore, the pattern is likely physical, but further PSP corrections are needed to ascertain the true extent.

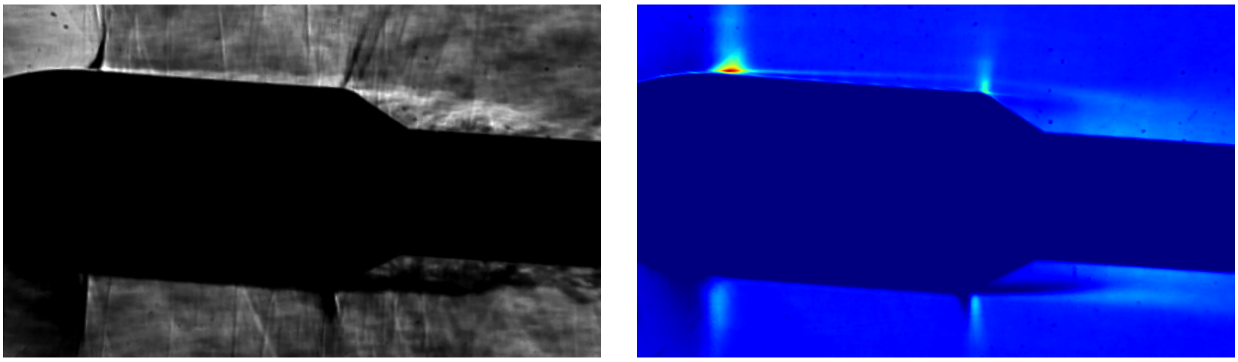

(a) Schlieren snapshot.

(b) Pixel standard deviation field.

Figure 8.14: Schlieren results for the Vega-E model at $M = 0.8$, $\alpha = 4°$ and no protuberances.

In addition, a Schlieren measurement was taken at $M = 0.8$ and $\alpha = 4°$. A snapshot and the σ_I field can be seen in Figure 8.14. As reported by D'Aguanno et al. [17], shock positions do not significantly change due to α. From these, the leeward shocks were found at $L/D = -1.58$ and $L/D = -0.30$ for the first and second shock respectively, and for the windward side at $L/D = -1.53$ and $L/D = -0.27$. Shock locations were extracted $1cm$ away from the surface. Both are very similar to the values obtained by D'Aguanno (see Table 2.1), with a more downstream shift for the windward shocks. Note that the Schlieren results here are suboptimal, as the spatial resolution is low and the sensitivity high, so differences are expected.

8.4. Protuberance Effect

The impact of the protuberances on the flow field was quantified using three different Mach numbers ($M = [0.8, 0.75, 0.7]$) at $\alpha = 0°$ and $\alpha = 4°$. Measurements were taken similarly to the no protuberance configurations (denoted here as "clean configuration"), except for one $M = 0.8$, $\alpha = 4°$ measurement that was taken with a sideways camera perspective. First, the surface C_P for these can be seen in Figure 8.15.

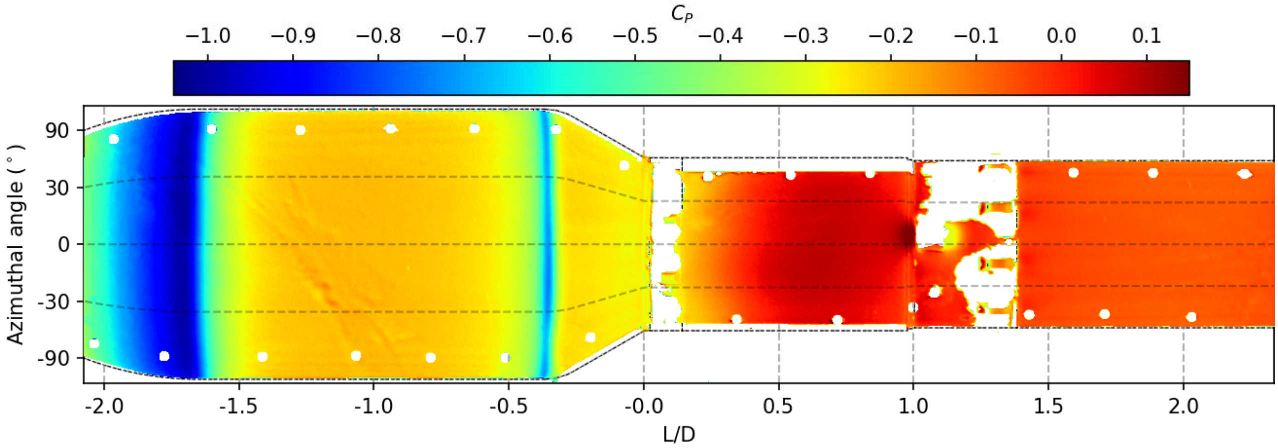

(a) M = 0.8, $\alpha = 0°$.

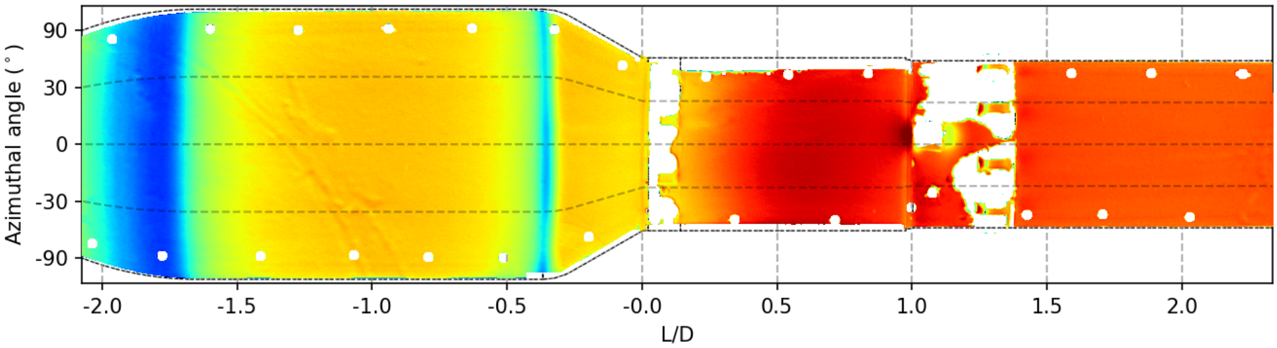

(b) M = 0.75, $\alpha = 0°$.

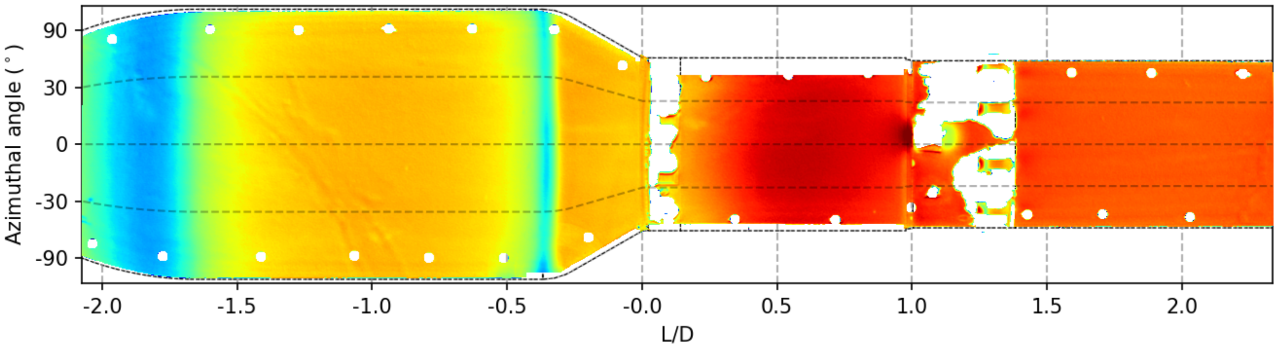

(c) M = 0.7, $\alpha = 0°$.

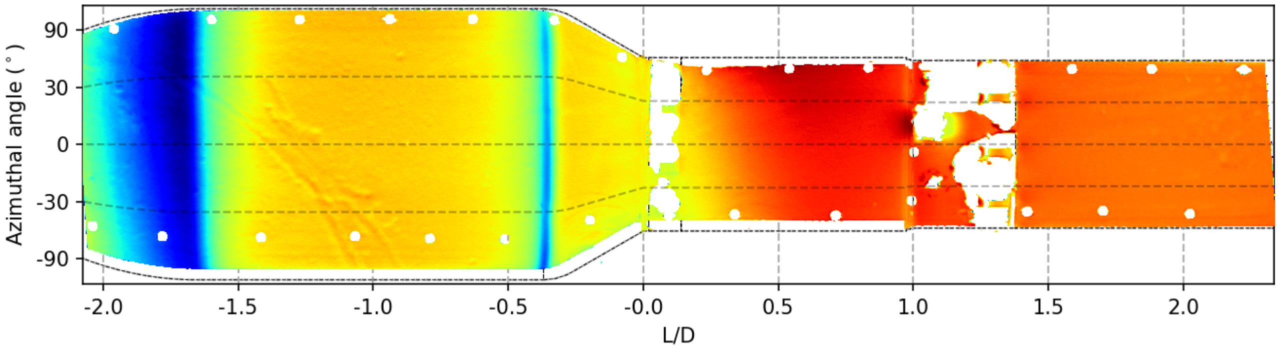

(d) M = 0.8, $\alpha = 4°$ with protuberance ring around $\phi = 20°$.

Figure 8.15: Surface C_P plots of protuberance measurements at different Mach numbers. In figure (d) the $\alpha = 4°$ results are additionally shown, for the sideways camera perspective that was used for $\alpha = 0°$.

Two types of protuberances are installed on the model, as can be seen in Figure 5.11. The first is a big protuberance that resembles a square cylinder. Here it can be seen around $\phi = 6°, L/D = 1.1$, with another placed 180° away out of the frame. The protuberance itself does not have any paint, but an area of high pressure can be seen upstream of it, with a low pressure zone downstream.

The second type are multiple smaller ones on the first protuberance ring and downstream of the big protuberance. The smaller protuberances on the first ring are hard to see due to paint peeling, but four are located in each image (see Figure 6.2 for better visibility in the reference image). Small protuberances on the second ring instead all have some paint on them, and can clearly be seen around $L/D = 1.35$. Note that the rings are rotated slightly ($\sim +10°$) in Figure 8.15d compared to the others.

In all protuberance experiments, most of the paint on the protuberance rings peeled off. Some luminophores stuck to regions of stripped paint, causing the peeled areas to have a non-zero intensity. However, the signal acquired in these did not follow the Unifib calibration and was therefore masked away. The masking is not perfect, so low or high pressure noise signal can be seen at the edges of the paint.

Measurements were also taken with the high and the low perspective for $M = 0.8$. Here, the azimuthal location of the big protuberance differed for the high and low perspective to better visualize the protuberances and investigate the impact of changing its position. As before, only 1 camera was dewarped and results for the PLF camera can be found in Appendix N. In addition, one measurement was taken with the upper perspective for $M = 0.7$, $\alpha = 4°$ to investigate the impact of filter spectral leakage (see Subsection 6.3.2). This measurement had no PLF camera. The surface C_P for these can be found in Figure 8.16.

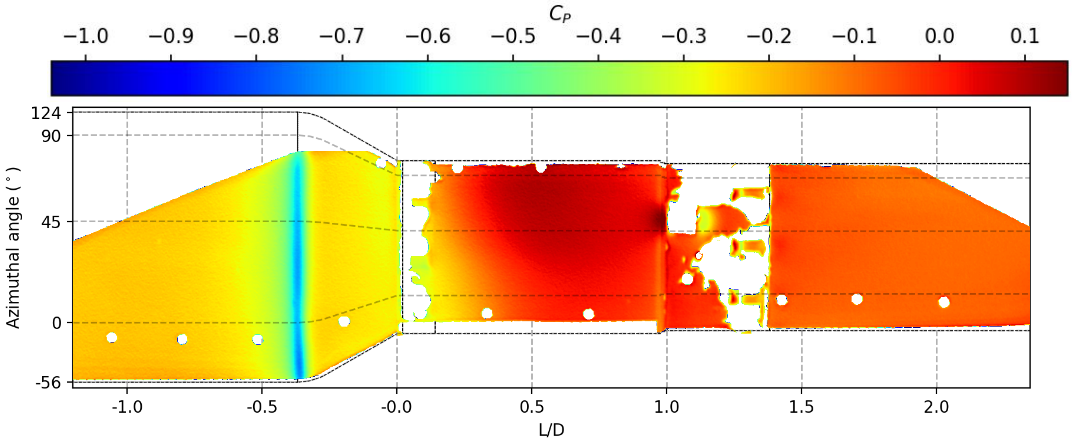

(a) M = 0.8 upper perspective.

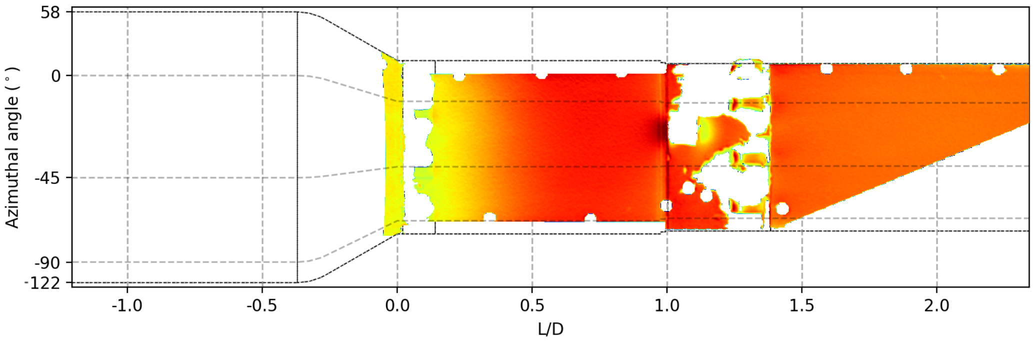

(b) M = 0.80 lower perspective.

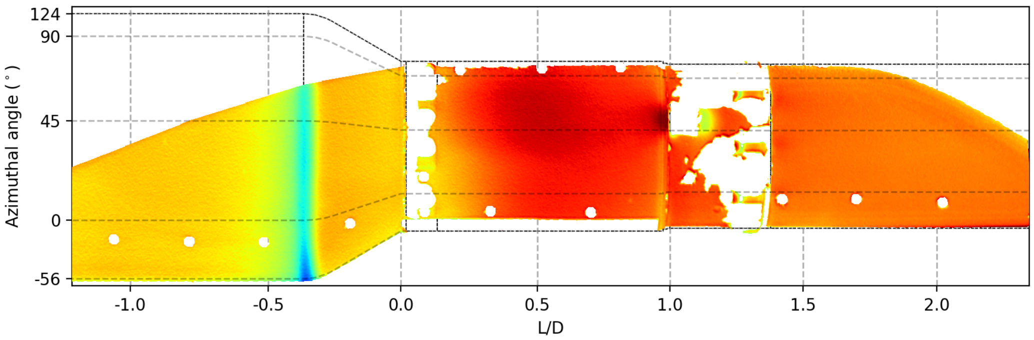

(c) M = 0.7 upper perspective.

Figure 8.16: Surface C_P plots of protuberance measurements at $M = [0.8, 0.7]$ and $\alpha = 4°$, taken with different perspectives.

In the TUPLE investigation [17], the small protuberances on the first ring were placed in line with the big protuberance on the second ring. Due to model limitations, this could not be achieved while putting the big protuberance in front of the painted area between protuberance rings. Therefore, it was chosen to put it at an offset near the center of the FOV. This could lead to some differences between the TUPLE results and the ones presented here, especially in the pressure distribution.

The following discussion on the impact of the protuberances is discussed in three parts. First, the next subsection discusses the effect of the protuberances on the shocks. This is followed by a portrayal of the pressure distribution surrounding the protuberances. Lastly, the impact on flow reattachment is discussed.

8.4.1. Impact on the Shock Waves

To study the impact of the protuberances on the shock waves, both shock strength and position are analysed. Here, shock strength is quantified using the pressure jump, by taking the minimum C_P before the shock and the stable C_P value after. First the shock position and strength were analysed at $\alpha = 0°$ for three different circumferential positions, namely $\phi = 40° \pm 10°$, at the azimuthal position around the protuberances ($\phi = 6° \pm 10°$) and at $\phi = -45° \pm 10°$. The three strips can be seen in Figure 8.17 for $M = 0.8$.

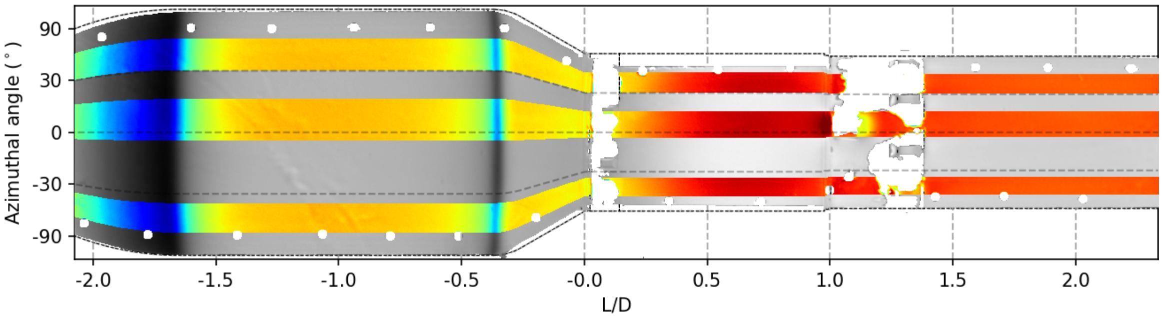

Figure 8.17: 20° strips used to extract flow features and calculate the C_P over L/D plots for the $\alpha = 0°$ and protuberances results. Shown here are the strips on the $M = 0.8$ surface C_P plot.

The analysis was performed for all Mach numbers, where the same pattern was found. Therefore, only the $M = 0.8$ results are shown (see Appendix O for other results). In Figure 8.18, the C_P over L/D plots can be found, whereas Table 8.4 shows the shock locations and the ΔC_P. Note that all the no protuberances results were found to have a pressure that was 0.6 to $0.9kPa$ higher (depending on M) than the protuberances results. The reason for this is uncertain, as it could have been caused by many factors. Given the consistency for all M, the likely cause is either a difference in wind tunnel total pressure (before, during or after the experiments) or a difference in blockage, as the big protuberance causes a large wake [44].

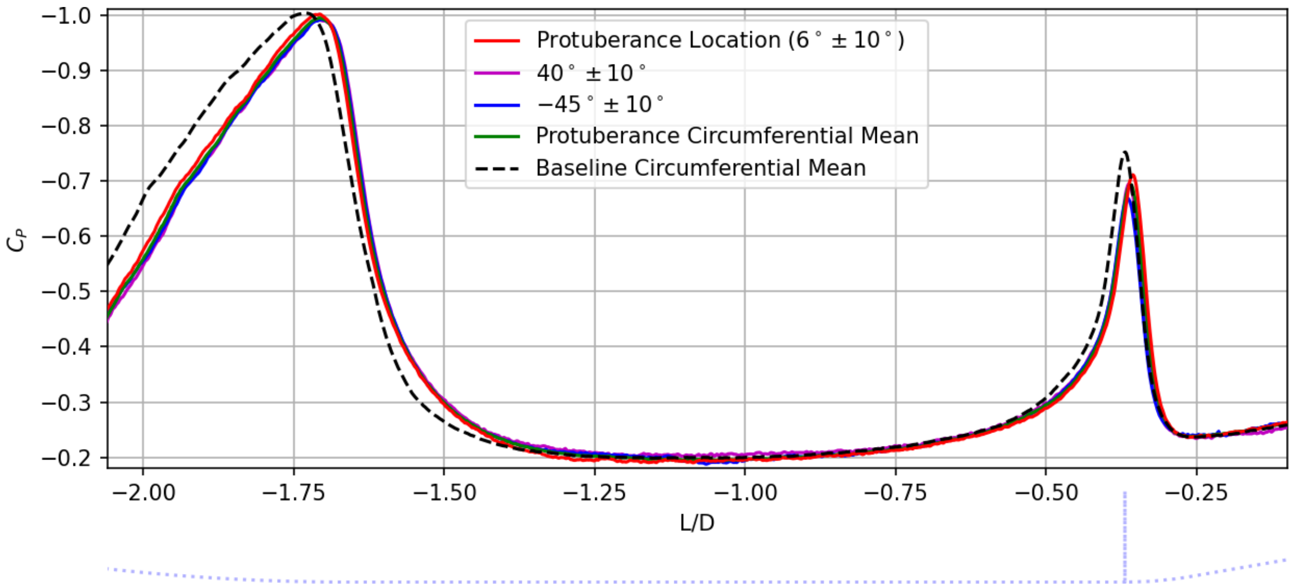

Figure 8.18: C_P distribution on the PLF of the Vega-E at $M = 0.8$, $\alpha = 0°$ with protuberances. Shown are different strips of $\phi = 20°$. In addition, the circumferential mean for this and the baseline configuration are also shown. The baseline results are scaled by $-0.8kPa$ to better match the protuberance results.

	Location (L/D)		**Pressure Jump (ΔC_P)**	
	Shock 1	**Shock 2**	**Shock 1**	**Shock 2**
$\phi = 40° \pm 10°$	-1.65	-0.34	0.79	0.46
Big protuberance ($\phi = 6° \pm 10°$)	-1.65	-0.34	0.81	0.48
$\phi = -45° \pm 10°$	-1.65	-0.35	0.79	0.43
Protuberance Circumferential Mean	-1.65	-0.34	0.80	0.46
Baseline Configuration	-1.67	-0.35	0.80	0.52

Table 8.4: Location of and pressure jump across the shock waves on the Vega-E PLF at different circumferential positions for the M = 0.8, $\alpha = 0°$ and protuberances measurements. The pressure jump is defined as the difference between the minimum pressure before the shock and the stable pressure after. Included is also the baseline configuration.

In Figure 8.18 pressure distribution seems to be shifted forward for the protuberance results. This is not physical and is instead caused by a difference in dewarping, as the protuberances are not expected to impact the C_P on the nose cone. On the PLF and nose cone, the results have a dewarping uncertainty of $0.02L/D$. As the protuberance and no protuberance results used different fiducial marks (see Appendix L), a maximum discrepancy of $0.04L/D$ is expected. At the first shock, a mismatch between $0.02L/D$ to $0.03L/D$ is found for all Mach numbers. More downstream, the mismatch diminishes and pressure distributions match closely after the boat tail. Furthermore, the shocks have some curvature due to improper dewarping (see Figure 8.15) which could account for some of the positional differences in the azimuthal direction.

D'Aguanno et al. [17] found little impact of the protuberances on the shock position. This is also seen in the PSP data, as differences are smaller than the dewarping error, with a mismatch of $0.02L/D$ and $0.01L/D$

for the first and second shock respectively. However, when looking at the pressure distribution past the second shock, the curves overlap almost perfectly for all M. The second shock was consistently found to be 0.01 L/D more upstream in the no protuberances cases. Due to the otherwise perfect matching after, it could be that the second shock of the no protuberance results is actually more upstream, instead of it being a dewarping error. This can not be concluded with absolute certainty, as differences are too small.

Differences can however be seen in the pressure jump. For the first shock, the jump is similar between all configurations, with an average ΔC_P of 0.80. The jump at the big protuberance was found to be slightly higher than other azimuthal positions for all M, but differences are within the PSP uncertainty. For the second shock, larger differences are found. The baseline configuration has a much higher pressure jump at $0.52\Delta C_P$ compared to the circumferential mean of the protuberance results at $0.46\Delta C_P$. Furthermore, in front of the big protuberance the ΔC_P was higher than at other azimuthal positions, at 0.48. The ΔC_P seemingly decreases with increasing distance from the protuberance.

From this it can be concluded that the main impact of the protuberances on the shocks, is on the strength of the second shock. Shock strength is lowered by the presence of the protuberances, although the big protuberance locally increases it compared to the mean. The cause can potentially be explained by the fact that the protuberances inside the separated flow field are decreasing the separation volume, effectively lowering the boat tail angle. D'Aguanno et al. [17] found a net reduction in velocity fluctuations in this volume due to the small protuberances, which could be related to the decrease in shock strength.

The above analysis assumes that the measured pressure at different azimuthal positions is accurate. To validate the results, the 20° strips were analysed in two different ways. First, when comparing other points on the curve outside the shocks, it was found that all curves are within $\pm 0.01 C_P$ ($\simeq 0.5 kPa$) of each other, with most points being within $0.005 C_P$ for all M numbers. Secondly, the pressure jump at different azimuthal positions was calculated in the baseline configuration results. For both shocks, a ΔC_P of at most 0.015 was found. This can be assumed to be the azimuthal uncertainty. Therefore, the uncertainty is lower than the differences in ΔC_P for the second shock. As differences are in the order of the uncertainty for the first shock, it can not be concluded that the protuberances change the distribution.

- **$\alpha = 4°$ configuration**

Lastly, the same analysis was performed for the $\alpha = 4°$ case. Different strips were taken to be more evenly spread across the circumference. The results can be found in Figure 8.18 and Table 8.5. Note that the $\phi = -60°$ data is noisy after the first and second shocks. To compare the pressure jumps, values after the shocks were taken from the $-20°$ curve instead, as the pressure is expected to be nearly identical.

As the $\alpha = 4°$ and no protuberances measurements could not be successfully dewarped, this also severs to quantify the angle of attack effect on the locations of the shocks. It can be seen that the first shock is more upstream on the leeward side and more downstream on the windward side, compared to the $\alpha = 0°$ case where it was situated at -1.65 L/D. This pattern was also seen in Schlieren. As the first shock was mostly unaffected by the protuberance for $\alpha = 0°$, the same can be assumed to hold here. Again, the pressure jump increases with increasing ϕ as previously reported for the no protuberances case. Around $\phi = 3°$ the pressure jump matches the $\alpha = 0°$ protuberance case.

For the second shock, the reported location is more uncertain due to the camera warping. The location that was found closely matches the $\alpha = 0°$ and no protuberance results around $-0.34 L/D$. Instead, large differences can be seen in the pressure jump. As reported previously, the opposite trend is found in the second shock, where ΔC_P decreases with increasing ϕ. The jump increases by more than 25% between $\phi = 60°$ and $\phi = -60°$, going from a ΔC_P of 0.42 to 0.55. Differences between 90° and −90° are expected to be even higher, but were not visualized.

To investigate the impact of the protuberance on the ΔC_P at the second shock, the pressure jump was computed next to the protuberance at $\phi = 33° \pm 10°$ and $\phi = -7° \pm 10°$. The ΔC_P was found to be 0.44 and 0.49 respectively. On the $\alpha = 0°$ case, the pressure jump in front of the big protuberance was larger than other circumferential positions, which is not the case here. As the pressure jump in front of the protuberance is not higher than that around it, this indicates a reduced impact of the protuberance compared to $\alpha = 0°$. Comparison with dewarped data from the no protuberance case would be needed to verify this.

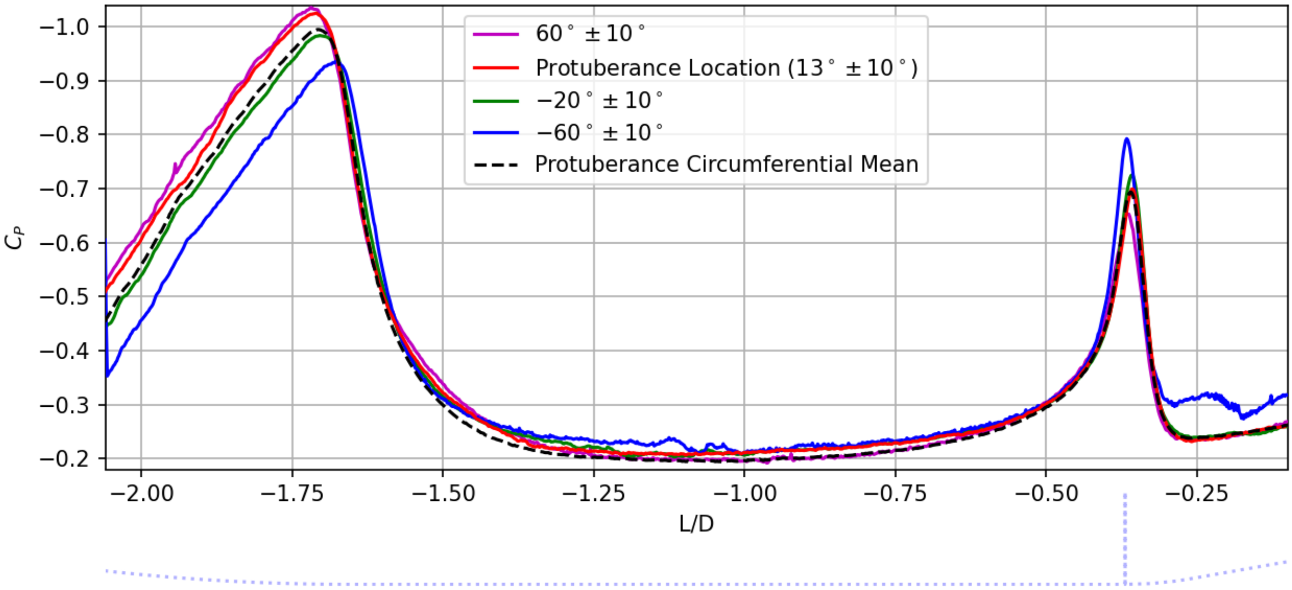

Figure 8.19: C_P distribution on the PLF of the Vega-E at $M = 0.8$, $\alpha = 4°$ with protuberances. Shown are different strips of $\phi = 20°$. In addition, the circumferential mean for the $M = 0.8$, $\alpha = 0°$ with protuberances configuration is shown.

	Location (L/D)		**Pressure Jump (ΔC_P)**	
	Shock 1	**Shock 2**	**Shock 1**	**Shock 2**
$\phi = 60° \pm 10°$	-1.66	-0.34	0.84	0.42
Big protuberance ($\phi = 13° \pm 10°$)	-1.66	-0.33	0.82	0.47
$\phi = -20° \pm 10°$	-1.64	-0.34	0.77	0.49
$\phi = -60° \pm 10°$	-1.62	-0.35	0.73	0.55

Table 8.5: Location of and pressure jump across the shock waves on the Vega-E PLF at different circumferential positions for the $M = 0.8$, $\alpha = 4°$ and protuberances measurements.

8.4.2. Local Impact Around the Protuberances

To highlight the pressure distribution surrounding the protuberances, a zoomed-in view downstream of the boat-tail can be seen in Figure 8.20a. All $\alpha = 0°$ cases have matching trends, therefore only $M = 0.8$ is shown with the baseline configuration in Figure 8.20b for comparison (see Appendix O for other Mach numbers). From these, it can be seen that the big protuberance has the largest impact on the flowfield. At $\alpha = 0°$, it causes a region of increased pressure that radiates upstream from the stagnation point and a low pressure region behind it due to shedding vortices. The C_P in front of the big protuberance was found to be independent of M number at around ~ 0.2. Instead, the C_P in the low pressure region was found to increase with M, going from a $-0.35 C_P$ at $M = 0.7$ to $-0.3 C_P$ at $M = 0.8$.

The impact of the small protuberances is harder to quantify due to the paint delamination. On the first protuberance ring at $\alpha = 0°$, one of the protuberances situated around $(\phi, L/D) = 20°, L/D = 0.1$ can be seen to cause a slight decrease in pressure in Figure 8.15 downstream of it. This decrease is around 0.02 C_P, or $1 kPa$. The protuberance in question is close to the azimuthal position of the big protuberance. The decrease in pressure is likely coupled to the interaction of the big protuberance with the reattachment point.

At other protuberances of the first ring, no trends can be seen at $\alpha = 0°$ or $4°$. The lack of pressure signal can be attributed to the low speed fluid inside the separated flow zone.

For the small protuberances on the second ring, a low C_P region can be found on top of the protuberances. However, due to the widespread delamination, the data here is unreliable and therefore no conclusions can be drawn. Furthermore, no clear impact can be seen far in front of the small protuberances. Downstream of the every small protuberance on the second ring, there is a slight increase in pressure of around 0.03 to 0.04 C_P. The impact is localised and does not change the pressure further downstream.

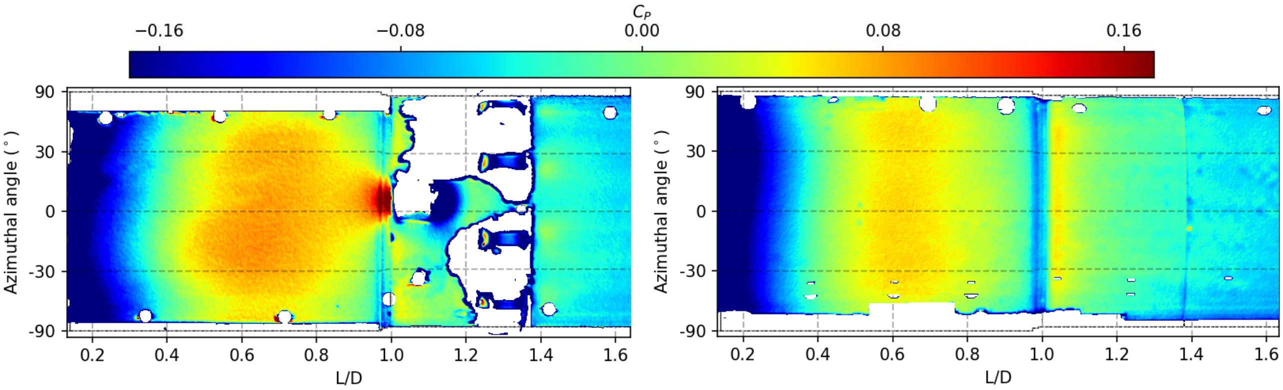

(a) Protuberances configuration

(b) Re-scaled baseline configuration ($-0.8kPa$).

Figure 8.20: Zoomed in view of the pressure distribution between 0.13 and 1.65 L/D at M=0.8, $\alpha = 0°$. In (a), the protuberances configuration is shown whereas in (b) the baseline can be seen. Here the baseline is scaled with $-0.8kPa$ to better match the pressure distribution of the protuberance configuration.

The C_P over L/D plots downstream of the second shock for $M = 0.8$ can be found in Figure 8.21 (see Figure 8.17 for 20° the strips used). In addition, the baseline results and TUPLE pressure tap data [17] is shown. As seen previously, p_{PSP} is within $1.5kPa$ of the pressure taps. The pressure tap data found higher C_P values in front of the protuberance, whereas at 90° away from the big protuberance, the C_P matched the baseline values. A similar trend is seen in the PSP data, as further away from the protuberance the distribution becomes more similar to the baseline distribution.

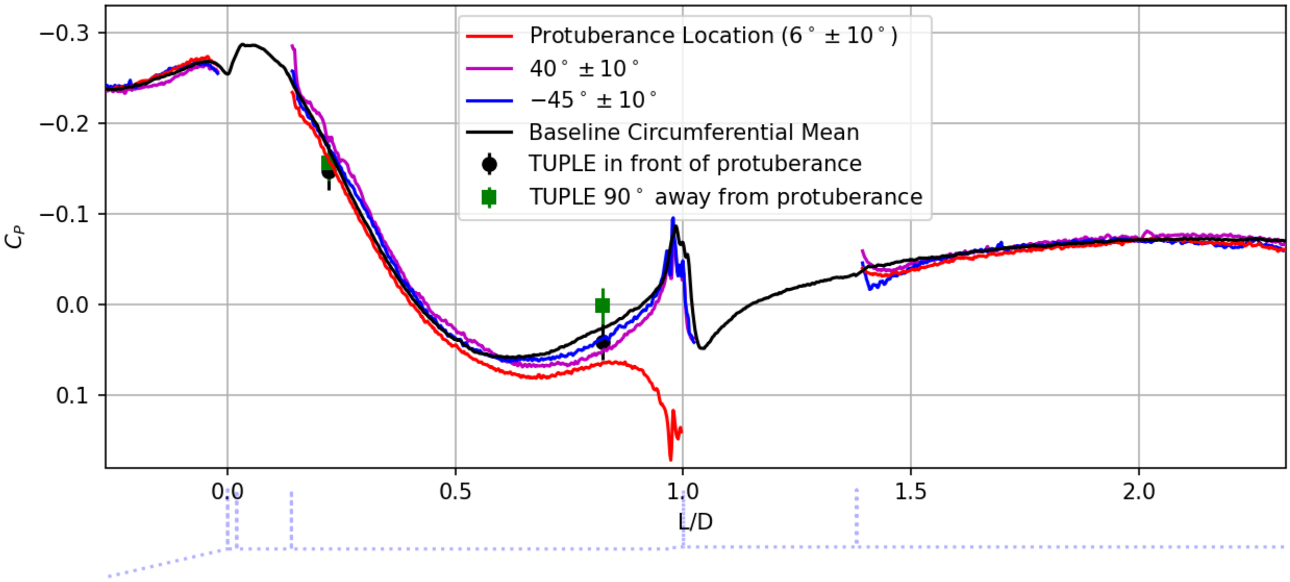

Figure 8.21: C_P distribution downstream of the second shock on the Vega-E at $M = 0.8$, $\alpha = 0°$ with protuberances. Shown are different strips of $\phi = 20°$. In addition, the circumferential mean for the baseline configuration is shown, along with TUPLE pressure tap results. Here the baseline is adjusted by $-0.8kPa$ to better match the protuberance data.

D'aguanno et al. [17] noted that the big protuberance caused a large wake downstream of it. In the PSP data, downstream of the second protuberance ring and upstream of the reattachment point, the C_P can be seen to match the baseline C_P distribution. Therefore, the wake caused by the big protuberance has a limited impact on the mean surface C_P. While the mean C_P remains unaffected, it is expected that the spectral content changes due to vortex shedding. Of particular interest would be to investigate whether the p_{rms} in the separated flow is impacted by the fluctuations in the wake of the big protuberance. If this is the case, some degree of flow control could be applied by changing the shape of the big protuberance. This would require further investigation with fast PSP or more pressure taps.

The $\alpha = 4°$ results for three different protuberance locations can be found in Figure 8.22. Measurements were taken at $M = 0.8$ with the protuberance at $\phi = [-21°, 13°, 52°]$ and one at $M = 0.7, \phi = 52°$. Here, there is a large difference between the impact of the protuberance on $M = 0.8$ and $M = 0.7$. In the $M = 0.8$ cases, the big protuberance does not seem to impact the C_P in front of it significantly. However, for the $M = 0.7$ case, a clear upstream increase in C_P can be seen. This can likely be attributed to the intermittent shock at $M = 0.7$, which might not even be there due to the α effect lowering the pressure jump at high ϕ. The author suspects that for subsonic separation, the big protuberance impacts the flow more.

The pressure in front of the protuberance is slightly lower for all ϕ compared to the $\alpha = 0°$ case. Here, values between 0.13 and 0.17 were found for the different protuberance locations. Similarly, the pressure was slightly lower at around $-0.31 C_P$ behind the big protuberance. No clear trends were found between different protuberance locations. In addition, the C_P behind the small protuberances does not seem to change with ϕ and α. The only difference is that the small protuberance on the first ring closest to being aligned with the big one was not found to cause a local decrease in C_P.

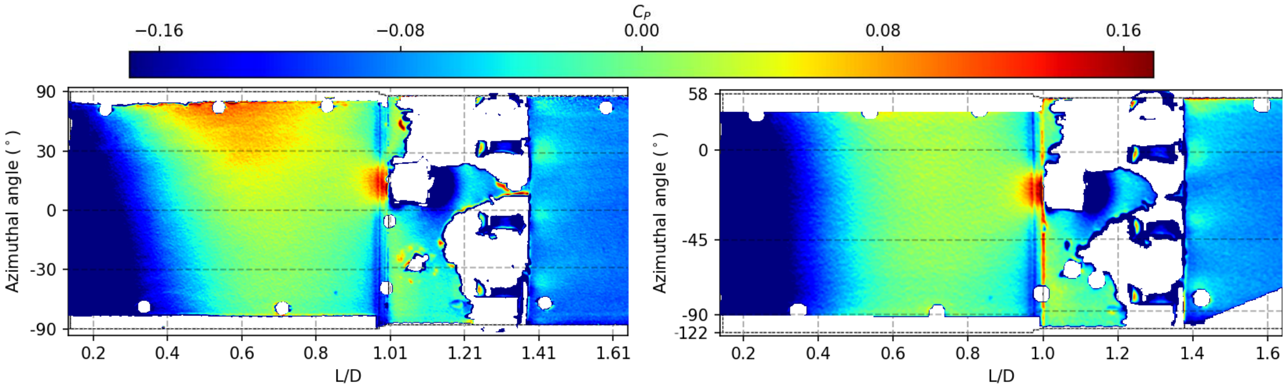

(a) $M = 0.8$ sideways view, big protuberance at $\phi = 13°$.

(b) $M = 0.8$ lower view, big protuberance at $\phi = -21°$.

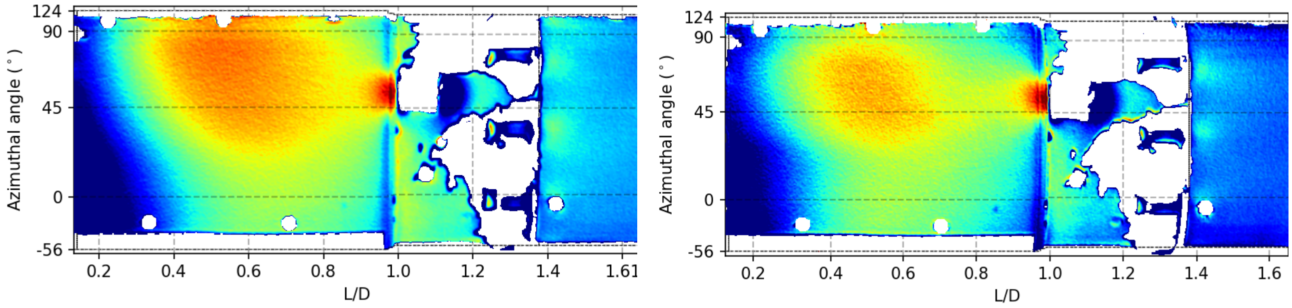

(c) $M = 0.8$ upper view, big protuberance at $\phi = 52°$.

(d) $M = 0.7$ upper view, big protuberance at $\phi = 52°$.

Figure 8.22: Zoomed in view of the pressure distribution between 0.13 and 1.65 L/D at $M = 0.8$ & 0.7, $\alpha = 4°$.

The impact of the big protuberances on the C_P distribution is further highlighted in the two C_P over L/D plots in Figure 8.23 and 8.24. Figure 8.23 shows the C_P distribution over three different azimuthal positions ($\phi = [90°, 52°, 0°] \pm 10°$) for the configuration with the protuberances at 52°. Here, the $\phi = 90°$ and $\phi = 52°$ look very similar to the $\phi = 90°$ and $\phi = 45°$ curves found in the no protuberance case (see Figure 8.12a). Up to $0.5L/D$, the shape of the distribution looks nearly identical, after which the C_P at $\phi = 52°$ is higher due to the presence of the protuberance. Again, the C_P decreases with decreasing azimuthal angle. The main difference with the no protuberances case is downstream of the second protuberance ring, where the C_P distribution is close to the same. This further indicates that the differences seen in Figure 8.12a are caused by measurement error.

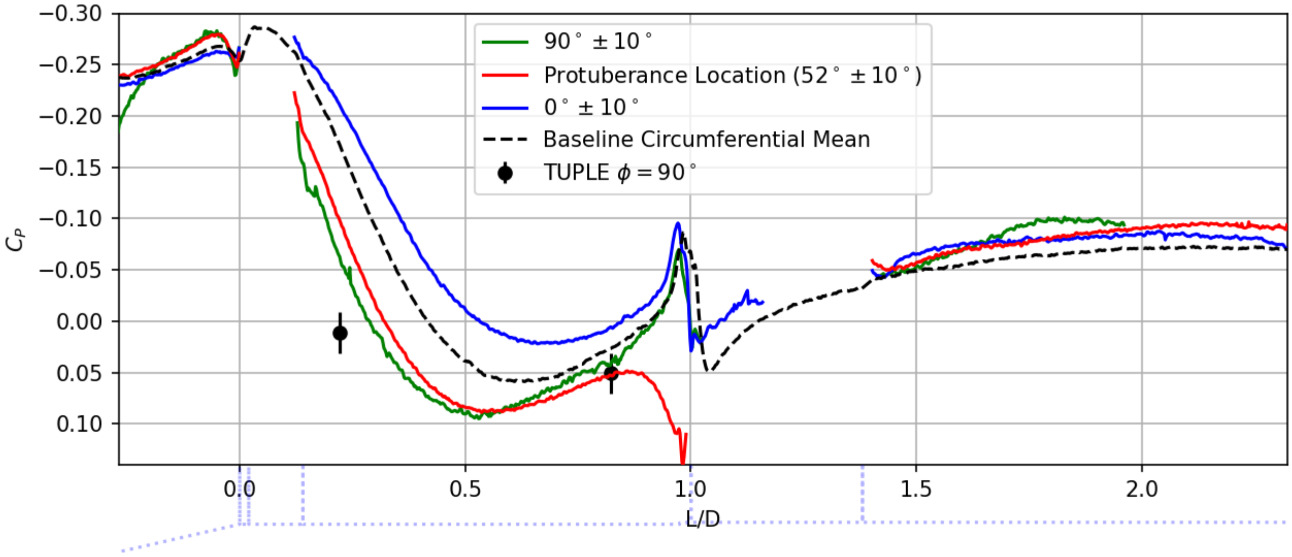

Figure 8.23: C_P distribution downstream of the second shock on the Vega-E at $M = 0.8$, $\alpha = 4°$ with protuberances placed at 52°. Shown are different strips of $\phi = 20°$. In addition, the baseline configuration is shown, along with TUPLE pressure tap results. Here the baseline is adjusted by $-0.8kPa$ as done for previous plots.

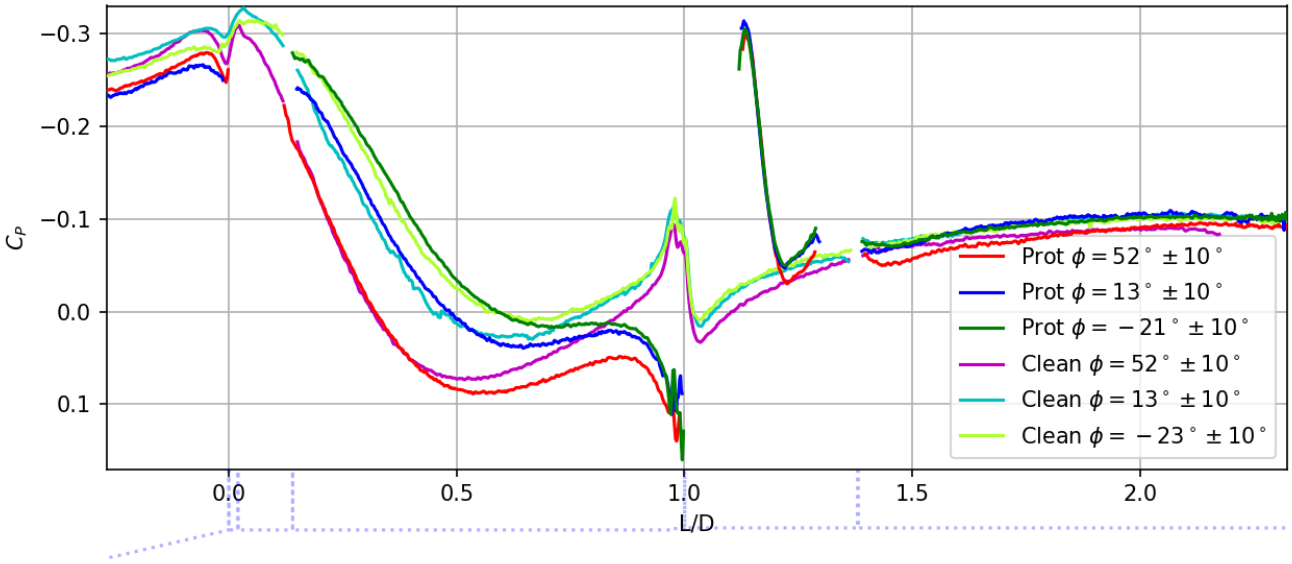

Figure 8.24: C_P distribution downstream of the second shock on the Vega-E at $M = 0.8$, $\alpha = 4°$ with and without protuberances. Shown are the pressure distributions at three different protuberance positions ($\phi = [52°, 13°, -21°] \pm 10°$, denoted as "prot") and the respective pressure for the clean configuration. Note that the clean configuration did not have data between $\phi = -11°$ and $-13°$, therefore $\phi = -23° \pm 10°$ was used instead. To allow for a more intuitive comparison, C_P values for the clean configuration were changed to match with the protuberance results from $1.75L/D$ to $2.25L/D$.

In Figure 8.24 the C_P distribution in front of the protuberances for the three different protuberance positions is compared to the clean configuration at $\alpha = 4°$ and the same circumferential positions. To allow for a better comparison, pressure levels on the clean cases were scaled by $[-0.024, -0.032, -0.012]C_P$ for $\phi = [52°, 13°, -23°]$ respectively. This was done under the assumption that the protuberance and no protuberance experiments should match downstream of the second ring, between $1.75L/D$ to $2.25L/D$. Here it can be seen that the pressure increase that starts at $L/D = \sim 0.1$ has the same slope and has a nearly identical magnitude between both configurations. However, the pressure keeps increasing slightly longer for the protuberance configuration, indicating a slightly more downstream reattachment position.

8.4.3. Impact on the Flow Reattachment

To determine the reattachment point in the protuberance measurements, the approach described in Subsection 6.2.3 had to be slightly adjusted, as the most upstream point (where the pressure starts increasing) can not be found due to paint delamination. This was done in two ways. The first is based on the observation that right before and after this point, the pressure shows a linear trend with L/D (decrease and increase respectively). By extending the linear trend both ways, the intersection point was found to closely align with the most upstream point. The resulting point can be seen in Figure 8.25 for the baseline configuration.

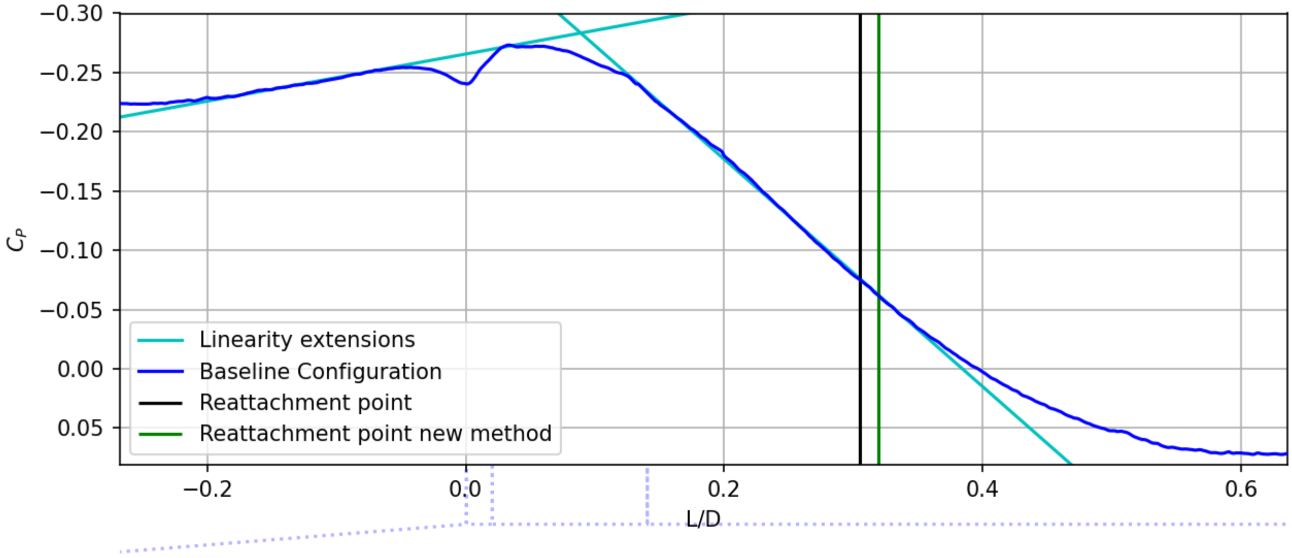

Figure 8.25: Second approach used to determine the most upstream point in the detection of flow reattachment for the protuberance experiments. Shown here is the method applied to the baseline configuration. In this case, a more downstream reattachment point can be found with the new method (0.32 compared to 0.305 in the original approach).

In some cases, this approach leads to a near-perfect match. Other times, it causes a mismatch that gives a more downstream reattachment position, such as in the example. The expected deviation of this method is within $+0.03L/D$ of the method given in Subsection 6.2.3. Instead, the second approach simply assumes that the most upstream point is the same as the clean configuration. This is based on the fact that between the second shock and the reattachment point, the shape of the C_P distribution is almost identical for $M = 0.8$, $\alpha = 0°$, as can be seen in Figure 8.21. It is expected that the "real" most upstream point is somewhere between the values found for both methods.

The reattachment point for difference protuberance configurations can be seen in Table 8.6 and Table 8.7. Here, the results using both approaches are shown as a range when they differ. As the $\alpha = 0°$ case shows a similar trend for all M numbers, only the $M = 0.8$ is shown (see Appendix O for others). In all cases, the reattachment point that was found for the protuberance configurations is more downstream than the clean configuration. A downstream shift between $0.01L/D$ to $0.06L/D$ is observed, with on average higher values found for $\alpha = 0°$. For $\alpha = 0°$, shift decreases further away from the big protuberance. The reattachment point is expected to be almost the same as the clean configuration at $\phi = 90°$ away from the big protuberance. Notable is also that for $\alpha = 4°$, the downstream shift is smaller at $\phi = 52°$ than at other ϕ values. This can indicate that other effects dominate the reattachment point position at higher ϕ.

A possible explanation for the downstream shift is that the big protuberance leads to an adverse pressure gradient, which could be the cause of the delay in flow reattachment. While this explanation is likely part of the reason, the whole system is more complex. The protuberances were also found to lower overall shock strength, which should have caused a more upstream reattachment. Lastly, the method used to detect reattachment points is unorthodox, and while proven to be accurate for the clean configuration, it may be erroneous for the protuberance cases.

PIV results from D'aguanno [17] for $M = 0.8$ suggest a more upstream reattachment point (by $-0.01L/D$ for all cases). However, the PIV data from the protuberance measurements was taken further from the surface than the clean configuration, which could be contributing to the discrepancy. It is possible that the shear layer in the clean configuration reattaches more perpendicular to the surface, while in the protuberance case the angle is shallower, giving higher discrepancies between PIV and PSP.

	Reattachment point (*L/D*)	**Separation ratio (L_s/H_b)**
Big protuberance	0.35-0.36	3.83-3.89
34° away from the big protuberance	0.34-0.36	3.78-3.89
−51° away from the big protuberance	0.33	3.78
Baseline configuration	0.305	3.61

Table 8.6: Boat-tail flow separation ratio (length divided by height) and reattachment point at three different ϕ for the $M = 0.8$, $\alpha = 0°$ and protuberances configuration. Values for the baseline configuration are also shown for comparison. Locations for the protuberance configuration were obtained from the 20° strips that can be seen in Figure 8.21. Due to noisier data, the values for the protuberance configuration are expected to be less accurate.

M	ϕ	**Protuberance Reattachment point (*L/D*)**	**Clean Reattachment point (*L/D*)**
0.8	$52° \pm 10°$	0.27	0.26
0.8	$13° \pm 10°$	0.32-0.35	0.30
0.8	$-21° \pm 10°$	***0.37***	0.35
0.7	$52° \pm 10°$	0.23-0.24	0.23

Table 8.7: Boat-tail reattachment point for the $M = [0.8, 0.7]$, $\alpha = 4°$ and protuberances configurations at three different protuberance locations ($\phi = [52°, 13°, -21°]$, only $\phi = 52°$ for M=0.7). Values for the clean configurations are also shown for comparison at the same ϕ positions. Locations for the protuberance configuration were obtained from the 20° strips at the protuberance location, which covers the entire protuberance. Note that for $M = 0.8$, $\phi = -21°$ the reattachment point was extracted only using the most upstream point from the clean configuration, while the others used both approaches.

9 Conclusions and Recommendations

In this thesis, Pressure Sensitive Paints were successfully employed in wind tunnel measurements for the first time in Delft. Measurements were taken in the TST-27 wind tunnel at transonic conditions with standard intensity-based PSP. These measurements allowed for the classification of different flow phenomena surrounding Hammerhead payload fairings. The classification was performed for various Mach numbers, angles of attack and models with and without protuberances, to quantify the effect of each variable.

First Research Objective: Implementation of PSP

The thesis had two main objectives. The first was to find the most optimal way to implement PSPs at the trans- and supersonic tunnels of the TU Delft. For this, a thorough literature study was performed to find all available PSP implementation options. Before experiments started, the standard intensity based PSP method was chosen. This method is capable of providing time averaged fields and has a relatively simple implementation compared to other methods. The implementation can further be used as building blocks to implement more advanced methods in future research, such as time resolved PSP.

A commercially available PSP formulation, UniFIB PSP, was used for the experiments. This was chosen instead of creating the paint on site, as the aerospace faculty lacks the necessary resources. The supplier of this formulation provides a calibration curve for the paint. In an attempt to verify that the same curve is obtained using in-house equipment, calibration experiments were performed on test coupons using a pressure vessel for both under- and over-pressure, and a peltier element to control coupon temperature. This approach is commonly used in literature. The same optical equipment was used as for the wind tunnel tests. The obtained points were mostly within 2% of the manufacturer's calibration data, but the calibration setup was found to have high uncertainties related to temperature and filter spectral leakage.

Due to these uncertainties and relatively close results to the manufacturer's data, it was chosen to reject the in-house calibration curve in favour of using the curve supplied by the manufacturer. As this curve does not cover the full temperature range of experiments, the curve was reconstructed and extrapolated using a least squares approximation of the Stern-Volmer equation. The approximation and resulting extrapolation were found to lead to at most a $1kPa$ error, which was deemed to be an acceptable uncertainty margin.

Experiments were performed by taking 200 images before, during and after measurements. The images before and after were reference images. Both were independently used to calculate the pressure and combined afterwards. By doing so, the uncertainty of measurements is expected to be statistically lowered. This approach further allowed for any errors in the reference images to be detected as large discrepancies in calculated pressure between both references. When no errors were present, the calculated pressure was within $1kPa$ between both references. To further statistically lower the uncertainty, at least two separate measurements were taken of the same configuration and combined to obtain the final pressure.

- **Temperature corrections**

The trans- and supersonic tunnels of the TU Delft are both blow down facilities, in which the temperature is expected to decrease significantly during a measurement. Therefore, temperature corrections were found to be necessary. From IR and thermocouple measurements, the wind tunnel and model temperature was found to significantly depend on experimental run time, starting temperature, aerodynamic flow features and model geometry. Due to this dependency, IR measurements taken separate from the PSP measurements were found to be unable to correct for temperature errors. Instead, thermocouple measurements were used to correct for temperature trends.

Thermocouples were placed at the end of the model, shielded away from the flow. Corrections were applied by assuming a constant model temperature equal to the thermocouple temperature. The pressure in each measurement image was calculated using the mean temperature of the model during reference image acquisition and the temperature of the model at the time of each measurement frame. The two measurements for each configuration were taken at different temperatures. By applying this correction, the pressure was almost identical between reference image sets and tests taken at the same configuration. Mean absolute differences were found to be within $1kPa$.

IR measurements taken separately were instead used to estimate the pressure uncertainty caused by temperature gradients along the model. For measurements taken on the Vega-E at M=0.8, $\alpha = 0°$ and a thermocouple temperature around $7.9°C$, the temperature gradients along the model lead to an uncertainty of at most $1.5kPa$. This uncertainty is expected to be dependent on the different factors mentioned previously, along with Mach number and angle of attack. Based on IR data, it is expected that the uncertainty is higher for higher thermocouple temperatures.

Lastly, the Vega-E model was found to have temperature gradients when the reference images were being taken. Reference conditions are therefore not taken at a constant model temperature, leading to an added uncertainty in the pressure of around $\pm 400Pa$. Proper temperature corrections would therefore require both the measurement and the references to be corrected on a pixel by pixel basis.

- **Other errors and corrections**

Along with temperature corrections, other error sources were found to lead to large errors in the PSP data. The most important ones which necessitated corrections were found to be:

- **Dark current (DC) and Ambient Light (AL):** The DC and AL contributed anywhere between 5% to 20% of the total intensity in images. DC & AL corrections were implemented to deal with this.
- **Paint Peeling and Rash Pattern:** Due to faulty painting practices, a rash-like pattern was found in the pressure signal of the paint. A new painting strategy of using more layers and less paint per layer yielded better results, but it can be further improved. In addition, the paint was seen to delaminate in some measurements. Areas where the paint peeled off led to a faulty pressure signal. Delamination started in places where the paint was masked away by tape and where air was trapped between model parts. The latter caused air to expand and burst during paint curing.
- **Erroneous pressure in the first run after opening the tunnel:** A recurring pattern was found where after the tunnel is opened, the first measurement had a large mismatch in measured pressure between the reference before and reference after (around $7kPa$ difference). The expected cause is humidity / condensation blocking out oxygen from reaching the luminophores, thereby increasing paint intensity. As the air used in the tunnel is dry, it is expected that this humidity was blown away during the first run. Data from first runs could not be used due to this.
- **Filter Spectral Leakage:** For the calibration, cone and Model 11 experiments, a $550nm$ long-pass filter was used. This was later replaced by a $610nm$ filter. The $550nm$ filter was found to have a spectral leakage equal to around 2.5% of the total intensity in images (depending on measurement). This leads to a reduction in pressure sensitivity and wrong pressure values. It is possible that the $610nm$ filter also has leakage, but this has not been quantified.
- **Image misalignment:** The image alignment approach used was found to lead to small sub-pixel misalignments. However, in areas where paint intensity significantly changed due to model geometry, sharp peaks were introduced in the pressure signal.

Second Research Objective: Hammerhead Fairing Research

The second main objective of this thesis was to investigate the aerodynamic flow features of HHF launchers using PSP. This was achieved by quantifying the changes of the flow features under varying Mach numbers and angles of attack. Two different launcher models, the Coe and Nute Model 11 and a model of the Vega-E launcher, were used during this study. The Model 11 is an often used test case in literature to study the aerodynamics of HHF, whereas the Vega-E is a launcher that is currently under development by the ESA. On the Vega-E launcher, an additional research parameter was the addition of protuberances to the model. These protuberances mimic the geometry of those that will be present on the full scale launcher.

The main flow feature of interest is the so called buffeting phenomenon. Buffeting occurs due to unsteady flow separation caused by the area decrease along with shock wave-boundary layer interactions (SWBLI). The focus of the investigation was on how these features change by changing the flow conditions. Outside these main flow features, the mean C_P was found to be relatively constant for all configurations.

On both models, two shocks are present over the HHF and the flow separates at the start of the boat tail. For the Model 11, the nosecone is bi-conic with shocks occurring after each cone. In Schlieren images, an expansion fan can be seen at the geometry transition. On the Vega-E, the nosecone smoothly transitions to the payload fairing. Here the flow expands, after which the first shock occurs. Instead, the second shock takes place due to the geometry transition between payload fairing and boat tail. It is assumed that this shock also causes flow separation. For both models, the first shock is stronger than the second. Lastly, the separation length of the Model 11 is larger than that of the Vega-E, likely due to the smooth geometry transition on the Vega-E.

Measurements were taken in the TST-27 at Mach numbers varying from M = 0.6 to M=0.8 and $\alpha = 0°$ or $4°$. For these, a solid wall test section was used. This test section yielded relatively high levels of blockage, with an expected increase of around $+0.05M$ compared to the freestream Mach number. The use of slotted walls would have improved blockage errors, but it was chosen to not make use of these to match previous experimental campaigns that used PIV, Schlieren and oilflow. In these campaigns, the solid walls were used to improve the PIV data. By using the same test section, direct comparisons were made between PSP data and those obtained from the other methods. Overall, a good match was found between PIV and PSP results, with small mismatches between Schlieren and PSP.

In order to validate the PSP results, first a comparison was made between the Model 11 data obtained here and historical data from the original Model 11 experiments. Without accounting for blockage, the C_P values were found to be much lower than the original data. When including a simple blockage correction, the data was found to closely match the historical data in most places, except the second shock. The historical data used for comparison was acquired under slightly different flow conditions and is discrete from pressure taps. Due to this, it is hard to estimate the exact extent of the mismatch. However, given that the data matches well in most places despite the different test condition and unknown blockage, the PSP results are assumed to give an accurate representation of the pressure distribution.

Furthermore, a comparison was made between Schlieren measurements taken during a previous study on the Model 11 in the TST-27 without paint and Schlieren with paint. This was done to verify that the mean flow is not changed by the presence of the paint. Shock positions were found to closely align between studies, indicating that the mean flow is not impacted by the paint. However, some local changes of the flow were seen in areas where the paint delaminated. Therefore, while the mean flow is not impacted, the paint was found to locally change the flow.

Lastly, pressure tap data on the Vega-E model was available from previous PIV and Schlieren investigations in the TST-27. These broke down before the experiments in this thesis took place and were therefore not used. The calculated pressure values with PSP were found to be within $1.5kPa$ of the pressure tap data at different configurations. The pressure tap data had an uncertainty of $\pm 1kPa$, with most PSP points being within that uncertainty. This again indicates that the correct pressure is calculated with the PSP. Given the temperature uncertainty and the calibration uncertainty, overall the PSP results are expected to have an uncertainty of at most $2.5kPa$, but due to the use of repeated measurements it is likely lower.

- **Mach Number Effect**

Increasing the Mach number was found to cause a downstream shift in shock position and reattachment point for both the Model 11 and the Vega-E. In addition, shock strength and oscillation region were observed to increase. This effect is also widely reported in HHF literature. On the model 11, both shocks showed a downstream shift of around 0.1 L/D with the second shock moving slightly less than the first. For the reattachment point, a small downstream shift was seen of 0.06 L/D, with pressure levels remaining relatively constant between M = 0.7 and M =0.8.

Unlike the Model 11, the flow expanded less before the shocks on the Vega-E, which indicates a lower shock strength. This occurs due the smooth transition between geometry features. Here the shocks at M = 0.7 were observed to be intermittent, which made them difficult to detect with PSP. For higher M numbers, a similar downstream shift was seen for the first shock on the Vega-E model. However, the second shock was found to remain relatively stationary, likely due to it being related to the flow separation. Despite the lower separation length, a similar downstream shift of 0.04 L/D was observed for the reattachment point of the Vega-E when going from M=0.7 and M=0.8. Furthermore, C_P was found to decrease in the separated flow with increasing M.

- **Angle of Attack Effect**

On the Model 11, changing the angle of attack was found to cause a downstream shift of the shocks on the leeward side and an upstream shift of the reattachment point, with the opposite pattern on the windward side. In addition, an increase in shock strength was observed on the leeward side. The changes in the shocks were larger for the first shock than for the second. These findings are commonly reported in HHF literature. In addition, the pressure was found to decrease in the separated flow region with decreasing ϕ (where $\phi = 90^\circ$ is the leeward side and $\phi = -90^\circ$ the windward side).

The same was reported for the first shock and the reattachment point on the Vega-E model. However, the first shock was found to shift less in position, which can likely be attributed to the smooth geometry transition. Furthermore, the reattachment point stopped shifting downstream between $\phi = -45^\circ$ and $\phi = -90^\circ$. However, a different pattern was found for the second shock. Here, shock strength decreased on the leeward side and increased on the windward side. The shock is furthermore expected to not change in position, similar to the $\alpha = 0^\circ$ case. However, due to improper dewarping this could not be verified.

- **Protuberance Effect**

As aforementioned, the protuberance effect was only studied for the Vega-E. Two protuberance rings were installed on the model, with small protuberances at evenly spread positions. The second protuberance ring also had a big protuberance that resembles a square cylinder. Due to most of the paint peeling off in the protuberance rings, the exact impact of the small protuberances was not quantified. Far up- and downstream, no impact could be detected. However, directly after the protuberances in the second ring, a small increase in pressure of 0.03 to $0.04C_P$ was observed. Instead, the big protuberance lead to an increase in pressure upstream of it, and a low pressure zone at around $-0.33C_P$ downstream of it.

Starting with the impact of protuberances on the shocks, for $\alpha = 0^\circ$ the protuberances were found to lower the strength of the second shock. At the azimuthal position of the big protuberance, an increase in ΔC_P was seen relative to other azimuthal positions, but the shock strength was still lower than in the no protuberance configuration. No impact or changes in position were observed on the first shock. The protuberances may also have impacted the shock strength $\alpha = 4^\circ$, but no direct comparisons could be made due to lack of data at $\alpha = 0^\circ$. However, no increase was detected at the big protuberance location.

The protuberances were found to significantly impact the separated flow. An overall increase in separation length was observed due to the protuberances. The biggest impact was found at the position of the big protuberance. Further away from this, the increase in separation length decreased. It is expected that the separation length is similar to the no protuberances configuration at 90° away from the big protuberance. This is also seen in pressure tap data. However, in the separated flow, the pressure levels matched closely to those observed in the no protuberance configuration until the reattachment point. This indicates a low impact of the first protuberance ring on the C_P.

9.1. Recommendations

The implementation of PSP presented in this report proved to be relatively successful for its intended purposes. The up to $2.5kPa$ uncertainty is relatively low in the transonic flow regime that was used to study the models. Furthermore, flow features were clearly recognised in the PSP data and the author was able to extract most of their locations. Despite this, there is still a lot of room for improvement and more to investigate on the models. To distinguish between PSP-related and HHF-related recommendations, this section is split into two parts. The first delves into potential improvements and other recommendations for future PSP implementations. The second focuses on the HHF investigation, highlighting what can be improved and what future steps could encompass.

9.1.1. Recommendations for PSP Improvements

In this subsection, suggested recommendations have been grouped into different groups. Some recommendations are relatively easy to implement, whereas others would require significant changes to the test setup and data analysis.

- **Painting and Curing Improvements**

As discussed in the report, the painting requires some significant improvement. Data quality on the Model 11 was relatively low due to the rash pattern found over the model. While this was somewhat improved for the Vega-E model, it is not perfected yet. Further improvements to the painting should be made to ensure that this does not occur anymore. This would be especially detrimental on investigations where a high spatial resolution is a must, as finding exact positions of flow features is complicated by the rash pattern. A potential way to do this is to ask for help from a partner institute, such as DLR. It would be good if someone at the faculty was trained specifically for painting PSP models.

Other improvements can also be made to the painting. First, the use of a basecoat is recommended to improve adhesion characteristics. Using a white basecoat can furthermore increase paint luminosity, which benefits the measurements. One of the biggest issues throughout all measurements was paint delamination. This was especially important near the edge of the paint and near steep geometry changes. If the delamination can eliminated, data quality would improve. In a similar vein to delamination, extra care should be taken at the steep geometry changes or other places where air could be trapped. During curing, this air expands causing bubbles in the paint, which enhance delamination and change the local flow.

In addition, the author suggests painting the models over a larger area than the expected measurement area. Measurement points at the edges of the paint were found to have large errors ($\pm 50kPa$) and had to be constantly masked away. This has not discussed in this report, but some of these "edge errors" can be seen in the PSP images. To reduce the amount of data processing, painting an area that is larger than the expected measurement area would improve overall image quality, and also mitigate some potential errors due to paint peeling at the edge of the paint.

Lastly, before curing, the model should be cleaned with pressurised air, to ensure that any paint flakes or dust is removed from the surface. After curing, these were found to stick to the surface and lead to local changes in the flow and PSP errors. This should always be done even when none are visible.

- **Calibration Improvements**

While the Paint could be used with the calibration that was provided by ISSI, performing a calibration on site would ensure that data for the correct P, T range is available and reduce the uncertainty of the measurement. Currently, the pressure uncertainty from the calibration uncertainty was around $1kPa$. With a proper calibration, this can be mitigated to the measurement error of the calibration setup ($400Pa$ or lower, mostly dependent on temperature errors).

The author believes that the calibration approach that was used during this project can work with some adjustment. The improvements that would be needed to do so are:

- A better way to acquire temperature and pressure data. During this thesis, both were acquired by manually noting the values down. Having a program capable of collecting both simultaneously when the camera is recording would massively improve the data acquisition process. This would allows the experiments to be finished faster, thereby diminishing the paint decay during measurements.
- Optimize thermocouple placement on the peltier element. Currently, the thermocouple was placed on the side of the peltier element. However, the temperature distribution of the coupon and the peltier element is unknown. Placing it somewhere that better represents the mean coupon temperature would decrease the temperature uncertainty. Furthermore, using multiple thermocouples could be used in conjunction to have a more accurate estimation of the true temperature.
- Improve the sealing on the calibration box. The box used for the calibration experiments was leaking, making it hard to hold a specific pressure value.

In addition, other smaller improvements can be made to the calibration process. These would not necessarily decrease the data uncertainty, but would slightly improve the calibration process.

- The coupons were made to be 4x4cm. These can be made smaller to save some paint (e.g. 3x3cm).
- Install a PID controlled to set the peltier element temperature. In this thesis, temperature were set manually by varying the peltier element voltage and current. Having this done automatically would increase the speed of the process.
- Change the cover of the calibration box. The plexiglass cover currently in use is scratched, leading to some uneven light refraction. It is unclear whether this impacts measurements.

- **Temperature Corrections**

In this thesis, two thermocouples were used at the edge of the model to correct for the trends in temperature. As aforementioned, this gave an uncertainty of up to $1.5kPa$ depending on model temperature. In addition, by combining pressure data calculated using the reference before and the reference after the run, some thermal errors are mitigated. While this was good enough for the current measurements, for other models temperature gradients may be larger. Especially in thin walled models, temperature errors could lead to large uncertainties in the pressure. As discussed in Section 4.5 there are a lot of different ways to account for temperature errors.

However, the author recommends three approaches to do so. The first is taking either TSP or IR measurements simultaneously to the PSP measurements. This first approach would intensify data processing. Here, TSP / IR data would need to be matched with PSP data, which in turn may require improvements in image dewarping. However, this would only be possible for symmetric models, as the TSP / IR measurements would need to be taken from the opposite side. Furthermore, painting would become more complicated if TSP is used. In turn, this would be the best way to mitigate thermal errors.

The second approach would be placing more evenly spread thermocouples throughout the model. An expected temperature distribution can then be created using the thermocouple data. This could potentially be done by doing separate IR measurements and relating the thermocouple temperatures to an IR distribution. This was also attempted in the current thesis to no avail, but should be more effective with more distribution thermocouples.

The last potential method would be to use multi-luminophore dyes. These have a negligible thermal quenching uncertainty, but would necessitate a much more complex PSP measurement and data processing setup, involving combining data from multiple cameras with different perspectives. Furthermore, additional bandpass filters would be needed, which may require very specific bandpass wavelengths depending on the dyes.

Lastly, it was also observed that the model had an uneven temperature distribution during the reference image acquisition. The most optimal temperature correction would also take this into account, again necessitating a more data processing and setup.

- **Dewarping Improvements**

While the image alignment using here worked almost perfectly, the dewarping procedure used in this thesis left much to be desired. A lot can be improved here that would give much better data quality, and allow more precise determination of flow features. First, the way fiducial marks were placed can be significantly improved. During this thesis, they were placed by hand using a whiteboard marker. This yielded unevenly spread fiducial "potatoes" of different shapes and sizes, which made detecting the fiducial marks an arduous process. Most of the time spent data processing went into ensuring that the correct fiducial marks were detected for the image alignment. By having more evenly sized fiducial marks, detection algorithm parameters can be made more strict, leading to less spurious marks being detected.

A possible way to improve this is by having a 3D printed outline of the model with holes the size of the fiducial marks. The holes can be painted with a different paint or filled in with markers. This would also solve the spreading issue. By 3D printing the outline, the exact position of the holes can be known. During this thesis, they were measurement by hand, which led to additional dewarping errors. In addition, only the x coordinate was measurement, which disallowed for 3D dewarping corrections. With the 3D printed outline approach, exact (x,y,z) coordinates would be known a-priori. These can also be optimized for the chosen dewarping procedure.

In addition, better dewarping algorithms should be implemented. The algorithms used in this thesis are intended and best applicable to dewarping of 2D objects and image registration. Implementation of image resection would yield a better dewarping results. This would however require a CFD or FEM mesh of the model. In addition, the resection procedure is computationally heavy. The added benefit of image resection would be that it allows for self-illumination corrections.

- **Suggestions for Future PSP Implementations**

Lastly, below some recommendations for future PSP implementations can be found:

- Find a way to make our own paint without relying on ISSI. This approach would be cheaper and allow the paint to be optimized for its intended application. However, this would be very time (and money) consuming to implement, as the aerospace faculty currently lacks all the necessary resources and expertise to do so. However, in the long run this would yield a reduction in costs and simplify the use of PSP in Delft.
- Move on to fast PSP. This would open up many different avenues of research. First improvements to the calibration and painting have to be made as suggested previously. If AA PSP is desired, a chemical setup is required beforehand. Instead, for PC-PSP a different spraying hood may also be required. PC-PSP can pose significant health risks as nanoparticles are used which can be dangerous, and may also be complex to implement.
- Implement a setup where camera flat-field corrections can be obtained. This is mostly relevant for standard PSP, but is expected to significantly reduce PSP noise.
- Make our own PSP lamps that and quantify the spectral characteristics of the lamps. Having a database of the spectral characteristics of the lamps would facilitate PSP usage.
- In the future, a wind tunnel run should be done after closing the tunnel without acquiring any data. In this thesis, the first experiments after closing the tunnel were found to have wrong pressure values. Further investigation into why this happens would also suffice if a correction method is available.
- For other applications, lifetime based PSP might be beneficial over the intensity based. This includes more flexible models (e.g. shock impingement experiments or airfoils) or rotating models. Adapting the code to enable this method to be used would be good, enabling users to choose which method is preferred. In terms of the changes to the setup, not much adaption is needed. Equipment used in lifetime based PSP is very similar to PIV equipment. The only new equipment that would be required is an UV lamp that can flash over short periods of time.

9.2. Future Hammerhead Research Recommendations

The HHF results obtained in this study will aid in the design of the Vega-E launcher and allow for verification and validation of future CFD simulations that are planned on the Vega-E model. However, the data that was obtained in this thesis can be further improved. In addition, further experimental research can be done on the Vega-E model.

The best way to improve the data that was obtained here is by performing a blockage correction. Blockage corrections in the transonic regime are difficult to obtain, but would significantly improve the obtained C_P distribution. This was seen for the Model 11, where a simple blockage correction allowed for the data to closely match the original dataset. Another approach would be to re-run experiments using slotted wind tunnel walls. However, the author believes that applying blockage corrections to already obtained results would be better.

In addition, D'Aguanno et al. [44] reconstructed pressure data around the Vega-E model using PIV. By using the PSP results, this reconstruction could potentially be improved. The combined reconstruction could again serve to better validate CFD computations.

Experimentally, a lot more research could be done on the Vega-E model. However, most interestingly would be to investigate the pressure fluctuations on the model at different configurations. The most optimal way to investigate this would be to use Fast PSP. This would allow the buffeting phenomenon to be fully quantified from an aerodynamic perspective. Further structural analysis could then be used to study the impact of the aerodynamic fluctuation on the structure of the launcher.

Implementing fast PSP would require a lot of steps, as mentioned in the PSP recommendations. However, the standard PSP implementation used in this thesis was created with the intention to in the future move to Fast PSP. It is therefore already geared to be used for fast PSP as a next step. The already obtained standard-PSP data would furthermore aid in the implementation of fast PSP. Alongside this, other areas of interest that could be investigated experimentally include:

- Looking at higher Mach numbers. The TST only allows up to M = 0.85, but supersonic Mach numbers could also be of interest.
- Changing the boat-tail angle. Other boat-tail angles could be study to determine their impact on the flowfield.
- Further investigate the pressure bump at the end of the boat-tail. This is low priority, as it likely does not cause any issues.
- Perform experiments with the lower stages. The model used here does not have the first stage of the Vega-E launcher, which has a larger diameter. On the Model 11, the lower stage was found to have high pressure fluctuations and slightly change the upstream C_P.
- If fast PSP is implemented, performing BOS simultaneously with fast PSP could provide valuable information about the overall flowfield.
- Investigate the strange pattern of the reattachment point seen at M=0.7, $\alpha = 4°$. This could hint at a flow feature that may require further investigation. It could also have been a measurement error.

References

[1] Avelar, A. C., Filho, J. B. P. F., Medeiros, J. G., and Romero, G. M., “Experimental analysis of flowfield on a hammerhead fairing satellite launch vehicle in transonic regime using Pressure Sensitive Paint (PSP),” 2015.

[2] Coe, C., and Nute, J., “X-646 The Effects of Some Variation in Launch-Vehicle Nose Shape on Steady and Fluctuation Pressures at Transonic Speeds,” Tech. rep., NASA, 3 1962.

[3] Coe, B. F. C., Nute, J. B., and Field, M., “X-778 STEADY AND FLUCTUATING PRESSURES AT TRANSONIC SPEEDS ON HAMMERHEAD LAUNCK VEHIC LES,” Tech. rep., NASA, 1962.

[4] Panda, J., Garbeff, T. J., Burnside, N. J., and Ross, J. C., “Unsteady pressure fluctuations measured on a hammerhead space vehicle and comparison with Coe and Nute’s 1962 data,” *International Journal of Aeroacoustics*, Vol. 17, 2018, pp. 70–87. doi:10.1177/1475472X17743626.

[5] Ericsson, L. E., “Hammerhead wake effects on elastic vehicle dynamics,” *Journal of Spacecraft and Rockets*, Vol. 34, 1997, pp. 145–151. doi:10.2514/2.3193.

[6] Suresh, B., and Sivan, K., *Integrated Design for Space Transportation System*, Springer, 2015. doi:0.1007/978-81-322-2532-4.

[7] Murman, S. M., Blonigan, P. J., and Diosady, L. T., “Comparison of transonic buffet simulations with unsteady PSP measurements for a hammerhead payload fairing,” American Institute of Aeronautics and Astronautics Inc., 2017. doi:10.2514/6.2017-1404.

[8] Sellers, M. E., Nelson, M. A., Roozeboom, N. H., and Burnside, N. J., “Evaluation of Unsteady Pressure Sensitive Paint Measurement Technique for Space Launch Vehicle Buffet Determination,” 2017.

[9] Heany, P., Soranna, F., Sekula, M., Piatak, D., and Ramey, J., “Analysis of Transonic Unsteady Aerodynamic Environments using Unsteady Pressure Sensitive Paint for the Space Launch System Block 1 Cargo Launch Vehicle,” *AIAA*, 2021.

[10] Liu, T., Sullivan, J. P., Asai, K., Klein, C., and Egami, Y., *Pressure and Temperature Sensitive Paints*, second edition ed., Springer International Publishing, 2021. doi:10.1007/978-3-030-68056-5.

[11] Mcmillin, S. N., Shea, P. R., Dalle, D. J., Rogers, S. E., Roozeboom, N. H., Meeroff, J. G., and Lee, H. C., “Comparison of Space Launch System Aerodynamic Surface Pressure Measurements from Experimental Testing and CFD,” 2019.

[12] Sellers, M. E., Nelson, M. A., and Crafton, J. W., “Dynamic Pressure Sensitive Paint Demonstration in the AEDC Propulsion Wind Tunnel 16T *,” 2016.

[13] Avelar, A. C., de Medeiros, J. G., and Filho, J. B. P. F., “EXPERIMENTAL STUDY OF GEOMETRIC VARIATIONS EFFECT ON THE FLOW PATTERNS ON A HAMMERHEAD SATELLITE LAUNCH VEHICLE,” 2016.

[14] Roozeboom, N. H., Murakami, D. D., Li, J., Shaw-Lecerf, M. A., Lash, E. L., Califano, N. W., Stremel, P. M., Lyons, K. R., Baerny, J., Barreras, C. E., Ortega, J., Kato, K. H., Hand, L. A., and Mclachlan, B. G., “NASA’s Unsteady Pressure-Sensitive Paint Research and Operational Capability Developments,” 2023.

[15] Niimi, T., Yoshida, M., Oshima, Y., Mori, H., Egami, Y., Asai, K., and Nishide, H., “Application of pressure- sensitive paints to low-pressure range.” *Journal of Thermophysics and Heat Transfer*, Vol. 19, 2005.

[16] Nakakita, K., Takama, Y., Imagawa, K., and Kato, H., “Unsteady PSP measurement of transonic unsteady flow field around a rocket fairing model,” American Institute of Aeronautics and Astronautics Inc., 2012. doi:10.2514/6.2012-2758.

[17] D’Aguanno, A., Schrijer, F. F. J., and van Oudheusden, B. W., “Transonic PIV based unsteady pressure measurements for launcher environment TUPLE,” Tech. rep., TU Delft, Unpublished, paper available from the authors, 2024.

[18] D’Aguanno, A., Romero, A. G., Schrijer, F. F. J., and van Oudheusden, B. W., “Flow analysis of hammerhead launcher geometries in the transonic regime,” American Institute of Aeronautics and Astronautics Inc, AIAA, 2024. doi:10.2514/6.2024-2145.

[19] Zandbergen, B., *Aerospace Design & System Engineering Elements I Part: Launcher Design and Sizing*, Faculty of Aerospace engineering, 2015.

[20] Sunil, K., Johri, I., and Priyadarshi, P., “Aerodynamic Shape Optimization of Payload Fairing Boat Tail for Various Diameter Ratios,” *Journal of Spacecraft and Rockets*, Vol. 59, 2022, pp. 1135–1148. doi:10.2514/1.A35215.

[21] Kumar, R., Viswanath, P. R., and Prabhu, A., “Mean and fluctuating pressure in boat-tail separated flows at transonic speeds,” *Journal of Spacecraft and Rockets*, Vol. 39, 2002, pp. 430–438. doi:10.2514/2.3826.

[22] Panda, J., “Aeroacoustics of Space Vehicles Presentation for Stanford Fluid Mechanics Seminar Jay Panda (NASA ARC),” Stanford Fluid Mechanics Seminar, 2014. URL `https://ntrs.nasa.gov/api/citations/20140008652/downloads/20140008652.pdf`.

[23] Camussi, R., Guj, G., Imperatore, B., Pizzicaroli, A., and Perigo, D., “Wall pressure fluctuations induced by transonic boundary layers on a launcher model,” *Aerospace Science and Technology*, Vol. 11, 2007, pp. 349–359.

doi:10.1016/j.ast.2007.01.004.

[24] Mehta, R. C., “Computational Fluid Dynamics Analysis and Design of Payload Shroud of Satellite Launch Vehicle,” *Scholars Journal of Engineering and Technology*, Vol. 10, 2022, pp. 16–34. doi:10.36347/sjet.2022.v10i04.001.

[25] Romero, A. G., “Experimental Investigation into the Aerodynamics of Hammerhead Launcher Configurations in Transonic Regime,” Master’s thesis, 2023.

[26] Romero, A. G., “Aerodynamic Study on Hammerhead Payload Configurations MSc. Literature Study Report,” Master’s thesis, 2023.

[27] Liu, Y., Wang, G., Zhu, H., and Ye, Z., “Numerical analysis of transonic buffet flow around a hammerhead payload fairing,” *Aerospace Science and Technology*, Vol. 84, 2019, pp. 604–619. doi:10.1016/j.ast.2018.11.002.

[28] Yanamashetti, G., Singh, D. B., Suryanarayana, G. K., and Mukherjee, R., “Passive control of transonic flow over a blunt body using aerospikes,” *Journal of Spacecraft and Rockets*, Vol. 57, 2020, pp. 945–955. doi:10.2514/1.A34668.

[29] Camussi, R., Marco, A. D., Stoica, C., Bernardini, M., Stella, F., Gregorio, F. D., Paglia, F., Romano, L., and Barbagallo, D., “Wind tunnel measurements of the surface pressure fluctuations on the new VEGA-C space launcher,” *Aerospace Science and Technology*, Vol. 99, 2020. doi:10.1016/j.ast.2020.105772.

[30] Panda, J., Roozeboom, N. H., and Ross, J. C., “Wavenumber-Frequency Spectra of Pressure Fluctuations on a Generic Space Vehicle Measured via Unsteady Pressure-Sensitive Paint,” *AIAA SciTech*, 2017, pp. 9–13.

[31] Priebe, S., and Martín, M. P., “Low-frequency unsteadiness in shock wave-turbulent boundary layer interaction,” *Journal of Fluid Mechanics*, Vol. 699, 2012, pp. 1–49. doi:10.1017/jfm.2011.560.

[32] Clemens, N. T., and Narayanaswamy, V., “Low-frequency unsteadiness of shock wave/turbulent boundary layer interactions,” *Annual Review of Fluid Mechanics*, Vol. 46, 2014, pp. 469–492. doi:10.1146/annurev-fluid-010313-141346.

[33] Chen, L., Asai, K., Nonomura, T., Xi, G., and Liu, T., “A review of Backward-Facing Step (BFS) flow mechanisms, heat transfer and control,” *Thermal Science and Engineering Progress*, Vol. 6, 2018, pp. 194–216. doi:10.1016/j.tsep.2018.04.004.

[34] Schrijer, Horchler, F., Deck, T., and Gent, S. V., “Comparison of high speed PIV experiments, unsteady pressure measurements and DES computations of a transonic Ariane 5 base-flow using POD: An experimental study,” 7th European Conference For Aeronautics And Space Sciences, 2017.

[35] Bitter, M., Hara, T., Hain, R., Yorita, D., Asai, K., and Kähler, C. J., “Characterization of pressure dynamics in an axisymmetric separating/reattaching flow using fast-responding pressure-sensitive paint,” *Experiments in Fluids*, Vol. 53, 2012, pp. 1737–1749. doi:10.1007/s00348-012-1380-7.

[36] Soranna, F., Heaney, P. S., Sekula, M. K., Piatak, D. J., and Ramey, J. M., “Coherence Analysis of the Space Launch System using Unsteady Pressure Sensitive Paint,” 2021. doi:10.2514/6.2021-1834.

[37] Vitagliano, P. L., Gregorio, F. D., Roncioni, P., Paglia, F., and Milana, C., “AERODYNAMIC CHARACTERISATION OF VEGA-C LAUNCHER,” , 9 2019.

[38] Tropea, C., Yarin, A., and Foss, J., *Springer Handbook of Experimental Fluid Mechanics*, 1st ed., Vol. first, springer, 2007.

[39] Murman, S. M., Blonigan, P. J., and Diosady, L. T., “Comparison of transonic buffet simulations with unsteady PSP measurements for a hammerhead payload fairing,” American Institute of Aeronautics and Astronautics Inc., 2017. doi:10.2514/6.2017-1404.

[40] Murman, S. M., and Diosady, L. T., “Simulation of a hammerhead payload fairing in the transonic regime,” American Institute of Aeronautics and Astronautics Inc, AIAA, 2016. doi:10.2514/6.2016-1548.

[41] Cole, H., Erickson, A., and Rainey, A., “NASA SPACE VEHICLE DESIGN CRITERIA (STRUCTURES) BUFFETING DURING ATMOSPHERIC ASCENT,” , 1970.

[42] Schwane, R., “Numerical prediction and experimental validation of unsteady loads on ARIANE5 and VEGA,” *Journal of Spacecraft and Rockets*, Vol. 52, 2015, pp. 54–62. doi:10.2514/1.A32793.

[43] Brouwer, K. R., Perez, R., Beberniss, T. J., and Spottswood, S. M., “Surface Pressure Measurements and Predictions in Shock-Dominated Flows,” American Institute of Aeronautics and Astronautics (AIAA), 2023. doi:10.2514/6.2023-4134.

[44] D’Aguanno, A., Schrijer, F., and Oudheusden, B., “Instantaneous Pressure Reconstruction From PIV In Compressible Launcher Environments,” *Proceedings of the International Symposium on the Application of Laser and Imaging Techniques to Fluid Mechanics*, Vol. 21, 2024, pp. 1–24. doi:10.55037/lxlaser.21st.173.

[45] Asai, K., “Basics of Unsteady PSP,” *9th Course on Pressure Sensitive Paints 2023*, German Aerospace Center (DLR), Göttingen, Germany, 2023.

[46] Imai, M., Nakakita, K., and Kameda, M., “Random-dot pressure-sensitive paint for time-resolved measurement of deformation and surface pressure of transonic wing flutter,” *Experiments in Fluids*, Vol. 63, 2022. doi:10.1007/s00348-022-03527-1.

[47] Hayashi, T., Kurihara, D., and Sakaue, H., "Differential luminescent imaging method for pressure field measurement," *Measurement: Journal of the International Measurement Confederation*, Vol. 187, 2022. doi: 10.1016/j.measurement.2021.110253.

[48] Klein, C., "Introduction to PSP and TSP," *9th Course on Pressure Sensitive Paints 2023*, German Aerospace Center (DLR), Göttingen, Germany, 2023.

[49] Numata, D., Fujii, S., Nagai, H., and Asai, K., "Ultrafast-response anodized-Aluminum pressure-sensitive paints for unsteady flow measurement," American Institute of Aeronautics and Astronautics Inc., 2017, pp. 1118–1125. doi:10.2514/1.J054886.

[50] Sant, Y. L., "Overview of the self-illumination effect applied to pressure sensitive paint applications," 2001, pp. 159–170. doi:10.1109/iciasf.2001.960247.

[51] Sugimoto, T., Sugioka, Y., Numata, D., Nagai, H., and Asai, K., "Characterization of frequency response of pressure-sensitive paints," Tech. rep., 2017. doi:10.2514/1.J054985.

[52] Henne, U., "Intensity method and pressure calculation," *9th Course on Pressure Sensitive Paints 2023*, German Aerospace Center (DLR), Göttingen, Germany, 2023.

[53] Gregory, J. W., and Sullivan, J. P., "Effect of quenching kinetics on unsteady response of pressure-sensitive paint," 2006, pp. 634–645. doi:10.2514/1.15124.

[54] Powell, J. M., Murman, S. M., Ngo, C. L., Roozeboom, N. H., Murakami, D. D., Baerny, J. K., and Li, J., "Development of unsteady-psp data processing and analysis tools for the nasa ames unitary 11ft wind tunnel," American Institute of Aeronautics and Astronautics Inc, AIAA, 2020. doi:10.2514/6.2020-0292.

[55] Roozeboom, N. H., Powell, J., Baerny, J. K., Murakami, D. D., Ngo, C. L., Garbeff, T. J., Ross, J. C., and Flach, R., "Development of Unsteady Pressure-Sensitive Paint Application on NASA Space Launch System," , 2019.

[56] Yorita, D., "Lifetime based PSP," *9th Course on Pressure Sensitive Paints 2023*, German Aerospace Center (DLR), Göttingen, Germany, 2023.

[57] Imai, M., Nakakita, K., and Kameda, M., "DMD Analysis of Simultaneous Pressure and Deformation Data of a Deformed Wing Measured by Random-dot PSP," 2023. doi:10.2514/6.2023-3537.

[58] Nakakita, K., Kurita, M., Mitsuo, K., and Watanabe, S., "Practical pressure-sensitive paint measurement system for industrial wind tunnels at JAXA," Institute of Physics Publishing, 2006, pp. 359–366. doi:10.1088/0957-0233/17/2/017.

[59] Huang, C. Y., Lin, Y. F., Huang, Y. X., and Chung, K. M., "Pressure-sensitive paint measurements with temperature correction on the wing of AGARD-B under transonic flow conditions," *Measurement Science and Technology*, Vol. 32, 2021. doi:10.1088/1361-6501/ac0073.

[60] Avelar, A. C., Filho, J. B. F., and Silva, L. M., "Transonic aerodynamic analysis of different forebody shapes of aerospace vehicles," *Journal of Aerospace Technology and Management*, Vol. 12, 2020. doi:10.5028/jatm.v12.1103.

[61] Pokela, R. C., Gustavsson, J., and Kumar, R., "Surface Pressure Measurements on an Axisymmetric Body with Fins Using Pressure Sensitive Paint," 2023. doi:10.2514/6.2023-3677.

[62] Mébarki, Y., "PSP image processing using open-source libraries," *9th Course on Pressure Sensitive Paints 2023*, German Aerospace Center (DLR), Göttingen, Germany, 2023.

[63] Avelar, A. C., Basso, E., Filho, J. B. P. F., Francisco, C. P. F., and Romero, P. G. M., "Analysis of the flow patterns on the fore-body section of a sounding vehicle in the transonic regime," *Journal of the Brazilian Society of Mechanical Sciences and Engineering*, Vol. 40, 2018. doi:10.1007/s40430-018-1030-y.

[64] Tang, L., Hand, L., Murakami, D., Roozeboom, N., and Shaw-Lecerf, M., "Unsteady Pressure-Sensitive-Paint Shot Noise Reduction," 2021.

[65] Li, J., Lash, E. L., Roozeboom, N. H., Garbeff, T. J., Henze, C. E., Murakami, D. D., Smith, N. T., Baerny, J. K., Hand, L. A., Shaw-Lecerf, M. A., Stremel, P. M., and Tang, L. Z., "Dynamic Mode Decomposition of Unsteady Pressure-Sensitive Paint Measurements for the NASA Unitary Plan Wind Tunnel Tests," , 2022.

[66] Bremner, P. G., "Noise Reduction and Calibration of Unsteady Pressure-Sensitive Paint," *Spacecraft and Launch Vehicle Dynamic Environment Workshop*, NASA, 2022.

[67] Shaw-Lecerf, M. A., Lash, E. L., Murakami, D. D., Roozeboom, N. H., Li, J., and Bremner, P. G., "Methodology for Validation of Unsteady Pressure-Sensitive Paint Measurements using Pressure Transducers," *AIAA*, Vol. 260, 2023.

[68] Fond, B., "Some error sources and corrections in PSP," *9th Course on Pressure Sensitive Paints 2023*, German Aerospace Center (DLR), Göttingen, Germany, 2023.

[69] Egami, Y., Konishi, S., Sato, Y., and Matsuda, Y., "Effects of solvents for luminophore on dynamic and static characteristics of sprayable polymer/ceramic pressure-sensitive paint," *Sensors and Actuators, A: Physical*, Vol. 286, 2019, pp. 188–194. doi:10.1016/j.sna.2018.12.034.

[70] Hayashi, T., and Sakaue, H., "Temperature effects on polymer-ceramic pressure-sensitive paint as a luminescent pressure sensor," *Aerospace*, Vol. 7, 2020. doi:10.3390/AEROSPACE7060080.

[71] Anderson, J. D., *Introduction to flight*, McGraw-Hill, 2008.

[72] Bustard, A., Hayashi, T., Gillespie, H., Davami, J., and Juliano, T. J., "Investigation of a High Speed Inlet/Isolator with Global Surface Measurements and Background Oriented Schlieren," American Institute of Aeronautics and Astronautics (AIAA), 2023. doi:10.2514/6.2023-0119.

[73] Konrath, R., Klein, C., Schröder, A., and Kompenhans, J., "Combined application of pressure sensitive paint and particle image velocimetry to the flow above a delta wing," *Experiments in Fluids*, Vol. 44, 2008, pp. 357–366. doi:10.1007/s00348-007-0445-5.

[74] Bustard, A., Hasegawa, M., Sakaue, H., Juliano, T. J., Noftz, M. E., Shuck, A. J., Jewell, J. S., Poggie, J., and Bisek, N. J., "Fast Pressure-Sensitive Paint Measurements of an Internal Osculating Waverider Inlet Under Quiet and Noisy Flow," American Institute of Aeronautics and Astronautics (AIAA), 2023. doi:10.2514/6.2023-3898.

[75] Huang, Y. X., Wu, H. Y., Chung, K. M., and Chang, K. C., "Pressure distributions on swept/unswept wings using pressure sensitive paint," Institute of Physics Publishing, 2020. doi:10.1088/1742-6596/1509/1/012003.

[76] Gregory, J. W., Sakaue, H., Liu, T., and Sullivan, J. P., "Fast pressure-sensitive paint for flow and acoustic diagnostics," *Annual Review of Fluid Mechanics*, Vol. 46, 2014, pp. 303–330. doi:10.1146/annurev-fluid-010313-141304.

[77] Bell, J. H., and Mclachlan, B. G., "Image registration for pressure-sensitive paint applications," *Experiments in Fluids*, Vol. 22, 1996, p. 86.

[78] Mérienne, M. C., Brion, V., and Abart, J. C., "Unsteady psp measurements of the shock dynamics on a transonic laminar airfoil," American Institute of Aeronautics and Astronautics Inc, AIAA, 2019. doi:10.2514/6.2019-0025.

[79] van Hinsberg, N., "CAMERA SYSTEMS AND THEIR PROPERTIES," *9th Course on Pressure Sensitive Paints 2023*, German Aerospace Center (DLR), Göttingen, Germany, 2023.

[80] Merchant, F. A., Castleman, K. R., and Periasamy, A., *Microscope Image Processing*, Elsevier, 2023, Chap. 10.4.1.1. doi:10.1016/C2019-0-01813-4.

[81] Peng, D., and Liu, Y., "Fast pressure-sensitive paint for understanding complex flows: from regular to harsh environments," *Experiments in Fluids*, Vol. 61, 2020. doi:10.1007/s00348-019-2839-6.

[82] Hilfer, M., "NOISE REDUCTION, IMAGE ENHANCEMENT AND FEATURE EXTRACTION," *9th Course on Pressure Sensitive Paints 2023*, German Aerospace Center (DLR), Göttingen, Germany, 2023.

[83] Kameda, M., Yoshida, M., Sekiya, T., and Nakakita, K., "Humidity effects in the response of a porous pressure-sensitive paint," *Sensors and Actuators, B: Chemical*, Vol. 208, 2015, pp. 399–405. doi:10.1016/j.snb.2014.11.052.

[84] Nebbeling, C., and Bannink, W., "Memorandum M-168: Meting van de specifieke vochtigheid van de lucht in het voorraadvat van de ST15 supersone windtunnel." Tech. rep., Tu Delft, 1969.

[85] D'Aguanno, A., "Physics and Control of Transonic Buffet," Ph.D. thesis, 2023. doi:10.4233/uuid:7e4f868b-7716-4c36-8fa0-b55572d1572b, URL `https://doi.org/10.4233/uuid:7e4f868b-7716-4c36-8fa0-b55572d1572b`.

[86] Giepman, R., "Flow control for oblique shock wave reflections," Ph.D. thesis, 2016. doi:10.4233/uuid:597489bb-0b41-4da2-8ec4-b1bc390f8d2c, URL `https://doi.org/10.4233/uuid:597489bb-`.

[87] van Rijswijk, N., "TST-27Transonic Control," Tech. rep., 2012.

[88] SCHOTT, "SCHOTT N-BK 7® 517642.251," Tech. rep., SCHOTT, 2014. URL `https://www.schott.com/shop/advanced-optics/en/Optical-Glass/N-BK7/c/glass-N-BK7`.

[89] Rabilotta, Z., "Investigation of Transonic Buffet Reduction Devices Using Pressure Sensitive Paint," Master's thesis, 2023.

[90] TAMBE, S. S., "Boundary-layer instability on rotating cones: An experiment-based exploration." Ph.D. thesis, 2022. doi:10.4233/uuid:40ed5b16-bf5a-409e-a28e-74f115f984cf.

[91] Goin, K. L., and Pope, A., *High-speed wind tunnel testing*, New York, JOHN WILEY AND SONS, INC, 1965.

[92] Egami, Y., "Principle of Temperature Sensitive Paint (TSP) method and its Application in Aerodynamic Testing," *9th Course on Pressure Sensitive Paints 2023*, German Aerospace Center (DLR), Göttingen, Germany, 2023.

[93] Mills, A., and Coimbra, C., *Basic Heat and MAss Transfer*, Temporal Publishing, LLC, 2015.

[94] Miller, J. L., Friedman, E., Sanders-Reed, J., Schwertz, K., and McComas, B., *Photonics Rules of Thumb*, 3^{rd} ed., SPIE, 2020. doi:10.1117/3.2553485.

[95] Bernard, V., Staffa, E., Mornstein, V., and Bourek, A., "Infrared camera assessment of skin surface temperature - Effect of emissivity," *Physica Medica*, Vol. 29, 2012. doi:10.1016/j.ejmp.2012.09.003.

[96] Sciacchitano, A., and Scarano, F., "AE4-180 2021 chapter6 Pressure measurements," AE4180 Flow measurement techniques course (2020/2021), 2020.

[97] Schmidt, B., "Schlieren Visualization Ae 104b," , 12 2015.

[98] Nadge, P. M., and Govardhan, R. N., "High Reynolds number flow over a backward-facing step: Structure of the mean separation bubble," *Experiments in Fluids*, Vol. 55, 2014. doi:10.1007/s00348-013-1657-5.

[99] Hudy, L. M., and Naguib, A., "Stochastic estimation of a separated-flow field using wall-pressure-array measurements," *Physics of Fluids*, Vol. 19, 2007. doi:10.1063/1.2472507.

[100] Gentile, V., Schrijer, F. F. J., van Oudheusden, B. W., and Scarano, F., “Organization of an axisymmetric turbulent wake in presence of a central protrusion,” , 2015.

[101] Oka, Y., Nagata, T., Kasai, M., Ozawa, Y., Asai, K., and Nonomura, T., “Practical Fast-Response Anodized-Aluminum Pressure-Sensitive Paint Using Chemical Adsorption Luminophore as Optical Unsteady Pressure Sensor,” *Sensors*, Vol. 22, 2022. doi:10.3390/s22176401.

[102] Ondrus, V., “Pressure sensitive paint- a chemical point if view,” *9th Course on Pressure Sensitive Paints 2023*, German Aerospace Center (DLR), Göttingen, Germany, 2023.

[103] Yomo, K., Ikami, T., Fujita, K., and Nagai, H., “Investigation of Formulations on Pyrene-Based Anodized-Aluminum Pressure-Sensitive Paints for Supersonic Phenomena,” *Sensors*, Vol. 22, 2022. doi:10.3390/s22124430.

[104] Sakaue, H., Tabei, T., and Kameda, M., “Hydrophobic monolayer coating on anodized aluminum pressure-sensitive paint,” *Sensors and Actuators, B: Chemical*, Vol. 119, 2006, pp. 504–511. doi:10.1016/j.snb.2006.01.010.

[105] Nakakita, K., “UNSTEADY AERODYNAMIC INFORMATION EXTRACTION USING FFT-BASED UNSTEADY PRESSURE-SENSITIVE PAINT MEASUREMENT,” 2016.

[106] Gongora-Orozco, N., Zare-Behtash, H., and Kontis, K., “Global unsteady pressure-sensitive paint measurements of a moving shock wave using thin-layer chromatography,” *Measurement: Journal of the International Measurement Confederation*, Vol. 43, 2010, pp. 152–155. doi:10.1016/j.measurement.2009.06.011.

[107] Funderburk, M. L., and Narayanaswamy, V., “Spectral signal quality of fast pressure sensitive paint measurements in turbulent shock-wave/boundary layer interactions,” *Experiments in Fluids*, Vol. 60, 2019. doi:10.1007/s00348-019-2799-x.

[108] Ahn, Y.-J., Musta, M. N., Eitner, M. A., Sirohi, J., and Clemens, N. T., “Unsteadiness of Mach 5 Ramp-Induced Shock-Wave/Boundary-Layer Interaction using high-speed PIV and fast-response PSP,” American Institute of Aeronautics and Astronautics (AIAA), 2023. doi:10.2514/6.2023-3573.

[109] Gregory, J. W., Ali, M. Y., and Pandey, A., “Dynamic mode decomposition of fast pressure sensitive paint data,” *Sensors (Switzerland)*, Vol. 16, 2016. doi:10.3390/s16060862.

[110] Liu, X., Qin, C., Tang, Y., Zhao, K., Wang, P., Liu, Y., He, C., and Peng, D., “Resolving dynamic features of kilohertz pressure fluctuations using fast-responding pressure-sensitive paint: measurement of inclined jet impingement,” *Experiments in Fluids*, Vol. 63, 2022. doi:10.1007/s00348-022-03419-4.

[111] Sugioka, Y., Arakida, K., Kasai, M., Nonomura, T., Asai, K., Egami, Y., and Nakakita, K., “Evaluation of the characteristics and coating film structure of polymer/ceramic pressure-sensitive paint,” *Sensors (Switzerland)*, Vol. 18, 2018. doi:10.3390/s18114041.

[112] Kasai, M., Suzuki, A., Egami, Y., Nonomura, T., and Asai, K., “A platinum-based fast-response pressure-sensitive paint containing hydrophobic titanium dioxide,” *Sensors and Actuators A: Physical*, Vol. 350, 2023. doi:10.1016/j.sna.2022.114140.

[113] Gardner, A. D., Klein, C., Sachs, W. E., Henne, U., Mai, H., and Richter, K., “Investigation of three-dimensional dynamic stall on an airfoil using fast-response pressure-sensitive paint,” *Experiments in Fluids*, Vol. 55, 2014, pp. 1–14. doi:10.1007/s00348-014-1807-4.

[114] Sugioka, Y., Koike, S., Nakakita, K., Numata, D., Nonomura, T., and Asai, K., “Experimental analysis of transonic buffet on a 3D swept wing using fast-response pressure-sensitive paint,” *Experiments in Fluids*, Vol. 59, 2018. doi:10.1007/s00348-018-2565-5.

[115] Gonzalez, R. C., and Woods, R. E., *Digital image processing*, 4th ed., Pearson Education, 2018.

[116] Burggraaff, O., Schmidt, N., Zamorano, J., Pauly, K., Pascual, S., Tapia, C., Spyrakos, E., and Snik, F., “Standardized spectral and radiometric calibration of consumer cameras,” *Optics Express*, Vol. 27, 2019, p. 19075. doi:10.1364/oe.27.019075.

[117] Possolo, A., Murman, S. M., and Maier, R., “Gauging uncertainty in pressure measurement due to spectral variability of excitation illumination,” The Boeing Company, 1998.

[118] Corcos, G. M., “Resolution of Pressure in Turbulence,” *The Journal of the Acoustical Society of America*, Vol. 35, 1963, pp. 192–199. doi:10.1121/1.1918431.

[119] Mansurov, N., “What is Vignetting?” https://photographylife.com/what-is-vignetting, april 2020.

[120] *Smear in CCD-Sensors*, PCO COMPUTER OPTICS, Ludwigsplatz 4, D-93309 Kelheim, Germany, 2005.

[121] Abdel-Aziz, Y. I., and Karara, H. M., “Direct linear transformation from comparator coordinates into object space coordinates in close-range photogrammetry,” *Photogrammetric Engineering and Remote Sensing*, Vol. 81, 2015, pp. 103–107. doi:10.14358/PERS.81.2.103.

[122] Crafton, J., Gregory, J., Sellers, M., and Ruyten, W., “Data processing tools for dynamic pressure-sensitive paint,” American Institute of Aeronautics and Astronautics Inc., 2017. doi:10.2514/6.2017-0701.

[123] Welch, P. D., “The Use of Fast Fourier Transform for the Estimation of Power Spectra: A Method Based on Time Averaging Over Short, Modified Periodograms,” *IEEE TRANSACTIONS ON AUDIO A N D ELECTROACOUSTICS*, Vol. 15, 1967.

[124] Taira, K., Brunton, S. L., Dawson, S. T., Rowley, C. W., Colonius, T., McKeon, B. J., Schmidt, O. T., Gordeyev, S.,

Theofilis, V., and Ukeiley, L. S., “Modal analysis of fluid flows: An overview,” *AIAA Journal*, Vol. 55, 2017, pp. 4013–4041. doi:10.2514/1.J056060.

[125] Weiss, J., “A Tutorial on the Proper Orthogonal Decomposition,” 2019 AIAA Aviation Forum., 2019, pp. 17–21. doi:10.14279/depositonce-8512, URL `https://doi.org/10.14279/depositonce-8512`.

PART IV

Appendices and Extra Material

A Overview of Luminophores

In this appendix a description is given of the most commonly used luminophores for PSP / TSP measurements.

A.1. Common Luminophore Types

This section describes the types of luminophores used for PSP measurements. An overview of all listed options can be found in Section A.3. First, the types of pressure sensitive luminophores that are used for PSP are discussed. A short description of other luminophores used for PSP then follows. Lastly, multi-luminophore paints are described. The paint used for this thesis project is a simple, single luminophore paint with FIB as polymer.

Pressure Sensitive Luminophores

For PSP there exist three families of pressure sensitive luminophores that are used for most experiments. All PSP measurement types can be done using members of these families. Each family is characterised by a shared molecular compound or chemical group. Members of the families are "chemical derivatives"[27] of the shared main molecule. That is to say, each member has slightly different atomic composition, but a similar overall structure. Different members of a family can have significantly different responses to excitation, temperature and oxygen quenching. The three families of luminophores are [10]:

- Pyrene derivatives
- Ruthenium polypyridyls
- (Platinum) Porphyrin derivatives

Note that most porphyrin derivatives that are used for PSP are platinum based. Due to this, literature often calls this group "Platinum Porphyrins"[10]. However, porphyrins that do not contain platinum are also used for PSP. An example of this is H_2TCPP, which has good lifetime characteristics that can be used for fast PSP measurements [101]. To avoid confusion in this regard, the Author chose to list this group as "(Platinum) Porphyrin derivatives".

Not all members of the families are suitable for fast PSP applications. Each family has multiple different members that can be used [53]. There is no consensus in literature about which luminophore is best applicable for which type of measurement. For the experiments that were performed in this thesis, the luminophore was a platinum porphyrin named PtTFPP. This was part of the commercial UniFIB[6] paint. In general, when not purchasing pre-made paint, the key selection requirements are commercial availability, excitation light availability and pressure and temperature sensitivity.

Table A.1 gives a list of the luminophores that were found in literature for each family. This is not a complete overview, as many different derivatives exist not listed here. Furthermore, the exact luminophores used for experiments are sometimes hidden by their respective research and commercial institutes. Table A.1 furthermore denotes which luminophores were used by articles cited in this report. Lastly, while luminescent response characteristics can highly differ between derivatives of the same family, each luminophore family has some overarching characteristics that can be attributed to the entire group. These are listed in the last column of Table A.1.

Other Luminophore Types

Alongside pressure sensitive luminophores, PSP measurements sometimes make use of temperature sensitive luminophores and reference dyes. These are used to give additional information on the flow field or apply corrections to PSP measurements. To do so they are either applied simultaneously with a pressure sensitive luminophore or by repainting the model and measuring at the same test conditions. Both groups

---

[27] `https://en.wikipedia.org/wiki/Derivative_(chemistry)`, retrieved July 2023

are described in the following text.

Luminophore	**Examples** [10]	**Used by**	**Main characteristics [10, 45, 102]**
Pyrene Derivatives	• Binary paints (B1, PyGd) • Gottingen Dyes • DLR02 • PBA • PSA	• DLR [10, 73] • TsAGI [10] • ONERA [10, 50] • Tohoku University [49, 103]	• $300-400nm$ excitation • Wide emission band • Short lifetime $\mathcal{O}(0.1\mu s)$ • Sublimation risk • Prone to photodegradation • Weak T dependence • Applicable with AA & PC-PSP • Can be cheap • High P sensitivity
Ruthenium Polypyridyls	• Ru(ph$_2$-phen) • Ru(bpy)$_3^{2+}$ • Ru(dpp)	• JAXA [15, 16, 58, 83, 104, 105] • Japan [106] • USA universities [47, 53] [70, 72, 74, 107, 108] • Tohoku University [51] • Taiwan [59, 75] • Onera [78]	• $337, 457nm$ excitation • $600nm$ emission peak • Wide emission band • Short lifetime $\mathcal{O}(10\mu s)$ • Low luminescence at p_{atm} • Applicable to fast PSP • Expensive • Difficult to apply to model when using polymers • Well absorbed by AA-PSP
(Platinum) Porphyrin Derivatives	• PtTFPP • PtOEP • PdOEP • PtTFPL • PtTCPP • PdTCPP • H_2TFPP • H_2TCPP	**PtTFPP** • ISSI PSPs used by: NASA [8, 12, 14, 109] AEB [1, 13, 60, 63] Other [43, 53, 107, 110] • Tohoku University [51, 111] [112] • DLR [35, 113] • JAXA [15, 46, 57, 58, 114] • Japan [69] • USA [61] **H$_2$TCPP** • Tohoku University [51, 101] **PtOEP** • JAXA [15]	• $394nm$ excitation peak • Can be excited with green light • $660nm$ emission peak • Long lifetime for metalloporphyrins (Pt, Pd) of $\mathcal{O}(10-100)\mu s$ • Low lifetime for H_2 porphyrins of $\mathcal{O}(0.1)\mu s$ • High O_2 sensitivity • Low luminescence at p_{atm} • Applicable to fast PSP • Very expensive • Metal atom can change • High photostability

Table A.1: Description of commonly used luminophore types and past applications of that luminophore.

Temperature Sensitive Luminophores

TSPs are used for heat transfer and temperature measurements. As one of the biggest error sources of PSP are temperature gradients [68], TSPs are often used as a way to correct for temperature. This is done various ways, as will be expanded upon in Section A.2 and Chapter 4. Unlike PSPs, TSPs often make use of oxygen impermeable binders as TSPs can be prone to oxygen quenching. Given that PSPs are always temperature sensitive, they can act as TSPs by using these oxygen impermeable binders [10]. This is sometimes done with ruthenium polypyridyls. Generally, other complexes or derivatives are used for TSP than PSP.

Similarly to PSP, there are two main groups of TSPs, namely the "Ruthenium complexes" and "Europium complexes" [10, 92]. Both groups contain a metallic working atom (Ru and Eu respectively) in different molecular families. Ruthenium complexes also include low oxygen sensitivity ruthenium polypyridyl derivatives. Outside these two groups, there are other different paint types that can be used as TSPs, such as 'quantum dots'. For more information on TSPs and other dyes, the book of Liu et al. [10] can be consulted.

Overall, the range of applicability of TSPs ranges from cryogenic to high temperature ($100-1000K$). Luminophores in either of the metallic complexes significantly differ in applicability, response time and sensitivity. Ruthenium complexes generally have a lower lifetime and can be used for both intensity and lifetime measurements. Europium complexes are only applicable to intensity based measurements.

Reference Dyes

Reference dyes are luminophores which can be considered to be insensitive to both temperature and pressure. These luminophores can be used to correct for changes in luminescent intensity due to changes in excitation light intensity [10]. This can occur for example due to model movement in a non-homogenous illumination field, or excitation light instability. These are often used in simultaneously with PSP or TSP as a multi-luminophore paint. Reference dyes have been used for both standard and fast PSP applications [81], but their use in fast PSP research is rare.

A.2. Multi-Luminophore Paints

Experiments often make use of a single luminophore in paints to measure pressure. Sometimes multiple luminophores are used, with the main goal being to correct for temperature related errors. Some studies paint half the model with a PSP and the other half with TSP [58, 59, 75]. A second approach is to first paint the model with a PSP and later run the same experiments with TSP, thereby using the TSP data to correct for temperature errors [72, 74]. A third option is to include multiple different luminophores in the same paint. The luminophores can be a combination of different pressure sensitive, temperature sensitive and / or reference dyes [47, 60, 73]. Benefits of using multi-luminophore paints include [10]:

- For the intensity based method, using reference dyes can eliminate the need to have a wind-off image. The ratio between the luminescent emission of the reference dye and the pressure sensitive luminophore can be used to obtain the pressure. However, luminophore mixing is nerve perfect, so instead a ratio-of-ratios method is used with a wind-off image.
- Reference dyes can be used to eliminate errors due to change in excitation light intensity.
- Simultaneous measurement of the pressure and temperature by using pressure and temperature sensitive luminophores, allowing for direct temperature correction.
- Two luminophores with similar temperature sensitive give an intensity ratio that is less sensitive to temperature, reducing temperature errors. This can be done with reference dyes, temperature sensitive luminophores or other pressure sensitive luminophores.

There are two mains constraints to multi-luminophore paints. Due to these, it is not possible to combine any luminophore with any other to create a multi-luminophore dye. The requirements are:

- Luminophores must not have overlapping emissions. In order to get a ratio between emissions, they must be sufficiently separated. An example of this is shown below in Figure A.1[28].
- The luminophores must not be chemically reactive with each other or chemically interfere with quenching mechanics of the other luminophore.

---

[28] `https://innssi.com/binary-psp/`, retrieved September 2023,

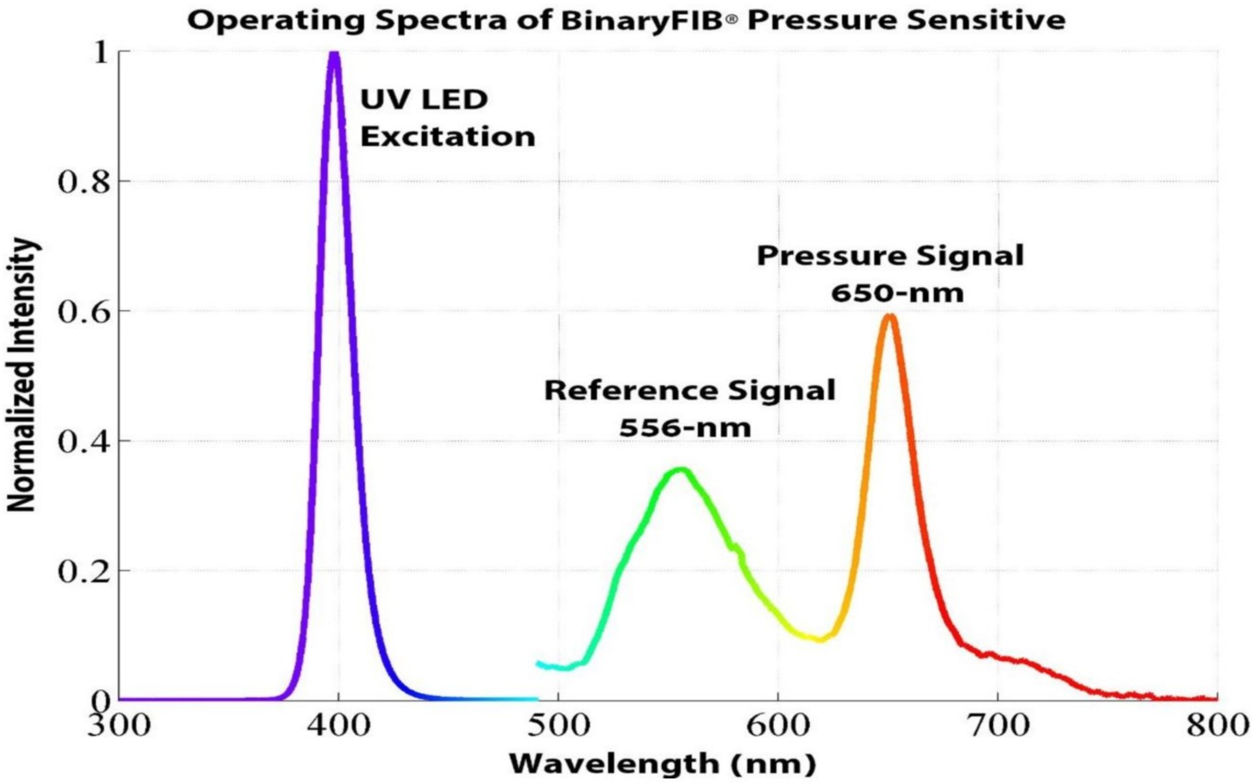

Figure A.1: Emission spectra of BinaryFIB® for a given excitation. BinaryFIB® contains PtTFPP and a reference dye. Source: ISSI[28]

A.3. Luminophore Types Chart

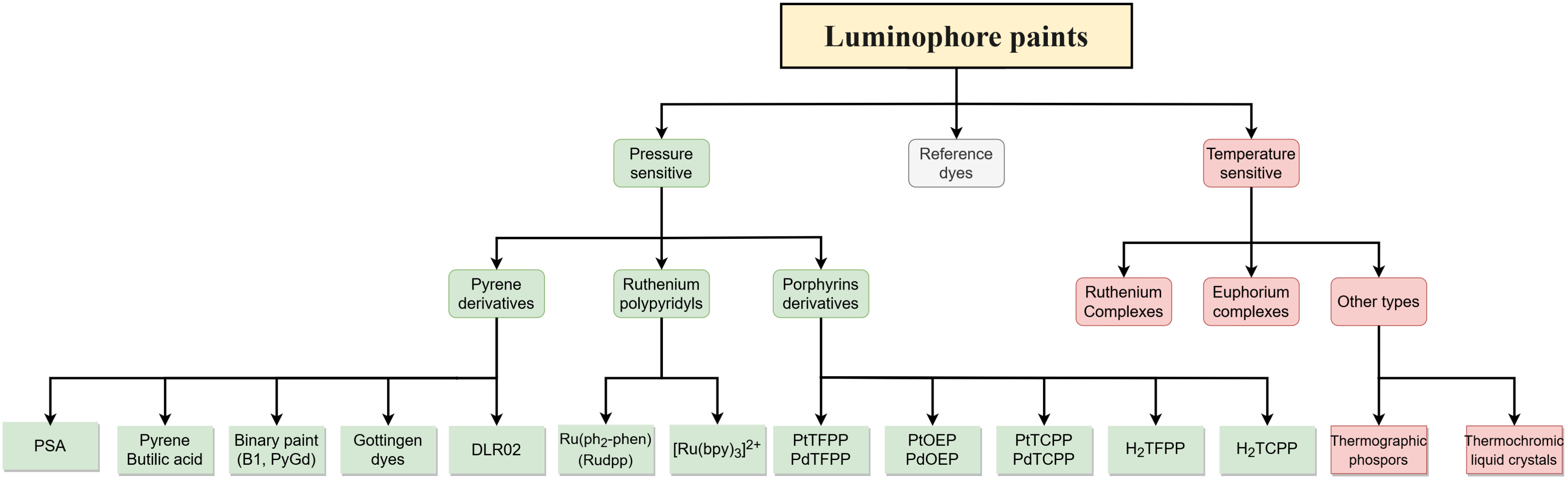

Figure A.2: The three main luminophore families and the most commonly used members of each family. Based on the book of Liu et al. [10], the DLR PSP lecture series [45, 102] and the various articles mentioned throughout the text.

B PSP Suppliers

Innovative Scientific Solutions Incorporated

Innovative Scientific Solutions Incorporated [29] (ISSI) offers a few different PSP paints including:

- Porous fast PSP with up to 10kHz frequencies
- Binary paints
- Fast PSP with up to 1kHz frequencies
- Standard PSP
- Basecoats for the aforementioned paints

Paints provided by this company have been used in various studies [1, 13]. Supplied in Europe by Aircraft Research Association Limited (ARA), a UK based wind tunnel testing facility [30]. Calibration data for Unifib PSP can be found below:

p_{rat}	$T = 278.15K$	$T = 283.15K$	$T = 288.15K$	$T = 293.15K$	$T = 298.15K$	$T = 303.15K$
0	0.116243	0.116243	0.117417	0.120352	0.118395	0.131115
0.1	0.258317	0.258317	0.244618	0.239726	0.236791	0.249511
0.2	0.378082	0.349902	0.348337	0.345401	0.335616	0.332681
0.3	0.476712	0.447358	0.441292	0.425636	0.423679	0.426614
0.4	0.570646	0.54364	0.530333	0.513699	0.510763	0.51272
0.5	0.661057	0.639922	0.611546	0.607632	0.59589	0.590998
0.6	0.745597	0.716243	0.697652	0.688845	0.679061	0.656556
0.7	0.830137	0.80017	0.782779	0.77593	0.748532	0.727006
0.8	0.911155	0.886497	0.850294	0.845401	0.823875	0.805284
0.9	0.994521	0.963992	0.922701	0.915851	0.891389	0.873777
1.0	1.07554	1.04149	0.996086	0.991194	0.957926	0.944227
1.1	1.15538	1.11898	1.07143	1.05675	1.02935	1.01566
1.2	1.22818	1.2	1.14971	1.12818	1.09206	1.08023
1.3	1.30802	1.2775	1.21722	1.19569	1.1683	1.14384
1.4	1.38317	1.34912	1.28195	1.26223	1.23386	1.21037
1.5	1.45949	1.41957	1.35421	1.32975	1.29843	1.27397
1.6	1.53581	1.49237	1.42661	1.4002	1.36106	1.34051
1.7	1.60861	1.56399	1.49413	1.46575	1.42857	1.4002
1.8	1.68258	1.64149	1.56262	1.53033	1.49217	1.45988
1.9	1.75656	1.70841	1.63112	1.59198	1.54697	1.52544
2.0	1.8317	1.78356	1.70059	1.65949	1.62329	1.58708

Table B.1: Calibration data for Unifib PSP. Extracted from a plot digitizer, accuracy of each point unknown. The author expects that some of the points on the original curve are noisy. These were instead interpolated using surrounding points. This concerns $(p_{rat}, T) = (0.7, 298.15K), (1.4, 293.15K), (1.2, 283.15K)$

Merck Sigma-Aldrich Lab & production materials

Sigma- Aldrich[31] supplies various pure luminophore chemicals in the netherlands. Available luminophores include:

- Porphyrin derivatives (no platinum options)
    - 75% dye content H2TCPP available
- Ruthenium polypyridyls

---

[29] `https://innssi.com/`, retrieved July 2023

[30] `https://www.ara.co.uk/`, retrieved July 2023

[31] `https://www.sigmaaldrich.com/NL/en`, retrieved July 2023

  - Ru(dpp) (Pricing not available as of July 2023)
  - $Ru[(bpy)_3]^{+2}$ (354,- € for 5g)
- Pyrene derivatives
  - Pyrene (104,- € for 100g)
  - PBA (255,- € for 5g)

Potential option if AA PSP is to be used. Pyrene itself is relatively very cheap.

C Optical devices

This appendix gives an overview of the the optical devices that are used in PSP measurement. Discussed here are the cameras, filters and excitation light sources. Section C.1 presents the design option tree with most equipment options. The experiments described in this thesis were performed with cameras. Therefore, other light detector types are not discussed. Alongside this, an IR camera was used for temperature corrections.

Cameras

Several camera types can be used for PSP measurements, each with their own benefits and negatives. The most used cameras are Charge Couple Devices (CCD) and Complementary Metal-Oxide-Semiconductor (CMOS), which are used for both lifetime and intensity measurements [10]. For the experiments in this thesis, both CCD (bobcat) and CMOS cameras were used. The main experiments were performed with the CCD cameras due to their availability. When not using filters, red, green and blue (RGB) cameras can be used for standard and multi-luminophore measurements [79]. The RGB sensors act as a filter for the different light wavelengths. Finally, Infra-red (IR) cameras can be used to apply temperature corrections to PSP. Below each camera type is briefly discussed.

CCD Cameras

At the TU-Delft, CCD cameras are often used for PIV measurements. Many types of CCD sensors exist, such as interline CCD, frame-transfer CCD, intensified CCD and multi-gated CCD cameras [56], among others [32]. CCD cameras range from consumer to scientific grade. According to Liu et al. [10], consumer grade cameras can be used for measurements in high gradient flows, but normally scientific grade cameras are used.

This type of camera has very low noise and high spatial resolution [79]. It is most commonly used for lifetime based PSP and standard PSP approaches, where low acquisition rates are present. For lifetime PSP, multi-gated CCD cameras are necessary unless high speed cameras are used [56]. The setup in lifetime PSP using CCD cameras is very similar to the setup used in PIV [10, 56]. Additional error sources associated with CCD cameras are blooming and smear (see Chapter 4).

CMOS Cameras

CMOS is the sensor type that is most often used in consumer products, such as phone cameras[33]. Scientific grade CMOS are generally used for high speed camera applications, allowing for fast readout rates. Generally, CMOS cameras have worse noise and spatial resolution performance than CCD cameras. For PSP, CMOS are generally used for fast measurements [79]. Additional error sources arise in CMOS cameras due to the way the chips work. The most prominent are the rolling shutter effect [115] and periodic noise [82].

RGB Cameras

RBG cameras are cameras which capture light in 3 distinct wavelength bands. As the name suggest, light is measured near the red, green and blue wavelengths. Most consumer grade cameras operate using this principle. For PSP measurements, this allows for wavelengths to be separated automatically, without requiring the usage of filters [79]. However, some overlap is present between the absorption bands for different colour sensors, most notably between green and the other two, which can lead to additional pressure errors.

RGB sensors are often used for multi-luminophore PSP and TSP measurements. With sufficiently separated emission and excitation bands, PSP measurements can in theory be performed with mobile phone cameras [10]. Phones are commonplace in spectroscopy based measurements in other scientific fields

---

[32] `https://en.wikipedia.org/wiki/Charge-coupled_device`, retrieved October 2023

[33] `https://en.wikipedia.org/wiki/Image_sensor`, retrieved October 2023

[116].

IR Cameras

IR cameras work on the principle that all bodies emit radiation as a function of temperature. By measuring the amount of emitted IR radiation, often around 1 to 14 μm[34], the temperature of a body can be determined. This requires determination of the emissivity of the body to calibrate the camera. More on IR thermography can be found in Subsection 5.4.1.

A disadvantage of IR cameras is that normal glass and plastics blot out IR radiation, thus specialized viewing windows are required to measure IR light inside a wind tunnel. These are often made of Germanium glass. Germanium windows do not allow for transmission of the visible light spectrum, thereby limiting optical access to the model at the position of the IR camera.

Filters

In order to blot out excitation light from hitting the light sensors two types of filters can be used, namely colour glass filters and interference filters [10, 79]. Both types can be created to act as long-pass, short-pass and band-pass filters. Long-pass filters block out any light with a wavelength smaller than the cut-off wavelength. Short-pass does the opposite, any light with a wavelength bigger than the cut-off frequency is removed. Band-pass allows a certain range of wavelengths to pass, centered around a central wavelength. Colour glass and interference filters are discussed below. Both filters used in this thesis were colour glass, Long-pass, with a cutoff wavelength of 550nm and 610nm respectively.

Colour Glass Filters

Colour glass filters are simple filters which are created from dyed glass. The dye makes the glass more absorbent or reflective to certain wavelengths while transmitting others. The transmission coefficient of the filter decreases with increasing thickness or travel path (as it effectively increases thickness).

Interference Filters

According to Liu et al. [10], interference filters select wavelength bands by using the interference phenomenon. The filter is created using multiple chemical layers that transmit certain wavelengths, while reflecting or absorbing others. Two types exist, edge- and band-pass interference filters. The former functions as either a long-pass or short-pass filter. An important error source for this type of filter are angular filter effects. The transmission wavelength changes with incidence angle. For PSP, the transmission wavelength of the filter must therefore be verified for all expected incidence angles, or this can lead to pressure errors. More on this error source can be found in Figure D.2.

Excitation Light Sources

Different types of excitation light sources can be used for PSP. Light source selection is heavily tied to the chosen luminophore, as excitation is often only possible certain wavelengths. Additionally, fast PSP measurements often have very low exposure times which require high intensity excitation for good SNR.

Lasers

Lasers are a common source of excitation light for PSP measurements. Numerous types of lasers exist that can be used, such as nitrogen, argon and nd:YAG lasers. Lasers can be used for all different PSP measurement types, by using continuous wave or pulse lasers.

The TU Delft possesses a large collection of nd:YAg lasers that are often used for PIV experiments. However, this laser emits light in the green wavelengths, which is not suitable for all PSP types. (Platinum) Porphyrins can often be excited with green light, along with some ruthenium polypyridyls.

---

[34] `https://en.wikipedia.org/wiki/Thermographic_camera`, retrieved October 2023

The biggest benefits of lasers are their tight emission wavelength band and collimated light. This allows for efficient and homogeneous illumination of the test model. However, laser illumination is prone to speckle interference noise due to the collimated light. This can be a significant error source, especially for fast and lifetime PSP.

Light Emitting Diode (LED) Arrays

LED lights have seen a high degree of technological advancement since PSP first started being used [10, 76, 81]. They are currently the most used excitation light type. LED lamps are capable of providing stable and high powered continuous or pulse illumination, at wavelengths often used in PSP.

Commercially a plethora of options are available, ranging from precise high cost lamps to cheaper options. The TU Delft currently has five AC UV lamps: two 10W LED arrays centered around 365nm, two 20W LED arrays centered around 400nm and one 45W lamp around 365nm. These lamps are used for oil flow experiments. They can serve as excitation source for a wide range of luminophores. The main disadvantage of these AC lamps is that their luminescent emission fluctuates over time, due to fluctuations in the input current. This can cause errors in the measured PSP signal. Additionally, as of the time of writing this report, DLR loaned the TU a 25W DC LED array centered around 400nm, which was used for most of the experiments. Note that all LED lamps have decrease light emissions with increasing lamp temperature, therefore the temperature should be stable before measurements are taken.

UV Lamps

UV lamps, as the name suggests, are lamps which emit light in the UV spectrum. Several options are available depending on the application, including xenon arc / flash lamps, tungsten-halogen lamps and fluorescent UV lamps. These can be used for both pulse and continuous illumination.

PSP luminophores often have excitation frequencies in the UV-A range (315-400 nm), with high peaks centered around specific wavenumbers. Lamps that operate in this range are often called "blacklight"[35]. A couple experiments mentioned in this report use of xenon arc / flash lamps [15, 49, 58]. The book of Liu et al. [10] gives a few experiments for which the other types of UV lamps are used.

Literature does not mention specific benefits or downsides of using this excitation light source type. The only mention is that variation in the spectral emissions between xenon flash lamp pulses leads to a pressure uncertainty of 0.05 Psi [10, 117]. However, the article that mentions this is over 20 years old. The technology has likely improved since then.

Luminescent Model

Currently research is ongoing on having the light sources embedded onto the model for PSP excitation [10]. This can be achieved in different ways, such as using organic LEDs and fluorescent molecules in the PSP paint. Peng and Liu [81] offer an extensive review of the available options and benefits as of 2020. The different methods are not fully mature yet and can thus not be applied for wind tunnel measurements.

---

[35] `https://en.wikipedia.org/wiki/Blacklight`, retrieved October 2023

C.1. PSP Optical Devices Chart

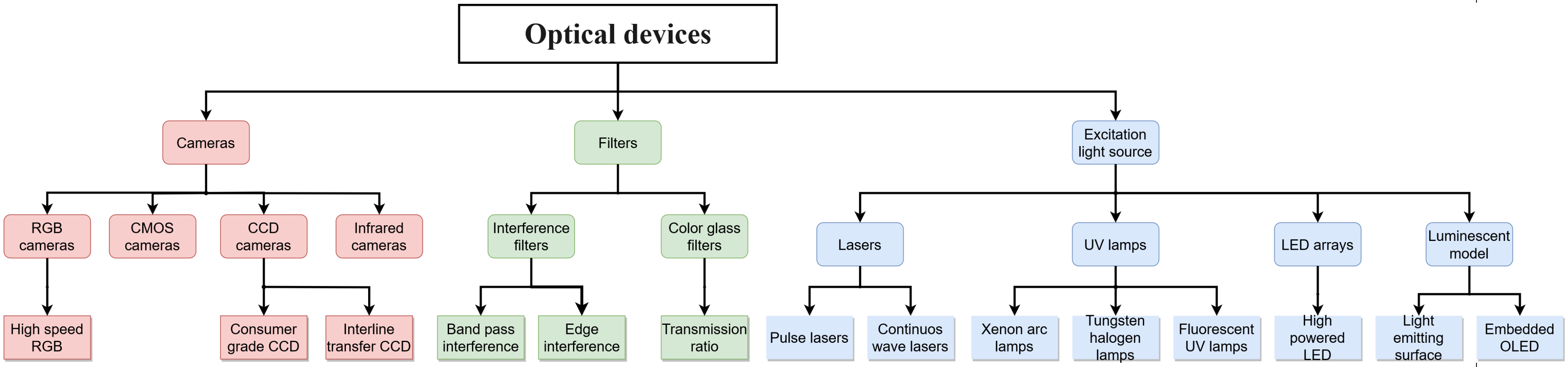

Figure C.1: All potential optical devies that are used for PSP measurements. Included are light detectors, filters and light sources. Based on the book of Liu et al. [10]

D Error Sources Overview

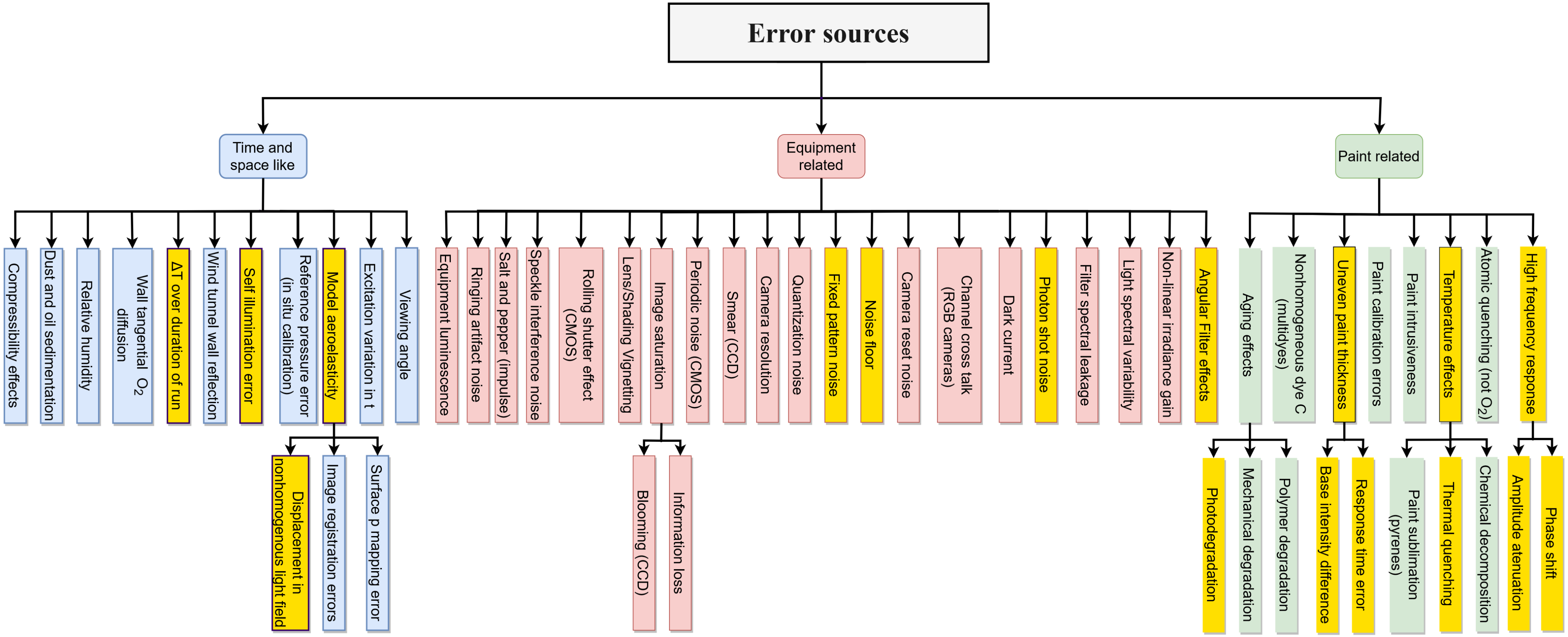

Figure D.1: All potential PSP error sources designated into 3 groups. Here the most important error sources are highlighted yellow. These are errors which are either hard to correct or give rise to extensive errors if not accounted for. Error sources that are not highlighted yellow can still lead to significant errors, but are either easy to correct or not commonplace. Based on the book of Liu et al [10] and the DLR PSP lecture series [62, 68, 79, 82]

The remainder of this appendix contains the description of error sources, corrections and data analysis approaches not mentioned in Chapter 4 due to them being irrelevant for this thesis.

D.1. Other Paint Related Errors

Heat Soaking of Wind Tunnel Models.

In the NASA SLS research campaigns [11, 14, 36, 54, 55] the model was heat soaked before wind-off reference images were taken. This was performed by running the wind tunnel for 20 minutes, thereby allowing the model to reach a steady state temperature similar to those during the runs. According to Roozeboom et al. [55] this practice showed better performance when taking reference images in previous NASA studies. This approach is not possible in the TU Delft wind tunnels, due to them being blowdown facilities.

Roozeboom et al. [55] stated that the exact impact of heat soaking has not been investigated. The reasoning for heat soaking over other methods is not given in the NASA papers, but it is likely similar to that of taking reference images after the runs. In addition, they performed the Stern-Volmer calibration on the model after heat soaking. The author presumes that the model's temperature changes slower post heat soaking as the core of model itself has also reached a steady state, giving more thermal inertia for the surface. This in turn allows for more thermally stable reference and calibration images.

Other Temperature Related Errors

The following two error sources are mostly relevant in high temperature flows, under specific circumstances. It is not expected that these will be encountered during the proposed thesis research. They have been added for completeness.

Paint Sublimation

Pyrene based luminophores have a relatively low paint sublimation temperature [10, 102]. For pure pyrene, temperatures as low as $45°C$ cause sublimation. Other pyrene derivatives are sometime still prone to sublimation but have higher sublimation points. Sublimation of the paint reduces signal intensity, thereby giving inaccurate predictions of pressure. Care has to be taken when using pyrene derivatives to ensure temperatures do not exceed the sublimation temperature. For the current thesis project, pyrene derivatives were not used. Additionally, total temperatures of most tunnels at the TU Delft are well below $45°C$.

Chemical Decomposition

For high wall temperatures, luminophores and polymers may start to decompose or burn [10]. Consequently, the paint stops working as pressure sensor. Polymers can additionally transition from a glassy state to a rubbery state at the so called "glass transition temperature". When this occurs, the oxygen permeability of the layer can significantly change, thereby changing the signal intensity. It is paramount to keep polymers below or above the glass transition temperature (depending on the formulation) at all times. Both of the aforementioned phenomena can simply be avoided by staying within the operational range of the chemical components. For this study these high temperature effects did not pose an issue.

High Frequency Response

The frequency response of fast PSP has an amplitude demodulation and phase delay that increases with increasing frequency. This can lead to various errors. By not taking the amplitude demodulation into account, wrong pressure fluctuations are measured using PSP at high frequencies. The author found that in various fast PSP articles measurements are mostly taken at twice the cut-off frequency or slightly lower, to satisfy the Nyquist criterion. Frequency based corrections are thus often needed between $1-2kHz$ and the cut-off frequency. Below this value fast PSP often does not have any amplitude attenuation.

The amplitude shift instead is less severe in the errors. It is of no impact when using frequency domain analysis [10]. However, when directly comparing the results of other methods (such as Schlieren or kulite pressure taps) to PSP data in the time domain, frequency domain corrections are needed to account for the phase shift. If not performed, direct time domain comparisons cannot be made.

Various methods exist to correct for the phase and amplitude shifts [10, 107, 110]. The simplest approach is to determine a best fit for the bode plots of the paint. This fit is then inversed and applied to the paint response in the frequency domain as a compensator. However, the frequency response is highly dependent on paint thickness. Therefore, to apply this approach correctly the local paint thickness at every point is needed. Often instead an average paint response is taken. Additionally, according to Funderburk and Narayanaswamy [107] the compensator does not take system noise into account. It therefore does not guarantee the spectral quality of the reconstructed signal.

Funderburk and Narayanaswamy Amplitude Corrections

To solve this issue, Funderburk and Narayanaswamy [107] developed a diffusion based model to correct the amplitude attenuation. This model requires the use of high speed pressure taps. Their approach allows for an accurate measure of frequencies above the cut-off frequency, as long as the spectral (frequency dependent) SNR is higher than 1. First they determined the amplitude attenuation based on the diffusion time of oxygen and response time of the paint, normalized by τ_{dif}. The attenuation is then given by

$$dB = -20log\left(\frac{\sigma_{P,PSP}}{\sigma_P}\right) \tag{D.1}$$

where $\sigma_{P,PSP}$ is the standard deviation of the paint signal, and σ_P is the true standard deviation of the pressure signal. Assuming the tap gives the true pressure signal, the power spectral density (PSD) ratio between tap and PSP response can be directly linked to the ratio of standard deviations according to:

$$\sqrt{\frac{G_{PSP}(f)}{G_{kulite}(f)}} \approx \frac{\sigma_{P,PSP}}{\sigma_P}(f) \tag{D.2}$$

where $G_{PSP}(f)$ is the PSD of the PSP signal, and $G_{kulite}(f)$ that of the high speed pressure tap. Using pressure taps for this furthermore indirectly accounts for thickness variations inside the paint. Inverting then gives the true PSD from the PSP response according to:

$$G_P(f) = G_{PSP}(f) \times \left(\frac{\sigma_P}{\sigma_{P,PSP}}(f)\right)^2 \tag{D.3}$$

When the data of multiple nearby taps is available, the best ratio of standard deviations can be found using a least squares approach. To ensure the spectral quality of the correction, a noise analysis to determine the frequency dependent SNR is required. The spectral SNR is then given by:

$$SNR(f) = \frac{G_{PSP} - G_{noise}}{G_{noise}} \tag{D.4}$$

Determining the PSD of noise can be non-trivial with all the possible noise sources. In their work, they assumed photon shot noise dominated results (see Subsection 4.4.1). Shot noise can be scaled with the intensity of measured light. By simply measuring the PSD of shot noise at constant illumination, the shot noise at every point could be scaled. Their new cut-off frequency was then set to the frequency where $SNR(f)$ became less than 1. This approach gave good match between kulite and PSP data well beyond the cut-off frequency of poly-TMSP based PSP. However, the cut-off frequency of the paint depended on local flow- and paint parameters. A higher number of taps therefore gives better predictions, similarly to the in-situ calibration. When they tried to apply their corrections to PC-PSP instead, they found that the noise floor was a limiting factor in the maximum resolvable frequency, rendering their corrections useless.

Camera Attenuation Correction

Alongside the amplitude attenuation caused by the frequency response of the paint, the signal is also attenuated by the cameras. As cameras measure the emitted intensity over the exposure they effectively act as box filters in the time domain. X. Liu et al. [110] developed a compensator based model that corrects PSP data using the inverse bode plots and the camera response. The paint response in the frequency domain can be modelled according to

$$p_{meas}(f) = p_{true}(f) \cdot r_{psp}(f) \cdot r_{camera}(f) \tag{D.5}$$

Where p_{meas} is the measured pressure signal, p_{true} the true pressure signal and r_{psp} & r_{camera} the frequency response functions of the PSP and the camera respectively. The PSD is then given by

$$G_{PSP} = G_P(f) \cdot \left| r_{psp}(f) \cdot r_{camera}(f) \right|^2 \tag{D.6}$$

Where the correction can be applied by dividing G_{PSP} with $\left| r_{psp}(f) \cdot r_{camera}(f) \right|^2$. The camera attenuation can in theory also be implemented in the model of Funderburk and Narayanaswamy.

Uneven Paint Thickness

Uneven paint thickness can lead to various errors [10, 45]. It causes a spatially dependent luminescent lifetime and frequency response. Furthermore, the aerodynamic shape can be slightly changed by uneven thickness (more on this under the paint intrusiveness error).

As an error source, uneven thickness is relevant mostly for the lifetime based approach in standard PSP and for most fast PSP uses. In standard PSP, the intensity method and ratio-of-ratios method eliminates this error source, assuming model aeroelasticity corrections are applied appropriately (see Section 4.2). The best way to avoid this error type is having a skilled painter paint the model carefully. It is an error source that is very dependent on the painter's skills. However, even the most skilled painters do not paint completely even surfaces. The only way to achieve this is by having an optimized robot arm paint the surface [10]. This approach is very expensive and time consuming to set up, making it not worth to using.

Uneven Paint Thickness for fast PSP

For fast PSP, uneven paint thickness can lead to different t_{dif} and a change in the frequency response. It is therefore of utmost importance to have the paint be as even as possible for fast PSP. To somewhat mitigate the response variation, instead of measuring at the Nyquist frequency of the paint, measurements can be done at a lower frequency, allowing some leeway due to thickness variations in the cut-off value.

Atomic Quenching

Chemicals other than oxygen are capable of quenching luminophores, but in standard test conditions very few airborne molecules can do this. However, when the luminophore concentration passes a certain threshold, self-quenching between luminophores can take place [10]. The linear relation between luminescent emission and luminophore concentration therefore only holds until a maximum concentration, where after it becomes non-linear.

This error source is only briefly mentioned in the book by Liu et al. [10]. It is included for in this report for completeness, but no additional measures are given to mitigate quenching errors. The Author expects that this type of quenching is generally not an issue for commercially available PSP formulations.

Non-Homogenous Dye Concentration (Multi-Luminophore Paints)

Multi-luminophore paints often use the emission ratio between two (or more) luminophores in order to account for temperature errors and movement in a non-homogenous illumination field. In theory when there is perfect mixing of luminophores, this removes the need of taking reference images at known conditions.

In practice, mixing of luminophores prior to painting is never perfect [10], no matter how meticulous the mixing is performed. This leads to spatial variations in the ratio of luminophore concentrations. When unaccounted for the non-homogeneity causes additional uncertainty in the pressure signal. To correct for this, a ratio-of-ratios approach should be used. By taking wind-off images the spatial ratio of luminophore signals can be standardised, similar to how the ratio-of-ratios approach works for lifetime based PSP.

D.2. Other Equipment Related Errors

Spatial Filtering for Shot Noise Reduction (Fast PSP)

The effectiveness of spatial filters for shot noise reduction relies on the following properties of fluctuations:

1. **Independent and identically distributed (i.i.d.) noise:** Adjacent pixels receive roughly the same luminosity, thus the variance in shot noise can be assumed to be identical over the filter. As the detection events are independent, photon shot noise can be assumed to be non-correlated between pixels.
2. **Correlated pressures:** For sufficiently small filter areas, the pressure fluctuations can be assumed to be fully correlated. As standard PSP is not used for time resolved flows, this property is mainly relevant for fast PSP

Theoretically, under the above assumptions, for a box filter the SNR increases proportionally to the square root of the number of pixels. Furthermore, the second assumption means that no "true" pressure fluctuations would be lost as pressure signals are perfectly correlated. In reality, other noise sources are present that are spatially correlated and the pressure signals are never fully correlated. This leads to a slower increase of SNR with the number of filtered pixels and attenuation of the pressure signal [64].

The spatial de-correlation of pressure occurs due to two factors [67]. First, turbulent flows have a low degree of spatial correlation, which decreases with increasing frequency [118]. Even when taking very small filter areas, high frequency signals will have low correlation. Secondly, wind tunnel models vibrate at low frequencies in wind-on conditions. While image registration (see Subsection 4.2.3) is used to align the wind-on and wind-off images, this never fully removes the vibration, leading to some nonphysical fluctuations in the signal that are correlated (see Section 4.2)[30, 35, 110].

Tang et al. [64] investigated the effect of different sized box filters and Gaussian blur filters on PSP measurement noise using NASA's 2.5% scale model of the SLS. Their research showed that blur filters can effectively be used to lower shot noise at different M numbers. Bremner et al. [66, 67] developed and showed the impact of a method to isolate shot noise in the frequency domain using blur filters. Alongside this, a method for estimating the spatial correlation between pixels is given. The methods described in these two articles can be used in setting up the PSP analysis code.

The above discussion focussed mostly on reducing photon shot noise for fast PSP in high speed flows. For reducing shot noise in low speed flows, see the review article of Peng and Liu [81] where an excellent overview of the available options is given.

Rolling Shutter Effect (CMOS)

Rolling shutter effect is a typical error source for CMOS cameras [79]. It causes objects to warp in the image plane due to object movement. This warping happens due to the way data is read out in CMOS cameras. While pixel rows are being read, others remain sensitive. The object can have moved considerably in the image plane by the time the last row is read, when compared to the first row. This effect can be entirely avoided by having a global shutter while pixel readout is ongoing. According to Hinsberg [79], most scientific CMOS cameras have global shutters. However, as the research model was rigid this error source would not have occurred regardless of whether the camera has a global shutter or not.

Speckle Interference Noise

Speckle interference noise appears as a "granular noise texture" [36] on images. An example of this can be seen in Figure D.2. It is caused by the interference of wavefronts with different phases, leading to a gamma or uniformly distributed random noise pattern [82]. The wavefronts attain different phases due to diffuse reflections of rough surfaces[36]. Laser based measurement systems are prone to this type of noise. It is commonplace for multi-gate lifetime methods that use laser excitation [56]. Spatial filters and image averaging can be used to correct for this noise type. Filtering can lead to image information loss, requiring a trade off between correcting for speckle and losing other information.

---

[36] `https://en.wikipedia.org/wiki/Speckle_(interference)#cite_note-Forouzanfar10-14`, retrieved July 2023

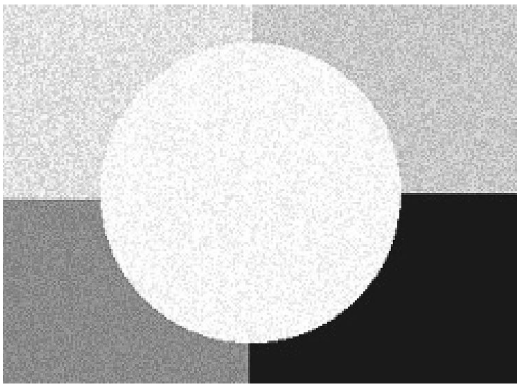

Figure D.2: Speckle noise example. Credit: Source, M. Hilfer [82]

Angular Filter Effects

Filter characteristics differ with incident light angle. For colour glass filters, the travel path increases with increasing incidence angle. This leads to a change in transmission coefficient while leaving the cut-off wavelengths unchanged [10]. For interference filters, the central transmission wavelength decreases with increasing incidence angle [68]. The central wavelength λ_ι for a given incidence angle ι is given by

$$\lambda_\iota = \lambda_0 \cdot \sqrt{1 - \left(\frac{n_{air}}{n_F}\right)^2 \cdot sin^2(\iota)} \tag{D.7}$$

where λ_0 is the central wavelength for a normal incidence, n_{air} is the refractive index of air and n_F the refractive index of the filter. When using a narrow filter transmission band, high incidence angles can cause partial blockage of the model's luminescence, leading to significant errors. Errors as high as 20% of the total pressure have been reported by Fond [68] for 50 and 30 kPa total pressures. Furthermore, due to filter shift excitation light leakage could take place, leading to additional pressure measurement errors.

Careful planning of the experimental setup can be used to fully avoid errors caused by filter angular effects. The maximum incidence angle ι can be computed beforehand using

$$\iota = tan^{-1}\left(\frac{H_0}{2 \cdot R_I}\right) \tag{D.8}$$

where H_0 is the FOV and R_I the focal plane-camera distance. In case R_I is unknown, it can be calculated using the focal length f_l and the magnification factor M by

$$R_I = f_l \cdot \left(\frac{M+1}{M}\right) \tag{D.9}$$

Note that a local change in incidence angle ensues from model aeroelasticity. Aeroelasticity related errors are further expanded in Section 4.5.

Noise Floor

The "noise floor", sometimes also called "read out noise" is a constant noise source present in imaging systems. According to van Hinsberg [79], the noise floor is caused by the transfer from photoelectrons into a measured voltage. The noise floor is "related to sensor-specific readout and amplifier circuits"[79].

The noise floor is normally supplied by the camera manufacturers. According to Liu et al., with careful camera optimization the noise floor can be reduced to single digit electron values [10]. It is most relevant in low light intensity measurement conditions, as can be seen from Figure 4.6.

Equipment Luminescence

Luminescence phenomena are not unique to the luminophores of PSPs. It is possible that some other equipment in the wind tunnel can be excited by the light source [52]. While this is a relatively minor noise source, verification that other sources of luminescence do not impact measurements should be done to avoid additional noise. In case luminescence of other equipment does take place, it is hard to correct for.

Lens / Shading Vignetting

Alongside the angular filter effects, incidence light angles can cause additional errors due to the lens. Lens / Shading Vignetting is a phenomenon that leads to a relative intensity decrease towards the edges of the image [79]. An example of this can be seen in Figure D.3. Different phenomena can cause Vignetting [119]. Vignetting can be reduced by increasing the f-number or lowering the incidence angle. Images taken in Scheimpflug conditions are especially susceptible to Vignetting.

Figure D.3: Example of Lens/Shading Vignetting. Source: photographylife.com [119]

Other Camera Errors

Alongside the four aforementioned noise types, other noise / error sources exist. Most can be found in all camera types but others are camera-specific (CMOS, RGB, CCD). Some are negligible or not correctable and can be ignored but have been included for completeness sake.

Channel Cross Talk (RGB Cameras)

RGB cameras use 3 different sensor types. These capture red, green or blue light to recreate the full visible light spectrum. There is a chance that charge from one sensor type spills over to the other sensor types. According to van Hinsberg [79] this can lead to reduced pressure sensitivity.

Camera Reset Noise

The reset noise is a temperature dependent noise source. Capacitors in the pixel sensors are reset to a reference level before the charge of each pixel is measured [37]. There is some uncertainty in this process associated with thermal noise. Most cameras have built in features that cancel this noise source. Thus it can be neglected unless specifically stated that it is not negated.

Quantisation Noise

Quantisation noise is a noise source that occurs due to the analog-to-digital conversion in the measuring equipment. This noise source is dependent on the system gain but is often small and can be neglected [79].

Camera Resolution

Camera resolution has an impact on the spatial resolution of the image. Low resolution can lead to flow structures being obstructed and overall image blurring. In case high resolution cameras are not available,

---

[37] `https://www.officinaturini.com/reset-noise.html`, retrieved June 2023

multiple cameras can be set up that capture different parts of the model. The images can then be overlapped to form a higher resolution image.

Smear (CCD)

Smear is a phenomenon that can occur in interline or frame transfer CCD cameras. It occurs due to unwanted charge being present in the shift registers [79]. Smear appears as a vertical line originating from a bright source in the image, as can be seen in Figure 4.8[38]. In frame transfer CCDs, smear can be avoided by cutting off light during charge transport from imaging sensor to storage. For interline transfer CCDs, smear can be avoided by switching off the light before and after the exposure time. This can be done by a pulsed laser or shutter [120].

Periodic Noise (CMOS)

Periodic noise appears as a repeating pattern in the image, as shown in Figure D.4 [82]. It can occur due to electrical interference during imaging [115]. For CMOS cameras, periodic noise is a result of the imaging system which can be eliminated using flat field corrections. The periodicity of this noise type appears as distinct peaks in the frequency domain. Application of frequency domain filters, such as the notch filter, can additionally mitigate this noise type [82, 115].

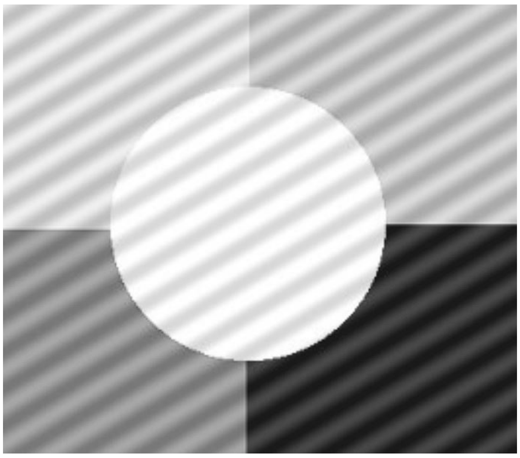

Figure D.4: Periodic noise example. The noise appears as diagonal light and dark bands. Source: DLR, M. Hilfer [82]

Ringing Artifact Noise

Ringing artifact is a noise source that appears as "bands" near sharp object edges [82]. An example of an imaging with and without ringing artifact noise can be seen in Figure D.5. This can be caused by low pass filtering of high frequency signals [39]. Frequency domain filters, such as the Gauss or Butterworth filters, can be used to mitigate ringing artifact noise.

---

[38] `https://commons.wikimedia.org/wiki/File:Vertical_smear.jpg`, retrieved July 2023

[39] `https://en.wikipedia.org/wiki/Ringing_artifacts`, retrieved July 2023

(a) Clean image

(b) Ringing artifact example.

Figure D.5: Example of the effect of ringing artifact noise on the sharp edges of an images. Figure D.5a shows the original image without noise, whereas in Figure D.5b noise is artificially added. Source: N. R. Barth, Wikipedia[39]

D.3. Other Time and Space Like Errors

Compressibility Effects

Compressibility effects can cause variation of the light intensity in space and time due to a change in refractive index with air density. This phenomenon allows for Schlieren measurements to take place and can significantly change the illumination over certain areas. However, most research papers do not mention this error source. Two examples have been found where this was a limiting factor in the measurements. First, in the axisymmetric straight PLF measurements of Nakakita et al. [16], the shock wave on the shoulder of the LV caused a band of optical noise further downstream on the LV as can be seen in Figure D.6. Secondly, in the supercritical laminar airfoil flow study of Merienne et al. (2019)[78], it is suspected that compressibility effects contributed a mismatch between the magnitude of PSP and kulite data. This was not verified as the effect would need to be carefully studied.

Dust and Oil Sedimentation

Over time, dust and oil particles can accumulate on the surface of the test model. These can originate from handling and test runs. While extra care is taken to reduce the amount of dust and oil particles inside wind tunnels, it is impossible to completely rid the tunnel of all particles. Furthermore, wind tunnel testing facilities are not dust free environments. The particles reduce optical access of the PSP paint to the excitation light and absorb some of the paint emissions [10]. The uncertainty associated with this can be classified together with the paint degradation quantity, as a percentage reduction of intensity over time.

Reference Pressure Error (In-Situ Calibration)

When using in-situ calibration to account for temperature effects, pressure values are taken from transducers or points with known pressure values. The pressure transducers have some pressure uncertainty, which adds to the uncertainty surrounding the PSP pressure. Often the uncertainty of pressure transducers is very low, leading to very small errors compared to errors from the in-situ calibration method itself [10].

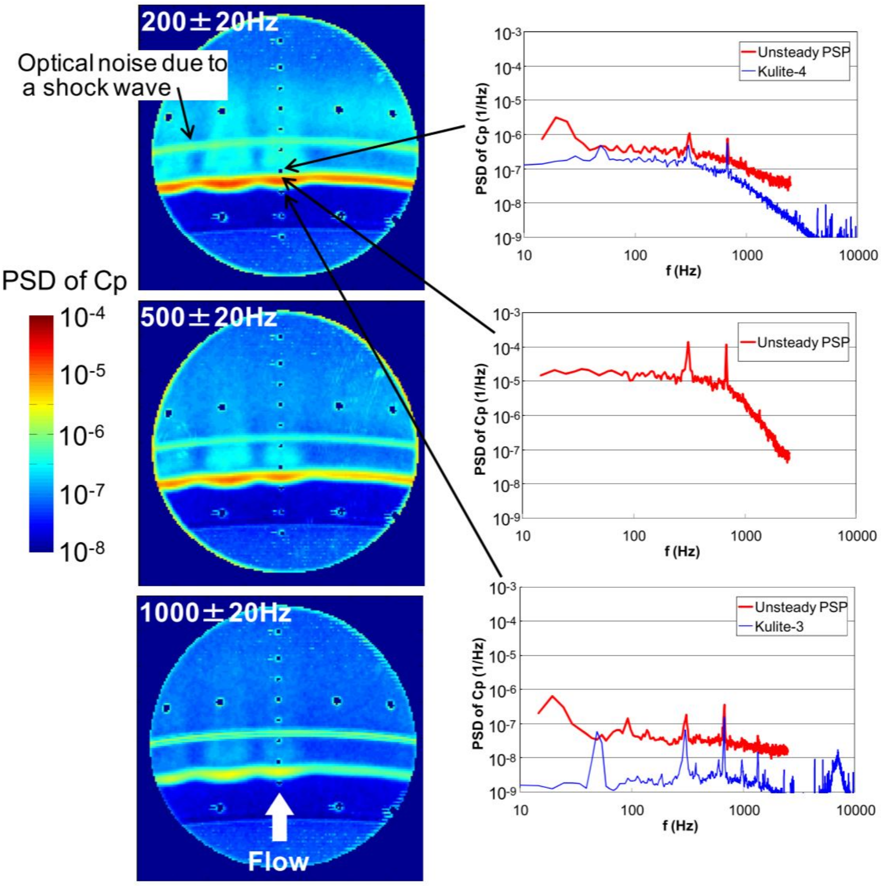

Figure D.6: Optical noise in the PSD of fast PSP measurements on a straight PLF rocket model. The error is seen in the left images as a narrow band downstream of the shock wave. On the left comparisons between PSP and kulites are shown, where PSP differs significantly due to various noise sources, especially upstream of the shock wave due to the noise floor. Source: Nakakita et al. [16]

Wind Tunnel Wall Reflections

Alongside the self-illumination error, reflections from the wind tunnel wall can lead to additional error sources [52]. This error type can be minimized with dark wind tunnel walls and proper equipment positioning. Theoretically, this can be corrected in a similar manner as self-illumination but it is too time consuming for realistic application. Checking whether the intensity is impacted by wind tunnel wall reflections can be done to ascertain whether this is a significant error source.

Wall Tangential O_2 Diffusion

So far when discussing the oxygen diffusion inside PSP, the wall normal oxygen diffusion was discussed. Concurrently with wall normal diffusion, wall tangential diffusion takes place inside PSP, due to concentration gradients creating a flux according to Fick's first law of diffusion. The wall tangential flux lowers the spatial resolution of PSP. This is mostly relevant for regions of high pressure gradients. Across shock waves, the wall tangential diffusion impacts the pressure concentrations of surfaces up to 5 times the thickness of the paint away from the shock [10]. This is mostly relevant for stable phenomena.

D.4. Image Resection

As previously stated, in PSP literature image resection refers to the process of reconstructing the 2D image obtained by the camera into a 3D grid of the model. To do so, the collinearity equations from photogrammetry are used [77]. These equations solve for the relationship between the 3D coordinates and the 2D image plane coordinates. To solve them, various cameras parameters must be determined. According to Liu et al. [10], these can be split into 3 categories:

- **Exterior camera orientation parameters** are the location of perspective centre and the camera orientation angles. The perspective centre refers to the camera aperture location with coordinates denoted by (X_c, Y_c, Z_c), whereas the camera orientation angles are three Euler angles (ω, ϕ, κ) denoting spatial orientation. This can be interpreted as the cameras roll, yaw and pitch angles.

- **Interior camera orientation parameters** give the relationship between the perspective centre and the image coordinates. Two parameters are used here, the principal distance f_c and the photogrammetric principal point with coordinates (x_p, y_p). The principal distance is given by the focal length when the camera is focused at infinity. The principal point is the location at which a perpendicular line (with length f_c) drawn from the perspective centre intersects with the "digital" image plane.
- **Lens distortion parameters** refer to the parameters which define image distortion caused by the lens. This distortion leads to a shift from the "ideal" coordinates of an imaging system with no distortion. They are denoted with $(\Delta x, \Delta y)$ and can be modelled due to "decentering distortion" and "radial distortion". Both can be calculated with four additional distortion parameters.

The collinearity equations themselves are given by

$$\begin{aligned} x - x_p + \Delta x &= -f_c \cdot \frac{m_{11} \cdot (X - X_c) + m12 \cdot (Y - Y_c) + m_{13} \cdot (Z - Z_c)}{m_{31} \cdot (X - X_c) + m32 \cdot (Y - Y_c) + m_{33} \cdot (Z - Z_c)} \\ y - y_p + \Delta y &= -f_c \cdot \frac{m_{21} \cdot (X - X_c) + m22 \cdot (Y - Y_c) + m_{23} \cdot (Z - Z_c)}{m_{31} \cdot (X - X_c) + m32 \cdot (Y - Y_c) + m_{33} \cdot (Z - Z_c)} \end{aligned} \tag{D.10}$$

where x, y are image plane coordinates, m_{ij} are functions of the Euler angles (see the book of Liu et al. [10] page 203 for the exact definition) and (X, Y, Z) are the objective space coordinates. To solve these equations, numerous different methods and open-source codes exist which go into various degrees of complexity. An overview of some can be found in the book of Liu et al. [10] and the DLR PSP lecture of Mérbaki [62]. Below a linearization approach called "Direct linear transformation" (DLT) is given, which was originally developed by Abdel-Aziz and Karara [121] in 1971.

Assuming that the camera lens distortion is negligible, the relationship between object space and image plane coordinates can be rewritten to:

$$\begin{aligned} x &= \frac{L_1 \cdot X + L_2 \cdot Y + L_3 \cdot Z + L_4}{L_9 \cdot X + L_{10} \cdot Y + L_{11} \cdot Z + 1} \\ y &= \frac{L_5 \cdot X + L_6 \cdot Y + L_7 \cdot Z + L_8}{L_9 \cdot X + L_{10} \cdot Y + L_{11} \cdot Z + 1} \end{aligned} \tag{D.11}$$

where L_i are coefficients that need to be determined. This system can be solved using the same approach as the image registration technique, namely by using control points whose exact coordinates are known in the object space. Solution of these equations requires at least six control points, with the error decreasing by using more points [77]. The over-determined system can again be solved using a least squares approach. Similarly, accuracy and error can be estimated using the method mentioned in Subsection 4.2.4.

In the article of Bell and Mclachlan, this approach was applied to both the rigid sting mounted model, and the half model. The pixel RMS error for the sting mounted model was below 0.5 pixels when using 10+ control points, whereas that of the half model did not go below 2 pixels. This result suggests the model works well for rigid body movements.

D.5. Time Resolved Pressure Field Calculation

For fast PSP, extracting time resolved data includes additional steps compared to standard PSP, as individual frames must be investigated. Two approaches are commonly used to do so in literature. The first is referred to as the "Direct Current" (DC) method. Here the intensity ratio is computed for each individual image using the wind-on and -off images. Afterwards an average intensity ratio over all images is computed. From this, both the time resolved and time averaged pressure fields are obtained separately. At the end, the time averaged pressure field is subtracted from the pressure fields obtained by the individual frames. This gives the time resolved pressure fluctuations relative to the mean.

Here the order of operations depends on the correction method. When in-situ calibration is done, the intensity field is averaged and corrected for using the averaged pressure tap data. Whereas when other temperature corrections are done, first the individual pressure fields are computed and corrected. Afterwards, a time average pressure field is obtained which is used to subtract the individual frames.

A second approach is, evidently, called the alternating-current (AC) method. This method was first described by Crafton et al. [122] (as far as the author is aware). It directly computes pressure fluctuations as a result of the intensity method. Here the averaged intensity field from the wind-on data is taken as a reference image. To do so requires all images to first be aligned, often to the first frame. The pressure fluctuation is then calculated from the intensity ratio between average intensity and the individual frames using:

$$p_{fluc} = \left(\frac{I_{avg}}{I_i} - 1\right) * G(p, T) \tag{D.12}$$

where p_{fluc} are pressure fluctuations relative to the mean and $G(p,T)$ is a gain function that describes the local slope of the intensity ratio with respect to the pressure fluctuations. The value of the gain function for different values of (p,T) can be obtained experimentally using a steady state paint calibration. In order to determine the spatial variation of $G(p,T)$ on the model, both the averaged local temperature and local pressure are needed. How these are acquired will impact the measurement accuracy. NASA [8] uses lifetime PSP to obtain the time averaged pressure field and simple adiabatic wall temperature calculations (see Subsection 4.1.2 and Equation 4.2) to estimate the temperature field. The gain function is then given by

$$G(p, T) = a + bT_{aw} + cT_{aw}^2 + (d + eT_{aw} + fT_{aw}^2) * p \tag{D.13}$$

where p and T_{aw} are defined over the entire model. Additional in-situ corrections can be applied to the computed pressure fluctuation using pressure tap data afterwards.

The benefits of the AC-method over the DC-method are that the AC-method is less affected by model movement, temperature changes, paint aging and dust segmentation between wind-on and -off images. Note that these errors are merely mitigated relative to when wind-off images are used. All these error sources are still present. The disadvantages of the AC method are mostly associated with time varying (p,T) fields. In the research of X. Liu et al. [110] the AC method was considered but rejected due to concerns of elevated error associated with time varying (p,T). The AC-method is additionally harder to implement than the DC one, due to the extra calibration requirement of the gain function.

D.6. Statistical Quantities

The following three sections cover data analysis approaches that can be applied to fast PSP data. The methods discussed here are often used to analyse time resolved pressure port and CFD data. PSP effectively functions as having pressure ports on every pixel, leading to literature sometimes calling PSP data points "virtual pressure taps" [12]. Therefore, standard analysis methods that hold for pressure tap data are also applicable to PSP. Note that due to the spatial limitation, some methods are not application to pressure tap data which can be used for PSP and CFD, such as POD and DMD.

In this section the focus lies on statistical data that can be extracted. More precisely, rms pressure fluctuations (p_{rms}), correlation and coherence are discussed here. These quantities are used to extract more information about the flow physics and are often used to compare PSP data with CFD and pressure tap data. Other standard statistical quantities are sometimes used but are not further discussed here due to their simplicity. This include quantities such as mean, standard deviation, variance, median etc.

Correlation and p_{rms} are quantities that are computed in the temporal domain. Instead, coherence is computed in the frequency domain. As data is obtained in the time domain, conversion to the frequency domain is needed. For this Fourier transforms are applied, most often using Welch's method. Both are discussed in the next section.

RMS Pressure Fluctuations

The most conventional way to analyse time resolved pressure data in the temporal domain is to look at the RMS pressure fluctuations. Practically all research campaigns on an aerodynamic model involving fast PSP and / or time resolved pressure taps measure and analyse this quantity. The exception for fast PSP lies in paint formulation studies. RMS pressure fluctuations are paramount in determining critical regions in the flow for structural design, as it shows regions with a high degree of pressure oscillations. An example can be seen below in Figure D.7 and in Figure D.9.

Sometimes, instead of stating the RMS Pressure fluctuations directly, the pressure coefficient $C_{P_{rms}}$ is used. The $C_{P_{rms}}$ is defined by

$$C_{P_{rms}} = \frac{\sigma_P}{q} \tag{D.14}$$

where σ_P is the standard deviation of the pressure fluctuations and q is the dynamic pressure of the freestream. Often the $C_{P_{rms}}$ or p_{rms} is normalized with respect to a reference value when it is displayed, as was done in Camussi's research on the vega launchers [23, 29]. Commonly it is given as a percentage of a reference C_P or with respect to the average $C_{P_{rms}}$.

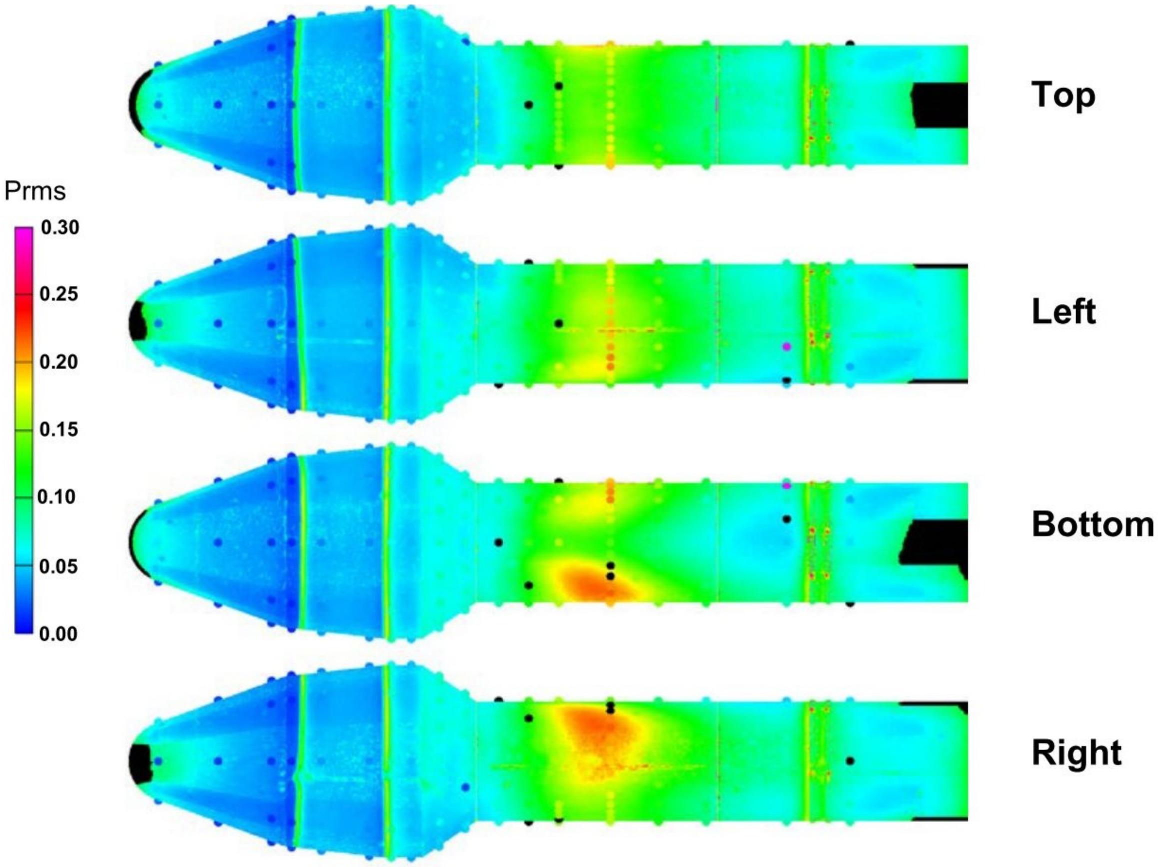

Figure D.7: p_{rms} for the Coe and Nute model 11 at M = 0.8 and $\alpha = -4°$. Pressure here is displayed in psi. Source: Sellers et al. [8] study on the model 11.

Correlation

Correlation is a measure of the dependence between two randomly distributed variables [122]. With the time resolved pressure data, correlation is often used to analyse the pressure fluctuations. It can determine the correlation lengths of fluctuations, the convective velocity of fluctuations and the spatio-temporal dependency and impact of fluctuations. Most Fast PSP articles use the auto- and cross-correlation to investigate these three parameters. The correlation length and convective velocity are often computed by plotting the cross-correlation between pressure signals on the model separated by an axial distance Δx and an azimuthal distance $\Delta\theta$. Panda et al. [30] defined the normalized cross-correlation using

$$r(x,\theta,\tau) = \frac{1}{\tau}\frac{1}{p_{rms}(x,\theta)\cdot p_{rms}(x+\Delta x,\theta+\Delta\theta)}\int_0^T p(x,\theta,t)\cdot p(x+\Delta x,\theta+\Delta\theta,\tau)\,dt \tag{D.15}$$

where r is the normalized correlation coefficient, τ is the time delay between signals, T the total signal duration and t the signal time used for integration. The normalized correlation coefficient ranges between [-1,1] where 1 is a perfect correlation, and -1 a perfect anti-correlation. In python, this quantity can be calculated using the library scipy.signal with the function correlate [40]. Using the cross-correlation, the convective speed (U_c) of axial pressure fluctuations is defined as

$$U_c = \frac{\Delta x}{\tau_{max}} \tag{D.16}$$

where τ_{max} is time delay for which the cross-correlation coefficient is maximized. Some examples of studies that investigates this are the Vega study of Camussi et al. [23], the Coe and Nute study of Panda et al. [30] and the inclined jet study of X. Liu et al. [110]. This can similarly be done in the azimuthal direction. The length of correlation is then simply defined as the length over which a correlation peak can be identified between signals.

Lastly the correlation is often used to compare movement of flow structures relative to each other, to pressure fluctuations and to compare quantities measured between different methods. An example can be found in Figure D.8, where a correlation analysis was performed between the shock location determined with PSP and the entire pressure field.

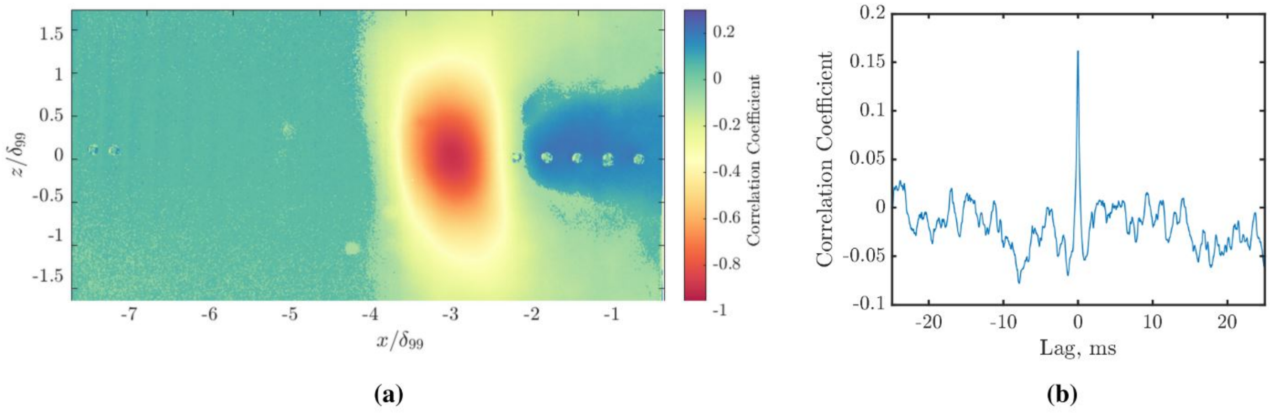

(a) **(b)**

Figure D.8: Cross-correlation analysis between shock foot location and pressure signal on a hypersonic compression ramp study. A negative cross-correlation indicates that a positive pressure rise moves the shock upstream. Figure (a) shows the relation between shock foot and the entire pressure field. Shown here is the area just before the ramp. Figure (b) shows the relation between the shock foot and the pressure at $x/\delta_{99} = -1$. Source: The work of Ahn et al. [108].

Coherence

The coherence is a property that can be used to evaluate how two different signals are related. It estimates how well one signal can be reconstructed through an optimal linear least squares transformation of another signal [122]. Varying between [0,1], a coherence of 1 indicates that two signals are linear transformations of each other, whereas a value of 0 means two signals are completely unrelated. Similarly to the correlation, it can be used to characterise the spatial dependence of pressure fluctuations in the frequency domain. The coherence function between two signals (ξ,ψ) can be computed using [36, 114, 122]

---

[40] `https://docs.scipy.org/doc/scipy/reference/generated/scipy.signal.correlate.html`, retrieved November 2023

$$C_{\xi\psi} = \frac{\left|G_{\xi\psi}\right|^2}{G_{\xi\xi}G_{\psi\psi}} \tag{D.17}$$

where $G_{\xi\psi}$ is the cross spectral density between signals (ξ, ψ), $G_{\xi\xi}$ and $G_{\psi\psi}$ are the PSD of signals ξ and ψ respectively and $C_{\xi\psi}$ is the coherence function, sometimes referred to as the magnitude-squared coherence.

Coherence lengths are of key importance in the creation of buffet forcing functions [36]. In PSP literature, the coherence fields at distinct frequencies are often computed to determine the length scale of coherent fluctuations. An example can be found in Figure D.9 for one of the SLS tests. Examples of fast PSP studies cited here that investigate coherence include the SLS tests, with an article focused on the coherence by Soranna et al. [36], the inclined jet impingement study of X. Liu et al. [110], the transonic swept wing study of Sugioka et al. [114] and the laminar transonic airfoil study of Merienne et al. [78], among others.

D.7. Fourier Transform

This section discusses data analysis methods for fast PSP that involve the application of Fourier transforms, except for the coherence which was discussed in the previous section. Almost all fast PSP articles use Welch's method for computing the PSD and other properties in the frequency domain. Therefore, a brief overview of this is given. PSD and Wavenumber-Frequency Spectrum are then briefly discussed afterwards.

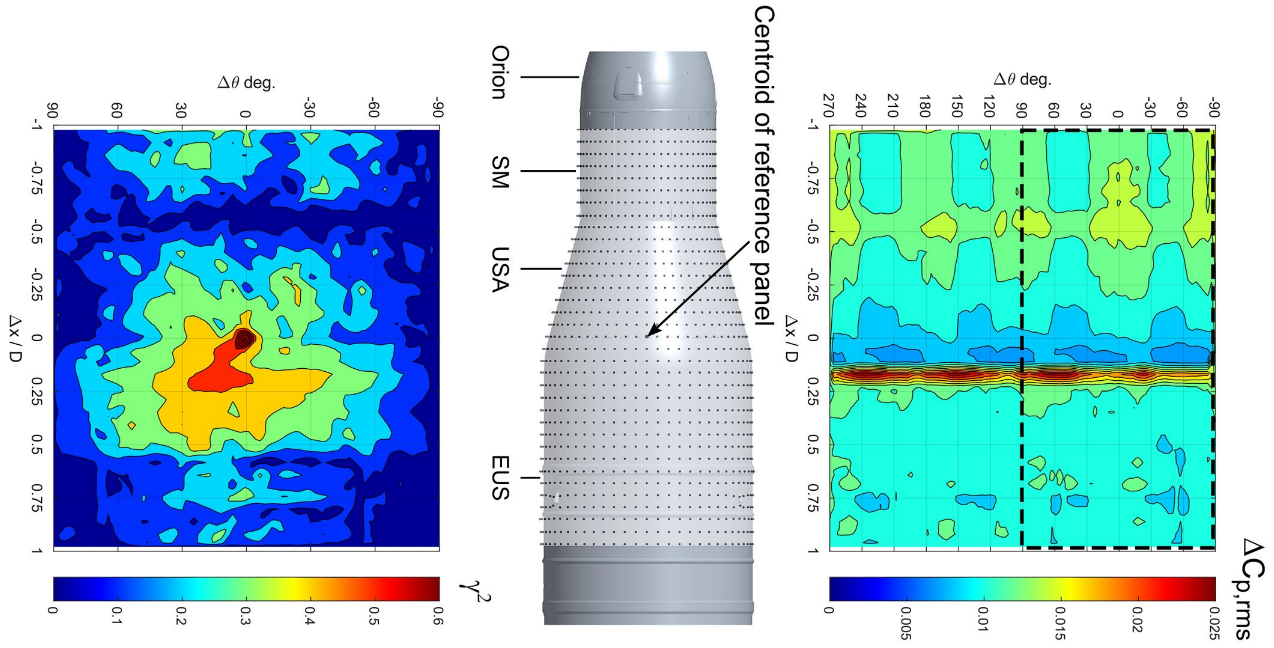

Figure D.9: $\Delta C_{P_{rms}}$ and coherence maps at Strouhal number of 0.2. The maps are unwrapped from the SLS geometry shown in the centre. Coherence is computed with respect to a marked reference panel on a 3D grid. Source: The work of Soranna et al. [36].

Welch's Method

Welch's method is used to compute the PSD (and coherence) of signals. The method, defined by Welch in 1967 [123], uses the FFT algorithm to determine the PSD of signals by splitting the original signal into multiple overlapping segments with N datapoints. These segments are windowed in the time domain before the FFT algorithm is applied. This results periodograms of the segments. Averaging over all the periodograms returns the PSD of the original signal, with a reduced frequency resolution. Due to the averaging operation, Welch's method significantly reduces noise in the computed spectrum and is often applied for this reason [41].

---

[41] `https://en.wikipedia.org/wiki/Welch's_method`, retrieved October 2023.

In fast PSP literature the most standard set up for Welch's method is to use 512 to 4096 image long sets with 50% overlap and a Hanning window in the time domain. Generally, window lengths are chosen that are powers of 2 (512, 1024, 2048, 4096). 50% overlap indicates that subsequent sets have an overlap of 50% with each other. A wide variety of window functions is available, but default applications of the PSD use the Hanning window due to its ability to mitigate spectra leakage[42]. The window reduces the spectral power of the signal, requiring a constant factor correction to the PSD. Examples of PSP articles that made use of the above settings are the NASA Coe and Nute model 11 study with PSP by Sellers et al. [12] and Panda et al. [4], the 3D swept airfoil study by sugioka et al. [114] and the shock impingement study of Brouwer et al. [43].

In python, Welch's method is the default approach used in various libraries that are capable of computing the PSD and coherence, such as scipy.signal.coherence, matplotlib.pyplot.psd and scipy.signal.welch.

Power Spectral Density

The PSD describes how much power each frequency of a signal has. Mathematically, it is defined as the Fourier transform of the autocorrelation function of the signal. The amplitude of the PSD in the spectral domain is given by the unit of the original signal squared divided by its frequency. For time resolved pressure measurements it returns Pa^2/Hz (or PSF^2/Hz in the imperial system).

PSD is commonly used to find the characteristic frequencies at each point in the flow, along with the power level of each frequency. For the turbulent SWBLI, separation and reattachment flows that will be studied in this thesis the important frequencies often lie around 100-1k kHz [29, 32]. Plots of a fixed frequency range / value can give additional insight into where certain phenomenon are dominant. By comparing the PSD of kulite pressure tap data to the surrounding PSP data, the signal quality and noise floor of the PSP data can furthermore be evaluated [107]. This is described in more detail in Chapter 4.

The noise floor forms an important parameter when analysis PSD data of fast PSP. This is impacted by various parameters which have also been previously described throughout the report (see Chapter 4):

- In areas with low pressure fluctuations, the signal is mostly noise dominated due to shot noise. This causes the PSD to be useless without significant corrections [12, 64, 66, 105].
- At the low frequency range (<150 Hz) noise from the image registration and resection technique can additionally lead to elevated PSD values compared to pressure tap data [30, 35, 110].
- Amplitude attenuation of the PSP response leads to an underestimation of the high frequency power content, requiring additional corrections relative to pressure tap data [10, 107].

An example of the PSD comparison between kulite and PSP data can be found below in Figure D.10 for NASA's Coe and Nute model 11 tests using PSP. In Figure D.11 the location of the pressure taps can be found.

---

[42] `https://www.sciencedirect.com/topics/engineering/hanning-window`,retrieved November 2023.

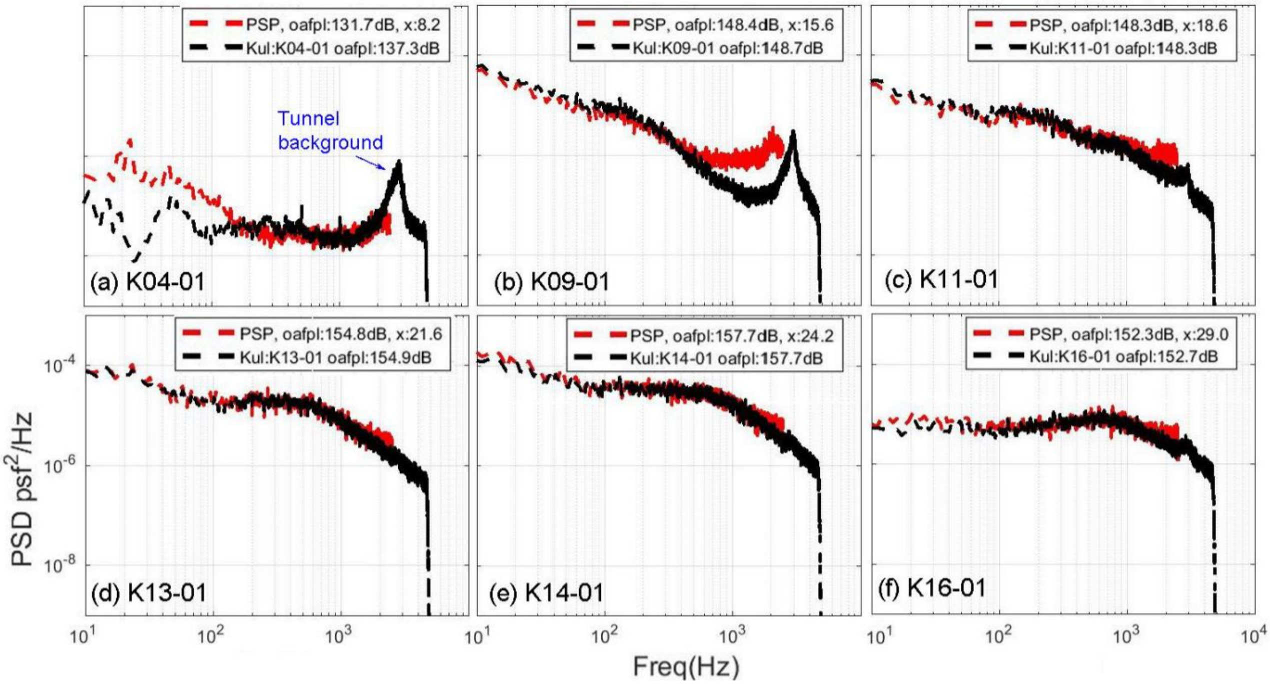

Figure D.10: Comparison between PSD constructed using kulite pressure taps and fast PSP data on the Coe and Nute model 11 at $M = 0.8$ and $\alpha = 0°$. Pressure is shown in imperial units. Source: Panda et al. [30].

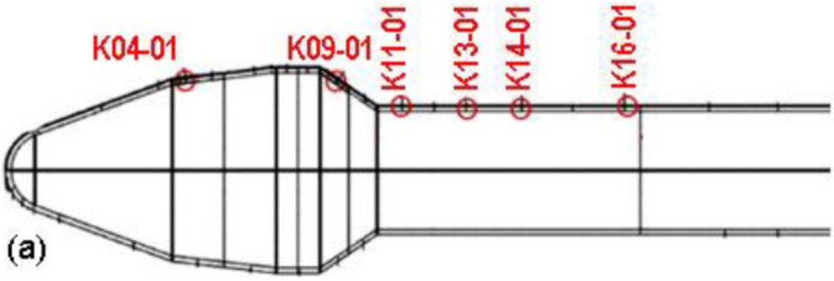

Figure D.11: Pressure tap locations on the Coe and Nute model 11 configuration used by NASA. Source: Panda et al. [30].

Wavenumber-Frequency Spectrum (k-ω)

According to Panda et al. [30], the "Wavenumber-Frequency Spectrum (k-ω)" is an analysis method that can be applied to the dense, regularly spread grid obtained from PSP. Panda et al. state that data obtained from this is "valuable for the vibro-acoustics analysis of aerospace vehicles". The exact implementation of this method involves applying three consecutive discrete Fourier transforms on the instantaneous ΔC_P data along x,θ or t for every point on the other two parameters. This yields plots relating the wavenumber in x,θ and the frequency ω. For more details on the implementation and application of the $k-\omega$ spectrum, the author refers to the work of Panda et al. [30].

For the current thesis project, this method is unlikely to be used, as it is mostly relevant for vibro-acoustic analysis. The author has no plans of performing such an analysis for the current thesis project. No other articles cited here mention or used this method. Future projects however may be interested in this. Furthermore, if fast PSP data is obtained from this thesis, it could be used for this analysis. For these reasons it has included in this section.

D.8. POD & DMD Basics

This section gives an overview of the basics of POD and DMD, with respect to their application in PSP literature. At this stage of the thesis project, the author does not plan to implement these methods in the data analysis unless the project proceeds much faster than anticipated, and some extra time remain. Therefore, the discussion presented here primarily just focuses on the basics and uses of POD and DMD.

POD

Proper orthogonal decomposition, in essence, is a technique that is used to decompose high dimensional (aerodynamic) data into a linear summation of orthogonal mode shapes [12]. It is closely related to the singular value decomposition algorithm and was originally used to extract coherent structures from turbulent flow fields [124]. The mathematical definition of the POD is given by

$$q(\xi,t)-\overline{q(\xi)}=\sum_{n=1} a_n(t)\phi_n(\xi) \tag{D.18}$$

where $q(\xi,t)$ is a vector field (of an aerodynamic quantity) with ξ being a spatial coordinate and t a temporal one and $\overline{q(\xi)}$ is the mean value of that vector field. $a_n(t)$ is a temporal coefficient and $\phi_n(\xi)$ are spatial POD modes that are orthogonal to each other. The POD modes are organized by decreasing energy level, with lower modes having most of the energy. The modes represent structures that are found inside the vector field, and their energy content relates to how much they impact the whole.

POD is commonly used to analyse PSP, PIV, IR and CFD data, such as the work of Schrijer et al. [34] on the baseflow of the Ariane 5 vehicle. Many POD variations exist for applications such as denoising data, reconstructing data, reduced-order modelling, analysing fundamental flow features among others.

Below follows some examples of applications of the POD technique to articles cited in this report, with some additional context for their application. For more information on POD, the author recommends the modal analysis overview article of Taira et al. [124] and the conference manuscript of Weiss [125].

- **Coe and Nute experiments**

Murman et al. [7] used POD to analyse the modes obtained with PSP and compare to those obtained with a hybrid-RANS turbulence model CFD simulation. This was done on the Coe and Nute model 11 PSP tests. No in-depth analysis is given regarding the patterns found on the modes. However, the energy contents of the modes obtained from PSP and CFD was very similar.

- **NASA, ISSI and AEDC experiments**

Crafton et al. [122] summarizes three experiments performed by ISSI, AEDC and NASA that used POD. This includes a cavity flow, a fighter aircraft [12] and an acoustic pressure field resonance experiment [109]. The first 6 modes of the fighter aircraft, along with a graph of the modal energies can be seen in Figure D.12.

- **Impinging jet experiment**

X. Liu et al. [110] used a special application of POD, called "spectral POD", to denoise fast PSP data in their impinging jet experiment. The PSP data was reconstructed using the most energetic, non-noise related modes. This denoising method was chosen over other shot noise reduction methods due to it maintaining the spatial resolution of the data. A total of 120 modes were used for denoising. To verify the effectiveness of the approach, a subsequent analysis was performed that compared the PSD of PSP with a kulite. Spatial filtering of data near a kulite tap showed a very similar trend in SNR improvement as the POD denoising.

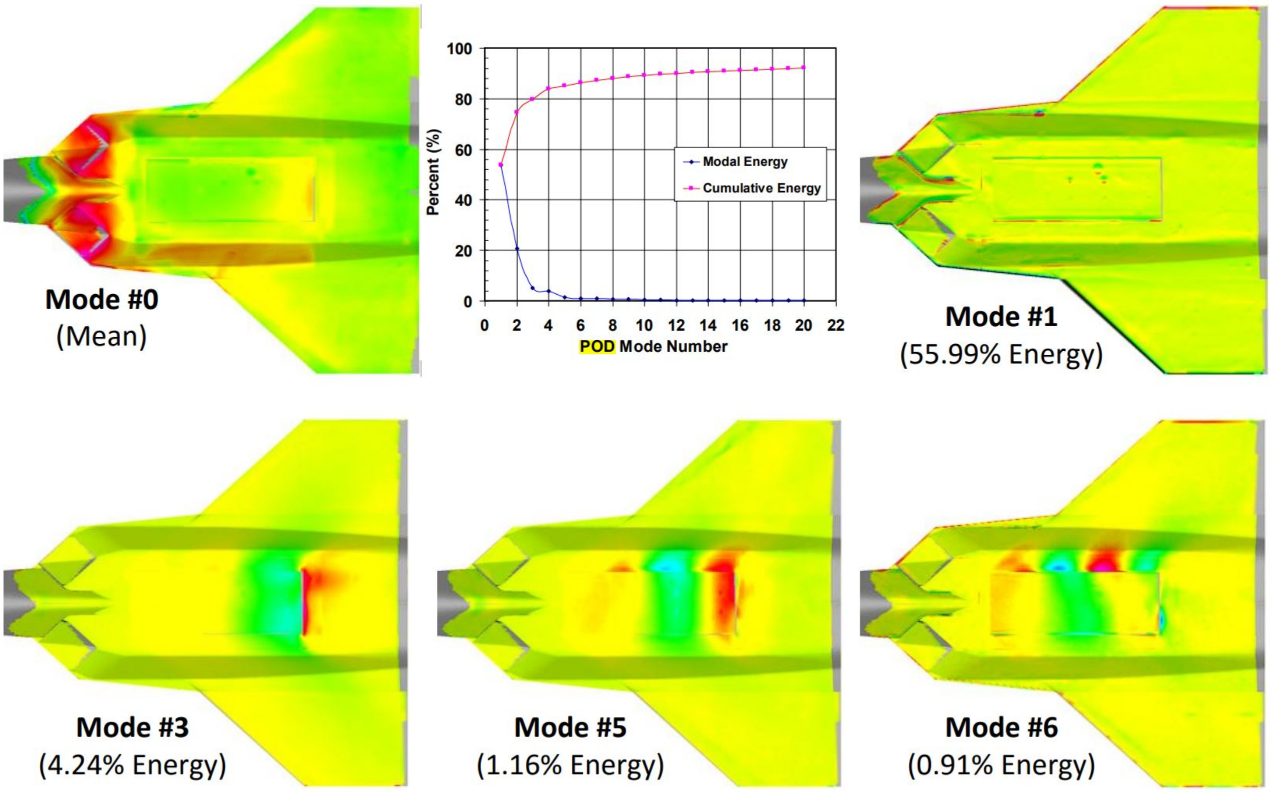

Figure D.12: POD of the PSP data of a full scale tactical fighter model. Also shown is the modal energy distribution and the 0th mode, which corresponds to the mean. Source: Sellers et al. [12]

A comparison between the noisy data and the POD reconstructed data can be found in Figure D.13 for a series of snapshots separated by 0.1 ms. From the obtained reconstruction the important flow features are much more prominent compared to the original noisy data. However, distinct stripped patterns are found in the denoised data due to coupling of modes with noise sources. These striped patterns can also be found in the POD analysis of Gregory et al. [109].

DMD

Similarly to POD, DMD decomposes a large data set into different modes. DMD modes show spatiotemporal coherent structures, as they are characterised by a spatial component coupled with an single oscillatory frequency and / or growth / decay rate. According to Taira et al. [124], it is often used for a diagnostic analysis of data to provide insight into the relevant systems. It was originally developed for fluid analysis application, but has since been used in many different fields.

The mathematical definition of DMD is as follows. Inputs to the DMD system are snapshots of a vector field obtained from physical experiments or CFD. Each snapshot is separated by a constant time, often the acquisition frequency of the system. The entire system is then written as a matrix V, where the columns are the individual snapshots written as vectors ($v(t_i)$). The matrix is then given by

$$V = [v(t_1), v(t_2), v(t_3).....v(t_n)] \tag{D.19}$$

The goal of DMD is to approximate the relationship between subsequent snapshots by a constant linear mapping matrix A such that

$$v(t_{i+1}) = Av(t_i) \tag{D.20}$$

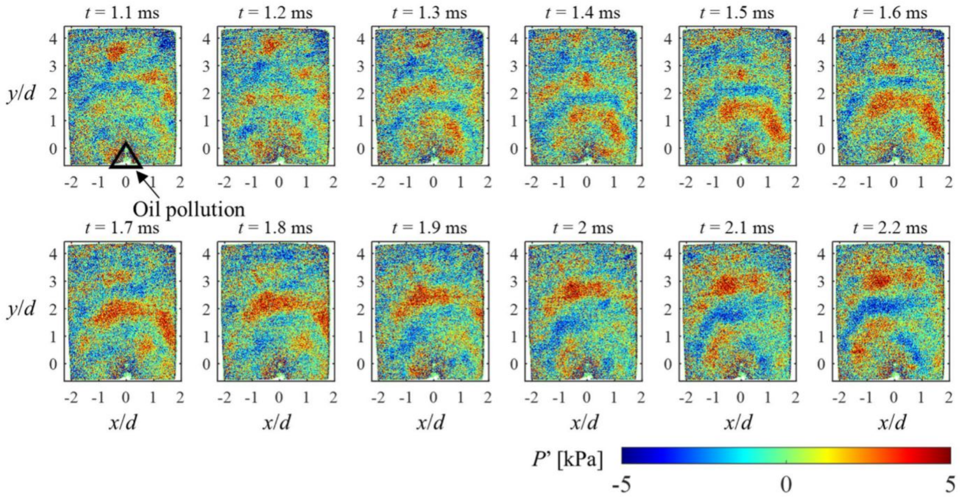

(a) Computed PSP snapshots without noise reduction.

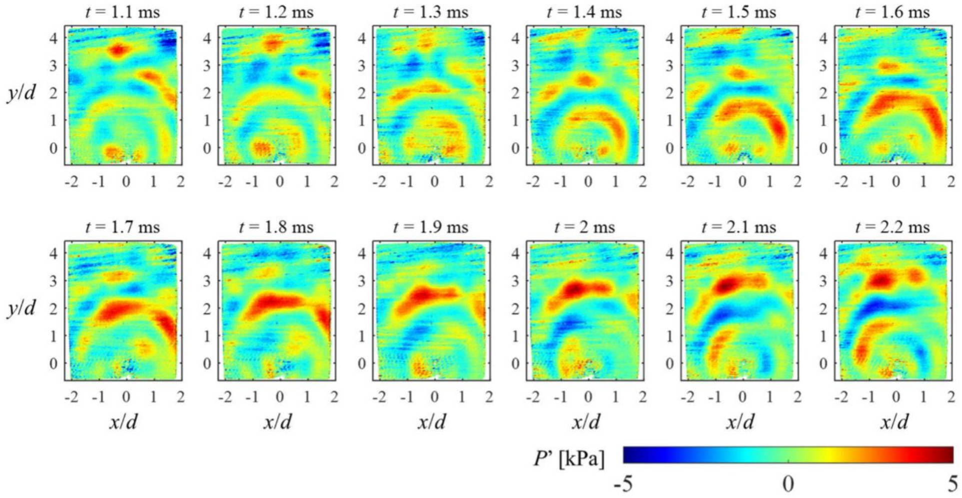

(b) Reconstructed PSP data using the first 120 POD noise modes.

Figure D.13: Results of noise reduction using POD reconstruction of PSP data of a jet impinging on a plate. Included in the reconstruction are the first 120 POD mods. Source: X. Liu et al. [110]

where the eigenvalues and eigenvectors of matrix A denote the dynamic behaviour of the system. The DMD eigenvalues and modes are then defined as the eigenvalues and eigenvectors of A respectively. Here the entire system can then be written by

$$V = [v(t_1), Av(t_1), A^2 v(t_1), A^3 v(t_1), ...A^n v(t_1)] \tag{D.21}$$

Often V is an immense system with a lot more rows than columns. Typically, there are millions of rows with only a few thousand columns [65]. Computing A explicitly would be very inefficient and extremely time consuming. Instead, the eigenvalues and eigenvectors are approximated through an algorithm.

Below follow three applications of DMD on PSP from articles cited in this report. For more detailed description of DMD the author refers readers to the works of Gregory et al. [109], Crafton et al. [122] or Taira et al. [124].

- **DMD analysis of random dot PSP on a wing.**

Imai et al. [57] used DMD to simultaneously analyse pressure fluctuation and structural deformation modes on a wing model. This was possible due to their novelty implementation of random dot PSP, allowing for simultaneous DIC and PSP measurements. Their DMD analysis successfully extracted the dominant modes of structural and pressure fluctuations, thereby opening future research opportunities for the random dot

PSP method in structural load analysis. The results of their analysis are shown in Figure D.14, which gives the computed structural modes, and Figure D.15, which shows the pressure modes. Most DMD modes are related to noise sources in the data and are not displayed. Only the physical modes are selected and shown.

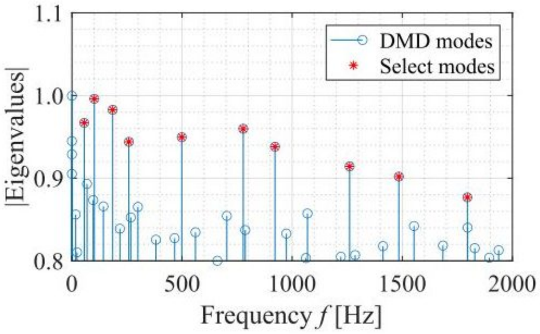

(a) Computed DMD frequencies and their respective eigenvalues for the structural modes. The selected modes are the main structural modes present for the wing. Other modes are mainly associated with measurement noise.

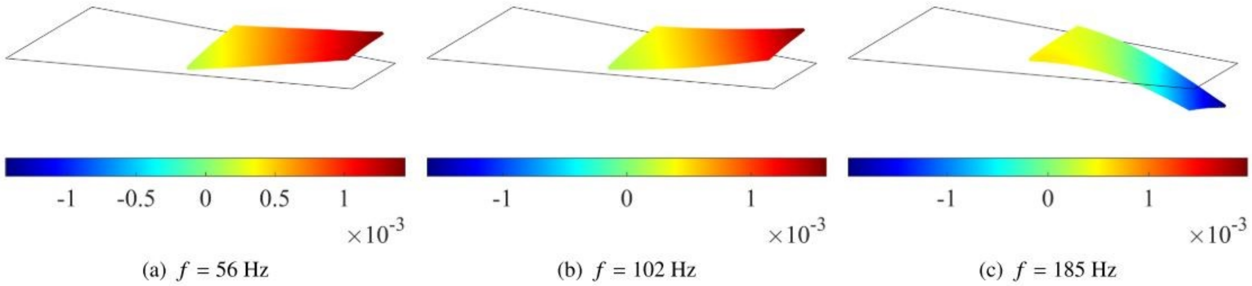

(b) First three selected structural modes at frequencies shown in plot (a). For a visualisation of all modes, see the original article.

Figure D.14: Results of the DMD analysis applied to DIC data from random dot PSP. Source: the work Imai et al. [57].

- **DMD analysis of the 2.5% model scale tests of the SLS using FFT.**

Li et al. [65] used a FFT based approach to compute the DMD modes of PSP data on the 2.5% scale model of the SLS. This required subtracting the measurement mean from the data, giving DMD data of the fluctuations. Details on the exact implementation can be found in their article. Benefits of this approach are a much shorter computational time, as FFT algorithms are much faster than the DMD algorithms.

- **Acoustic pressure field resonance experiment DMD analysis.**

Gregory et al. [109] used DMD to compute the modes in an acoustic pressure field inside a cavity. DMD was compared with POD, phase averaging methods and analytical solutions of the problem. DMD showed good agreement with the other two methods and with the analytical solution. A summary of the results is also given in the work of Crafton et al. [122].

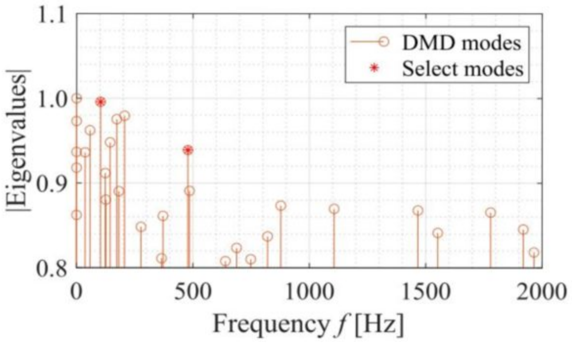

(a) Computed DMD frequencies and eigenvalues for the pressure modes. Similarly to the structural modes, the selected pressure modes are the main physical modes, whereas other modes are noise dominated.

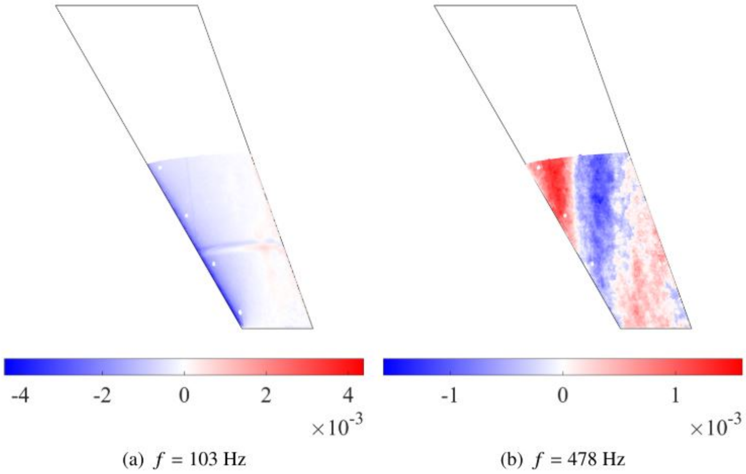

(b) Two selected pressure modes on the wing.

Figure D.15: Results of the DMD analysis applied to pressure data from random dot PSP. Source: the work Imai et al. [57].

E List of LVs with HHF

Vega family launchers

All 3 launchers in the Vega family use HHF[43]. They are shown in Figure E.1.

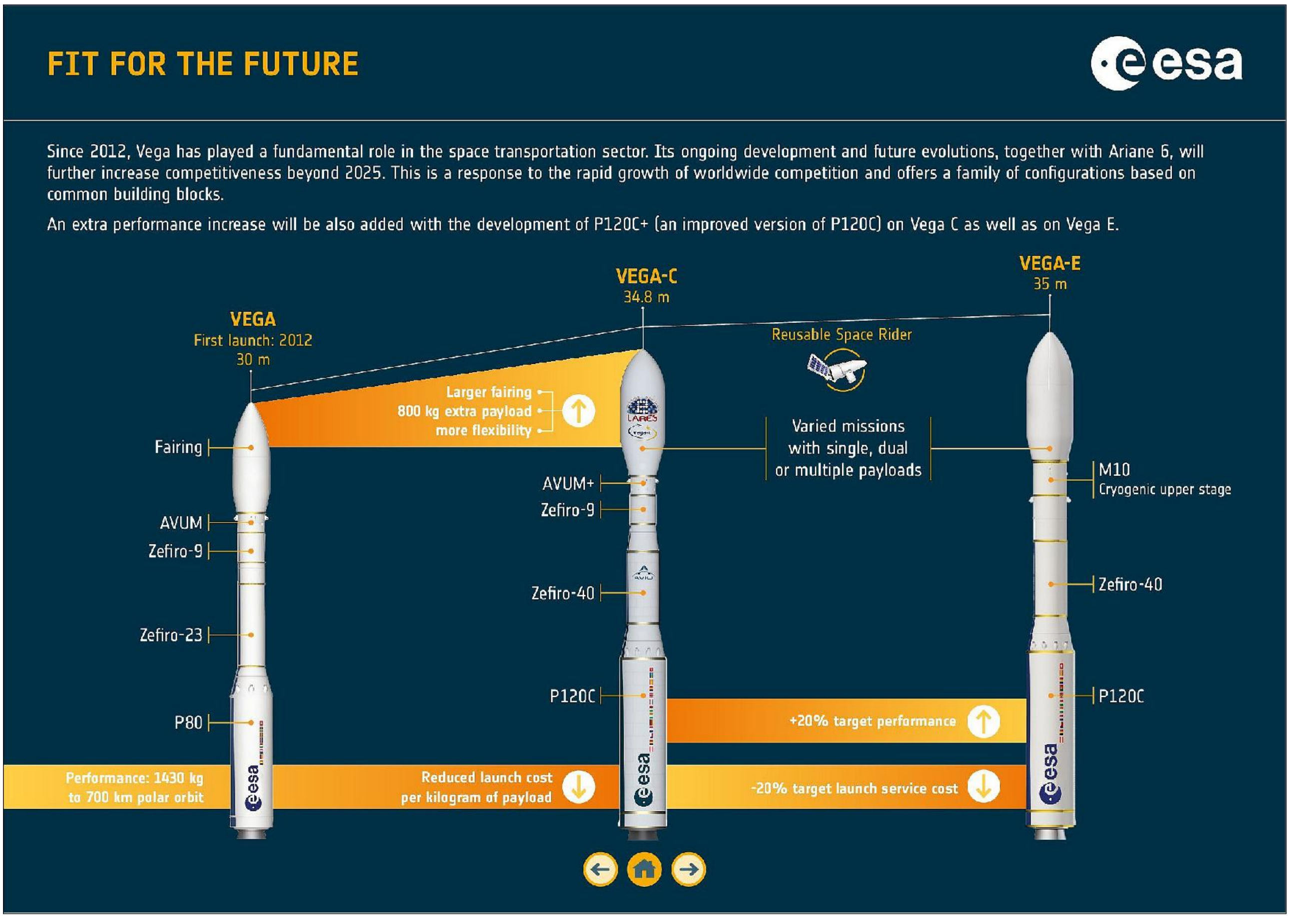

FIT FOR THE FUTURE

Since 2012, Vega has played a fundamental role in the space transportation sector. Its ongoing development and future evolutions, together with Ariane 6, will further increase competitiveness beyond 2025. This is a response to the rapid growth of worldwide competition and offers a family of configurations based on common building blocks.

An extra performance increase will be also added with the development of P120C+ (an improved version of P120C) on Vega C as well as on Vega E.

Figure E.1: Vega launcher family. Source: ESA[43]

Space X launchers

The most configurations on the Falcon family of launchers use HHF[44], as shown in Figure E.2.

---

[43] https://www.eoportal.org/ftp/satellite-missions/a/Ariane6_140722/Ariane6_Auto67.jpeg, Retrieved November 2023

[44] https://en.wikipedia.org/wiki/Falcon_9/media/File:Falcon9_rocket_family.svg, Retrieved November 2023

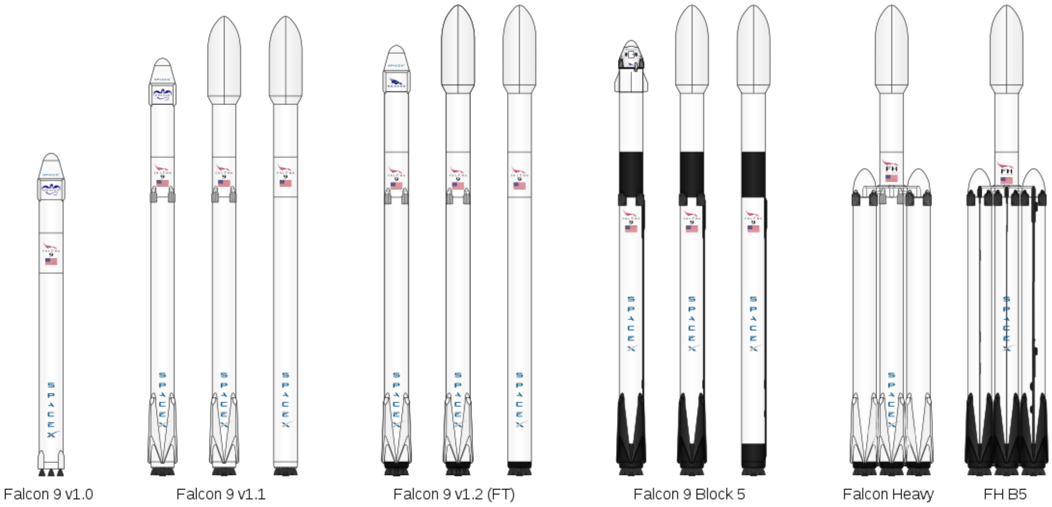

Figure E.2: Falcon launcher family and payload configurations. Source: Wikipedia[44].

Atlas V

The Atlas V launcher has many HHF[45] configurations which can be seen in Figure E.3.

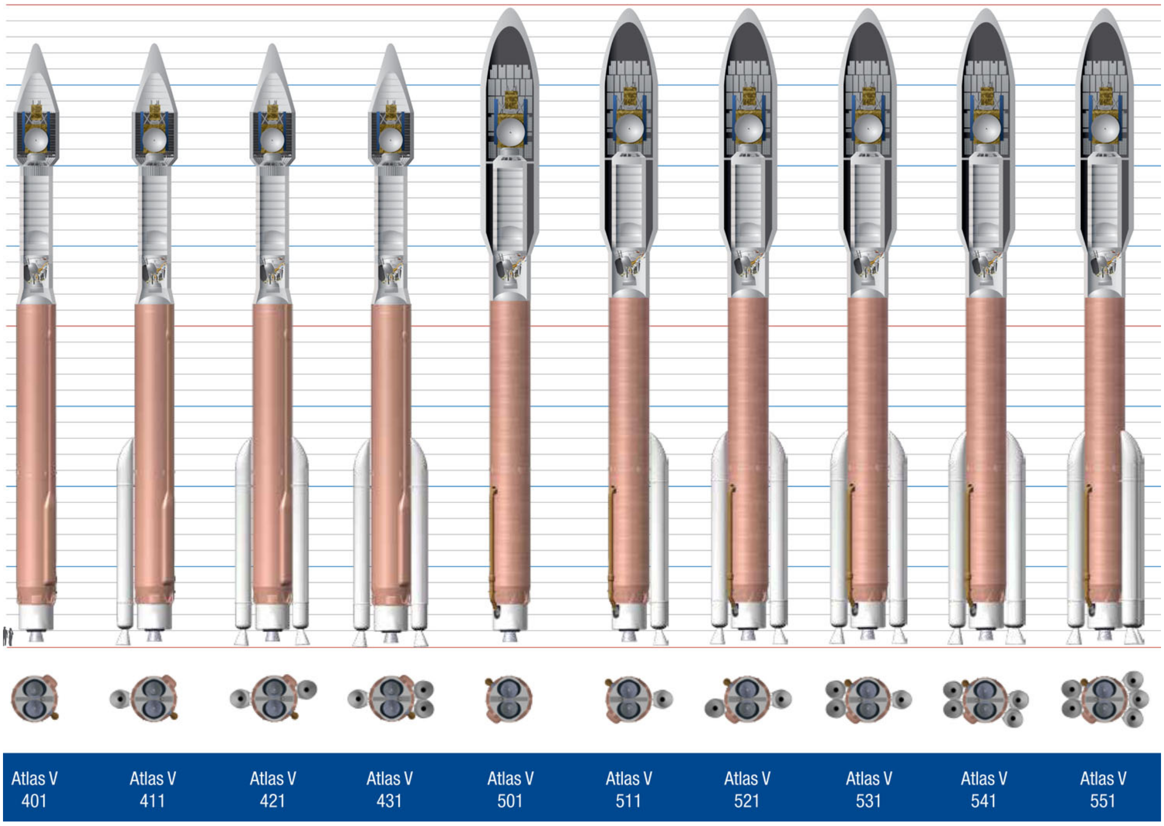

Figure E.3: Atlas V payload configurations. Source: United Launch Alliance[45].

---

[45] `https://www.ulalaunch.com/rockets/atlas-v`, Retrieved November 2023

Long March Family

Numerous configurations from the chinese Long March family of launchers uses the HHF[46]

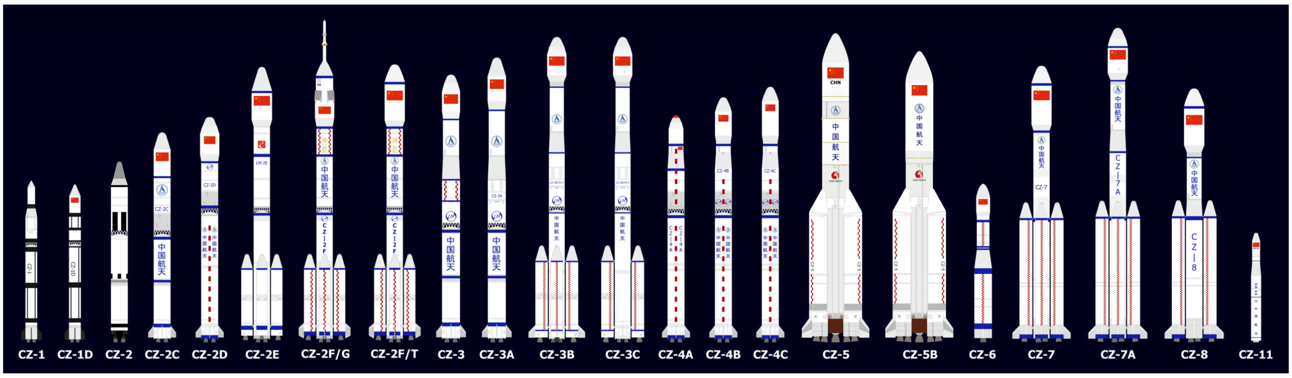

Figure E.4: Different Long March family launchers. Source: Wikipedia[46].

Other

Other launchers that have used the HHf configuration include:

- The Brazilian VLS-1 LV
- Delta-II launcher from the united launch alliance
- The American Minotaur I
- Indias LVM3

---

[46] `https://en.wikipedia.org/wiki/Long_March_(rocket_family)`, Retrieved November 2023.

F Solid Blockage Estimation

In order to have a simple verification of the +0.05 ΔM observed by Romero and D'Aguanno [18, 26], 1D wind tunnel flow theory is applied to estimate the impact of solid blockage[47]. This is done purely on a geometric basis, without accounting for the growing wind tunnel wall boundary layer. For this, the following equations are used:

$$(1 - M^2) \cdot \frac{dV}{V} = -\frac{dA}{A} \tag{F.1}$$

$$\dot{m} = \rho \cdot V \cdot A \tag{F.2}$$

$$\rho \cdot V \cdot dV = -dp \tag{F.3}$$

$$a = \sqrt{\frac{dp}{d\rho}} \tag{F.4}$$

$$\Delta M = \frac{V + dV}{a} - M \tag{F.5}$$

where M is the setpoint Mach number, V the calculated test section freestream velocity, A the wind tunnel area ($0.255m \cdot 0.28m = 0.0714m^2$), $\dot{m}$ the massflow, ρ the freestream density, p the freestream pressure, a the speed of sound of the flow including blockage and the dx values are the changes in one of the variables due to the blockage. Free stream conditions were taken from Table 5.1. Two blockage ratios were used to calculated ΔM, namely 2.75% and 2.757%, as described in Subsection 5.2.6. The obtained change in Mach number for different test conditions using the lower blockage ratio can be found below in Table F.1. Changes for the higher blockage ratio are within +0.001 and therefore not shown.

M	T_{tot}	V *(m/s)*	ρ (kg/m^3)	p *(kPa)*	$\dot{m}$ $(kg/s$	dV (m/s)	$d\rho$ (kg/m^3)	dp (kPa)	a *(m/s)*	ΔM
0.8	**286K**	256	1.81	132.8	33.08	19.56	-0.08	-9.1	316.5	0.071
	270K	248	1.93		34.17	18.94	-0.09	-9.1	306.5	0.071
0.75	**286K**	242	1.88	139.4	32.48	15.21	-0.06	-6.9	319.3	0.055
	270K	234	2.00		33.42	14.71	-0.07	-6.9	309.6	0.053
0.7	**286K**	227	1.94	146.0	31.44	12.24	-0.05	-5.4	322.5	0.042
	270K	220	2.07		32.52	11.86	-0.05	-5.4	321.2	0.043

Table F.1: 1D flow geometric blockage calculations using 2.75% blockage ratio.

From this it can be concluded that the estimated $+0.05M$ is realistic, as it is close to the values that would be expected purely from 1D solid blockage.

---

[47] `https://www.grc.nasa.gov/www/k-12/airplane/tunnozt.html`,retrieved September 2024

G PSP analysis flowchart

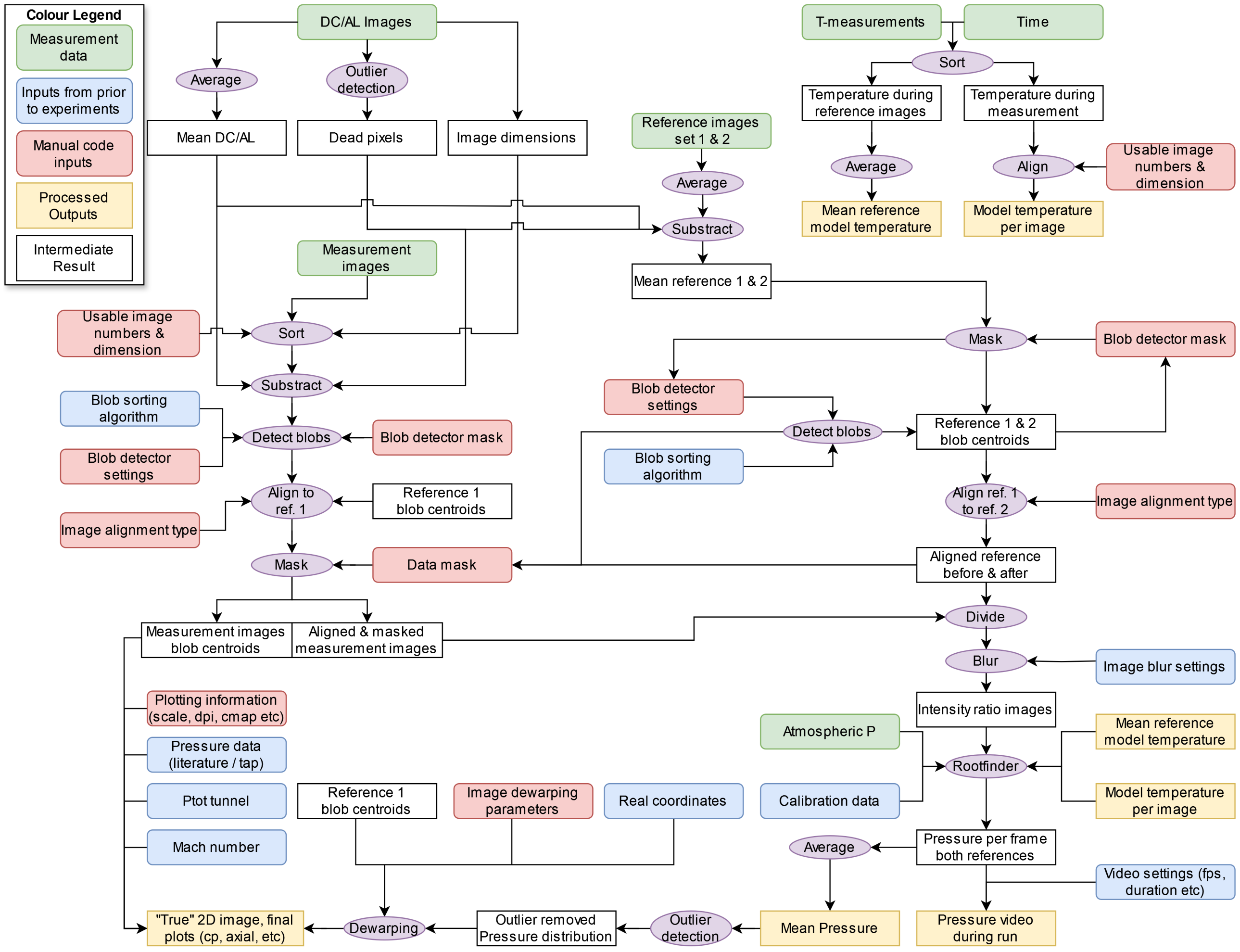

Figure G.1: Full PSP analysis code flowchart. Oval, purple cells are processing operations.

H Coupon Measurement tables

Run	p_1 (kPa)	p_2 (kPa)	T_1 ($°C$)	T_2 ($°C$)	Time ($min:s$)	Notes
5	103.0	atm	18.7	?	?	54980 μs exposure time and +6 db Pre-amp gain used for all runs. **Measurements done using Eurolite lamps until run 13**.
6	12.0	12.1	18.15	?	?	
7	53.0	56.6	15.6	?	?	
8	78.6	80.5	16.3	?	?	
9	89.0	90.1	17.2	?	?	
10	168.6	167.4	18.7	?	?	
11	160.8	159.4	18.7	?	?	
12	137.6	136.9	18.7	?	?	
13	116.3	116.1	18.7	?	?	
14	atm	atm	18.1	?	?	**Checking paint linearity with lamp power until run 19.** DLR LED set to 12.9V and 1.97A.
15	atm	atm	18.1	?	?	DLR LED set to 12.8V and 1.71A.
16	atm	atm	18.0	?	?	DLR LED set to 12.8V and 1.51A.
17	atm	atm	18.1	?	?	DLR LED set to 12.7V and 1.30A.
18	atm	atm	18.0	?	?	DLR LED set to 12.6V and 1.09A.
19	atm	atm	18.0	?	?	DLR LED set to 12.5V and 0.88A.
DC3	-	-	-	-	-	**Over-pressure runs with coupon 1 until run 39**. DC3 is the dark current image used for this measurement set
20	102.9	102.9	18.0	?	00:00	Measurements took place 30s after lamp turned on. Time until run 39 is with respect to the starting time run 20.
21	162.4	162.9	18.0	?	03:12	
22	147.0	145.0	17.9	?	04:32	
23	192.3	192.0	18.6	?	06:56	
24	140.6	138.1	18.1	?	10:20	
25	125.7	124.6	17.9	?	11:36	
26	186.5	186.3	18.4	?	13:18	
27	206.1	206.6	18.3	?	16:42	
28	205.9	205.9	6.0	6.0	22:56	
29	205.6	205.6	11.4	11.4	26:06	
30	161.9	159.3	11.5	11.5	27:48	Outlier compared to rest of the dataset
31	164.7	164.6	1.6	1.7	33:42	
32	127.9	126.6	15.2	15.2	40:32	
33	102.9	atm	14.7	14.7	42:36	Atmospheric pressure (atm) until run 39. Around 102.9 with some uncertainty.
34	102.9	atm	10.5	10.0	44:36	

Table H.1a: Coupon measurement table part 1. p_1 and p_2 are the starting and ending pressure of the measurement respectively. When the p_1 and / or p_2 is denoted as atm, either have not been explicitely measured, but were instead equal to atmospheric pressure. Similarly, T_1 and T_2 are the starting and ending temperature. Cells with - indicate that the quantity is not relevant for the measurement. Cells with ? indicate that the measurement was not taken despite being relevant.

Run	p_1 (kPa)	p_2 (kPa)	T_1 ($°C$)	T_2 ($°C$)	Time ($min:s$)	Notes
35	102.9	atm	5.1	5.1	46:02	
36	102.9	atm	1.2	1.4	48:00	
37	102.9	atm	18.1	?	53:10	Temperature is oddly high, higher than room temperature.
38	102.9	atm	20.0	19.6	56:36	Temperature is oddly high, higher than room temperature.
39	102.9	atm	20.0	20.2	57:26	Temperature is oddly high, higher than room temperature.
LDC	-	-	-	-	-	**L-runs were used to quantify the paint decay rate using the first coupon**. LDC is the dark current image for this measurement set.
L1	103.4	atm	16.7	?	00:39	L1 lasted 1 minute, from 9s to 01:09s. Subsequent L runs were around ~ $20s$.
L2	atm	atm	16.8	?	07:36	
L3	atm	atm	16.8	?	13:56	
L4	atm	atm	?	?	19:56	
L5	atm	atm	16.8	?	23:59	
L6	atm	atm	16.9	?	32:21	
L7	atm	atm	16.9	?	38:32	
L8	103.0	atm	?	?	43:06	
U1	103.0	103.0	17.4	?	00:7	**U-runs are the under-pressure runs with coupon 1.** Starting time is 3 min 50s after the lamp was turned on. Time until run U16 is with respect to this first run.
U2	66.2	68.7	17.1	17.2	01:21	
U3	68.6	71.3	17.0	17.3	02:27	
U4	66.1	68.6	17.6	17.6	03:59	
U5	80.6	82.5	17.6	17.6	05:41	
U6	88.4	89.7	17.6	?	06:59	
U7	68.4	70.9	12.4	12.5	10:19	
U8	59.6	61.9	12.0	12.0	11:13	
U9	79.4	80.9	11.9	11.8	13:31	
U10	85.0	86.5	7.0	7.0	16:01	
U11	78.0	80.0	6.5	6.6	16:55	
U12	60.2	62.8	5.8	6.1	17:49	
U13	52.5	55.0	5.8	5.8	18:41	
U14	73.0	75.0	8.9	8.9	20:49	
U15	96.3	97.5	15.4	15.7	26:19	
U16	101.7	101.9	16.7	16.8	29:31	
UDC	-	-	-	-	-	Dark current image for U runs.
N1	102.9	atm	17.8	17.8	00:00	**N-runs are the under-pressure runs with coupon 2.** Starting time is 3 min 30s after lamp first turned on. Time for all N- and H-runs are with respect to this first run.
N2	atm	atm	13.0	12.9	02:41	

Table H.1b: Coupon measurement table continued, part 2. p_1 and p_2 are the starting and ending pressure of the measurement respectively. When the p_1 and / or p_2 is denoted as atm, either have not been explicitely measured, but were instead equal to atmospheric pressure. Similarly, T_1 and T_2 are the starting and ending temperature. Cells with - indicate that the quantity is not relevant for the measurement. Cells with ? indicate that the measurement was not taken despite being relevant.

Run	p_1 (kPa)	p_2 (kPa)	T_1 ($^\circ C$)	T_2 ($^\circ C$)	Time ($min:s$)	Notes
N3	atm	atm	9.8	9.8	04:42	
N4	85.6	87.0	10.0	10.6	06:00	
N5	53.1	56.5	11.7	12.3	07:30	
N6	73.4	75.5	14.8	15.0	08:46	
N7	64.4	68.3	15.1	15.4	09:48	
N8	60.0	63.5	16.3	16.6	12:25	
N9	75.9	77.8	17.2	17.4	13:30	
N10	86.8	88.0	17.6	17.7	14:50	
N11	92.4	93.6	17.8	17.8	16:00	
N12	72.4	74.9	17.2	17.2	17:10	
N13	52.2	54.9	17.2	17.4	18:20	
N14	55.6	58.5	8.0	8.2	22:10	
N15	74.0	75.9	8.3	8.3	23:50	
N16	82.8	84.6	8.1	8.1	25:05	
N17	69.5	73.1	5.3	5.8	27:20	
H1	102.8	102.8	18.0	18.1	35:20	**H-runs are the over-pressure runs with coupon 2.** Thermocouple position put closer to the edge compared to N runs. Time is with respect to first N run
H2	131.8	130.0	18.8	18.7	37:00	
H3	156.1	153.5	19.0	18.9	38:30	
H4	142.4	140.8	18.8	18.8	39:59	
H5	202.1	201.8	19.4	19.3	41:30	
H6	183.6	180.3	18.9	18.9	43:42	
H7	166.2	166.0	19.1	19.1	45:42	
H8	132.0	130.5	18.7	18.7	47:40	
H9	117.1	116.4	18.6	18.7	49:20	
H10	169.0	168.7	13.1	13.2	52:20	
H11	143.1	143.1	12.8	12.9	53:40	
H12	173.9	173.7	8.7	8.8	57:27	
H13	134.4	134.1	6.0	6.2	60:10	Coupon paint delaminated; invalid data.
H14	121.7	122.0	10.6	11.8	61:30	Coupon paint delaminated; invalid data.
H15	103.4	103.4	17.8	18.0	66:52	Coupon paint delaminated; invalid data.
DC6	-	-	-	-	-	Dark current image for N- and H-runs.
DC15	-	-	-	-	-	Dark current image for the paint and lamp decay run.
Decay	103.2	atm	16.7	16.9	17:02	Continuos run at lowered fps to measure paint decay rate and lamp stability. Suspected that lamp instability was partially caused by instability in the power supply.

Table H.1c: Coupon measurement table continued, part 3. p_1 and p_2 are the starting and ending pressure of the measurement respectively. When the p_1 and / or p_2 is denoted as atm, either have not been explicitely measured, but were instead equal to atmospheric pressure. Similarly, T_1 and T_2 are the starting and ending temperature. Cells with - indicate that the quantity is not relevant for the measurement. Cells with ? indicate that the measurement was not taken despite being relevant.

I Wind Tunnel Test Matrix

Run	Name	M	$\alpha(°)$	Tc	p_{atm}	p_{tot}	Notes
1	IR-ESA 1	0.8	0	no	-	-	Long IR run to characterize wind tunnel temperature over time. Measures temperature before and after the wind tunnel is turned on. Later observations showed that this temperature is highly dependent on outside weather, but a clear pattern can be seen due to model geometry and aerodynamic forces. Perspective of this run focused on the payload fairing.
2	IR-ESA 2	0.8	0	no	-	-	Same as the first run using a different perspective, focused more downstream of the boat tail. Run took place ~ 50 minutes after the first run to let model temperature stabilize.
3	IR-ESA 3	0.8	0	no	-	-	Same as previous two runs, with the perspective of the second run. This run took place a couple (~ 3 minutes after the second run to see the effect of consecutive runs.
4	Cone 1	~0.65	0	no	100.8	?	p_{tot} = 1.5 bar. No T or p data. M number did not stabilize. Some paint peeling visibile near pressure taps. **Not analysed in this report.**
5	Cone 2	0.658	0	two	100.8	?	p_{tot} = 1.5 bar. M number did not stabilize. Significant paint peeling throughout the model. One thermocouple on model, one on sting. Sting one likely unreliable. Reference before taken a long time before the run, giving significant photo-degradation between measurements.
6	Cone 3	0.6	0	two	100.8	202.1	Significant paint peeling throughout the model. One thermocouple on model, one on sting. Sting one likely unreliable.
7	Cone 4	0.6	0	one	100.7	202.2	Significant paint peeling throughout the model. One thermocouple on the sting, likely has unreliable data. Other thermocouple was blown off the model.
8	Cone 5	0.65	0	one	100.7	202.3	Paint peeling throughout the model. One thermocouple on the sting, likely has unreliable data. Other thermocouple was blown off the model.
9	CN 1	0.7	0	two	101.4	202.5	Significant differences between reference before and after for pressure calculation. Likely attributed to higher degrees of paint decay during the first run.
10	CN 2	0.8	0	two	101.4	202.5	
11	CN 3	0.8	0	two	atm	202.4	Long run to make a video (bobcat).

Table I.1a: Wind tunnel measurement table. The Tc column indicates the number of thermocouples, p_{atm} the pressure of the reference measurements and p_{tot} the total pressure of the wind tunnel. Runs are numbered from 1 to N and also named after the activity. Runs starting with S- are schlieren runs used to analyse the impact of the paint on the aerodynamic behaviour. When runs have an "u" at the end, measurements were taken from a high up perspective. Similarly, runs with d at the end were taken from a "down" perspective. ESA runs marked by P# are runs with protuberance rings installed. When the p_{atm} column is set to "atm", the atmospheric pressure was not directly recorded. It therefore may have changed slightly, leading to some degree of uncertainty.

Run	Name	M	$\alpha(°)$	Tc	p_{atm}	p_{tot}	Notes
12	CN 4	0.7	0	two	atm	202.5	Long run to make a video (bobcat).
13	CN 5	0.75	0	two	atm	202.5	Long run to make a video (sCMOS). Mean ref before temperature $14.8°C$.
14	CN 6	0.75	0	two	atm	202.1	
15	CN 7	0.8	4	one	atm	202.3	First thermocouple detached from the model during run.
16	CN 8	0.8	4	one	atm	202.2	Thermocouple 1 still detached.
17	S-CN 9	0.8	4	-	-		Pilot run 1. Vertical knife edge, noisy data.
18	S-CN 10	0.8	4	-	-		Pilot run 2. Veritcal knife edge, less light blockage than previous run.
19	S-CN 11	0.8	4	-	-		Pilot run 3. Horizontal knife edge.
20	S-CN 12	0.8	4	-	-		Full run. Horizontal knife edge, more sensitive than previous run.
21	S-CN 13	0.8	4	-	-		Same as S-CN12.
22	S-CN 14	0.8	0	-	-		Same as S-CN12.
23	S-CN 15	0.8	0	-	-		Same as S-CN12.
24	ESA 1	0.8	0	two	103.2	202.7	Similarly to CN 1, high differences found between reference before and reference after. Recurring pattern also seen in ESA P1. First paint coat used until ESA 16d.
25	ESA 2	0.7	0	two	103.2	202.8	Multiple runs right after eachother until ESA 4.
26	ESA 3	0.8	0	two	atm	202.6	
27	ESA 4	0.7	0	two	atm	202.8	
28	ESA 5	0.6	0	two	atm	202.5	Multiple runs right after eachother until ESA 8.
29	ESA 6	0.8	0	two	atm	202.5	
30	ESA 7	0.75	0	two	103.2	202.4	
31	ESA 8	0.75	0	two	103.2	202.2	
32	ESA 9u	0.7	4	two	103.0	202.7	Multiple runs right after eachother until ESA 12u. High up perspective with an additional fiducial marker placed to highlight the top of the model.
33	ESA 10u	0.8	4	two	103.0	202.6	
34	ESA 11u	0.8	4	two	103.0	202.7	
35	ESA 12u	0.7	4	two	103.0	202.7	
36	S-ESA	0.8	4	-	-	-	Recorded with a high speed camera at 5000 fps. Schlieren setup found to be optimal in the first run, similar to the S-CN runs.
37	ESA 13d	0.8	4	two	100.1	202.7	Multiple runs right after each other until ESA 16d. Low camera perspective to image bottom of the model. Attempted to use lower fiducial marks to mark the bottom, but these were misplaced.
38	ESA 14d	0.7	4	two	100.1	202.8	Small amount of paint peeling
39	ESA 15d	0.8	4	two	100.1	202.8	High paint peeling at the edges.
40	ESA 16d	0.7	4	two	100.1	202.8	High paint peeling at the edges.

Table I.1b: Wind tunnel measurement table. The Tc column indicates the number of thermocouples, p_{atm} the pressure of the reference measurements and p_{tot} the total pressure of the wind tunnel. Runs are numbered from 1 to N and also named after the activity. Runs starting with S- are schlieren runs used to analyse the impact of the paint on the aerodynamic behaviour. When runs have an "u" at the end, measurements were taken from a high up perspective. Similarly, runs with d at the end were taken from a "down" perspective. ESA runs marked by P# are runs with protuberance rings installed. When the p_{atm} column is set to "atm", the atmospheric pressure was not directly recorded. It therefore may have changed slightly, leading to some degree of uncertainty.

Run	Name	M	$\alpha(^\circ)$	Tc	p_{atm}	p_{tot}	Notes
41	ESA P1	0.8	0	two	101.3	203.3	New paint coat for remainder of the runs. Multiple runs right after eachother until ESA P3. Wrong protuberance ring orientation, **not analysed in this report due to this.**
42	ESA P2	0.7	0	two	101.3	203.2	Wrong protuberance ring orientation, **not analysed in this report due to this.**
43	ESA P3	0.8	0	two	atm	203.2	Wrong protuberance ring orientation, **not analysed in this report due to this.**
44	ESA P4	0.7	0	two	atm	203.1	Wrong protuberance ring orientation, **not analysed in this report due to this.**
45	ESA P5	0.7	0	two	atm	203.1	Wrong protuberance ring orientation, **not analysed in this report due to this.**
46	ESA P6	0.8	4	two	atm	202.9	High protuberance ring rotation, data likely invalid. Small amount of paint peeling.
47	ESA P7	0.8	4	two	atm	202.9	Long run. Some model rotation and image frame model movement present.
48	ESA P8	0.8	0	one	102.2	203.3	One thermocouple detached during the run. Back and forth model rotation resulting in relatively big final twist. Significant paint peeling.
49	ESA P9	0.7	0	two	102.2	203.0	Detached thermocouple re-attached. Small back and forth rotational vibration. Some paint peeling.
50	ESA P10	0.8	0	two	102.2	203.0	Small rotational vibration.
51	ESA P11	0.7	0	two	102.2	203.1	Very small model vibration.
52	ESA P12	0.75	0	two	102.2	203.1	Some model rotation.
53	ESA P13d	0.8	4	one	101.0	203.3	Low camera perspective to measure windward side. Thermocouple cable broke before runs. Not repaired for remainder of campaign. Downward model movement in image frame. Fiducial marks placed at the bottom of the model
54	ESA P14d	0.8	4	one	101.0	203.3	
55	ESA P15u	0.8	4	one	atm	202.7	High camera perspective to image leeward side. Additional fiducial mark placed to highlight top of the model.
56	ESA P16u	0.8	4	one	atm	202.8	
57	ESA P17u	0.7	4	one	101.0	202.7	Comparison between 550nm and 610nm longpass filters.

Table I.1c: Wind tunnel measurement table. The Tc column indicates the number of thermocouples, p_{atm} the pressure of the reference measurements and p_{tot} the total pressure of the wind tunnel. Runs are numbered from 1 to N and also named after the activity. Runs starting with S- are schlieren runs used to analyse the impact of the paint on the aerodynamic behaviour. When runs have an "u" at the end, measurements were taken from a high up perspective. Similarly, runs with d at the end were taken from a "down" perspective. ESA runs marked by P# are runs with protuberance rings installed. When the p_{atm} column is set to "atm", the atmospheric pressure was not directly recorded. It therefore may have changed slightly, leading to some degree of uncertainty.

J Protuberance Ring Rotation

Run Name	Model Movement Observations	Net Rotation $\Delta\phi$ (°)
ESA P1	Small back and forth rotation of the model at and upstream of the second protuberance, likely due to model vibration. Movement both cw and ccw.	Not processed
ESA P2	Very small rotational vibration of the model at and upstream of the second protuberance. Movement both cw and ccw.	Not processed
ESA P3	No discernible movement.	Not processed
ESA P4	No discernible movement.	Not processed
ESA P5	No discernible movement.	Not processed
ESA P6	High cw rotation of the model at and upstream of the second protuberance.	Not processed
ESA P7	Small cw rotation of the model at and upstream of the second protuberance in addition to a small amount of downward model or camera movement in the image.	$-0.8° \pm 0.2°$
ESA P8	Small back and forth rotation of the model at and upstream of the second protuberance ring resulting in a relatively large net ccw rotation.	$4.6° \pm 0.3°$
ESA P9	Very small rotational vibration of the model at and upstream of the second protuberance. Movement both cw and ccw.	$-0.4° \pm 0.2°$
ESA P10	Very small rotational vibration of the model at and upstream of the second protuberance resulting in a small cw rotation. Movement both cw and ccw.	$-0.1° \pm 0.2°$
ESA P11	Very hard to notice small rotational vibration of the model at and upstream of the second protuberance.	$0.0° \pm 0.2°$
ESA P12	Brief back and forth rotation of the model at around a third of the images at and upstream of the second protuberance.	$0.2° \pm 0.2°$
ESA P13d	Small amount of downward movement in image plane, likely due to camera or model movement.	$-0.5° \pm 0.3°$
ESA P14d	No discernible movement.	$-0.4° \pm 0.2°$
ESA P15u	No discernible movement.	$-0.2° \pm 0.2°$
ESA P16u	No discernible movement.	$-0.1° \pm 0.2°$
ESA P17u	No visually discernible rotation. Downstream model movement in camera plane between references.	$0.5° \pm 0.2°$

Table J.1: Observations with regards to model movement on the ESA measurements with protuberance rings during the run. Shown is also the relative final rotation ($\Delta\phi$) of the model between the reference before the run and the reference after the run. This is **not** always same as the observation of the rotations during the measurement, as model rotation also took place before and after camera acquisition. "cw" stands for clockwise and "ccw" for counter-clockwise. Here a ccw rotation is defined as a point moving up in the image plane after rotating, and cw as a point moving down. As the positive azimuthal position is defined on top of the model, ccw is a positive rotation and cw a negative one. Rotation uncertainty shown is either the spread between points or an assumed blob misalignment of 0.5 pixels, whichever is the biggest.

K Temperature Data

Run	Name	T_{start} ($°C$)	T_{end} ($°C$)	ΔT (K)	Run time (s)	$\dot{T}$ (K/s)
9	CN 1	10.3	6.4	-3.9	14	-0.279
10	CN 2	4.6	2.5	-2.1	16	-0.131
11	CN 3	3.5	2.0	-1.5	11.54	-0.130
12	CN 4	2.8	1.4	-1.4	12	-0.117
13	CN 5	7.9	5.3	-2.6	12	-0.217
14	CN 6	4.4	2.2	-2.2	16	-0.138
15	CN 7	11.4	7.7	-3.7	16	-0.231
16	CN 8	5.5	1.8	-3.7	20	-0.185
24	ESA 1	13.5	8.8	-4.7	17.66	-0.266
25	ESA 2	8	5.3	-2.7	17.66	-0.153
26	ESA 3	3.9	2.3	-1.6	17.66	-0.091
27	ESA 4	2.5	1.7	-0.8	17.66	-0.045
28	ESA 5	14.3	11.2	-3.1	17.66	-0.176
29	ESA 6	9.2	6.6	-2.6	17.66	-0.147
30	ESA 7	6.5	4.8	-1.7	17.66	-0.096
31	ESA 8	5.1	3.9	-1.2	17.66	-0.068
32	ESA 9u	18.4	16.0	-2.4	20.00	-0.120
33	ESA 10u	14.9	12.6	-2.3	20.00	-0.115
34	ESA 11u	12.5	11.0	-1.5	20.00	-0.075
35	ESA 12u	10.9	10.4	-0.5	20.00	-0.025
37	ESA 13d	15.8	11.4	-4.4	13.333	-0.330
38	ESA 14d	7.4	5.3	-2.1	13.333	-0.158
39	ESA 15d	3.4	1.9	-1.5	13.333	-0.113
40	ESA 16d	1.1	0.5	-0.6	13.333	-0.045
47	ESA P7	8.9	3.8	-5.1	27.4	-0.168
48	ESA P8	13.6	9.5	-4.1	17.35	-0.236
49	ESA P9	10.1	7.1	-3.0	17.35	-0.173
50	ESA P10	4.4	2.4	-2.0	17.35	-0.115
51	ESA P11	1.7	0.6	-1.1	17.35	-0.063
52	ESA P12	0.3	-0.4	-0.7	17.35	-0.040
53	ESA P13d	14.4	10.2	-4.2	16.45	-0.255
54	ESA P14d	8.0	5.4	-2.6	16.45	-0.158
55	ESA P15u	13.1	9.9	-3.2	16.9	-0.189
56	ESA P16u	6.7	4.7	-2.0	16.9	-0.118
57	ESA P17u	9.8	6.8	-3.0	24	-0.125

Table K.1: Theremocouple measurement data table for the HHF measurements. Shown here are the start and end temperature for each measurement, along with the temperature change during the run and mean temperature change rate. When multiple thermocouples were present, the data is the average of both.

L Fiducial mark placement

General notes

- Placed in a zigzag pattern due to analysis and alignment code set up.
- Fiducial marks are sometimes not detected by blob detection program.
- Made with a black whiteboard marker by hand. Better approach would have been to print a mould with exact known locations. Lack of exact locations lead to less optimized alignment. In Figure L.1 an example is given of the process used to find the fiducial mark locations.
- Azimuthal position with respect to eachother not always known. Mostly focused on recording the longitudinal position of each mark.
- Cone images were first dewarped, then the fiducial positions were determined in the dewarped image for alignment.
- Other blobs not shown were used for image alignment. Highly dependent on run and level of paint decay. Here only the pressure taps are shown due to their know location
- In some image sets fiducials may or may not be in view.
- Red circles indicate fiducials detect by SimpleBlobDetector. Red rectangles indicate manually placed fiducial marks

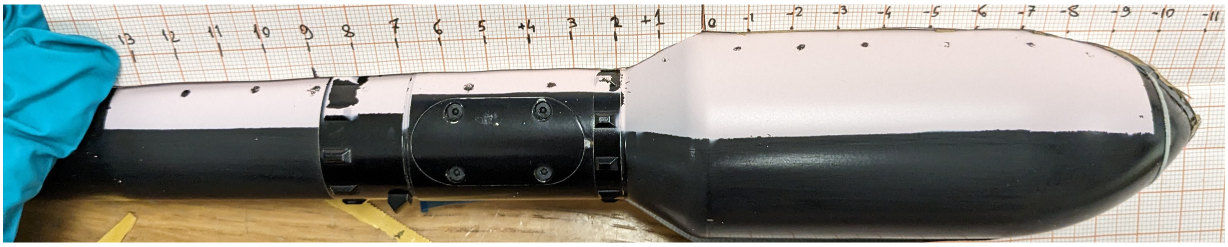

Figure L.1: Part of the measuring process of the location of the fiducial marks. Here a cardbox outline of the model that is glued with mm paper is placed on the model to allow for an estimation of the location of each fiducial mark. This damages the paint and has to be done after the runs. Further verification is then achieved using a caliper to measure the location of each point with respect to each other and other geometrical features. The hatch used to access the pressure taps can also be seen.

L.1. IR Measurements Geometry Features

For the IR measurements, geometry features were used for image dewarping as the author thought there were sufficient features to dewarp. While these are hard to detect, individual images do not have to be aligned as rigorously as PSP images. This combined with the rigidity of the model, allows for them to be detected in a few frames and then be assumed to hold over all frames. While the number of features would in theory suffice, their placement is too close together to allow for proper alignment, leading to some warping in the images. In addition, detection of corners in the IR image proved to be rather tricky due to the low resolution, and similar radiation levels originating in the background. Ideally, more fiducial marks (of which the exact coordinates are known) should have been placed near the edges of the frames. This is especially true for the second POV used in IR-ESA 2-3, as the camera is placed under multiple angles relative to the model, causing more warping.

The coordinates shown in Table L.1 were obtained from the CAD file for the model, with the exception of the pressure tap coordinates (1,2,3). These had to be manually measured as no CAD file was available with the final pressure tap positions. Therefore, all points with the exception of the pressure taps are exact to the manufacturing tolerance. The pressure tap locations were measured by hand using a caliper, with expected inaccuracies of around $\pm 0.2mm$. As for the manually detected pixel coordinates, errors of the order of up to 3 pixels are expected in the final position.

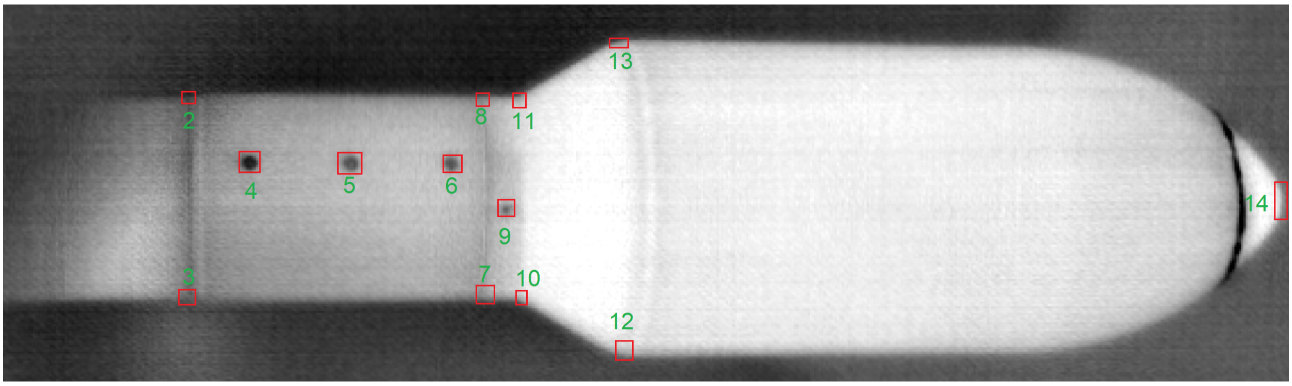

Figure L.2: Geometry features used as fiducial marks in the first IR measurement. All had to be manually found. As there were thousands of frames, it is assumed that there is no model movement during measurements. Coordinates were instead extracted from a couple different frames. Real model movement is sufficiently small for this assumption to hold.

Num	IR1 X,Y (mm, mm)	θ in IR1 (deg)	IR2-3 X,Y (mm, mm)	θ in IR1 (deg)
0	-	-	(198.0, 15.5)	90
1	-	-	(198.0, -15.5)	-90
2	(178.4, 16.0)	90	(178.4, 16.0)	90
3	(178.4, -16.0)	-90	(178.4, -16.0)	-90
4	(170.0, 5.3)	19.2	(170.0, 5.4)	19.8
5	(155.0, 5.3)	19.2	(155.0, 5.4)	19.8
6	(140.0, 5.3)	19.2	(140.0, 5.4)	19.8
7	(135.9, -16.0)	-90	(135.9, -16.0)	-90.0
8	(135.9, 16.0)	90	(135.9, 16.0)	90.0
9	(133.0, -1.9)	-6.9	(133.0, -1.8)	-6.3
10	(128.9, -16.0)	-90	(128.9, -16.0)	-90.0
11	(128.9, 16.0)	90	(128.9, 16.0)	90.0
12	(110.5, -25.0)	-90	(110.5, -25.0)	-90.0
13	(110.5, 25.0)	90	(110.5, 25.0)	90.0
14	0,0	all	-	-

Table L.1: Fiducial mark coordinates for the IR measurements. X,Y are the real 3D coordinates with a right handed coordinate system starting at the the tip, where Y is pointing up and X pointing downstream. θ is the ccw positive angle of the fiducial marks on the model cylinder with respect to the x axis. Angle is taken to be zero at side of the Y = 0 plane facing the camera.

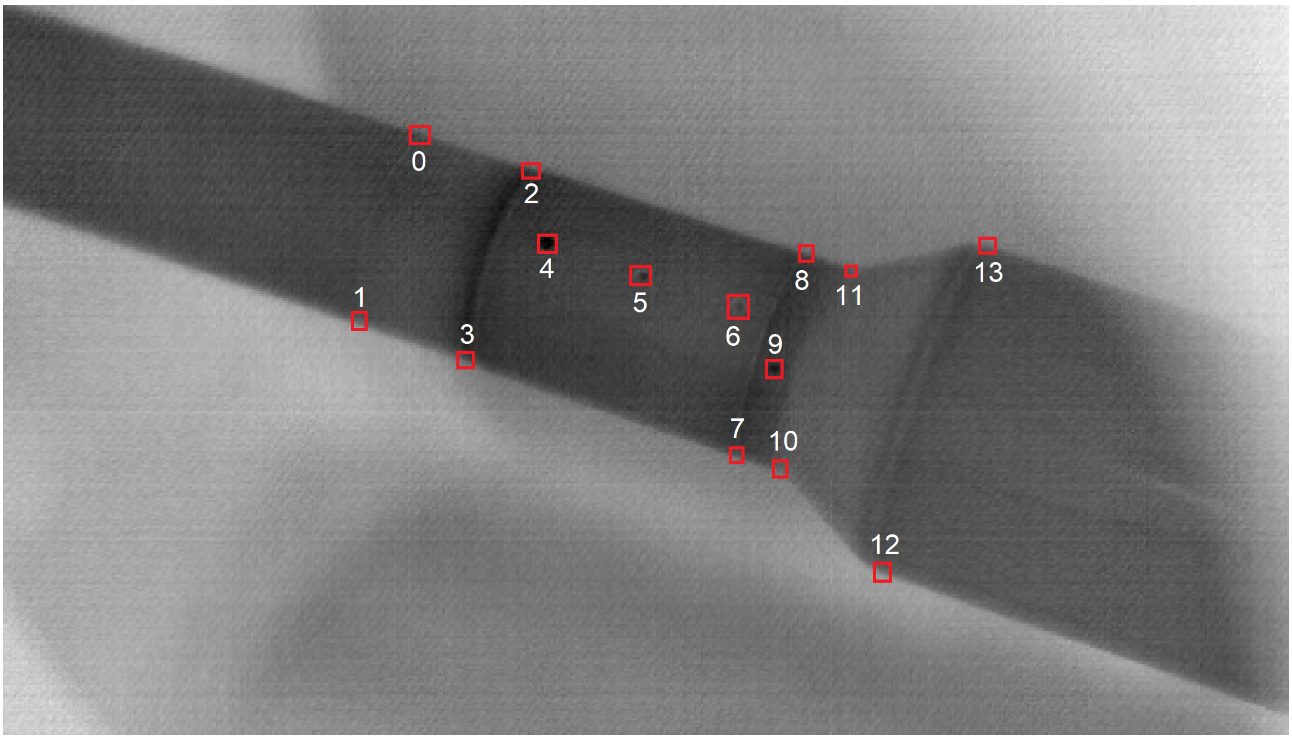

Figure L.3: Geometry features used as fiducial marks in the second and third IR measurement. All had to be manually found. As there were thousands of frames, it is assumed that there is no model movement during measurements. Coordinates were instead extracted from a couple different frames. Real model movement is sufficiently small for this assumption to hold.

L.2. Cone Fiducial Marks for Image Registration (Pressure Taps, Tip & TE)

For the cone measurements the author was originally under the impression that the spread out pressure taps and the LE / TE would be sufficient to align images. However, the author did not take image dewarping into consideration, which would require more evenly spread fiducial marks. Furthermore, due to the significant paint decay seen in these experiments, the pressure taps became impossible to see. An attempt was made to place further fiducial marks after the first run on the model, but most if not all these did not survive the measurements. As no position measurements were taken beforehand, they can not be used for image dewarping. Surviving fiducial marks were used for image alignment as much as possible. This section merely highlights the positions of the geometrical fiducial marks and the runs in which they are visible.

In addition to the constant loss of fiducial marks throughout runs, the highly 3-D shape of the model makes image dewarping more difficult. An attempt was made to have the camera be perpendicular to the surface of the model such that every point along the $Y = 0$ plane were equidistant to the camera plane. Here the Y axis is defined to be positive pointing to the left, with the origin at the tip. However, it proved to be quite difficult to have an exact alignment, leading to the camera having some angle with respect to the ideal case.

Lastly, due to the fact that the pressure taps eventually became fully invisible, dewarping was instead done using the LE and TE of the model. Due to the camera angle with respect to the model, this is not the most optimal solution but it improves data quality.

Num	X (mm)	Surface L/D	Visible in Cone runs:
1	0	0	1, 2, 3, 4, 5
2	13.8	0.18	1, 2, 3
3	19.9	0.26	1, 2, 3
4	26.0	0.34	1, 2, 3
5	32.2	0.42	1, 2, 3
6	38.3	0.50	1, 2, 3
7	44.4	0.58	1
8	50.6	0.66	1
9	56.7	0.74	1
TE	59.6	0.78	1, 2, 3, 4, 5

Table L.2: Fiducial mark coordinates for the Cone measurements. X is the longitudinal position relative to the tip, positive moving towards the TE. Surface L/D is the position of the fiducial marks along the surface of the cone, with the tip being at 0 and the positive direction from the tip to the TE. The last column notes in which measurements each point can be distinguished and used for image registration.

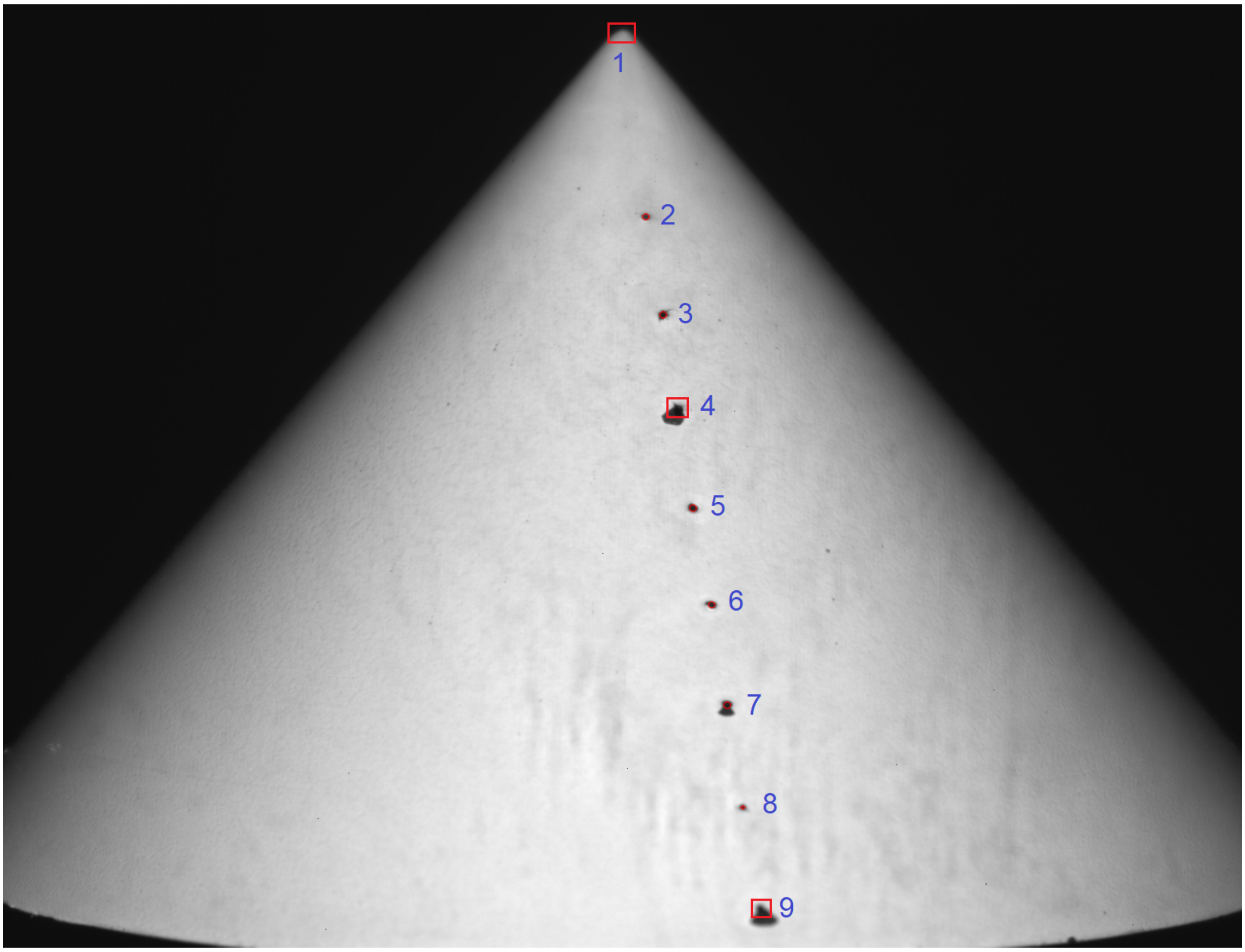

Figure L.4: Fiducial marks used for image registration on the Cone measurements. Shown is the reference after for the first Cone measurement; As the paint showed high degrees of peeling during the cone runs, not all fiducial marks could be used or were detected by the SimpleBlobDetector during the different runs. Fiducial marks includes the pressure taps and the cone tip. Other fiducial marks were put on the model using a whiteboard marker for image alignment, but were often blown off due to paint peeling and therefore not used for image registration. In addition to the marks shown, the TE of the model was also used for image registration.

L.3. Coe and Nute Fiducial Marks

For the Coe and Nute measurements fiducial marks were placed by hand using a black whiteboard marker. During the runs some of these marks slowly vanished over time. This can likely be attributed to wear due to shear forces. This caused some marks to become hard to detect in the measurements for later runs. In addition, the previously mentioned paint bubbles left two circular surfaces that could be used as fiducial marks. These are marks 13 and 16 in Figure L.5.

Fiducial marks were placed in a zigzag pattern with increasing x coordinate. It was attempted to make the spacing more or less evenly, but this proved to be challenging leading to marks having a more or less random spread. No marks were placed in the boat tail, which proved to be a mistake as this makes the dewarping of the boat tail area more difficult. In addition, due to the biconic shape of the nosecone, dewarping is complex in that region, and would ideally require knowledge of the exact y and z positions.

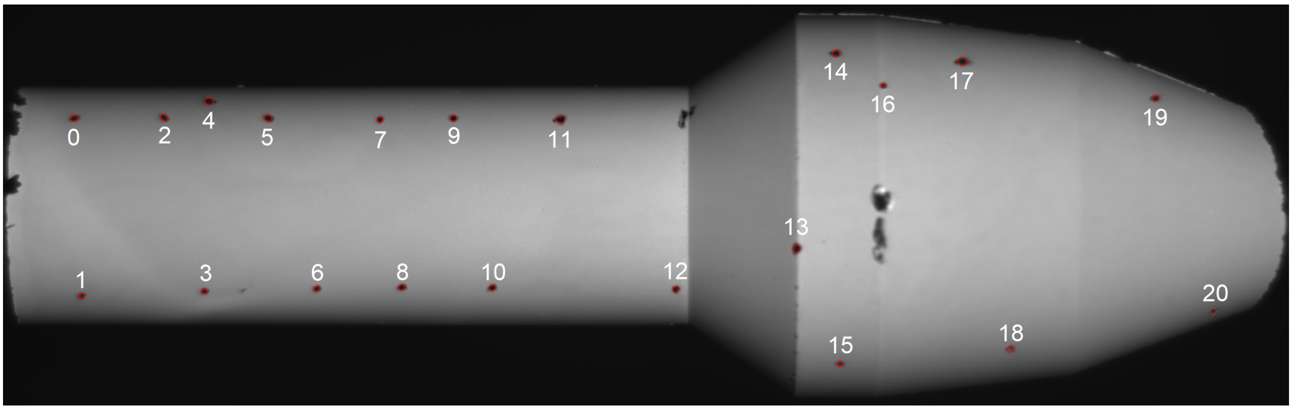

Figure L.5: Fiducial marks used for image alignment and image registration for the Coe and Nute experiments. Shown is the mean reference after of the **CN 6** run with the sCMOS camera. The bobcat camera had a lower FOV, therefore the four fiducials at the edges are not visible in those images. Here all but fiducial marks 13 and 16 were placed by hand using a black whiteboard marker; Fiducials 13 and 16 are remains of paint bubbles that were blown away during runs. This made a circular hole that could be used for image alignment and registration. Due to mechanical wear, not all the fiducial markers could be detected using the SimpleBlobDetector in all measurements.

Num	X (mm)	Num	X (mm)
0	170.5	11	107.6
1	170.0	12	92.6
2	159.7	13	76.7
3	153.8	14	72.3
4	153.0	15	71.7
5	145.0	16	66.0
6	139.6	17	55.6
7	130.5	18	49.5
8	128.4	19	30.4
9	120.9	20	22.2
10	116.4	-	-

Table L.3: Fiducial mark coordinates for the Coe and Nute measurements. X is the axial distance in mm from the tip, positive moving downstream. Measured using a cutout of the model with millimeter paper and a caliper. Accuracy of the measurement is in the order of $\pm 0.2mm$. However, there is likely an additional mismatch in these coordinates due to differences in the fiducial center found by the blob detection algorithm and the center found by manual measurement. The author estimates that overall error should remain smaller than $1mm$.

L.4. Vega-E Fiducial Marks

Two different paint coats were used for the experiments on the Vega-E model, with two different sets of fiducial marks. The locations of both are given in the following subsections.

Vega First Paint Coat Fiducial Marks

For the Vega tests the model was painted two times, thereby requiring two sets of fiducial marks. The first set is discussed in this section and can be seen in Figure L.6. Here 34 fiducial marks were placed throughout the length of the model. The author intended to place less originally, but mistakenly made the spacing between marks too small.

In addition, an extra set of marks exists for the top row of the marks on the payload fairing (each denoted by a or b). Set a was placed first, which was deemed to be too far away from the bottom marks. This led to bad visibility of the bottom marks, which makes detecting them difficult. To solve this, the author originally wanted to place another set at the same positions as the bottom markers, but slightly close to the a set on top. However as can be seen in Figure L.6, the first camera is flipped horizontally. This led to the author misunderstanding where the marks should have been placed, and instead set b was placed on the top row. This was only noted when the run was about to start.

In Table L.4, only the coordinates for the b set are shown as these were the ones that were measured by hand. The a set can still be used for aligning images, but it should be avoided for image dewarping. Lastly, the 0th fiducial mark is a dent in the model created during manufacturing. As its exact coordinates are known, it can be used for dewarping.

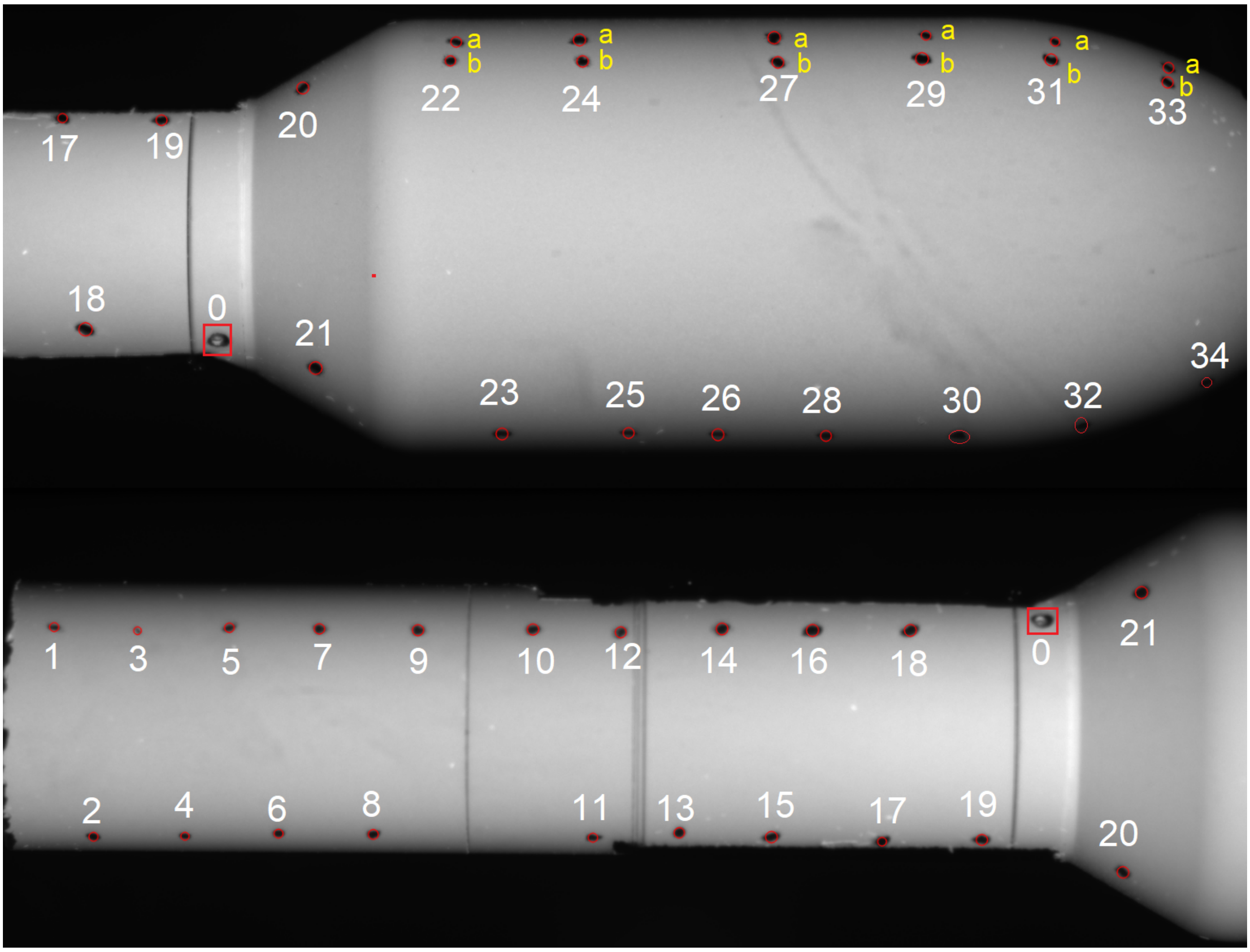

Figure L.6: Caption

Num	X (cm)	Num	X (cm)	Num	X (cm)
0	13.3	12	18.1	24b	9.0
1	24.4	13	17.4	25	8.5
2	24.0	14	16.9	26	7.5
3	23.5	15	16.4	27b	6.8
4	23.0	16	15.9	28	6.3
5	22.5	17	15.1	29b	5.1
6	21.9	18	14.8	30	4.8
7	21.5	19	13.95	31b	3.6
8	20.8	20	12.35	32	3.4
9	20.4	21	12.15	33b	2.25
10	19.1	22b	10.5	34	1.85
11	18.4	23	10.0	-	-

Table L.4: Fiducial mark coordinates for the Coe and Nute measurements. X is the axial distance in mm from the tip, positive moving downstream. Measured using a cutout of the model with millimeter paper and a caliper. Accuracy of the measurement is in the order of $\pm 0.2mm$. Mismatch in fiducial center found by blob detection algorithm and the manual measurement but likely smaller than $1mm$.

Vega Second Paint Coat Fiducial Marks

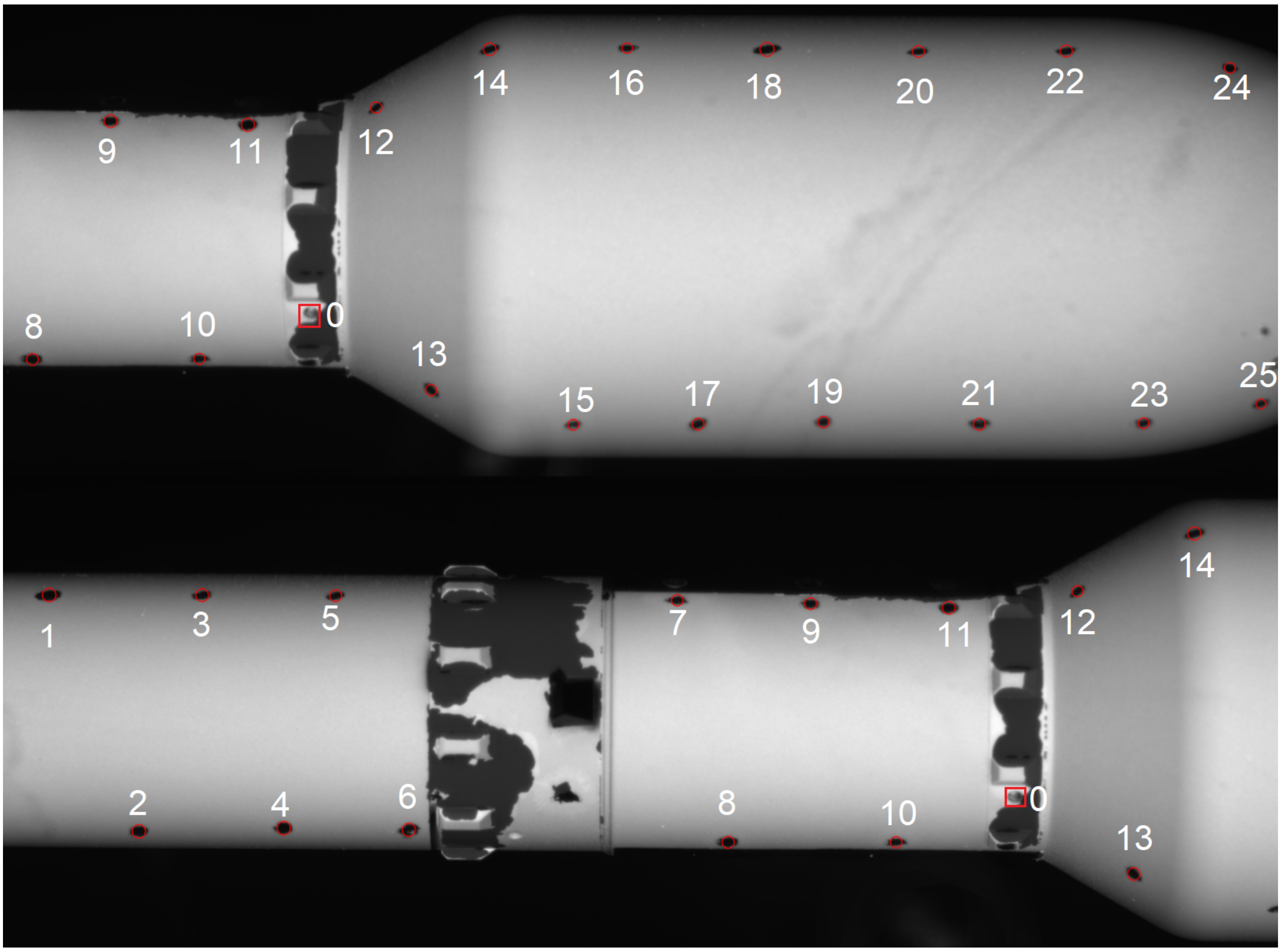

Figure L.7: Caption

Num	X (cm)	Num	X (cm)	Num	X (cm)
0	13.3	9	15.5	18	8.2
1	24.0	10	14.5	19	7.6
2	23.0	11	14.0	20	6.5
3	22.3	12	12.6	21	5.8
4	21.4	13	11.9	22	4.9
5	20.8	14	11.3	23	4.0
6	20.0	15	10.3	24	3.1
7	17.0	16	9.7	25	2.7
8	16.4	17	8.9	26	1.7

Table L.5: Fiducial mark coordinates for the Coe and Nute measurements. X is the axial distance in mm from the tip, positive moving downstream. Measured using a cutout of the model with millimeter paper and caliper. Accuracy in the order of $\pm 0.2mm$.

M IR data

In this appendix, the circumferential mean IR measurement results at different points in time are given.

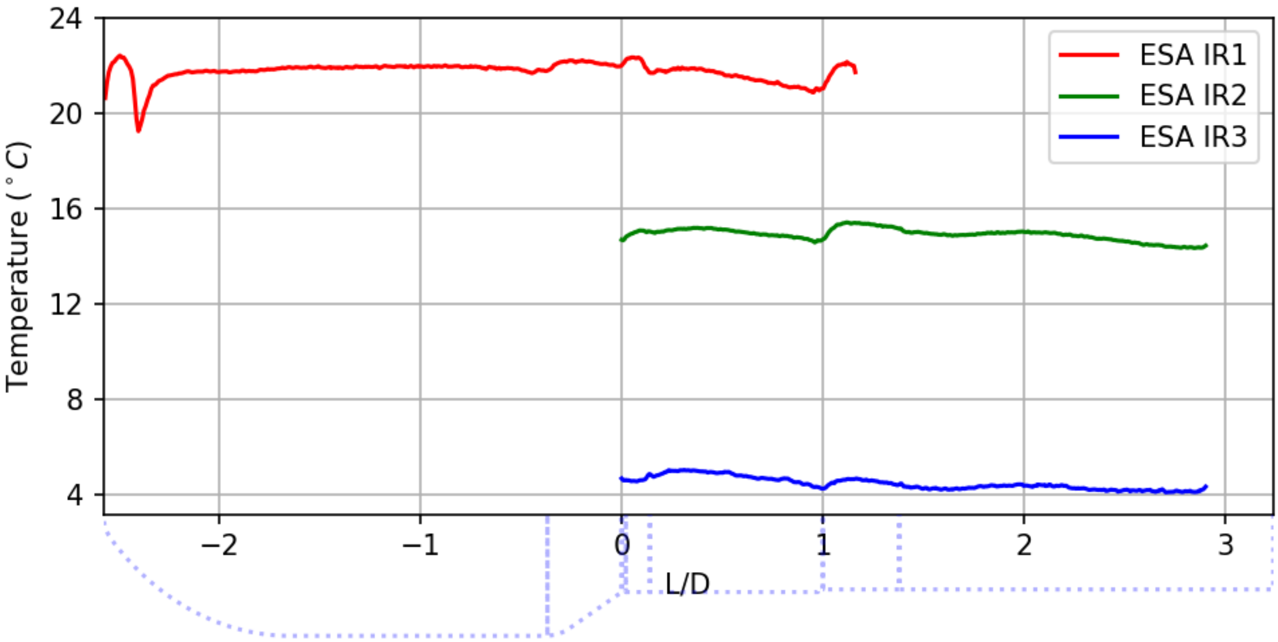

Figure M.1: IR data on wind tunnel startup. Here the model has a small, but notable, temperature gradient, before any air passes through.

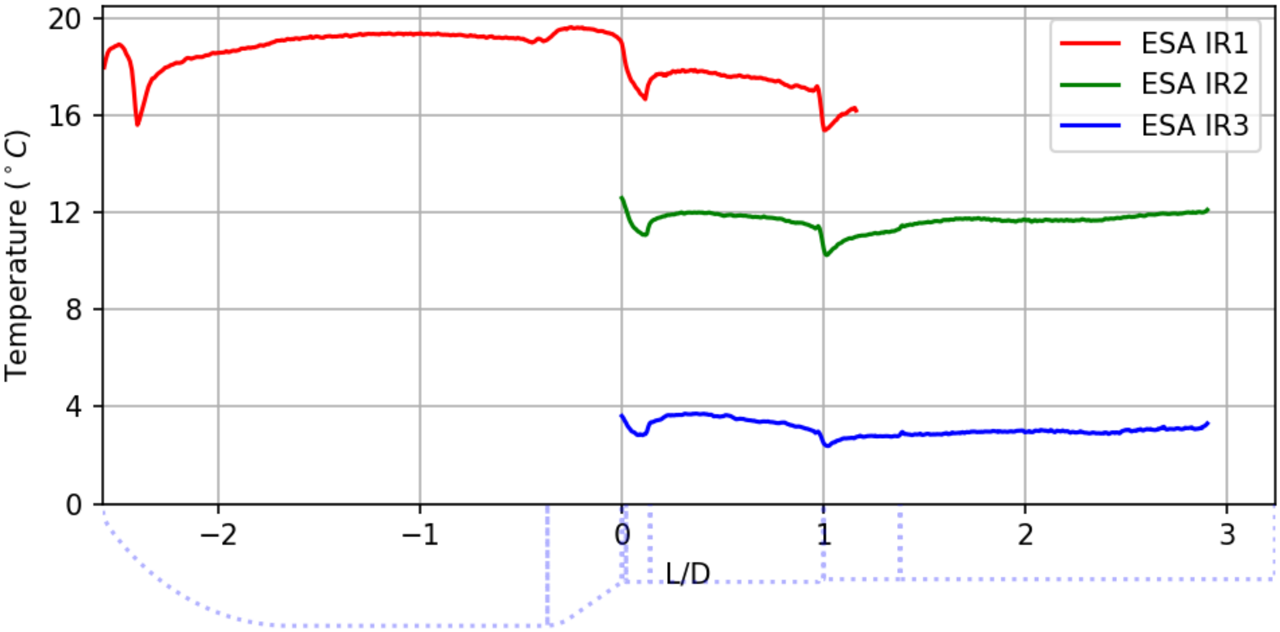

Figure M.2: IR data 5s after wind tunnel startup.

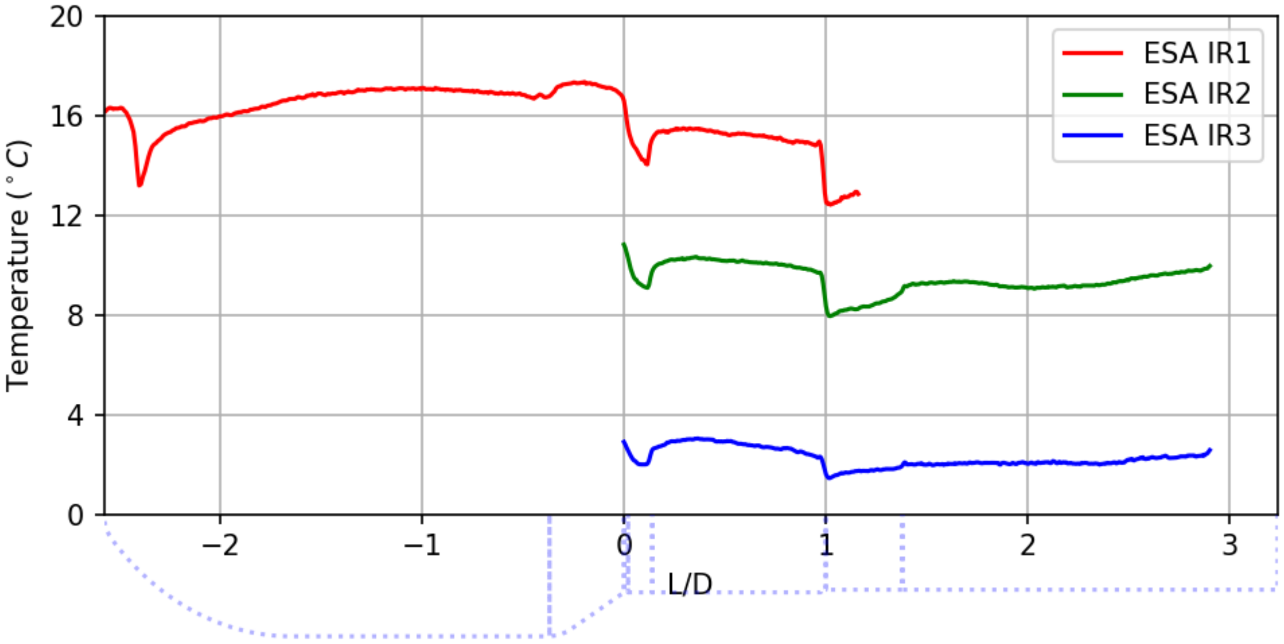

Figure M.3: IR data 10s after wind tunnel startup.

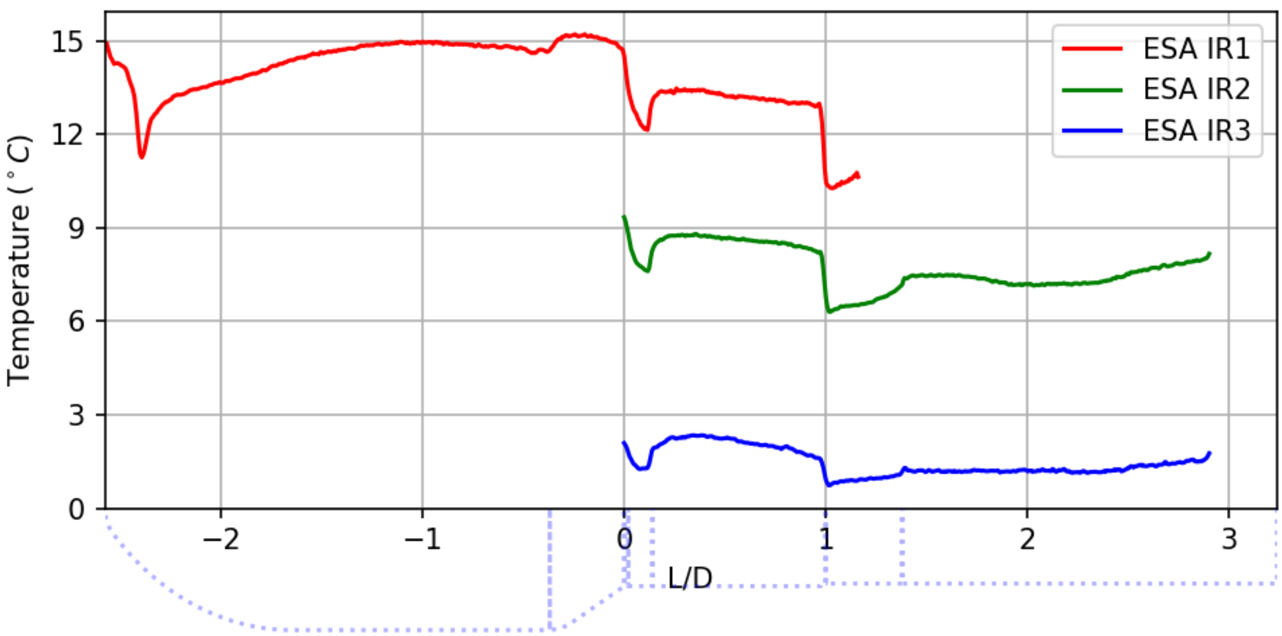

Figure M.4: IR data 15s after wind tunnel startup.

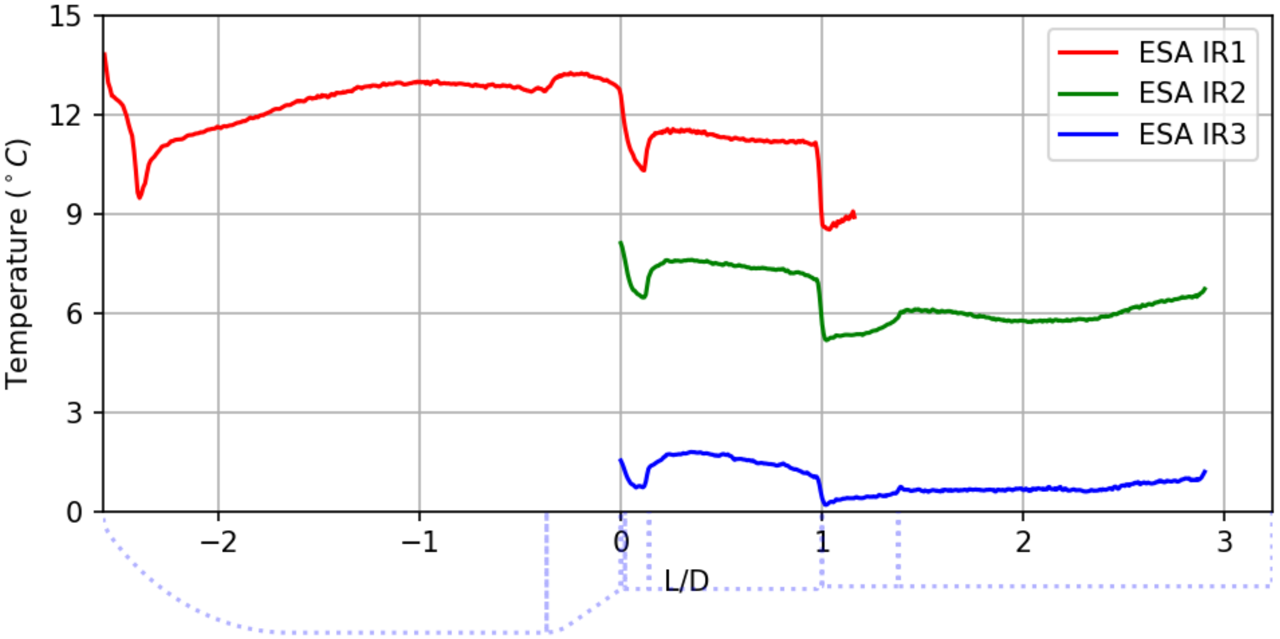

Figure M.5: IR data 20s after wind tunnel startup.

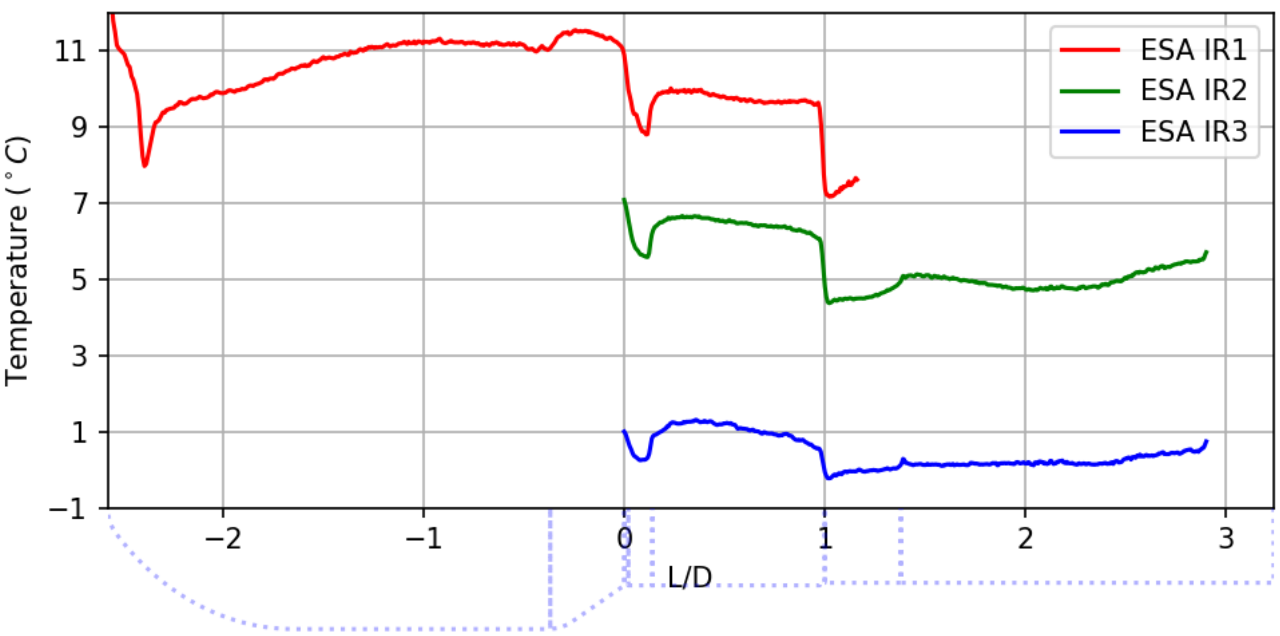

Figure M.6: IR data 25s after wind tunnel startup.

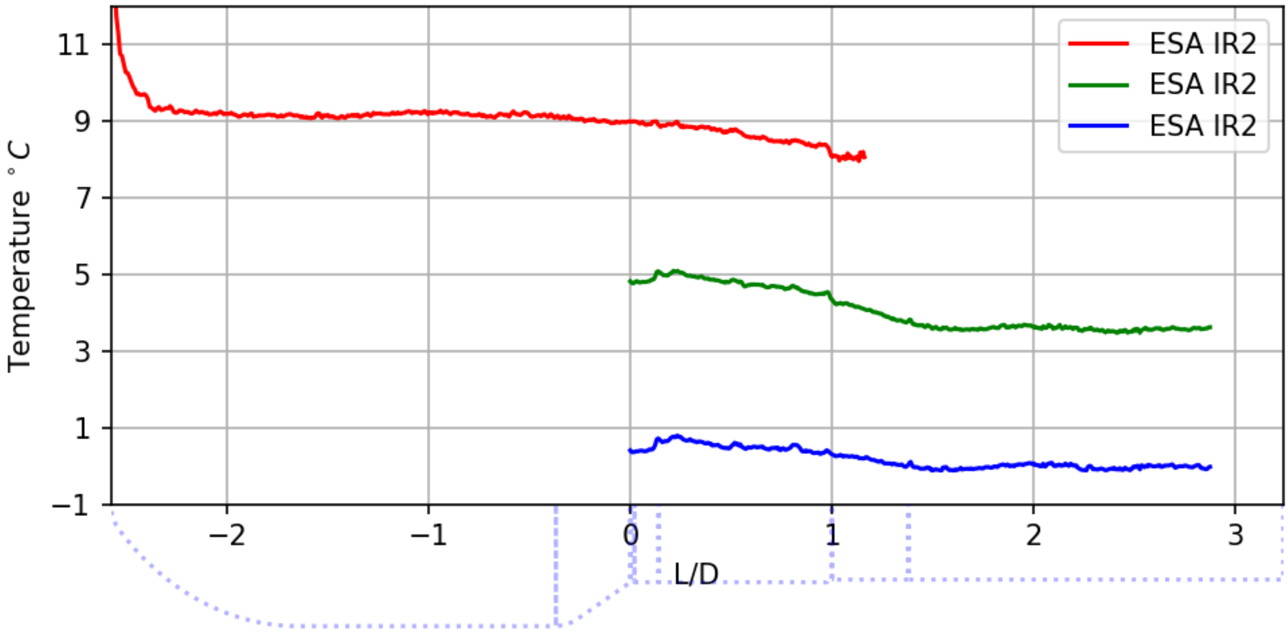

Figure M.7: IR data 60s after the wind tunnel turns off. Notable is that there is still a temperature gradient over the model, that is different to the gradient during the run.

N Warped PLF images for $\alpha = 4°$

This appendix contains the warped PLF images from the $\alpha = 4°$ runs. The following plots all use the shared colormap scaling shown in Figure N.1. Note that the plots shown here were attempted to be dewarped with the "flattening the curve" approach described in Subsection 6.2.1. L/D positions shown are only valid for the masked out fiducial marks, as the circumferential direction is warped.

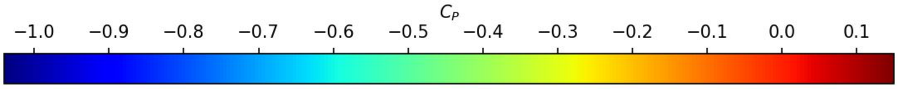

Figure N.1: Scale used in the Vega-E plots shown in this appendix.

N.1. Runs without Protuberances

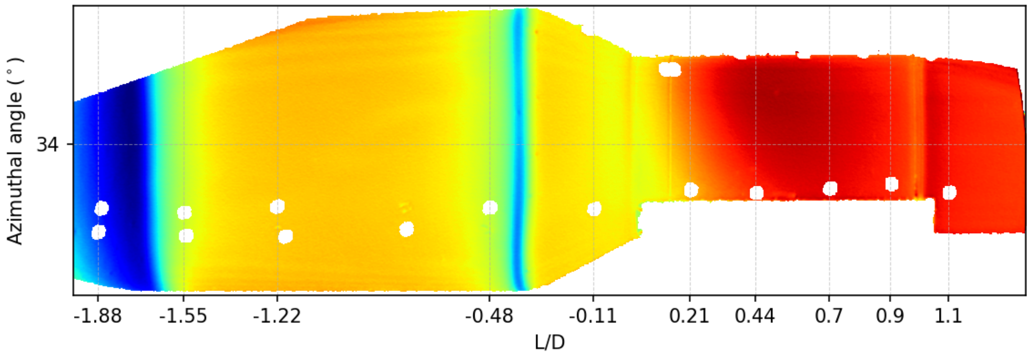

Figure N.2: $M = 0.8$, $\alpha = 4$, protuberances, upper perspective.

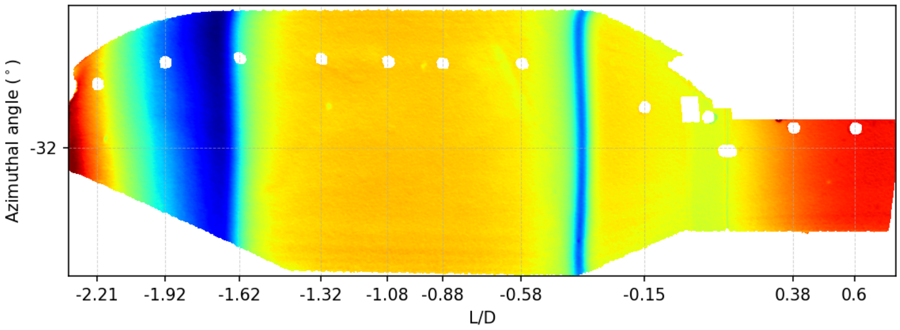

Figure N.3: $M = 0.8$, $\alpha = 4$, protuberances, lower perspective.

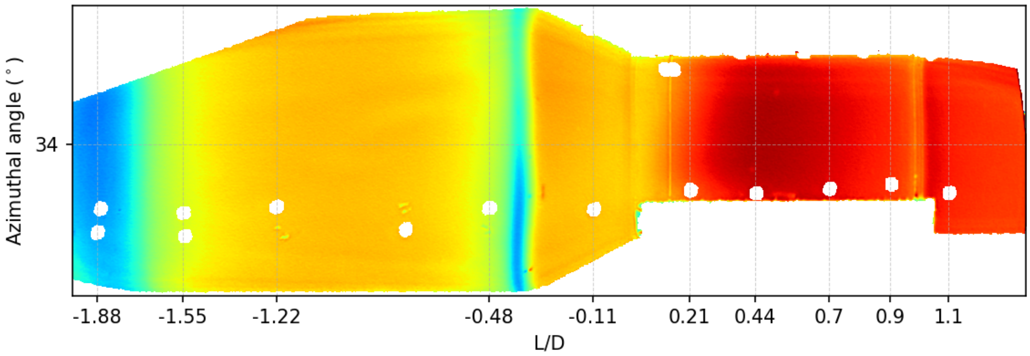

Figure N.4: $M = 0.7$, $\alpha = 4$, no protuberances, upper perspective.

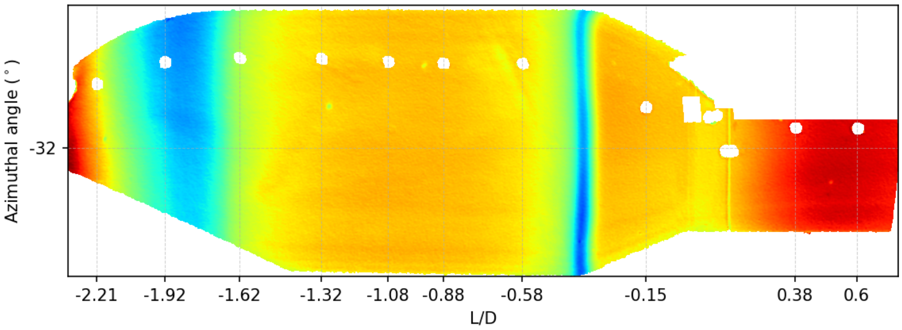

Figure N.5: $M = 0.7$, $\alpha = 4$, no protuberances, lower perspective.

N.2. Runs with Protuberances

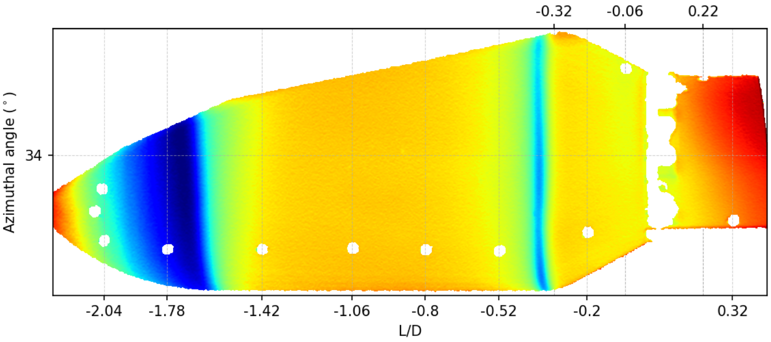

Figure N.6: $M = 0.8$, $\alpha = 4$, protuberances, upper perspective.

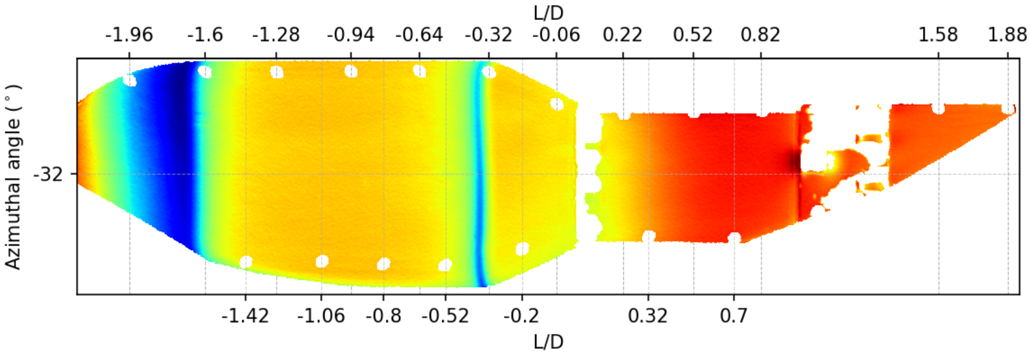

Figure N.7: $M = 0.8$, $\alpha = 4$, protuberances, lower perspective.

O Additional Vega-E Protuberance Results

O.1. Shock waves

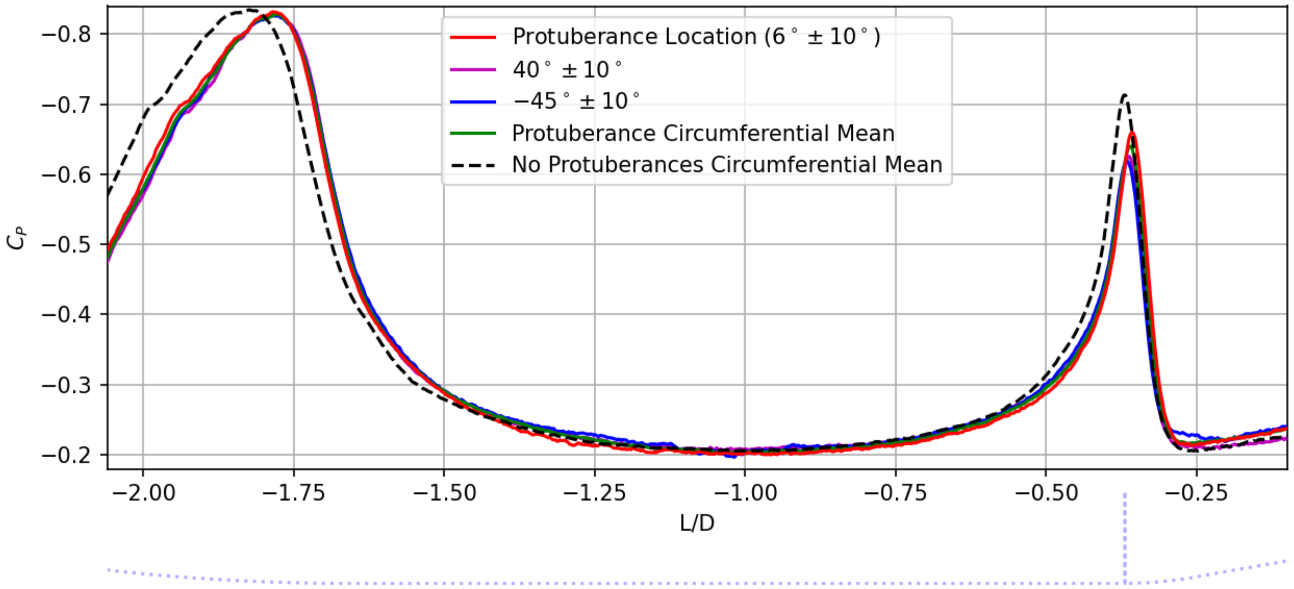

Figure O.1: C_P distribution on the PLF of the Vega-E at $M = 0.75$, $\alpha = 0$ with protuberances. Shown are different strips of $\phi = 20^\circ$. In addition, the circumferential mean for this and the $M = 0.75$, $\alpha = 0$ and no protuberances configuration are also shown. The no protuberances result was scaled by $-0.9kPa$ to better match the other curves.

	Location (L/D)		**Pressure Jump (ΔC_P)**	
	Shock 1	**Shock 2**	**Shock 1**	**Shock 2**
$\phi = 40^\circ \pm 10^\circ$	-1.70	-0.34	0.62	0.41
Big protuberance ($\phi = 6^\circ \pm 10^\circ$)	-1.71	-0.33	0.63	0.45
$\phi = -45^\circ \pm 10^\circ$	-1.70	-0.34	0.62	0.39
Protuberance Circumferential Mean	-1.70	-0.33	0.62	0.42
Clean Configuration	-1.73	-0.34	0.60	0.51

Table O.1: Location of and pressure jump across the shock waves on the Vega-E PLF at different circumferential positions for the $M = 0.75$, $\alpha = 0$ and protuberances measurements. The pressure jump is defined as the difference between the minimum pressure before the shock and the stable pressure after. Included is also the $M = 0.75$, $\alpha = 0$ and no protuberances configuration.

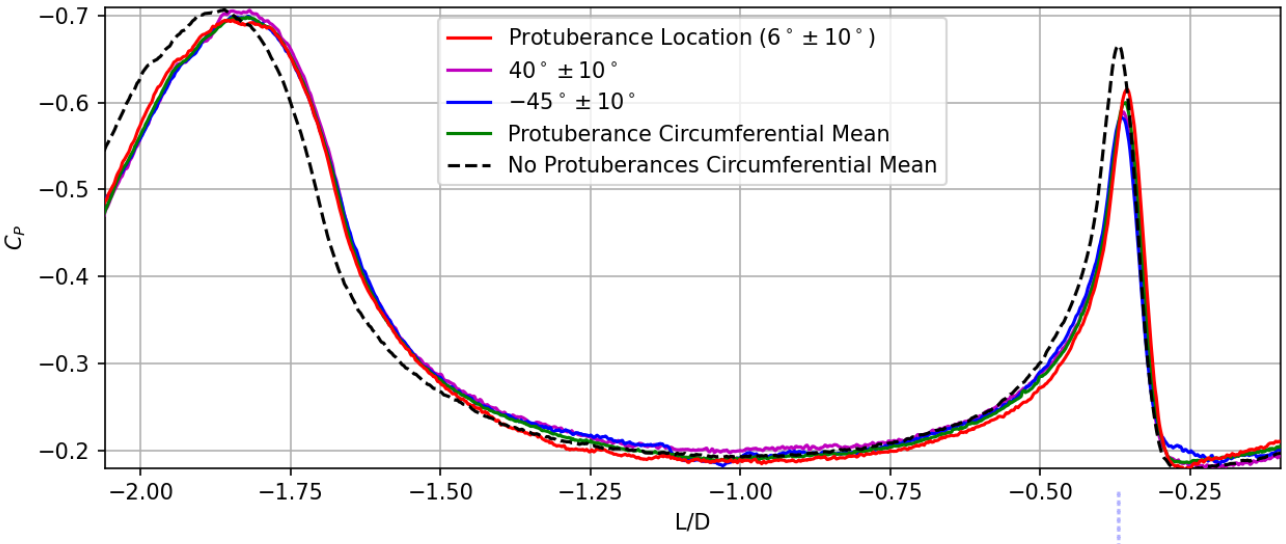

Figure O.2: C_P distribution on the PLF of the Vega-E at $M = 0.7$, $\alpha = 0$ with protuberances. Shown are different strips of $\phi = 20^\circ$. In addition, the circumferential mean for this and the $M = 0.7$, $\alpha = 0$ and no protuberances configuration are also shown. The no protuberances result was scaled by $-0.6kPa$ to better match the other curves.

	Location (L/D)		**Pressure Jump (ΔC_P)**	
	Max C_{P_X} 1	**Max C_{P_X} 2**	**Expansion 1**	**Expansion 2**
$\phi = 40^\circ \pm 10^\circ$	-1.67	-0.33	0.50	0.40
Big protuberance ($\phi = 6^\circ \pm 10^\circ$)	-1.68	-0.32	0.50	0.43
$\phi = -45^\circ \pm 10^\circ$	-1.67	-0.33	0.5	0.38
Protuberance Circumferential Mean	-1.67	-0.33	0.50	0.41
Clean Configuration	-1.70	-0.34	0.51	0.49

Table O.2: Location of the maximum pressure gradient and the pressure jump across where shock waves are located at on the Vega-E PLF at higher Mach numbers. The locations were found at different circumferential positions for the $M = 0.7$, $\alpha = 0$ and protuberances measurements. 1 is around where the first shock is, whereas 2 is at the start of the boat tail around the second shock position. Included is also the $M = 0.7$, $\alpha = 0$ and no protuberances configuration.

O.2. Pressure around protuberance rings

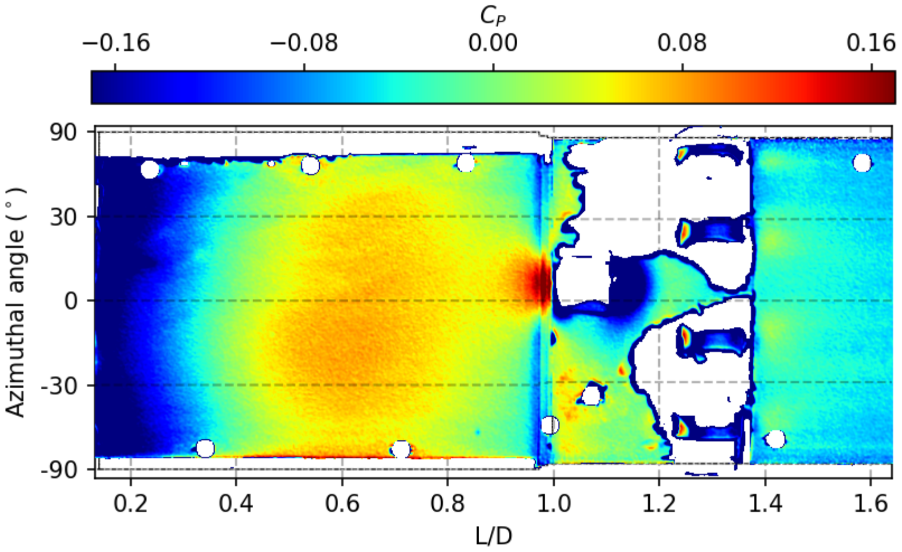

Figure O.3: Zoomed in view of the pressure distribution between 0.13 and 1.65 L/D at M=0.75, $\alpha = 0°$ with protuberances.

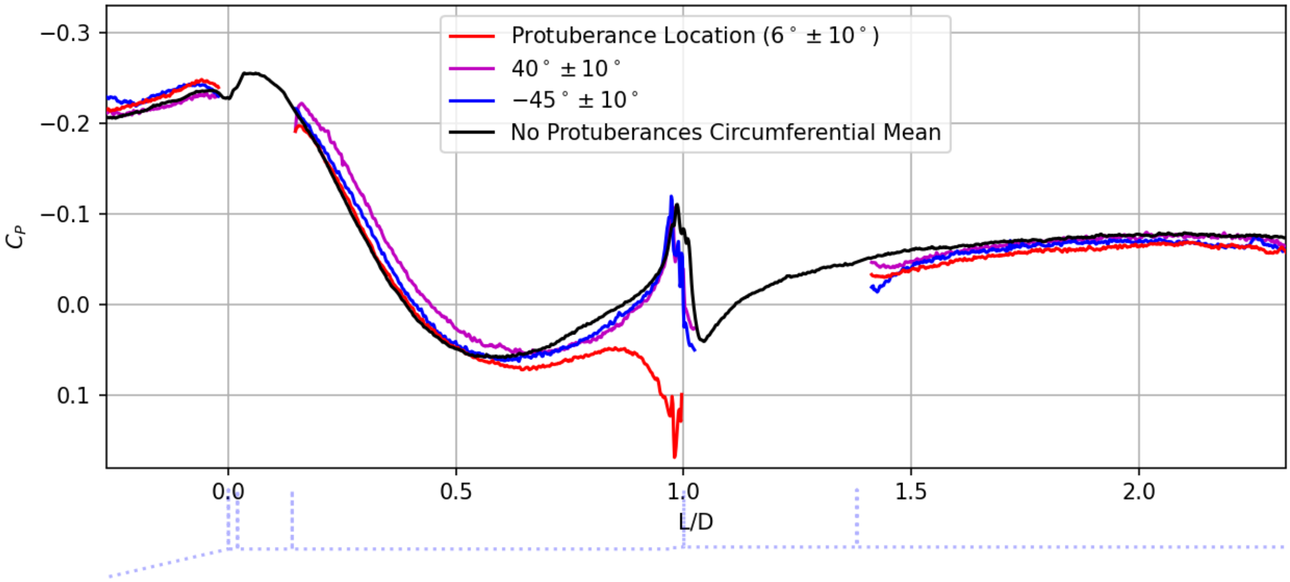

Figure O.4: C_P distribution downstream of the second shock on the Vega-E at $M = 0.75$, $\alpha = 0°$ with protuberances. Shown are different strips of $\phi = 20°$. In addition, the circumferential mean for the $M = 0.75$, $\alpha = 0°$ and no protuberances is shown. Here the no protuberances measurement is adjusted by $-0.9 kPa$ to better match the protuberance data.

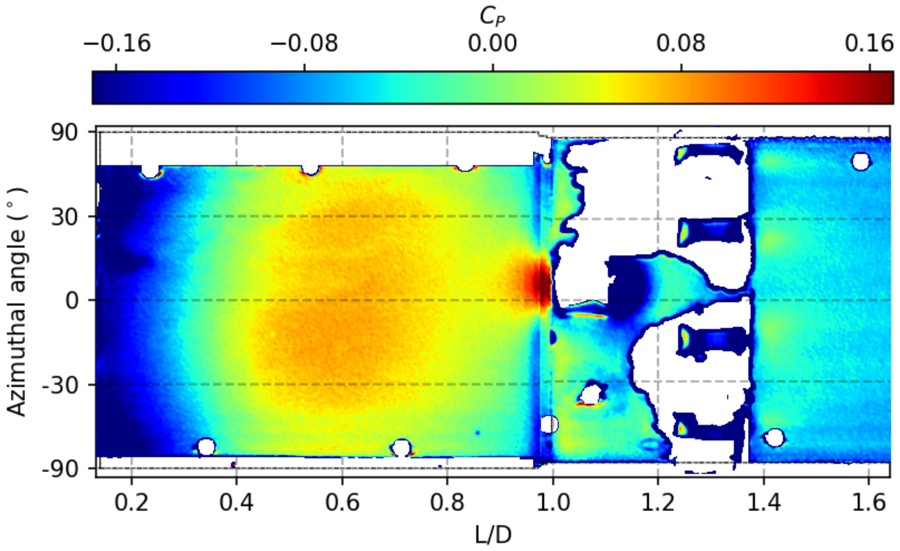

Figure O.5: Zoomed in view of the pressure distribution between 0.13 and 1.65 L/D at M=0.70, $\alpha = 0°$ with protuberances.

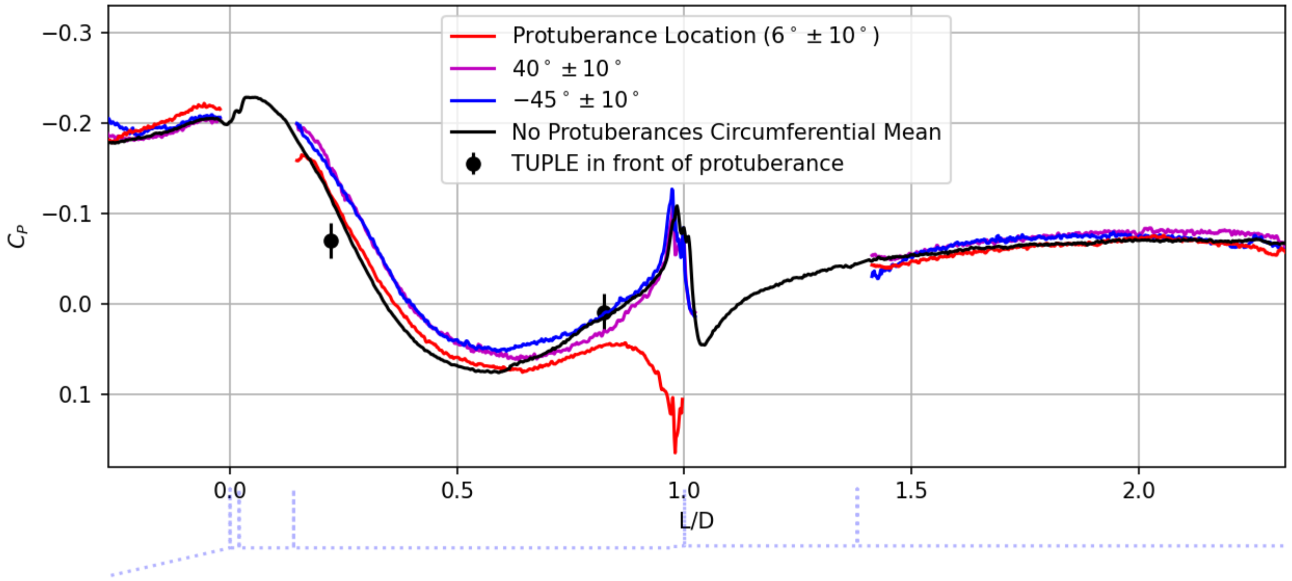

Figure O.6: C_P distribution downstream of the second shock on the Vega-E at $M = 0.7$, $\alpha = 0°$ with protuberances. Shown are different strips of $\phi = 20°$. In addition, the circumferential mean for the clean configuration is shown, along with TUPLE pressure tap results. Here the baseline is adjusted by $-0.6kPa$ to better match the protuberance data.

O.3. Reattachment point

	Reattachment point (*L/D*)	**Separation ratio (L_s/H_b)**
Big protuberance	0.33-0.34	3.67-3.72
34° away from the big protuberance	0.32-0.36	3.72-3.89
−51° away from the big protuberance	0.31-0.32	3.61-3.67
Clean configuration	0.286	3.49

Table O.3: Boat-tail flow separation ratio (length divided by height) and reattachment point at three different ϕ for the $M = 0.75$, $\alpha = 0°$ and protuberances configuration. Values for the clean configuration are also shown for comparison. Locations for the protuberance configuration were obtained from the 20° strips that can be seen in Figure 8.21. Due to noisier data, the values for the protuberance configuration are expected to be less accurate.

	Reattachment point (L/D)	**Separation ratio (L_s/H_b)**
Big protuberance	0.31-0.32	3.50-3.56
34° away from the big protuberance	0.30-0.33	3.50-3.67
−51° away from the big protuberance	***0.27***	3.33
Clean configuration	0.265	3.34

Table O.4: Boat-tail flow separation ratio (length divided by height) and reattachment point at three different ϕ for the $M = 0.7$, $\alpha = 0°$ and protuberances. Values for the clean configuration are also shown for comparison. Locations for the protuberance configuration were obtained from the 20° strips that can be seen in Figure 8.21. Due to noisier data, the values for the protuberance configuration are expected to be less accurate. Note that no data could be extracted for the most upstream position at $\phi = -51°$ from the protuberance, so instead only the clean configuration was used.